

Contents

1	Introduction	11
1.1	Statistical mechanics and Computer simulation	11
1.2	Phase transitions	13
1.3	Liquid-vapor transition	14
1.4	What are colloids?	16
1.5	Potential of mean force	16
1.6	Phase behavior of colloidal dispersions	17
1.7	Depletion forces	18
1.8	Statistical mechanical formalism	20
1.9	Non-spherical colloids	21
1.10	Outline of the thesis	22
2	Mixtures of spherical colloids and rodlike polymers	25
2.1	Introduction	25
2.2	Simulations	26
2.2.1	<i>Configurational Bias Monte Carlo in the Gibbs-Ensemble</i>	26
2.2.2	<i>Fluid-fluid coexistence</i>	28
2.2.3	<i>Solid-fluid transition</i>	30
2.3	Theory	32
2.3.1	<i>Perturbation theory</i>	32
2.3.2	<i>The limit $L \rightarrow \infty$</i>	32
2.3.3	<i>Comparison with simulation results</i>	33
2.4	Discussion	34
3	Isostructural solid-solid transition	37
3.1	Introduction	37
3.2	Square well systems in two and three dimensions	38
3.2.1	<i>Solid-solid coexistence</i>	38
3.2.2	<i>Fluid-solid coexistence</i>	41
3.2.3	<i>Results</i>	42
3.2.4	<i>High density limit</i>	44
3.3	Cell model calculations	47
3.4	Yukawa potential	50
3.5	Square shoulder potential	52
3.6	Polydispersity	54
3.7	Conclusion	55

4	Freezing of polydisperse hard spheres	57
4.1	Introduction	57
4.2	Semigrand ensemble	59
4.3	Gibbs-Duhem integration	60
4.4	The initial slope	61
4.5	Scaling	63
4.6	Results	64
4.7	The infinite pressure limit	68
4.8	Conclusion	71
5	The phase diagram of hard spherocylinders	73
5.1	Introduction	73
5.2	Brief summary of the phase diagram	76
5.2.1	<i>Phase diagram for $L/D \leq 5$.</i>	76
5.2.2	<i>Phase diagram for $L/D > 5$.</i>	77
5.3	Simulation techniques	78
5.3.1	<i>Equilibration</i>	78
5.3.2	<i>Free energy calculations</i>	80
5.3.3	<i>Kofke's Gibbs-Duhem integration</i>	84
5.4	Phase diagram for $L/D \leq 5$	85
5.4.1	<i>Phase behavior for $0 \leq L/D \leq 3$</i>	85
5.4.2	<i>Phase behavior for $3 \leq L/D \leq 5$</i>	87
5.5	The rotator phase	91
5.5.1	<i>Finite densities</i>	91
5.5.2	<i>Close packing limit</i>	93
5.6	Phase diagram in the $L/D = 5-60$ region	98
5.6.1	<i>Numerical Techniques</i>	98
5.6.2	<i>Results</i>	101
5.6.3	<i>The AAA crystal phase</i>	102
5.7	The Onsager limit	104
5.7.1	<i>Scaling</i>	104
5.7.2	<i>Results</i>	104
5.7.3	<i>What is the order of the nematic-smectic transition?</i>	105
5.8	Conclusion	108
6	Mixtures of spherocylinders and polymers	111
6.1	Introduction	111
6.2	Perturbation theory	113
6.3	Spherocylinders with attraction	116
6.3.1	<i>The angle dependent pair potential</i>	116
6.3.2	<i>Simulation</i>	119
6.3.3	<i>Results</i>	120
6.4	Nematic-Nematic coexistence in the Onsager limit	121
6.4.1	<i>Infinitely long-ranged attraction for long rods</i>	123
6.5	Overview of demixing transitions	125

6.6	Conclusion	126
7	Binary mixtures of hard ellipsoids	129
7.1	Introduction	129
7.2	Simulation results	133
7.3	Conclusion	137
	Bibliography	139
	Summary	143
	Samenvatting voor iedereen	145
	Curriculum Vitae	151

INTRODUCTION

1

In this introductory chapter we briefly review how computer simulations can be used to study first-order phase transitions. We then focus on phase transitions in colloidal systems. First, we discuss how we can change the qualitative features of the phase diagram by changing the range of the interactions between the colloids,. In practice, such variations in the range of the inter-colloidal interactions can be achieved by mixing the colloids with polymers of different sizes. Before embarking on the actual numerical study of colloids and colloid-polymer mixtures, we give a brief general introduction to such systems. In particular, we give an outline of the statistical mechanical framework that allows us to describe such complex systems with relatively simple models.

Statistical mechanics and Computer simulation

1.1

The state of a liter of water can be described using only a few macroscopic equilibrium properties. This is remarkable, considering that the fluid consists of some 10^{25} mutually interacting atoms. The secret lies in the word *macroscopic*. All atomic processes and fluctuations take place extremely fast on a very small distance scale and will be averaged out while we perform our measurement. Only those particular combinations of atomic coordinates that are essentially time independent can be macroscopic observable. To compute the equilibrium properties of a bulk substance, there is little need to know the exact trajectory of every atom in the system. Rather, we like to calculate the *average* properties starting from a proper atomistic model. Thermodynamics relates macroscopic equilibrium properties with each other and statistical mechanics provides the link between these quantities and the atomistic description on a microscopic level [1, 2].

The fundamental quantity in equilibrium statistical mechanics is the partition function, the sum of the Boltzmann factors over all possible states s of a canonical system of N atoms in a volume V at a temperature T

$$Z = \sum_s e^{-E_s/k_B T}. \quad (1.1)$$

Here k_B is Boltzmann's constant and E_s is the total energy of the system in state s . The Boltzmann factors $e^{-E_s/k_B T}$ are proportional to the probability of finding the system in state s . One therefore can also calculate the average of any dynamical property A as

$$\langle A \rangle = \frac{1}{Z} \sum_s A_s e^{-E_s/k_B T}. \quad (1.2)$$

The ergodic theorem states that this *ensemble* average $\langle A \rangle$ is equal to the time average of A that would be obtained by following the natural dynamics of the system for a sufficiently long time [2]. The canonical partition function Z is connected to the thermodynamic Helmholtz free energy F by

$$F = -k_B T \ln Z. \quad (1.3)$$

The average value of most equilibrium properties is related in one way or another to (derivatives of) the Helmholtz free energy F , and can therefore be expressed in terms of the partition function Z . For instance, the energy E can be calculated as follows,

$$\begin{aligned} E &= \frac{1}{Z} \sum_s E_s e^{-E_s/k_B T} \\ &= k_B T^2 \frac{\partial \log Z}{\partial T} = \frac{\partial F/T}{\partial (1/T)}. \end{aligned} \quad (1.4)$$

In view of the central role played by the partition function, the aim of many theoretical studies in equilibrium statistical mechanics is to find (approximate) expressions for the partition function, for specific model systems. An alternative route to extract the macroscopic information from a microscopic model, is to perform computer simulations [3]. There are two basic styles of computer simulations: Monte Carlo (MC) and molecular dynamics (MD). In an MD simulation one solves Newton's equation of motion numerically for a system containing several hundreds up to several millions of molecules, in discrete time steps. The desired macroscopic observables are computed simply by time averaging. Hence, the MD simulation follows the natural time evolution of the system, which includes dynamical information. With the use of periodic boundaries, a small number of atoms (usually 100-10000) is usually already enough to approximate the behavior of an infinite system.

The Monte Carlo method can be considered a numerical implementation of Gibbs' concept of averaging over an ensemble of equilibrium states: in MC simulations, macroscopic observables are obtained by directly computing properly weighted averages over the accessible states of a many-particle system (cf. eqn. 1.2). Because the order in which this averaging is carried out has no physical meaning, the MC method contains no dynamical information. In practice, the averaging over the most probable states of this system is achieved by using a random sampling procedure. Starting from a configuration, one or more particles are moved randomly. Each move is accepted or rejected with a certain probability, such that the probability of finding the system in a state s is proportional to the Boltzmann factor $e^{-E_s/k_B T}$ (in practice, only the potential energy U_s needs to be considered in this sampling).

As computer simulations of classical many-body systems are, in principle, exact (i.e. can be carried out to any desired accuracy), they can be used to test the assumptions made in approximate theories of many-body systems. Simulations are also of great practical use in predicting the macroscopic properties of new materials or novel substances, before embarking on the expensive task of actually making these materials. Moreover, computer simulations can be used to assess the behavior of materials under conditions that are not easily achieved in experiments. Finally, computer simulations sometimes allow us to predict qualitatively new behavior, or new phases of known substances, and thereby act as a guide to both theoretical and experimental work.

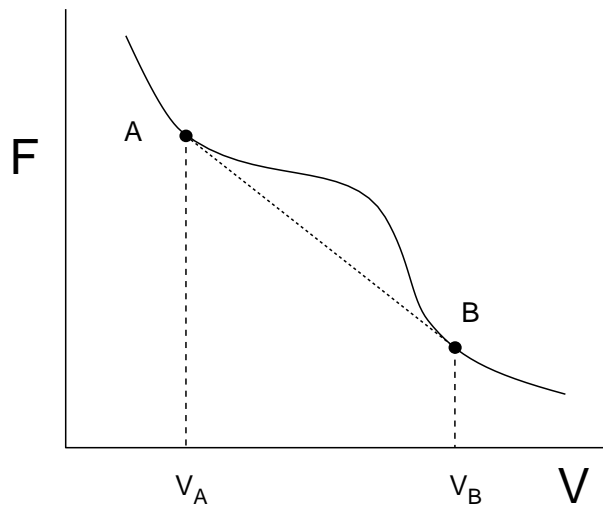
Phase transitions

The early Greek natural philosophers already knew that all matter could be classified in one of the four primary elements: air, water, earth and fire. Nowadays, this classification is still largely valid, although we now use the word “phases” where the Greek spoke about “elements”. The four most abundant phases of matter are the vapor, the liquid, the solid and the plasma. (The last phase is a special case because it does not consist of the same building blocks as the other three: it is basically an ionized gas).

Matter can transform from one phase to the other by a “phase transition”. For instance, increasing the temperature of a liquid results in boiling and evaporation. Different phases can be in equilibrium with each other, coexisting together, without changing visibly in time. An example is the hot coffee in our thermos flask, where the liquid coffee is in equilibrium with its vapor. Atoms move continuously from the liquid to the vapor phase and vice versa, but on average the situation does not change.

How can we establish the properties of such coexisting phases? This question can be answered by thermodynamics [1]. In equilibrium a system has minimized its free energy. This minimized free energy F will in general be a complicated function of the volume V and the number of particles N (both extensive parameters), and the temperature T (an intensive parameter). The precise form of the dependence of F on N , V and T is determined by the Hamiltonian of the system. In figure

1.1 we show a schematic plot of the free energy F as a function of the volume V . At small V , i.e. high density, we have, for instance, a liquid phase. Expanding the volume at constant temperature, the free energy of the system will follow the curve, until point A is reached. Beyond that point the system can lower its total free energy by splitting up into two phases, one with V_A and one with V_B . As it is extensive, the free energy of the total system is just a linear combination of the free energy of the liquid and that of the vapor phase, as indicated by the dotted straight line. If we increase the volume, more and more liquid will



evaporate, but the densities of the coexisting phases remain fixed. When the volume reaches point B, there is only a vapor phase and the free energy follows the solid line again. The coexisting densities are determined by the coexistence relations

$$\begin{aligned} T_{\text{vap}} &= T_{\text{liq}}, \\ P_{\text{vap}} &= P_{\text{liq}}, \\ \mu_{\text{vap}} &= \mu_{\text{liq}}, \end{aligned} \tag{1.5}$$

where μ denotes the chemical potential. These densities can be found directly from the free energy curve by the so-called “common tangent construction” [1]. The tangents of

the free energy curve at points A and B have to be equal to the slope of the straight line connecting those points. This geometrical procedure is equivalent to imposing eqn. 1.5. The kind of phase transition we discussed above is called first-order and can be recognized by the difference in density between two coexisting phases. In contrast, during a continuous (or second-order) phase transition, the system will lower its free energy by undergoing a transformation from one phase to the other at a single density, instead of splitting up in two distinct coexisting phases.

The properties of coexisting phases can be plotted as a function of thermodynamic control variables in a phase diagram. The common $P - T$ diagram consists of curves delimiting the areas in pressure-temperature space where a single phase is stable. Phase transitions can be indicated in a $P - T$ diagram by single curves because, at coexistence, both the pressure and the temperature of the two phases are equal. In contrast, if we were to indicate the location of a phase transition in a temperature-density $T - \rho$ diagram, the curves that describe the densities of the coexisting phases do not coincide, because there is no thermodynamic condition stating that the densities of coexisting phases should be equal. Hence, in a $T - \rho$ diagram, stable phase regions are separated by a density gap, called the two phase or coexistence region, where neither pure phase is stable and the system is forced to phase separate.

1.3 Liquid-vapor transition

Since the work of van der Waals [4], we know that there is no essential distinction between a liquid and a vapor. Above the critical temperature T_c , a vapor can be compressed continuously all the way to the freezing point. Yet below T_c , a first-order phase transition separates the dilute fluid (vapor) from the dense fluid (liquid). In the van der Waals model the molecules are described by hard spheres with an infinitely weak, infinitely long-ranged attraction. Application of thermodynamic perturbation theory results in the complete phase diagram for the van der Waals model. The diagram in the density-temperature phase plane shown in figure 1.2a includes besides the usual liquid vapor transition also crystallization. This feature was not incorporated in the original van der Waals equation because the hard sphere crystallization transition was not recognized at the time. At high temperatures the molecules behave effectively as hard spheres, which show only crystallization but do not have a liquid vapor transition [2]. At lower temperatures, between the critical point and the triple point temperature a liquid-vapor transition is possible. Below the triple-point temperature the liquid phase becomes meta-stable and there is only a gas-solid transition. Although the van der Waals theory becomes exact in the limit of weak, long-ranged intermolecular interactions [5], there is no fundamental reason why the liquid-vapor transition should occur in every atomic or molecular substance, nor is there any rule that forbids the existence of more than one fluid-fluid transition. Whether a given compound will have a liquid phase, depends sensitively on the range of the intermolecular potential: as this range is decreased, the critical temperature approaches the triple-point temperature, and when T_c drops below the latter, only a single stable fluid phase remains (see figure 1.2b). This phenomenon is well known in mixtures of spherical colloidal particles and non-adsorbing polymer, where the range of the attractive part of the effective colloid-colloid interaction can be varied by changing the size of the polymer [6–10]. Experiment, theory and simulation all suggest that when the width of the attractive well becomes less than approximately one third of

the diameter of the colloidal spheres, the colloidal ‘liquid’ phase disappears. In fact, there is numerical evidence that in a molecular compound (C_{60}), the range of the intermolecular attraction may be sufficiently short to suppress the liquid-vapor transition [11, 12]. The fact that the liquid-vapor transition is just metastable can result in special properties. For example, most successful crystallizations of globular proteins have been carried out under circumstances where the liquid-vapor transition was suppressed [13]. Apparently, the absence of an intermediate liquid phase is of great importance for the success of protein crystallization.

As will be discussed later in this thesis, systems with a very short-ranged interaction may exhibit a novel type of phase transition that occurs entirely at the solid phase side of the phase diagram, but is otherwise in many ways reminiscent of the liquid-vapor transition

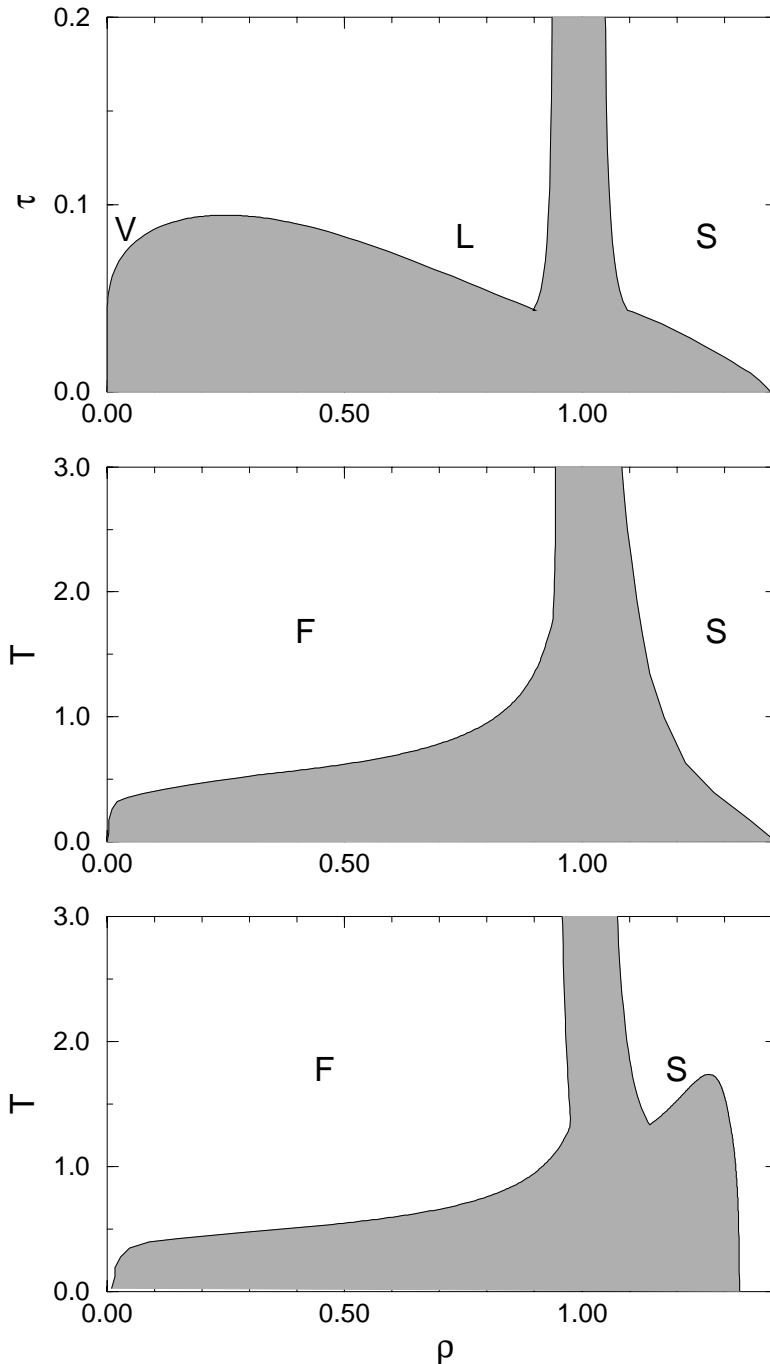


Figure 1.2. *Generic temperature–density phase diagrams. Top: The van der Waals limit shows besides the fluid-solid transition a liquid-vapor transition. Middle: for a medium ranged potential the liquid phase becomes metastable. Bottom: For very short ranged potentials the critical point reappears inside the solid phase. Here, a expanded solid is in coexistence with a condensed crystal.*

(see figure 1.2c). Again this kind of phase behavior should be observable in certain colloid-polymer mixtures (although, at the time this thesis is written, it has not yet been observed). Because the properties of colloidal dispersions and colloid-polymer mixtures constitute the main themes of this thesis, we first explain what they are.

1.4 What are colloids?

A colloidal dispersion consist of microscopic solid (or liquid) particles dispersed in a solvent [14]. The linear size of those particles is typically between 1nm and 1 μ m. Small enough to exhibit Brownian motion caused by the surrounding solvent molecules but still much larger than those molecules. Biological complexes like viruses, proteins, micelles, vesicles consisting of membranes, blood cells but also synthetic polymers belong to this class of particles. Colloids are important in many industrial processes as well, as they occur in, for example, paints, cosmetics and foods. During the past decades, much effort has been devoted to the synthesis of well characterized colloidal particles that have a very narrow distribution in sizes and shapes. Such mono-disperse colloids can act as model systems to study the factors that determine the structure, dynamics and phase behavior of such systems [8]. There is a surprising analogy between the statistical behavior of such colloidal dispersions and that of simple atomic fluids. The statistical thermodynamic properties can be derived in the same way as for atomic systems, by treating the solvent as a continuous background that exerts fluctuating forces on the colloidal particles. These Brownian forces can be averaged and replaced by the so-called potential of mean force. Onsager [15] and McMillan and Mayer [16] showed that by using this effective potential as input the full statistical mechanical machinery developed for atomic systems can be used to describe the thermodynamic phase behavior of colloidal dispersions.

1.5 Potential of mean force

As we wish to use the concept of the potential of mean force later on for the description of polymer colloid mixtures it is instructive to derive it first for colloidal particles dispersed in a solvent. This treatment is largely taken from Lekkerkerker et al [17].

We consider a suspension of N colloidal particles dispersed in a solvent in a volume V which is in equilibrium with a large reservoir solely containing the solvent. In the reservoir the solvent has a (hydrostatic) pressure P_0 and a fugacity $z_0 = \exp(\beta\mu_0)$ where μ_0 is the chemical potential of the solvent and $\beta = 1/kT$ is the inverse temperature. Since we are imposing the fugacity of the solvent, the colloidal suspension can be regarded an open system and the proper partition function for the system is then

$$\Xi(N, V, T, \mu_0) = \sum_{m=0}^{\infty} z_0^m Z(N, V, T, m), \quad (1.6)$$

where $Z(N, V, T, m)$ is the canonical configurational partition function for N colloidal particles and m solvent molecules at constant V and T

$$Z(N, V, T, m) = \frac{1}{N!m!} \int e^{-\beta U(\mathbf{r}^N, \mathbf{r}^m)} d\mathbf{r}^N d\mathbf{r}^m, \quad (1.7)$$

where $U(\mathbf{r}^N, \mathbf{r}^m)$ is the interaction potential of the configuration given by the positions \mathbf{r} of the N colloids and the m solvent molecules. We define the potential of mean force

$W(r^N, \mu_0)$ by writing the grand canonical partition function as

$$\Xi(N, V, T, \mu_0) = \frac{1}{N!} \int e^{-\beta W(r^N, \mu_0)} dr^N. \quad (1.8)$$

Combination of last three equation shows that the potential of mean force is given by

$$e^{-\beta W(r^N, \mu_0)} = \sum_{m=0}^{\infty} \frac{z_0^m}{m!} \int e^{-\beta U(r^N, r^m)} dr^m. \quad (1.9)$$

All possible solvent configurations contribute to $W(r^N, \mu_0)$. It is the average potential the colloidal particles feel due to all interactions of and with the solvent. If one takes the derivative of the $W(r^N, \mu_0)$ with respect to a particle's position r_i it becomes clear why the $W(r^N, \mu_0)$ is called the potential of *mean* force.

$$\frac{\partial W(r^N, \mu_0)}{\partial r_i} = \left\langle \frac{\partial U(r^N, \mu_0)}{\partial r_i} \right\rangle = \langle F_i \rangle. \quad (1.10)$$

This is the average force on the colloidal particle due to the collisions with the solvent particles. One can connect the partition function to the thermodynamic grand potential by the familiar equation

$$\Omega(N, V, T, \mu_0) = -kT \ln \Xi(N, V, T, \mu_0). \quad (1.11)$$

From this potential all the thermodynamical quantities can be derived. For example, the osmotic pressure, which is the difference between the pressure in the suspension and the reservoir pressure is

$$\Pi = P - P_0 = -\frac{\partial \Omega}{\partial V} - P_0. \quad (1.12)$$

McMillan and Mayer also showed how the potential of mean force approach can be used to obtain the virial expansion of the osmotic pressure [16]. Because of the far-reaching analogy, it is possible to apply theories that were designed for simple liquids to the phase behavior of colloidal dispersions, and what is more important for this thesis, it is possible to conduct computer simulations of colloidal suspensions, as if the colloids were large atoms interacting through the potential of mean force. These kind of simulations can be used to test the assumptions made in the theories, they can provide reference data that can be compared both to experiments and theory, and they may provide new insights in the usually complicated phase behavior of colloidal dispersions.

Phase behavior of colloidal dispersions

1.6

A dispersion of colloidal particles in a solvent is not always stable. In many cases, the strong van der Waals forces between colloidal particles cause them to aggregate and sediment out of solution [8]. This phenomenon is called flocculation. In order for a colloidal suspension to be stable towards flocculation, the interaction potential must have a repulsive barrier to prevent the particles getting at the distances where the strong van der Waals attraction takes over. In general this is achieved by the charges on the surface on the colloidal particle. In a solvent with added salt, this induces a double layer repulsion, which counteracts the van

der Waals attraction arising from the dielectric properties of the colloidal particle and the solvent. The total interaction potential shows a repulsion at short distances followed by an attraction further away [18]. Another possibility to prevent flocculation is steric stabilization of the particles by grafting the surface with short polymer chains [19]. These polymers cause a very short ranged repulsive steric interaction which prevents the irreversible flocculation. As colloidal dispersions can, to a first approximation, be described as simple fluids, it is natural to assume that spherical colloids will exhibit the same phase behavior as atomic substances. That is, one would expect that these colloidal suspensions can occur in the solid, liquid and vapor phase. However, although the fluid-solid transition is found in systems of charge- or sterically stabilized colloids, the liquid-vapor transition is not, even if there is an attractive part in the potential. In the absence of attraction, the fluid-solid transition is similar to the freezing transition of hard spheres. As attraction becomes stronger (or the temperature is lowered), the fluid-solid density gap broadens (see figure 1.2b). Clearly, there must be a fundamental difference between these colloidal systems and molecular systems that obey the van der Waals equation (see section 1.3). We recall that the van der Waals approach becomes exact in the limit of infinitely long-ranged, infinitely weak attractive forces. However, in charge- or sterically stabilized colloids, the range of the attraction is quite small compared to the diameter of the particles (quite unlike the attractive interaction in the Lennard-Jones model that is often used to model simple liquids, such as argon [2]). As we discussed in section 1.3, the stability of the liquid phase is very sensitive on the potential range. The liquid region is large in the van der Waals limit, or for the Lennard-Jones model, but decreases as the range of attraction shrinks. When this range becomes less than about one third of the hard-core diameter of the particles, the triple point approaches the critical point and the liquid-vapor transition will disappear completely .

In order to study the effect of the interaction potential on the phase behavior, one would need to be able to “tune” the range of the attractive interaction between particles, while keeping their hard-core repulsion fixed. For molecular systems, it is not possible to tune the attractive van der Waals forces in this way. However, in colloidal dispersions there is a neat way to control the strength and range of the interparticle attraction: adding polymer.

1.7 Depletion forces

The range and strength of the attraction between colloids can be varied by the addition of free non-adsorbing polymer to the colloidal dispersion (free and non-adsorbing as opposed to the polymers used to coat the particles for steric stabilization). These polymers, when in an appropriate (*theta*-)solvent, behave as random coils with a radius of gyration r_g . On average, they are excluded from a shell of thickness r_g around the colloidal particle, called the depletion zone. When two colloidal particles are brought together, these depletion zones will overlap and the total volume accessible to the polymer will increase. It is this increase in free volume that causes an effective attraction; the so-called depletion force. The range of the attraction is directly related to the radius of gyration r_g , whereas the strength is proportional to the osmotic pressure of the polymers. When the diameter of the polymer is larger than approximately 1/3 of the colloid hard-core diameter, a gas-liquid phase separation can be observed in the phase diagram of the suspension. This transition takes place because the increase in free energy associated with the condensation of the colloidal particles is more than offset by the decrease in free energy due to the gain of

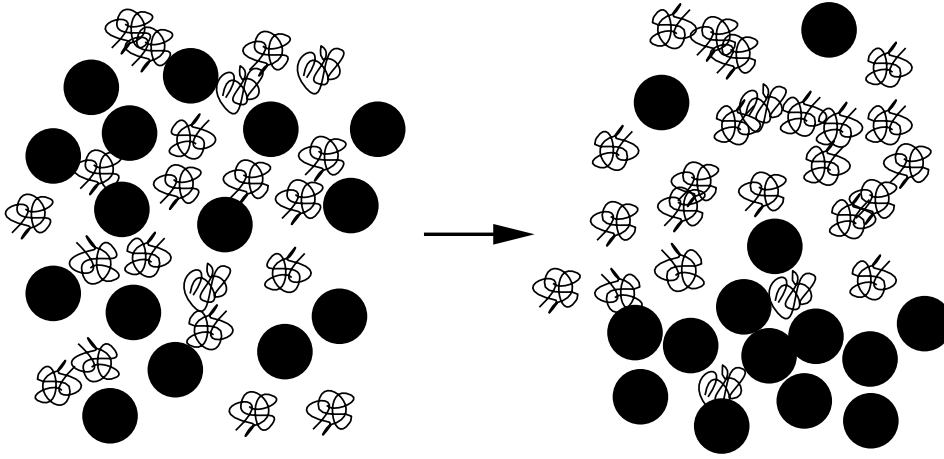


Figure 1.3. Sketch of a liquid-vapor phase separation in a colloid-polymer mixture. The polymers gain in free volume when they push the colloidal particles together.

free volume accessible to the polymers. A cartoon of this phase separation is displayed in figure 1.3.

A simple, yet qualitatively correct model of polymer-colloid mixtures was first proposed by Asakura and Oosawa [7] in the early fifties and subsequently analyzed by Vrij [20] and Lekkerkerker et al. [21]. In the Asakura and Oosawa (AO) model, the colloids are represented by hard spheres of diameter σ , while the polymers are assumed to be spheres of diameter $\sigma_{\text{pol}} = 2r_g$ that are mutually interpenetrable, but cannot penetrate the colloidal particles. The colloid-colloid interaction potential U_{HS} and the colloid-polymer potential U_{cp} can then be written as

$$\begin{aligned}
 U_{\text{HS}}(r) &= \begin{cases} \infty & \text{if } 0 < r < \sigma, \\ 0 & \text{if } r > \sigma. \end{cases} \\
 U_{\text{cp}}(r) &= \begin{cases} \infty & \text{if } 0 < r < (\sigma + \sigma_{\text{pol}})/2, \\ 0 & \text{if } r > (\sigma + \sigma_{\text{pol}})/2. \end{cases}
 \end{aligned} \tag{1.13}$$

How realistic is the Asakura-Oosawa model? The hard sphere potential is a good approximation for the colloid-colloid interaction, certainly in the case of sterically stabilized particles [22, 8], but also for charged colloids dissolved in a solvent with a high ionic strength (short screening length). The assumption that the polymer are interpenetrable is only valid for dilute solutions of polymer in a *theta*-solvent [23]. The next question is, whether it is realistic to model a polymer by a sphere. Is the deformability of the (ideal) polymer not important? This question was the subject of a study performed by Meijer and Frenkel [10]. They compared simulations of colloid-polymer mixture using the AO model, with simulation using real, interpenetrable lattice polymers. Meijer and Frenkel found that, if the radius of gyration of the polymers was less than 70 % of the radius of the colloid, the AO model works quite well .

1.8 Statistical mechanical formalism

In this section we describe the thermodynamic treatment of the polymer-colloid mixture within the AO model developed by Lekkerkerker et al. [21]. This approach is analogous to the derivation of the potential of mean force discussed in section 1.5. We consider a system of N colloidal particles dispersed in a polymer solution, in a volume V . This system is in osmotic equilibrium with a large reservoir containing only a polymer solution, at fixed fugacity $z = \exp(\beta\mu_p)$, where μ_p is the polymer chemical potential. As we are imposing the fugacity of the system, the proper thermodynamic quantity is the grand canonical partition function

$$\Xi(N, V, T, \mu_p) = \sum_{m=0}^{\infty} z^m Z(N, V, T, m), \quad (1.14)$$

where $Z(N, V, T, m)$ is the canonical partition function of a system of N colloid and m polymers. As the AO-model states that the bare colloid-colloid interaction $U_{HS}(r^N)$ is a hard sphere potential that does not depend on the presence of the polymers, we can write

$$Z(N, V, T, m) = \frac{1}{N!} \int e^{-\beta U_{HS}(r^N)} Z_p(r^N, V, m) dr^N, \quad (1.15)$$

where $Z_p(r^N, V, m)$ is the canonical partition function of the polymers in a *particular* configuration of the colloidal particles. As the polymers were assumed not to interact with each other in this model, $Z_p(r^N, V, m)$ can be expressed as the m th power of the one polymer partition function which is in turn equal to the free volume available to a polymer

$$Z_p(r^N, V, m) = Z_p(r^N, V, 1)^m = [V_{\text{free}}(r^N)]^m. \quad (1.16)$$

The integration over the translational degrees of freedom of the polymer yields the free volume, i.e. that part of the volume that is not excluded to the polymers by the hard-core colloids. The grand canonical partition function of eqn. 1.14 now becomes

$$\begin{aligned} \Xi(N, V, T, \mu_p) &= \frac{1}{N!} \int dr^N \exp[-\beta U_{HS}(r^N)] \exp[z V_{\text{free}}(r^N)] \\ &= \frac{1}{N!} \int dr^N e^{-\beta W(r^N, z)}, \end{aligned} \quad (1.17)$$

where $W(r^N, z)$ is again the potential of mean force but now due to the presence of the polymer

$$\beta W(r^N, z) = \beta U_{HS}(r^N) - z V_{\text{free}} = \beta U_{HS}(r^N) - \beta P_R V_{\text{free}}, \quad (1.18)$$

where P_R is the osmotic pressure of the polymers in the reservoir (we have used the fact that, for ideal polymers, the (osmotic) pressure and the fugacity are identical). $W(r^N, z)$ can be interpreted as an effective potential. If the displacement of a colloidal particle decreases the free volume available to the polymers, then $W(r^N, z)$ increases (i.e. becomes more repulsive). This potential is of purely entropic origin because we have assumed only hard-core interactions. Up to this point, the derivation has been exact (at least, in the context of the AO model). However, $W(r^N, z)$ is a many-body potential because the free

volume V_{free} depends not just on binary but also on multiple overlap of depletion zones. This complicates the theoretical description of the free volume and it is usually necessary to introduce approximations at some level. However, no such approximations are needed in the numerical simulation of the depletion interaction. Hence, simulations can be used to test the validity of the approximations used in the theory.

The simplest theoretical approximation of the depletion interaction is based on thermodynamic perturbation theory. We replace $V_{\text{free}}(r^N)$ by its average value in the corresponding hard-spheres reference system. This yields the following approximation for the grand potential

$$\begin{aligned}\beta\Omega(N, V, T, \mu_p) &= -\ln \Xi(N, V, T, \mu_p) \approx -\ln \left\langle \exp(-\beta U_{\text{HS}}(r^N)) \right\rangle - z \left\langle V_{\text{free}}(r^N) \right\rangle \\ &= \beta F_{\text{HS}} - z_p \alpha V.\end{aligned}$$

Here the brackets stand for an ensemble average over the colloid configurations, F_{HS} is the free energy of the hard spheres, which only depends on the density $\rho = N/V$ and α is the average fraction of the total volume available for a polymers.

From the grand potential one can calculate the osmotic pressure P and the chemical potential μ_s of the colloidal spheres

$$\beta P = -\beta \left(\frac{\partial \Omega}{\partial V} \right)_{N, \mu_p, T} = \beta P_{\text{HS}} + z \left(\alpha - \rho \frac{\partial \alpha}{\partial \rho} \right), \quad (1.19)$$

$$\beta \mu_s = \beta \left(\frac{\partial \Omega}{\partial N_s} \right)_{V, \mu_p, T} = \beta \mu_{\text{HS}} - z \frac{\partial \alpha}{\partial \rho}. \quad (1.20)$$

Together with expressions for the Helmholtz free energy F_{HS} and for the available free volume fraction α these equations can be used for a theoretical study of the phase behavior of a colloid-polymer mixture. The above formalism is also applicable to hard colloidal particles with non-spherical shapes, provided that we use the appropriate expression for F and α .

Non-spherical colloids

1.9

Many colloidal particles are non-spherical. For instance, clay consists of platelets, red blood cells are toroidal and other colloids have a rodlike shape. Examples of colloidal rods are TMV and fd viruses, inorganic V_2O_5 -particles and boehmite needles. Rodlike particles have a richer phase diagram than spherical colloids, because the rods can form a variety of liquid-crystalline phases [24]. The term “liquid crystal” refers to a structure that is in between a crystalline solid and an isotropic liquid. Only sufficiently non-spherical objects can form liquid crystals.

Already in the 1940's, Onsager showed that an isotropic dispersion of hard, infinitely long rods, must undergo a first order orientational ordering transition at sufficiently high density [25]. The resulting *nematic* liquid-crystalline phase is characterized by long-range orientational ordering of the particles. There is, however, no translational ordering: i.e. there are no long-range positional correlations of the centers of mass of the particles.

When compressed further, the system of hard rods can transform into another liquid crystalline phase, called *smectic*. This phase has not only orientational ordering but it also forms layers, in which the particles are still free to move. There is only long-range positional order

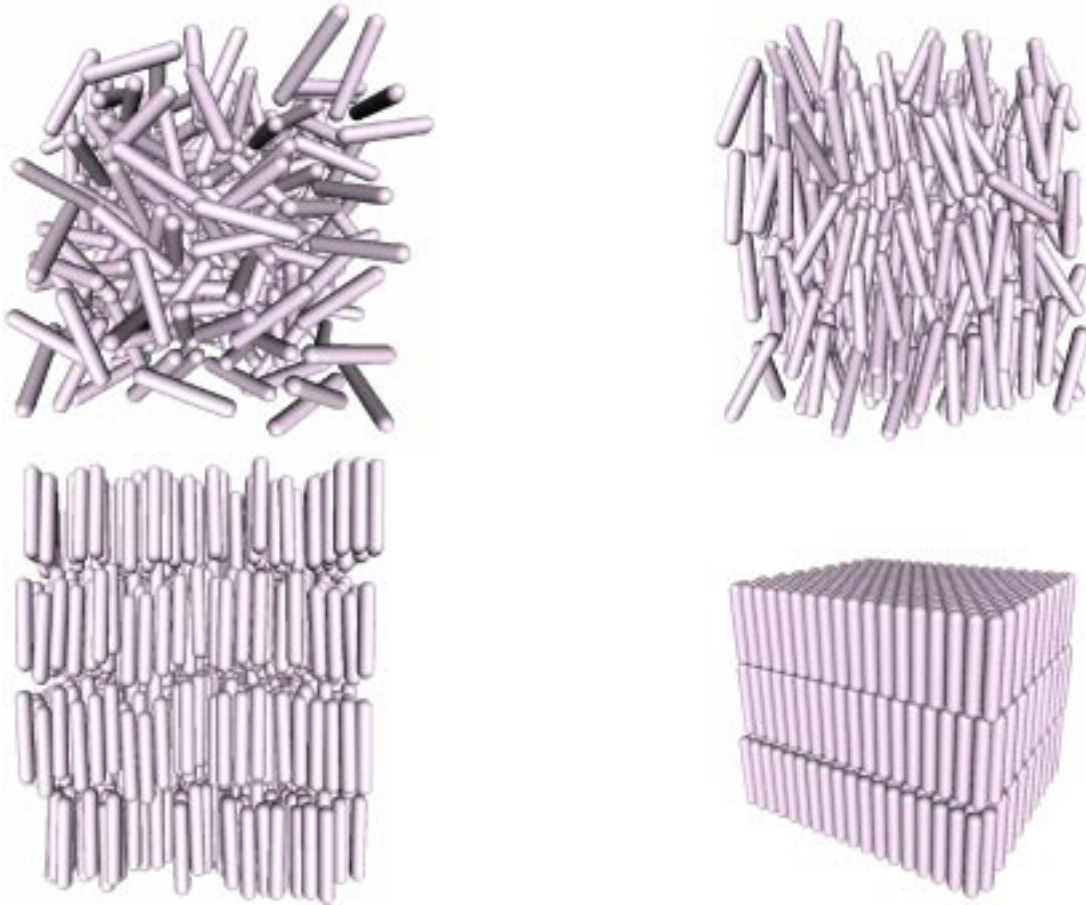


Figure 1.4. *Sequence of phases of a system of hard spherocylinder for increasing density. Top left: isotropic phase, no translational and orientational ordering. Top right: nematic liquid crystal, orientational ordering but no translational. Bottom left: smectic liquid crystal, with besides orientational ordering, translational ordering in the z-direction. Bottom right: crystal phase*

in one direction. Eventually, at sufficiently high pressures, crystallization will take place, with long-range positional order in all three directions. We show the sequence of liquid crystalline ordering in figure 1.4 for the case of a simple model of rodlike particles, namely hard spherocylinders.

Non-adsorbing polymers will also induce depletion interactions between non-spherical colloids. In fact, the addition of polymer can have a large effect on the stability of the liquid crystalline phases in dispersions of rodlike colloids. The phase behavior of mixtures of spherocylinder and polymers is one of the issues that will be addressed in this thesis.

1.10 Outline of the thesis

This thesis contains several computer simulation studies of the influence of the interaction potential range on phase behavior of colloidal dispersions. The first half of this thesis will be devoted to the phase behavior of colloidal systems consisting of spherical particles. The next chapter contains a numerical study of the phase diagram of a mixture of spherical colloids and rodlike polymers. In the subsequent chapter we address the question what

the phase diagram will be like if we consider very short-ranged depletion interactions. It will turn out that the phase behavior of such mixtures is very sensitive to polydispersity of the colloids. As synthetic colloidal dispersions always exhibit some size polydispersity, we need to study the effect of polydispersity on the phase behavior of spherical colloids. The combination of polydispersity and short-ranged depletion interactions of spherical colloids, is studied at the end of chapter 3. The effect of polydispersity on the freezing transition of hard, spherical colloids is discussed in detail in chapter 4.

The second half of the thesis deals with the phase behavior of rodlike particles, and mixtures of rodlike particles and polymers. First, we investigate the full phase diagram of the simplest hard core model for rodlike particles, the hard spherocylinder, in chapter 5. Part of this phase diagram had been determined previously [26, 27]. However, in the present study we investigate the phase behavior in all limiting cases (aspect ratio going from 1 to ∞ , density going from zero to close packing). In the subsequent chapter, we examine the effect of the addition of polymer on the phase behavior of spherocylinders. The last chapter comprises a study of phase separation in mixtures of rods and plates.

Quite a few of the numerical techniques that were used in the work described in this thesis, were either novel or non-standard. For the reader who is primarily interested in novel numerical techniques, we end this introduction with a list of the non-standard simulation methods that were employed in this thesis, and we indicate where they are described in the text.

- Section 2.2.1: Configurational Bias Monte Carlo in the Gibbs-Ensemble for clusters of particles
- Section 3.2.4: Simulations in the close packing limit for spheres
- Section 5.5.2: Simulations in the close packing limit for spherocylinders
- Section 5.3.2: Absolute free energy calculations in the liquid crystalline phases of hard spherocylinders
- Section 5.6: Multiple overlap criterion for simulations of very long spherocylinders
- Section 5.7: Simulations of hard spherocylinders in the limit $L/D \rightarrow \infty$
- Section 5.3.3: Generalized Gibbs-Duhem integration for spherocylinders, to trace coexistence curves as a function of the aspect ratio L/D
- Section 4.3: Generalized Gibbs-Duhem integration to trace the freezing curve for polydisperse hard spheres, as a function of the polydispersity.
- Section 4.2: Semi-grand ensemble description of polydisperse hard sphere systems
- Section 4.5: Scaling of the polydisperse hard sphere systems
- Section 6.3: Construction of an effective pair potential to model the polymer induced attraction between spherocylinders

MIXTURES OF SPHERICAL COLLOIDS AND RODLIKE POLYMERS

2

Fluid-fluid phase separation in a simple model for a colloid dispersed in a solution of stiff rodlike polymers is studied by means of Gibbs-Ensemble Monte Carlo simulations. The fluid-solid transition for this model is computed using first-order perturbation theory. The phase diagrams clearly show that a stable critical point is not possible for polymer lengths smaller than 30% of the colloidal particle diameter. For very large polymers, the phase diagram can be derived directly from the hard sphere equation of state.

Introduction

2.1

In the previous chapter we saw that a suspension of uncharged colloidal particles mixed with a sufficiently concentrated solution of non-adsorbing polymer, undergoes a phase separation into a dense colloidal phase and a phase that contains mainly polymer [7, 20, 21]. This transition takes place because the increase in free energy associated with the condensation of the colloidal particles is more than offset by the decrease in free energy due to the gain of free volume accessible to the polymers.

In the Asakura-Oosawa model, the colloids are represented by hard spheres of diameter σ , while the polymers are assumed to be spheres of diameter σ_{pol} that are mutually interpenetrable, yet cannot penetrate the colloidal particles. As a consequence, every colloidal particle excludes a sphere of volume $\frac{1}{6}\pi(\sigma + \sigma_{\text{pol}})^3$ to the polymers. When two colloidal particles are brought together, these spherical volumes will overlap and the volume accessible to the polymer will increase. It is this increase in free volume that causes an effective attraction and the eventual phase separation of the colloids. Recent computer simulations of polymer-colloid mixtures [10] indicate that the Asakura-Oosawa model is quite realistic if $\sigma_{\text{pol}} < \sigma$.

Of course, the above mechanism for polymer-colloid phase separation is more general: spherical colloids and globular polymers are just the simplest example. In this chapter, we focus on another limiting example, namely a mixture of spherical colloids and thin rodlike polymers. In the limit that the polymers are infinitely thin, this mixture is expected to resemble the Asakura-Oosawa model, because the polymer-polymer excluded volume vanishes, while the polymer colloid excluded volume is a spherocylinder with a length to width ratio $1 + L/\sigma$, where L is the length of the rodlike polymers. As in the case of the flexible polymer-colloid mixture the free volume for the rodlike polymer can be increased by clustering of the colloids. One would therefore expect to see phase separation in such mixtures. However, although a light-scattering study of a mixture of colloids and fairly rigid rod-like polymers was reported by Tracy et al. [28], phase separation was not observed.

In this chapter we report a systematic numerical study of mixtures of hard-sphere colloids

with thin rodlike polymers of varying length. The aim of the study is threefold: first of all, we wish to establish if there is indeed a fluid-fluid phase separation in this mixture. This is not a-priori obvious because both the spheres and the rodlike polymers are convex bodies. The existence of a fluid-fluid phase separation in the simplest mixture of convex bodies, viz. hard spheres, continues to be a matter of speculation [29, 30]. For other mixtures of convex bodies, firm data are lacking. A second aim of the study is to provide a guide for experiments: we intend to indicate under what conditions (colloid density, polymer fugacity, L/σ ratio) phase transitions are to be expected. We shall consider both the possibility of fluid-fluid and fluid-solid transitions. Finally, we wish to verify if the theoretical description of polymer-colloid mixtures discussed in ref [21] and section 1.8 can be generalized to rod-like polymers.

In our numerical study of possible fluid-fluid coexistence, we have made use of the Gibbs-ensemble method of Panagiotopoulos [31–33]. However, as will be explained below, a naive implementation of this scheme is extremely inefficient in the present case. We have therefore generalized the Gibbs-ensemble method to perform multi-particle exchanges, where the configurational-bias Monte Carlo method [34] is used to achieve a high acceptance probability of trial moves. This simulation scheme is described in section 2.2.1. In section 2.2.2 we present the simulation results of the fluid-fluid demixing. The solid-liquid coexistence is discussed in section 2.2.3. The application of first-order perturbation theory to the mixture is described in section 2.3.1, followed by a discussion of the limiting case of infinitely long rods, $L \rightarrow \infty$. In section 2.3.3 we compare the simulation results with the theory.

2.2 Simulations

2.2.1 Configurational Bias Monte Carlo in the Gibbs-Ensemble

To calculate the phase equilibria directly, we use the Gibbs-Ensemble Monte Carlo simulation approach developed by Panagiotopoulos [31, 32]. In this method, the coexisting phases are simulated in parallel. $V^I(V^II)$ denotes the volume of the periodic box containing phase I(II). The total volume is denoted by V . The number of spheres and rods in either box is denoted by N_s^I, N_r^I, N_s^{II} and N_r^{II} .

During the simulation ordinary MC displacement steps are performed in both phases and occasionally particles and volume are exchanged between the boxes to maintain respectively chemical and mechanical equilibrium. The particle moves inside a box are accepted according to the conventional Metropolis scheme. For trial moves to change the volume, we follow the procedure described in ref. [33].

The exchange rules are slightly more complicated. The rods can be exchanged without any difficulty and we can use the usual acceptance rule for moving a rod from box I to II:

$$P_{\text{acc}} = \min\left(1, \frac{V^{II}N_r^I}{V^I(N_r^{II} + 1)} \exp(-\beta\Delta U_r)\right), \quad (2.1)$$

where ΔU_r is the change in potential energy upon exchange of a rod.

The spheres however, cannot be exchanged directly because the insertion probability in both phases will be very low due to the presence of rods. Nearly always a sphere will overlap with one or more needles. To overcome this we can make use of the Configurational Bias Monte Carlo scheme originally derived by Biben [35] who in turn based it on a scheme suggested in ref. [34].

The procedure is as follows. First one tries to move a sphere from one box to the other. When the sphere overlaps with any other sphere the trial move is rejected. Otherwise, rods overlapping with the sphere in its new position are removed and are randomly inserted into the former box in such a way that they would have intersected the sphere in its original position. This procedure creates a bias in the sampling. In the following we show how to correct for this bias. Before discussing particle exchange between two boxes, we focus on a scheme for moving particles within the same box. Suppose we want to swap a sphere with the overlapping needles on the new position. The acceptance rule for this step is governed by detailed balance:

$$\frac{P_{a \rightarrow b}^{\text{gen}} P_{a \rightarrow b}^{\text{acc}}}{P_{b \rightarrow a}^{\text{gen}} P_{b \rightarrow a}^{\text{acc}}} = \exp(-\beta(U_b - U_a)). \quad (2.2)$$

Here $P_{a \rightarrow b}^{\text{gen}}$ is the probability to generate and $P_{a \rightarrow b}^{\text{acc}}$ the probability to accept the move from configuration a to configuration b . $\Delta U = U_b - U_a$ is the potential energy difference between a and b . To satisfy the detailed balance condition one can use the Metropolis scheme with the acceptance rule

$$P_{a \rightarrow b}^{\text{acc}} = \min\left(1, \frac{P_{b \rightarrow a}^{\text{gen}} \exp(-\beta U_b)}{P_{a \rightarrow b}^{\text{gen}} \exp(-\beta U_a)}\right). \quad (2.3)$$

In normal simulations $P_{b \rightarrow a}^{\text{gen}}$, the chance of generating configuration a is equal to $P_{a \rightarrow b}^{\text{gen}}$. In the present case the generating probabilities depend on the volume, the number of particles and the specific configuration. If we try to move n rods starting from configuration a , the probability to generate a certain configuration b is given by

$$P_{a \rightarrow b}^{\text{gen}} = \prod_{i=1}^n \frac{\exp(-\beta U_{b_i})}{Z_{b_i}}, \quad (2.4)$$

where U_{b_i} denotes the energy of the i^{th} moved rod in configuration b , the weight factor $Z_{b_i} = \sum_{j=1}^k \exp(-\beta U_{b_j})$ plays the role of the single rod partition function. Once we have moved a sphere, we try to move the overlapping rods into the old position of the sphere. For each of the n overlapping rods the weight factor is calculated by inserting rods k times randomly in the overlap volume of the rod and the moved sphere.

Using eqn. 2.2 - eqn. 2.4 and the relation $\Delta U = \sum_{i=1}^n (U_{b_i} - U_{a_i}) + U_{b,\text{HS}} - U_{a,\text{HS}}$ the acceptance probability becomes,

$$P_{a \rightarrow b}^{\text{acc}} = \min\left(1, \frac{Z_b}{Z_a} \exp(-\beta \Delta U_{\text{HS}})\right), \quad (2.5)$$

where $\Delta U_{\text{HS}} = U_{b,\text{HS}} - U_{a,\text{HS}}$ takes into account the interaction of the moved sphere with all other spheres and $Z_a = \prod_{i=1}^n Z_{a_i}$ for configuration a . For convenience, it is assumed that the number of trial insertions k is the same in both Z_a and Z_b . The weight factors Z_a and Z_b of the old and the new situation respectively, must be calculated. Notice that besides the moved sphere the only difference between a and b are the position of the n overlapping rods, so we only need to calculate the weight factors for those rods.

The above scheme is valid for a move within one box. In the Gibbs-Ensemble scheme the situation is somewhat different. Suppose we want to move a sphere from box II to I.

The overlapping n needles in box I in situation a are moved to box II. The probability to generate the new configuration b is now given by

$$P_{a \rightarrow b}^{\text{gen}} = \frac{1}{N_s^{\text{II}}} \frac{1}{V^{\text{I}}} \prod_{i=1}^n \frac{\exp(-\beta U_{b_i})}{Z_{b_i}}, \quad (2.6)$$

where the factor $1/N_s^{\text{II}}$ is the probability to pick one of the spheres in box II and the volume factor is due to the random choice of the sphere position in box I. The product in eqn. 2.6 gives the probability to move n rods between boxes and is the same as in eqn. 2.4. For the reverse move, $P_{b \rightarrow a}^{\text{gen}}$ can be written as

$$P_{b \rightarrow a}^{\text{gen}} = \frac{1}{N_s^{\text{I}} + 1} \frac{1}{V^{\text{II}}} \prod_{i=1}^n \frac{\exp(-\beta U_{a_i})}{Z_{a_i}}, \quad (2.7)$$

where the additional 1 in the first factor arises because in the reverse move one extra sphere can be chosen.

Using $\Delta U = \sum_{i=1}^n U_{b_i} - U_{a_i} + U_{b,\text{HS}} - U_{a,\text{HS}}$ and the definition of the weight factor Z , the total probability of accepting a sphere exchange from box II to I is:

$$P_{a \rightarrow b}^{\text{acc}} = \min\left(1, \frac{V^{\text{I}}}{V^{\text{II}}} \frac{N_s^{\text{II}}}{N_s^{\text{I}} + 1} \frac{Z_b}{Z_a} \exp(-\beta \Delta U_{\text{HS}})\right). \quad (2.8)$$

Note that the number of rods does not occur in this acceptance rule, because the rods cannot be chosen freely once a particular sphere has been randomly selected. At first sight it seems strange that the acceptance rule does not contain the number of displaced rods. In the limit in which the rods shrink to ideal point particles, however, it is immediately clear that the thermodynamics of the hard sphere fluid cannot depend on the configurations of an ideal gas.

The calculation of the Z_a and Z_b is as follows. The orientation of the rod to be inserted is chosen randomly and it is placed within the overlap volume of the rod and the sphere. This is repeated k times. Z_a and Z_b are equal to the number of times the rod does not overlap with another sphere in the old configuration a respectively in the new situation b . To check chemical equilibrium one may want to know the chemical potential of the rods. The chemical potential of the rods is measured by the Widom insertion method which is slightly altered due to the Gibbs-ensemble [33].

$$\beta \mu = \beta \mu^0 - \ln \left\langle \frac{V^{\text{I}}}{(N_r^{\text{I}} + 1)} \exp(-\beta \Delta U) \right\rangle. \quad (2.9)$$

With the above steps it is possible to calculate phase equilibria in rod sphere mixtures directly.

2.2.2 Fluid-fluid coexistence

In the model studied in our simulations the colloidal particles are represented by hard spheres with a diameter σ while the rodlike particles are modeled by infinitely thin needles of length L . As these needles are infinitely thin, their mutual excluded volume vanishes. However the needles cannot intersect with the hard core colloidal particles.

In order to establish fluid-fluid phase separation we performed modified Gibbs-ensemble Monte Carlo simulations for rod lengths $L/\sigma=2, 3, 4, 5, 6$ at different fugacities. The overall starting density of colloidal particles in the two boxes was $\rho\sigma^3=0.25$ which located the system in a two phase region of the phase diagram.

The total number of spheres in the system was 110. We did not fix the number of rodlike polymers, but rather kept their fugacity z fixed. During the simulations the number of rods varied from 100 to 1000.

As a test, we measured the chemical potential of the needles and the spheres using Widoms particle insertion technique [36] during a simulation. The chemical potential μ_r of the rods is directly related to the fugacity by $z = \exp(\beta\mu_r)$. We checked that the actual chemical potentials of the two species remained constant in both phases.

For equilibration of every system 10,000 MC cycles were executed, whereas 20,000 cycles were performed for data collection. During a cycle every particle on average was moved once. In addition the average cycle contained 80 attempted particle exchanges and 1 volume exchange between the two phases. The maximum step sizes of the particle moves were adjusted in order to keep the acceptance probability around 30 - 40 %. The acceptance probability of hard sphere exchanges which involved the Configurational Bias Monte Carlo step was $\sim 5\%$. This means that on average during every cycle 2 % of the total number of particles was exchanged. The acceptance probability for the exchange of the needles was $\sim 40\%$.

Figure 2.1. Coexistence curves for mixtures of hard spheres and rods. On the x-axis the number density of hard spheres is set out. The fugacity of the rods, z , is plotted versus the reduced number density of hard spheres, $\rho_s\sigma^3$. The data points refer to the Gibbs-Ensemble results. From top to bottom the sets of points denote the binodals for $L/\sigma=2,3,4$ and 5. The dashed curves are fits to eqn. 2.10 with an exponent $1/3$.

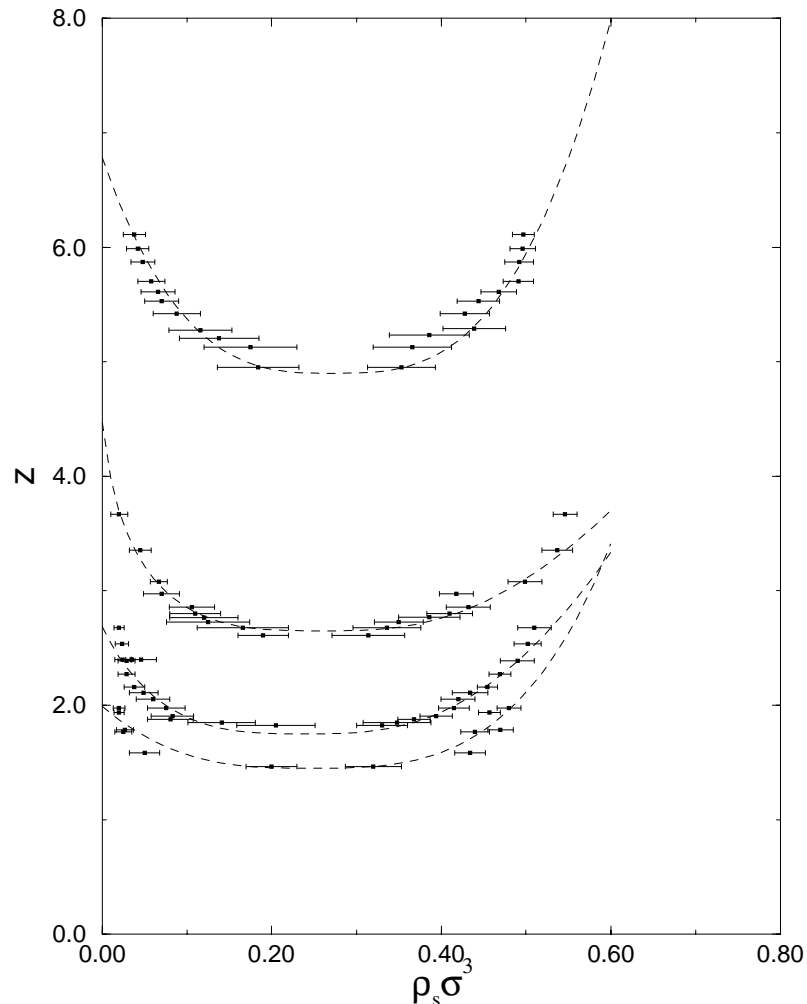


Figure 2.1 shows the fluid-fluid coexistence curves obtained in the Gibbs-ensemble simulations. As the length of the needles is increased, the coexistence curves shift to lower fugacity. This is to be expected because the range of the depletion interaction increases with length. Therefore, fewer rods are needed to induce the phase separation.

Because of the analogy between this phase separation and the liquid-vapor coexistence in simple fluids we expect that the shape of the coexistence curve in the neighborhood of the critical point is given by the scaling form

$$\rho_l - \rho_g \sim (z - z_c)^\beta, \quad (2.10)$$

where $\rho_l - \rho_g$ is the density difference between the dense and the dilute phase and we assumed $\beta=0.33$, the usual 3D Ising critical exponent. From these simulations it is not possible to obtain a good estimate of the actual critical exponent. The dashed curves shown in figure 2.1 are fits of the scaling form (2.10).

The critical density shifts to lower values and the coexistence curves become more asymmetrical with increasing needle length. In the case of very long rods every sphere will be expelled from the dilute vapor like phase, which causes the critical density to go asymptotically to zero for $L \rightarrow \infty$. This limit will be discussed in more detail in section 3.2.

2.2.3 Solid-fluid transition

Although the Gibbs-ensemble simulations described above indicate that a fluid-fluid like demixing occurs in the sphere-needle mixture, it is not obvious that this phase equilibrium can indeed be observed in experiments. In particular, the fluid-solid transition might take place before the fluid-fluid two phase region is reached. It is therefore essential to study the stability of the fluid phase with respect to the solid. To locate the freezing transition we must compute the Helmholtz free energy of both the fluid and solid phases. This free energy is best computed by thermodynamic integration, using the hard-sphere system as a reference. The Helmholtz free energy of a sphere-needle mixture at volume-fraction ϕ of spheres and fugacity z of the needles is given by

$$F(\phi, z) = F_{\text{HS}}(\phi) + \int_0^z dz' \frac{\partial F}{\partial z'} = F_{\text{HS}}(\phi) - \int_0^z dz' \langle V_{\text{free}} \rangle, \quad (2.11)$$

where F_{HS} is the hard sphere reference energy and $\langle V_{\text{free}} \rangle$ the average free volume available to the rods. This free volume is a function of the fugacity. We performed simulations to obtain the free volume for a rod in the dense fluid and the solid phase at different fugacities. For the solid we assumed an *fcc* crystal structure which is presumably the most stable solid phase of hard spheres.

Figure 2.2 shows the measured average free volume fraction for one rod as a function of the hard sphere volume fraction for several needle fugacities. The free volume available to the needles is almost independent of the fugacity. The fluid structure is therefore only slightly affected by the addition of needles. Because the free volume is effectively independent of fugacity we can use first order perturbation theory to calculate the free energy at higher fugacities. Therefore eqn. 2.11 reduces to

$$F(\phi, z) = F_{\text{HS}}(\phi) - z \langle V_{\text{free}} \rangle_{\text{HS}}, \quad (2.12)$$

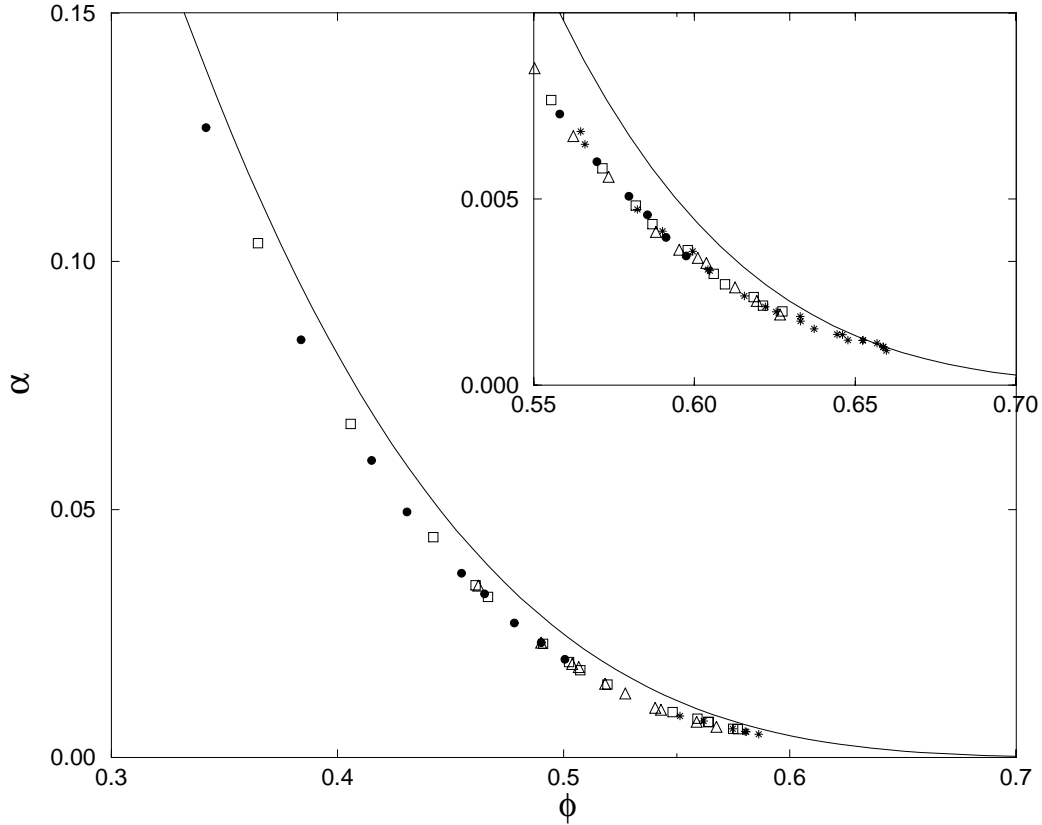


Figure 2.2. Simulated free volume fraction α for infinitely thin rods of length $L/\sigma=2$ as a function of hard sphere volume fraction ϕ . Simulation parameters as given in the text. The main figure gives the free volume in the fluid phase, whereas in the inset the much smaller free volume of the solid phase is plotted. The symbols refer to different rod fugacity: \bullet $z=2.7$, \square $z=7.4$, \triangle $z=12.2$ and $*$ $z=20.1$. The solid curve is the scaled particle theory approximation to the free volume for $L/\sigma=2$. Note that the relative difference of the simulated data and the SPT curve is larger in the solid phase.

where $\langle V_{\text{free}} \rangle_{\text{HS}}$ is the free volume for one rod in the hard sphere reference system. From this equation the coexistence densities of both the fluid and the solid phase can be obtained by equating the pressure and chemical potentials in both phases. For the fluid hard sphere equation of state we used the Carnahan-Starling expression [37] whereas the solid hard-sphere equation of state and reference free energy were obtained from simulation data [38, 39].

Although $\langle V_{\text{free}} \rangle_{\text{HS}}$ could be obtained from simulation data, we found that in the fluid phase it could be approximated quite well by scaled particle theory (SPT) [40]. In the solid phase the SPT considerably overestimates the free volume. This is not surprising as the theory was derived for the fluid region. However, as the free volume in the solid is very small anyway, the overestimate will not alter the thermodynamic properties of the mixture unless one considers very high polymer fugacity [10].

2.3 Theory

2.3.1 Perturbation theory

To compute the fluid-fluid coexistence curves of the rod-sphere mixture we used the perturbation theory approach developed by Lekkerkerker et al. [21, 30] and discussed in detail in chapter 1. In this approach, the grand potential of a system of N hard spheres with diameter σ in a volume V and in osmotic equilibrium with a reservoir containing an ideal gas of rods of length L at a fugacity $z = \exp -\beta\mu_r$, where μ_r is the chemical potential of the rods, is approximated by

$$\beta\Omega(N, V, T, \mu) \approx \beta F_{\text{HS}}(N, V) - z\alpha V. \quad (2.13)$$

Here F_{HS} is the free energy of the hard spheres, which only depends on the density $\rho = N/V$ and α is the average fraction of the total volume available for a rod.

To calculate the phase equilibria, one needs the pressure and the chemical potential μ_s of the spheres

$$\beta P = -\beta \left(\frac{\partial \Omega}{\partial V} \right)_{N, T, \mu_r} = \beta P_{\text{HS}} + z \left(\alpha - \rho \frac{\partial \alpha}{\partial \rho} \right), \quad (2.14)$$

$$\beta \mu_s = \beta \left(\frac{\partial \Omega}{\partial N} \right)_{V, T, \mu_r} = \beta \mu_{\text{HS}} - z \frac{\partial \alpha}{\partial \rho}. \quad (2.15)$$

For the pressure of the hard sphere reference system P_{HS} we use the Carnahan-Starling equation of state

$$\frac{\beta P_{\text{HS}}}{\rho} = \frac{1 + \phi + \phi^2 - \phi^3}{(1 - \phi)^3}, \quad (2.16)$$

where $\phi = \rho \frac{1}{6} \pi \sigma^3$ is the volume fraction of hard spheres. The chemical potential of the hard sphere fluid can be obtained from the standard thermodynamic relations. For the free volume fraction α one can use the scaled particle theory for one rod in a solution of spheres [40]

$$\beta \mu_r^{\text{ex}} = -\ln \alpha = -\ln(1 - \phi) + \frac{3L}{2\sigma} \frac{\phi}{1 - \phi}. \quad (2.17)$$

This is an underestimation of the chemical potential, therefore an overestimation of the free volume as we already saw in figure 2.2. Nevertheless, it turns out that this equation gives quite accurate results as we shall see in section 3.3. Substitution of eqn. 2.17 in eqn. 2.14 and eqn. 2.15 yields explicit expressions for the pressure and chemical potential in terms of the volume fractions in phase I and phase II. The coexistence curves were obtained by equating the pressure and chemical potentials in both phases.

2.3.2 The limit $L \rightarrow \infty$

The liquid-vapor coexistence terminates in a critical point. If the rod length increases the critical density shifts to lower values. For $L \rightarrow \infty$ this density is proportional to $1/L$, as can be derived from perturbation theory by setting the first and second derivative of the

pressure (eqn. 2.14) with respect to the density equal to zero. The critical volume fraction ϕ_c then follows as a function of L

$$\phi_c = \frac{10 + 3L/\sigma - 3\sqrt{4 + 12L/\sigma + (L/\sigma)^2}}{16 - 12L/\sigma} \underset{L \rightarrow \infty}{=} \frac{2\sigma}{3L}. \quad (2.18)$$

Using this result we can obtain the critical rod fugacity from eqn. 2.14 as well.

$$z_c = \frac{4\sigma^2}{9L^2} \frac{1 + 4\phi_c + 4\phi_c^2 - 4\phi_c^3 + \phi_c^4}{1 - \phi_c} \exp\left(\frac{3L}{2\sigma} \frac{\phi_c}{1 - \phi_c}\right) \underset{L \rightarrow \infty}{=} \frac{2\sigma e}{3L}. \quad (2.19)$$

Another remarkable fact is that the theoretical coexistence curve has a simple asymptotic form for very long rod lengths. If the critical density becomes zero the hard sphere vapor density also has to vanish. In this region the liquid vapor coexistence curve is easy to calculate by equating the pressures of the liquid and the vapor phase. The chemical potential is not important in the limit of long rods because the coexistence density of the vapor is effectively independent of the chemical potential. In the vapor phase the pressure is simply equal to the fugacity of the rods because there are no spheres present. The pressure in the fluid phase follows from eqn. 2.14

$$\beta P = \beta P_{HS} + z \left(\alpha - \phi \frac{\partial \alpha}{\partial \phi} \right). \quad (2.20)$$

In the $L \rightarrow \infty$ limit the free volume fraction α available to the rods in the liquid vanishes. The pressure of the fluid therefore reduces to the hard sphere equation of state. Equating the pressure in both phases gives

$$\beta P = \beta P_{HS} = z. \quad (2.21)$$

This result provides an alternative route to measure the hard sphere equation of state in experiments by measuring the rod concentration of the vapor phase as a function of the density of spheres in the liquid phase.

Comparison with simulation results

2.3.3

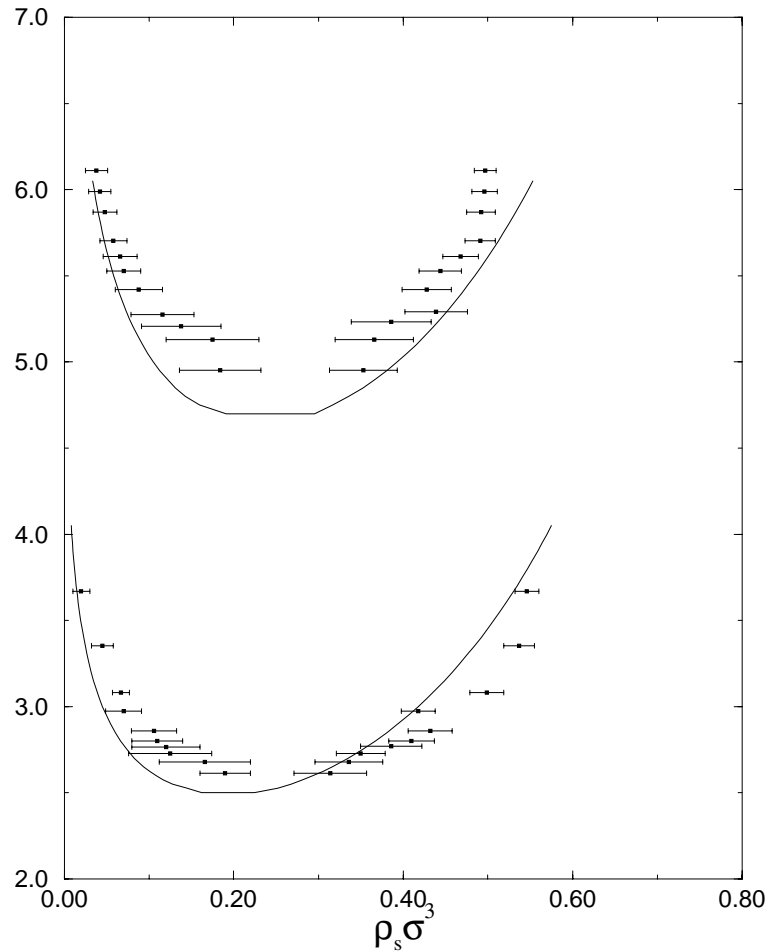
In figure 2.3 the binodal curves from first order perturbation theory are compared with the Gibbs-ensemble results. The critical points are well predicted for small length but become worse for longer rods. Because there is no adjustable parameter in the model, the accuracy of the theoretical curves is surprising. This good agreement is probably due to the accuracy of the SPT expression for the free volume eqn. 2.15.

In section 2.2.3 we concluded that the free volume available to a rod is independent of fugacity. Therefore the complete phase diagram for the needle-sphere mixtures including the fluid-solid transitions can be obtained using first-order perturbation theory. The coexistence densities for the solid-liquid and the solid-gas transition are easily calculated from the chemical potentials and the pressures in eqn. 2.14-2.15. The resulting phase diagrams for different rod lengths are shown in figure 2.4. The most obvious result is that a stable liquid-gas two-phase region is indeed possible. If the rods get smaller than 0.3σ the vapor-liquid phase separation becomes metastable. One can imagine that at this point the rods start to fit in the interstitial spaces of the solid phase. This causes the free energy of the solid

vapor equilibrium to be lower than that of the liquid vapor equilibrium.

As discussed above the coexistence curves shift to lower fugacities with increasing rod length. The interaction range between the particles becomes larger and the necessary depth of the effective potential to induce phase separation which is governed by the rod fugacity is smaller. The fluid-solid coexistence region becomes wider at high fugacity. This is a common phenomenon in fluid-solid transitions. If the fugacity increases, the free energy in the fluid decreases more than the free energy of the solid. To compensate this, the equilibrium solid phase has to become denser and the fluid phase more dilute.

Figure 2.3. *Binodal curves obtained from perturbation theory compared with simulation results. The fugacity of the rods, z , is plotted versus the reduced number density of hard spheres, $\rho_s \sigma^3$. The upper curve and points correspond to $L/\sigma=2$, the lower to $L/\sigma=3$.*



2.4 Discussion

When infinitely thin needles are added to a hard sphere solution a phase separation will occur in a dense, hard-sphere-rich, liquid-like phase and a dilute vapor-like phase that contains few hard spheres. This is a pure entropic effect as only hard core interactions are involved. The phase separation is caused by an increase in the available volume for the needles as the spheres cluster. This increase in entropy of the rods will outweigh the loss in entropy of the spheres at high rod fugacity. The fluid-solid transition will preempt this phase separation for a system with a rod length $L/\sigma < 0.3$ and a liquid phase will not be stable for these rod lengths. We expect that for very short rods the critical point will reappear in the solid phase. In the next chapter we show that in systems with very short ranged attraction a phase transition can occur between a dense packed crystal and a less dense crystal (see also ref. [41]). This phase transition is first order, ends in a critical point and is similar to the

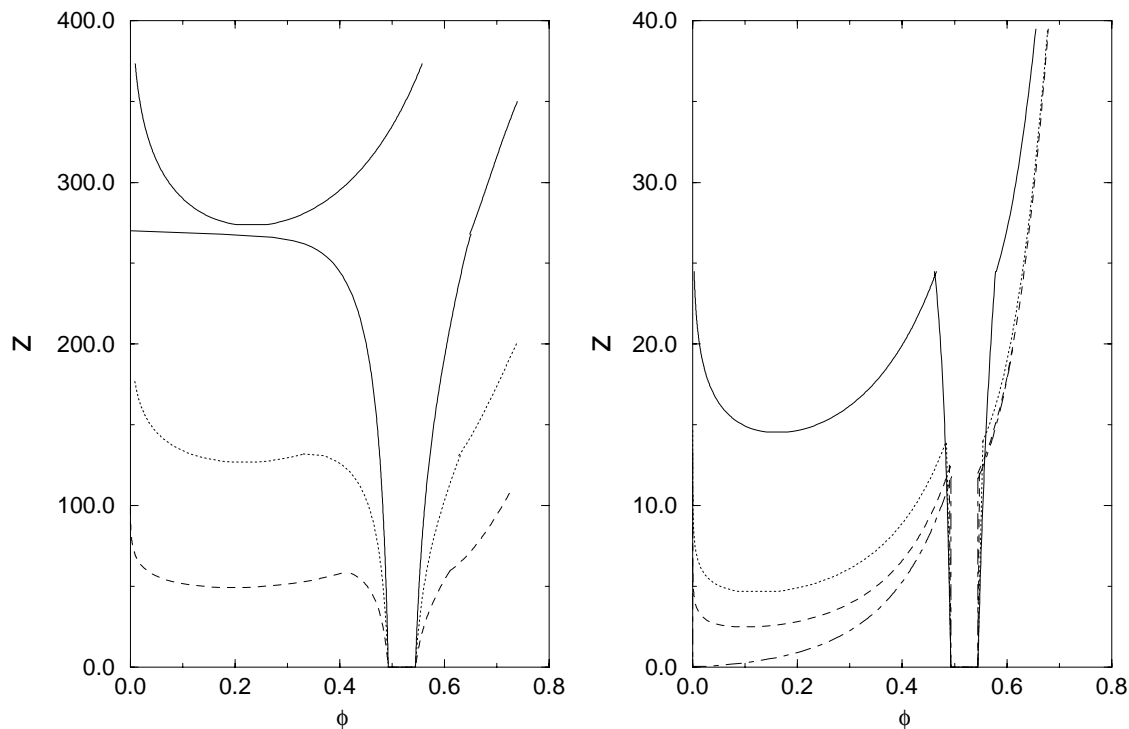


Figure 2.4. *Phase diagrams of hard sphere-rod mixtures. The fugacity of the rods, z , is plotted versus the volume fraction of hard spheres, $\rho\sigma^3$. The lines correspond to the phase boundaries and are obtained by first-order perturbation theory as given in the text. Left picture: solid line $L/\sigma=0.2$, dotted line $L/\sigma=0.3$, dashed line $L/\sigma=0.5$. Right picture: solid line $L/\sigma=1$, dotted line $L/\sigma=2$, dashed line $L/\sigma=3$ and dot dashed line $L \rightarrow \infty$. The solid curve in the left picture is the metastable fluid-fluid binodal for $L/\sigma=0.2$.*

liquid-vapor transition.

The features of the phase diagrams of the rodlike polymer are completely comparable with that of the fully flexible chains [10], although in the latter case the disappearing of the liquid region is predicted at polymer radii of gyration $2R_g/\sigma < 0.45$. However, the latter estimate is quite crude. It is therefore not obvious that the difference with the value obtained here is significant.

The liquid-gas separation in the rod like polymer colloid mixture can be described by first order perturbation theory. This theory predicts the location of the critical point well at rod lengths $L/\sigma < 4$, although this accuracy decreases for higher values of L/σ . The perturbation theory is accurate because the rods do not significantly affect the structure of the hard sphere dispersion. Hence, the free volume for a rod in a dispersion of spheres is effectively independent of the concentration of rods. Of course this is only valid in the case of ideal polymers. If the polymers would interact with each other the free volume would decrease considerably with the fugacity.

In the limit $L \rightarrow \infty$, the critical point shifts to zero density and zero polymer fugacity. The binodal curve is in this limit equivalent to the equation of state for hard spheres. The fugacity of the rods is equal to the pressure of the coexisting hard sphere fluid phase because in the vapor phase no spheres are present and the liquid phase is free of needles. This fact may provide an alternative route to obtain the equation of state of hard spheres experimentally

by measuring the concentration of rods in the vapor phase of a phase separated mixture of colloids and stiff polymers as a function of the volume fraction of spheres in the liquid phase.

The simulations discussed in this chapter show that for mixtures of hard spherical particles and thin needles liquid-vapor phase separation will occur. However, one could object that the limiting case of infinitely thin needles is unrealistic. Hence, it is important to know whether the demixing transition will still occur if the needles have a finite diameter D . Recently, Mao et al. [42] have investigated the effect of the finite thickness of the rods on the potential of mean force between two spheres. They find that, for rods of finite thickness, the effective pair potential develops a repulsive barrier at finite separation, in addition to the attractive well at contact. In particular for small L/σ values, this barrier can be high enough to lead to kinetic stabilization of the suspension and prevent any phase separation. Moreover, one should also consider the possibility that the rodlike particles will undergo a transition from the isotropic to the nematic phase. This transition will take place when $\rho_r B_2 = O(1)$, where B_2 is the second virial coefficient of the rods and ρ_r their number density. To see at what value of the rod osmotic pressure the isotropic-nematic transition occurs, we consider the Onsager limit of rods with high L/D ratio [25]. In this limit the osmotic pressure of the rods can be written as

$$\beta P_r = \rho_r \left(1 + \frac{\pi}{4} D L^2 \rho_r \right), \quad (2.22)$$

where we used the diameter of the spheres as unit of length. The isotropic phase becomes unstable at a density of $\frac{\pi}{4} D L^2 \rho_r \approx 3.3$ [25], which corresponds to an osmotic pressure $P_{IN} \approx 18/(D L^2)$. To observe the liquid-vapor phase separation, this pressure has to be larger than the critical pressure P_c for the phase separation.

In the limit that $D \rightarrow 0$ while L remains finite, the I-N transition occurs at infinite pressure. For rods with a finite diameter, demixing can compete with the I-N transition. To be specific, on basis of the perturbation theory and eqn. 2.19 we assume that for $L/\sigma \gg 1$, $P_c = 2\sigma e/3L$. If we equate P_c to P_{IN} , we find that demixing is preempted by an I-N transition if $LD/\sigma^2 > 10$. This implies that for small D/σ the liquid-vapor phase separation occurs well before the I-N transition.

Of course, the finite thickness of the rods will alter the simulated phase diagrams, especially for small L/D ratios. This will probably shift the phase separation region as well as the isotropic-nematic transition to higher fugacities. So we expect that the liquid-vapor phase separation still occurs at lower fugacities than the isotropic-nematic transition for reasonable L/D ratios ($L/D > 5$), provided that the transition is not prevented by any kinetic stabilization [42].

ISOSTRUCTURAL SOLID-SOLID TRANSITION

3

Monte Carlo simulations show that dense systems of spherical particles with a short-ranged attractive interaction, can undergo a first-order transition from a dense to a more expanded solid phase with the same structure. This phase-transition is analogous to the liquid-vapor transition in systems with longer-ranged attractive forces. In particular, the solid-solid transition terminates in a critical point. Numerical simulations on a square-well model indicate that a solid-solid transition will occur both in two and in three dimensions, if the width of the attractive well is less than 7% of the hard-core diameter. For a hard-core Yukawa model, the transition occurs at a comparable value of the width of the attractive well. Introduction of size-polydispersity tends to suppress the solid-solid transition. We argue that the solid-solid phase transition should be experimentally observable in mixtures of uncharged colloids and non-adsorbing polymers.

Introduction

3.1

In this chapter, we consider what happens in colloidal systems with a very short ranged attraction, where the liquid-vapor transition is absent. We show that these systems may exhibit a type of solid-solid transition that is in many ways reminiscent of the liquid-vapor transition: in particular,

1. the transition takes place between two phases that have the *same* structure,
2. the line of (first-order) solid-solid transitions ends in a critical point, and
3. the transition depends strongly on the range of the intermolecular attraction.

As a first approximation, we use the square well potential to model short-ranged interactions in colloids. This model, although simple, should provide an adequate description of a wide class of uncharged colloidal particles with short-ranged attraction. The square well model has been the subject of many theoretical and simulation studies [43, 44]. In particular, the molecular dynamics studies of Young and Alder [44] on the phase diagram of a long ranged square well system already show the possibility of a solid-solid phase transition. However, as the authors of ref [44] correctly point out, the latter transition is an artifact of the square well model and is not expected to occur in any real system. As we shall show below, the occurrence of the solid-solid transition in systems with short ranged potentials is not sensitive to the precise form of the potential and is therefore more likely to be experimentally observable. Additional evidence for the insensitivity of the solid-solid transition to the precise shape of the intermolecular potential comes from recent theoretical work by Tejero et al. [45] and by Rascon et al. [46]. These authors predict the existence of a solid-solid transition in different models of particles with a short-ranged attractive potential.

An interesting question that we address in the present study is whether or not the solid-solid transition exists in other dimensions than three. It is well known that systems with a short-ranged attraction cannot exhibit a phase transition in one dimension, but the solid-solid phase separation could occur in two-dimensional colloidal systems. Our simulations show that this is indeed the case. The existence of the transition in two dimension has consequences for the issue of stability of the hexatic phase [47–49]. Bladon and Frenkel [50] showed that a hexatic stable phase region can occur in the vicinity of the 2D solid-solid critical point.

The simulation results also indicate that the critical temperature of the solid-solid transition remains finite in the limit of infinitely narrow well-width. We study this limit by simulation of a lattice model and compare the results of the lattice model with that of the well-known adhesive sphere model introduced by Baxter [51].

In section 3.2, we present our simulation results on the square-well model for both two and three dimensions, followed by the discussion on the infinitely narrow well-width limit. In section 3.3, we discuss the application of a simple uncorrelated cell model to the square-well system. These calculations provide considerable insight in the mechanism of the phase transition.

To verify that the solid-solid transition is not an artifact of the square-well model we also performed extensive simulations on hard-core systems with an attractive Yukawa potential. The latter model is thought to provide a fairly realistic description of the effective colloid-colloid interaction in mixtures of uncharged colloids and non-adsorbing polymer [7, 9, 10]. The results of the Yukawa simulations are presented in section 3.4. Solid-solid transitions can also occur for repulsive potentials [52]. In section 3.5 we discuss the simulations we performed on a repulsive “square shoulder” potential. Finally, because most colloidal dispersions exhibit a certain amount of size-polydispersity, we explore the influence of polydispersity on the solid-solid transition in section 3.6.

3.2 Square well systems in two and three dimensions

3.2.1 Solid-solid coexistence

The square-well model provides a very simple description of particles interacting through a pair potential that is harshly repulsive at distances less than a characteristic diameter σ and has an attractive interaction with a characteristic range δ , outside the repulsive core. The functional form of the square-well potential is:

$$v(r) = \begin{cases} \infty & 0 \leq r < \sigma, \\ -\epsilon & \sigma \leq r < \sigma + \delta, \\ 0 & r \geq \sigma + \delta. \end{cases} \quad (3.1)$$

where ϵ is the depth of the attractive well. In order to compute the phase diagram of the square-well system, we first must determine the dependence of the Helmholtz free energy of the solid on density and temperature. As the free energy of the solid cannot be measured directly in a Monte Carlo simulation, we use thermodynamic integration to relate the free energy of the square-well solid to that of a reference hard-sphere solid at the same

density [53].

$$F(\rho, \epsilon^*) = F_{\text{HS}}(\rho) + \int d\epsilon^* \left(\frac{\partial F}{\partial \epsilon^*} \right) = F_{\text{HS}}(\rho) + \int d\epsilon^* \frac{\langle E \rangle_{\epsilon^*}}{\epsilon^*}, \quad (3.2)$$

where ϵ^* is the reduced well-depth $\epsilon/k_B T$ and $\langle E \rangle$, the average internal energy of the system, a quantity that *can* be measured in a Monte Carlo NVT simulation. The instantaneous energy is equal to the number of pairs of atoms N_p that are within the range of the potential times the depth of potential well ϵ . The dimensionless free energy per particle now is simply

$$\frac{F(\rho, \epsilon^*)}{Nk_B T} = \frac{F_{\text{HS}}(\rho)}{Nk_B T} - \int d\epsilon^* \frac{\langle N_p \rangle_{\epsilon^*}}{N}, \quad (3.3)$$

The free energy of the three dimensional hard-sphere solid F_{HS} is well known and can be accurately represented using the analytical form for the equation of state proposed by Hall [54]. In two dimensions the free energy of the hard-disk “solid” can be obtained from simulations done by Alder et al. [55].

The presence of a first-order phase transition in the square-well solid is signaled by the fact that the Helmholtz free energy becomes a non-convex function of the volume. The densities of the coexisting phases can then be determined by a standard double-tangent construction.

In order to map out the phase diagram of the square-well solid over a wide range of densities and temperatures as a function of the width of the attractive well, several thousand independent simulations were required. To keep the computational costs within bounds, we chose to simulate a relatively small system. With a small system size, finite-size effects are expected, in particular in the vicinity of a critical point. However, away from critical points finite-size effects should be so small that they will not affect the conclusions that we draw below.

In what follows, we use reduced units, such that ϵ/k_B is the unit of temperature, and σ , the hard-core diameter of the particles, is the unit of length.

For the two dimensional case, the simulation parameters were as follows: All simulated systems consisted of a periodic triangular lattice of 200 disks, placed in a rectangular simulation box with side ratio $\sqrt{3}$. The densities ranged from $\rho=0.8$ which is below the hard-disk “melting point” to $\rho=1.154$ which is almost at close packing ($\rho_0 = 2/\sqrt{3}$). The temperature of the system was varied in the range $0 \leq 1/T \leq 2$, in steps of 0.1. Simulations were performed for $\delta=0.01, 0.02, 0.03, 0.04, 0.05, 0.06$ and 0.07 .

All simulations on the three-dimensional system were performed on a face-centered cubic (*fcc*) solid consisting of 108 particles. This is presumably the stable solid structure for hard-spheres¹ and for the square-well model with short-ranged attraction (i.e. only nearest neighbor interaction). The simulation box was chosen to be cubic and periodic boundaries were applied. The densities ranged from $\rho=0.9$ which is below the hard-sphere melting point to $\rho=1.414$ which is almost at close packing ($\rho_0 = \sqrt{2}$). The temperature

¹In fact, the difference in free energy of the face-centered cubic and hexagonal close packed (*hcp*) structures is so small that it is not known which one is the more stable. Our calculations were performed for the *fcc* structure, but the results would have been virtually the same for the *hcp* structure. Other crystal structures (e.g. simple-cubic and body-centered cubic) can be safely ignored because they have a much lower maximum packing density.

of the system was varied over the same range as in the two dimensional case. Simulations were performed for $\delta=0.001, 0.002, 0.003, 0.004, 0.005, 0.01, 0.02, 0.03, 0.04, 0.05$ and 0.06 . For every value of the well-width δ in both the two and three dimensional case, we performed some 1000 MC simulations of 20000 cycles each.

In order to perform the double-tangent construction on the Helmholtz free energy, all simulation data were fitted to an analytical function of ρ , δ and T . We chose to use a fit function that reproduced the correct limiting behavior at close packing. In particular, for the 2D case, we used the following functional form

$$N_p(\delta, T^{-1}, x)/N = \frac{3}{2} + \frac{3}{2} \operatorname{erf}\left(\frac{3}{4}x - \frac{1}{2}\right) + e^{-x} \sum_{i,j,k=0}^{1,2,6} c_{ijk} \delta^i T^{-j} x^k, \quad (3.4)$$

and in the three dimensional case we chose the following form

$$N_p(\delta, T^{-1}, x)/N = 3 + 3 \operatorname{erf}\left(x - \frac{3}{4}\right) + e^{-x} \sum_{i,j,k=0}^{1,2,6} c_{ijk} \delta^i T^{-j} x^k. \quad (3.5)$$

The parameter x in eqn. 3.4 and eqn. 3.5 is defined as the ratio of well width d to the distance a , that characterizes the expansion of the solid from close packing: $a \equiv r_{nn} - \sigma$, where r_{nn} is the average nearest neighbor distance and σ is the hard sphere diameter. x is simply related to the density, through:

$$x = \frac{\delta}{a} = \frac{\delta}{\left(\frac{\rho_0}{\rho}\right)^{\frac{1}{D}} - 1}, \quad (3.6)$$

where D is the dimensionality of the system. For large x - i.e. near close packing - the functions given in eqn. 3.4 and eqn. 3.5 go to the value of half the number of nearest neighbors per particle. The coefficients of the best fits to the numerical data are given in tables 3.2.1 and 3.2.1. These fits reproduce the numerical data to within the statistical error. Using the functional forms given by eqn. 3.4 and eqn. 3.5 to represent the numerical data, we computed the free energy of the solid as a function of temperature and volume, using eqn. 3.3. The resulting free energy functions were checked for possible non-convex dependence on the volume V . Whenever such an indication of a first-order phase transition was found, the densities of the coexisting phases were determined by equating the pressures and chemical potentials in both phases using the standard double tangent construction.

Table 3.1. *Best fit coefficients c_{ijk} for eqn. 3.4*

		k							
i	j	0	1	2	3	4	5	6	
0	0	-0.7269	0.3120	-0.2565	1.1129	-1.4978	0.6959	-0.1072	
0	1	-0.0372	1.2463	5.7100	-16.6730	15.6246	-6.1377	0.8720	
0	2	0.0285	0.97298	-6.0705	12.6428	-11.2989	4.5205	-0.6691	
1	0	5.2537	-34.7536	101.2833	-150.7283	112.8653	-40.9099	5.7120	
1	1	9.6639	0.1742	-165.0934	387.6826	-351.9945	141.4178	-20.9747	
1	2	5.8289	-66.8558	245.3414	-396.6194	310.5089	-115.3634	16.2825	

Table 3.2. *Best fit coefficients c_{ijk} for eqn. 3.5*

		k							
i	j	0	1	2	3	4	5	6	
0	0	-0.8423	-0.1755	1.0990	-2.3972	0.7528	0.2267	-0.0860	
0	1	-0.0941	2.3340	12.7626	-34.8155	31.4724	-11.8692	1.5970	
0	2	0.0999	1.4633	-7.5912	11.8632	-7.7087	2.0971	-0.1873	
1	0	0.5899	16.7503	-66.3909	86.7700	-59.3664	20.5255	-2.7624	
1	1	43.0163	-354.0380	968.0612	-1239.2203	808.6414	-259.2023	32.3219	
1	2	-13.2762	87.4591	-212.7239	240.1007	-134.4559	36.0477	-3.6622	

The critical temperature of the solid-solid coexistence curve was estimated to be the point where the free energy curve first developed an inflection point. Of course, this estimate is likely to depend somewhat on the system size. Moreover, the analytical form of eqn. 3.4 and eqn. 3.5 forces the classical (mean-field) critical behavior on the solid-solid binodal. We have not attempted to study the true critical behavior of the solid-solid transition.

Fluid-solid coexistence

3.2.2

Although the solid-solid transition coexistence curves can be obtained from simulations, we have yet to demonstrate that this transition involves phases that are thermodynamically stable. In particular, the melting transition might preempt the solid-solid phase separation. It is therefore essential to study the fluid-solid transition as well. We computed the solid-fluid coexistence curve by means of thermodynamic integration. The Helmholtz free energy of square-well solid was calculated according to eqn. 3.2 using our simulation data. The free energy of the fluid phase was obtained by combining data from our simulations of a square-well fluid with the known free energy of the hard-sphere reference fluid [37]. In the two dimensional case the fluid simulations were performed on a system consisting of 200 disks with square well potential in a square box. The densities ranged from $\rho=0.81$, which is below the hard-disk fluid-solid transition at $\rho=0.87$ [56], to $\rho=0.95$, well above the melting density. The other simulation parameters were the same as in the two dimensional square-well solid simulation.

To simulate the fluid in three dimensions, we used a system of 108 square-well spheres in a periodic cubic box. The density was varied from $\rho=0.9$ to $\rho=1.0$ and the well width ranged from $\delta=0.01$ to $\delta=0.06$. The simulation parameters were equal to those chosen for the solid simulations. For both the 2D and 3D simulations the initial random configuration was compressed to the required density and equilibrated for 20,000 cycles before data was collected in a production run of 20,000 cycles. To calculate the fluid-solid coexistence one needs the absolute free energy of both the reference fluid and the reference solid phase. For the free energy of the hard disk fluid we used a Padé approximation proposed by Hoover and Ree [56]. The hard disk solid free energy was obtained from simulation data by Alder et al. [55]. The free energy of the hard-sphere fluid was calculated using the accurate Carnahan-Starling equation of state [37], whereas the Hall equation of state [54] was used in the solid region together with an absolute free energy value obtained from simulations of Frenkel and Ladd [39].

Using these reference free energies and the simulated average internal energies in eqn. 3.2

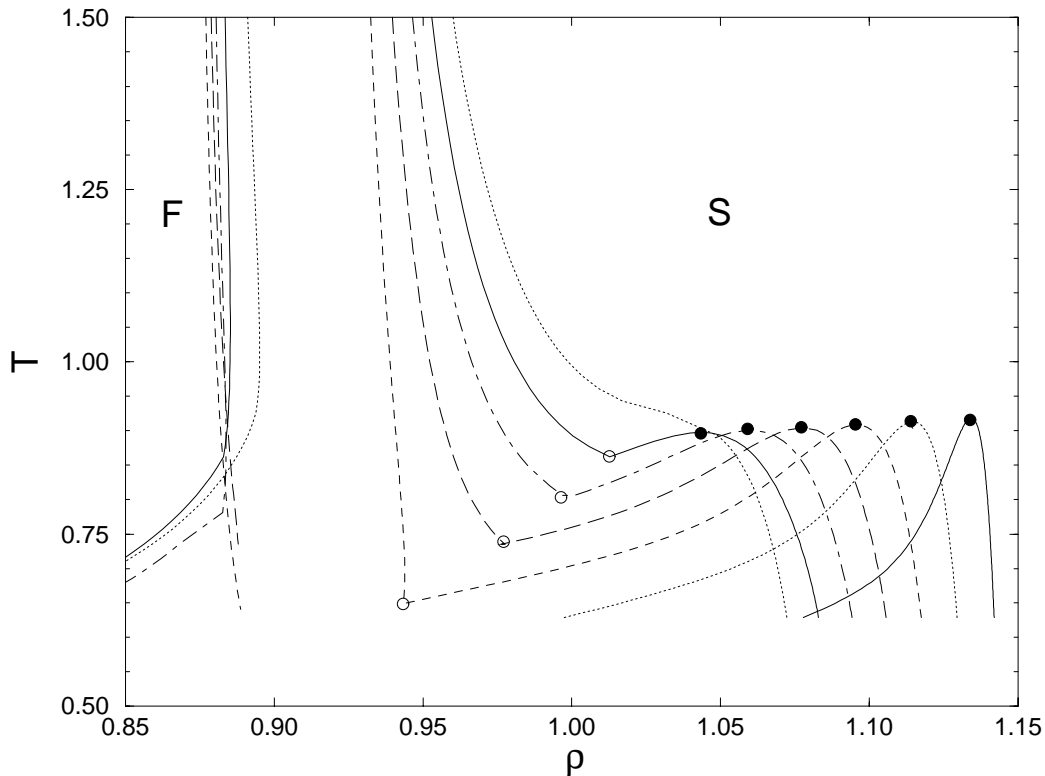


Figure 3.1. Simulated T, ρ phase diagrams for triangular lattice of 200 square well particles in two dimensions. Starting with the coexistence curve on the right, from right to left the curves correspond to the well widths $\delta/\sigma=0.01, 0.02, 0.03, 0.04, 0.05, 0.06$ and 0.07 . Solid-fluid coexistence curves are shown for all systems with $\delta/\sigma \geq 0.03$. The critical points are indicated by filled circles, the triple points by open circles.

we were able to obtain the coexistence curves for the fluid-solid transition for both the two and three dimensional square-well models.

3.2.3 Results

Figure 3.1 and 3.2 show the computed solid-solid and fluid-solid coexistence curves in the ρ, T plane for the two and three dimensional square-well models. We first focus on the solid-solid transition. The density gap between the dense and expanded *fcc* solids is wide at low temperatures and shrinks to zero when the solid-solid critical point is approached. Because of the analogy with liquid-vapor coexistence, one would expect that the solid-solid critical point should be of the 2D and 3D-Ising universality class.

The coexistence curves are asymmetric, especially in the limit $\delta \rightarrow 0$. In this limit, the reduced critical temperature T_c goes to a finite limiting value of approximately 1.7 for $D=3$ and 0.92 for $D=2$. As we shall argue below, the phase behavior in this limit can be investigated by studying a peculiar lattice model.

As can be seen in figure 3.1 and 3.2, the critical temperature depends only weakly on δ . In contrast, the solid-solid coexistence region shifts to lower densities as the well-width is increased. This effect can easily be understood by noting that a dense square-well solid

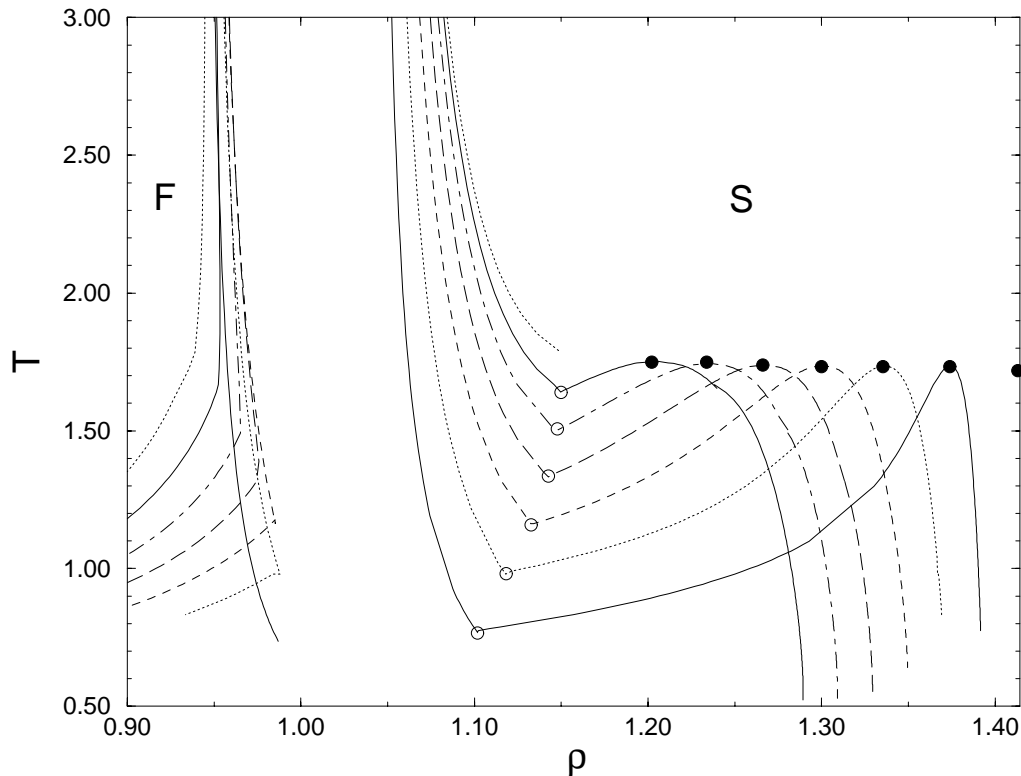


Figure 3.2. Simulated T, ρ phase diagrams for the fcc structure of 108 square well particles. Starting with the coexistence curve on the right, from right to left the curves correspond to the well widths $\delta/\sigma=0.01, 0.02, 0.03, 0.04, 0.05$ and 0.06 . The upper dashed fluid-solid coexistence curve refers to a well width of $\delta/\sigma=0.07$ and shows that the solid-solid transition has become metastable at this point. The critical points are indicated by filled circles, the triple points by open circles. The critical point at $\rho = \sqrt{2}$, corresponding to $\delta/\sigma=0$ was computed using the lattice model described in section 3.2.4.

can be expanded at virtually no cost in potential energy, up to the point where the nearest-neighbor separation is $1+\delta$, that is $\alpha = \delta$. It is only when the solid is expanded beyond this limit that the potential energy increases steeply and a transition to the expanded solid may occur. Hence, the larger δ , the lower the density where the phase transition will take place.

The fluid-solid coexistence curves are also dependent on δ . For small δ the width of the coexistence density gap between fluid and solid remains effectively constant as a function of temperature, although as a whole it shifts to higher density as the temperature is lowered. If δ is increased the density gap widens at low temperature.

The point where the coexistence curves cross the solid-solid binodals is the triple point T_p where the three phases (fluid, solid I and solid II) are in equilibrium. At temperatures below the triple point the high-density solid is in equilibrium with a dilute gas. When δ becomes larger, the triple point shifts to higher temperatures and densities, until it reaches the critical temperature. At that point the solid-solid transition disappears because for larger values of δ it is preempted by the melting transition. Both in two and three dimensions, this happens

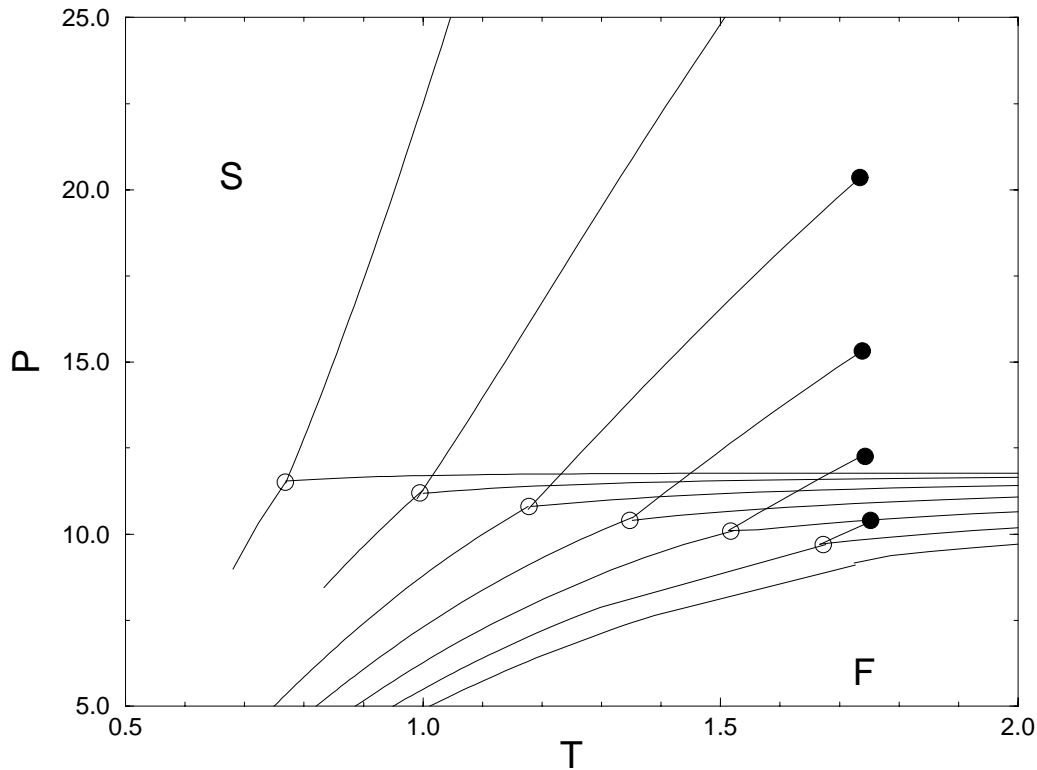


Figure 3.3. Simulated phase diagrams of the three-dimensional square-well system plotted in the P, T plane. The solid-solid transition lines run from the triple point, denoted by an open circle to the critical point, marked by a filled circle. The lower curves are the melting lines of the square well system. From left to right the diagrams correspond to $\delta/\sigma=0.01, 0.02, 0.03, 0.04, 0.05$ and 0.06 . Note that this phase diagram is almost a mirror image of the fluid-gas P, T phase diagram. Also note that the slope of the solid-solid transition has to be positive.

when $\delta > 0.06$.

It is instructive to draw the phase diagram in the P, T plane. In figure 3.3 the phase diagrams for the three dimensional square well system are shown in the P, T plane. The solid-solid transition lines run from the triple point to the critical point and lie above the melting lines of the square well system. The phase diagram for short-ranged attractive potential is the mirror image of the usual P, T phase diagram for longer ranged potentials in which the liquid-gas transition is present. Note that the slope of the solid-solid transition line cannot be negative, because the critical temperature has to be higher than the triple point temperature.

3.2.4 High density limit

The simulations discussed above seem to indicate that there is a solid-solid transition even in the limit where $\delta \rightarrow 0$. At first sight this seems surprising, because one would not expect an infinitely narrow potential well to affect the phase behavior at finite temperature. However, at close packing, even an infinitely narrow potential will give a finite contribution to the potential energy. Surprisingly, it turns out that it is possible to perform simulations

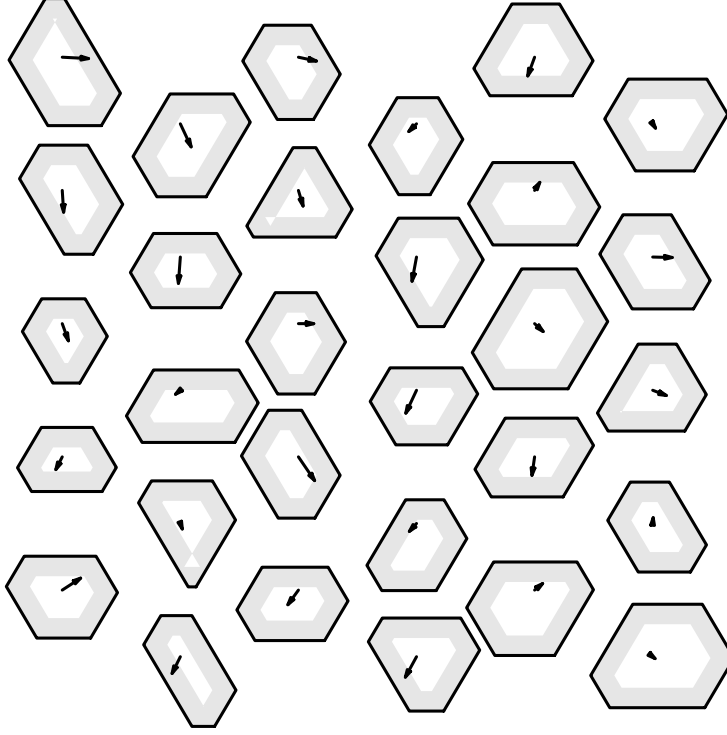


Figure 3.4. *Schematically drawn scaled configuration of the (2D) square-well solid in the limit $\delta/\sigma \rightarrow 0$. The lines of the hexagons give the momentary boundary of the cell to which a particle is confined. All the cells are scaled up to finite size, as the cells are infinitely small in the limit $\delta/\sigma \rightarrow 0$. The cell boundaries will change position if the nearest neighbors move. The arrows give the particle displacement from their original lattice positions. In the shaded area the particles are within the interaction range of their neighbors.*

of the phase behavior in the limit $\delta \rightarrow 0$. To see how this can be achieved, it is convenient to consider first the more general case that δ is finite. In the dense crystalline solid, any given particle i is constrained to move in the vicinity of its lattice site - i.e. its average position - \vec{r}_i^0 . In that case, we can re-express the potential energy as a function of the displacement $\vec{\Delta}_i$ of the particles, from their respective lattice sites: $\vec{\Delta}_i \equiv \vec{r}_i - \vec{r}_i^0$. The potential energy of a pair of particles can then be written as

$$v(\vec{r}_{ij}) = v(|\vec{r}_i^0 - \vec{r}_j^0 + \vec{\Delta}_i - \vec{\Delta}_j|), \quad (3.7)$$

where we have used the obvious notation $\vec{r}_{ij} \equiv \vec{r}_i - \vec{r}_j$. For nearest neighbors, $|\vec{r}_i^0 - \vec{r}_j^0| = \sigma$ at close packing. At lower densities, $|\vec{r}_i^0 - \vec{r}_j^0| = \sigma + a$ where a has been defined in eqn. 3.6. The potential energy of a pair of square-well particles is a function of $z_{ij} \equiv (|\vec{r}_{ij}| - \sigma)/\delta$. We can now express \vec{r}_{ij} in terms of $\vec{\Delta}_i$ and $\vec{\Delta}_j$. This yields the following result for z_{ij}

$$z_{ij} = \frac{\sqrt{\sigma^2 + 2\sigma(a + \hat{r}_{ij} \cdot \vec{\Delta}_{ij}) + a^2 + \vec{\Delta}_{ij}^2 + 2a\hat{r}_{ij} \cdot \vec{\Delta}_{ij}} - \sigma}{\delta}, \quad (3.8)$$

where \hat{r}_{ij} is a unit vector in the direction of \vec{r}_{ij}^0 and $\vec{\Delta}_{ij} = \vec{\Delta}_i - \vec{\Delta}_j$. In the limit $\delta/\sigma \rightarrow 0$, z_{ij} takes on a very simple form

$$\lim_{\delta/\sigma \rightarrow 0} z_{ij} = \frac{a + \hat{r}_{ij} \cdot \vec{\Delta}_{ij}}{\delta}. \quad (3.9)$$

In this limit, the square-well model is equivalent to a lattice model, with a fixed, but arbitrary lattice spacing as shown in figure 3.4. The state at every lattice point i is characterized by a scaled displacement vector $\vec{v}_i \equiv \vec{\Delta}_i/\delta$. Note that a finite \vec{v}_i corresponds to an infinitesimal real displacement $\vec{v}_i\delta$. The nearest-neighbor interaction is a function of $a/\delta + \vec{v}_i \cdot \hat{r}_{ij}$. Clearly, the density in the original square-well model now only enters in the problem through the parameter a/δ . We can now perform Monte Carlo simulations on this lattice model by moving a randomly selected atom i from its initial scaled displacement \vec{v}_i to the trial displacement \vec{v}'_i in such a way that microscopic reversibility is satisfied. Knowledge of the new scaled displacement of atom i is sufficient to compute the change in potential energy associated with the trial move, using eqns 3.7 - 3.9 above. We now use the conventional Metropolis rule to accept or reject the trial move. By combining the results of a series of simulations for a range of values of δ/a and a range of temperatures (twenty temperatures and thirty δ/a values for every temperature) with the hard-sphere equation of state near close packing [57], we can compute the free energy of this model system as a function of temperature and volume by thermodynamic integration and construct the solid-solid phase diagram in the limit $\delta/\sigma=0$. In the ρ, T plane, the binodal would simply be a vertical line segment at close packing ending in a critical point. It is more convenient to plot the binodal as a function of δ/a . In figure 3.5, the solid-solid binodal is plotted in the $\delta/a, T$ plane. As can be seen from the figure the critical temperature is indeed finite. Moreover, the binodal becomes quite symmetric in this representation compared to figure 3.2.

It is interesting to consider the square-well solid at *finite* δ/σ in terms of the lattice model described above. As can

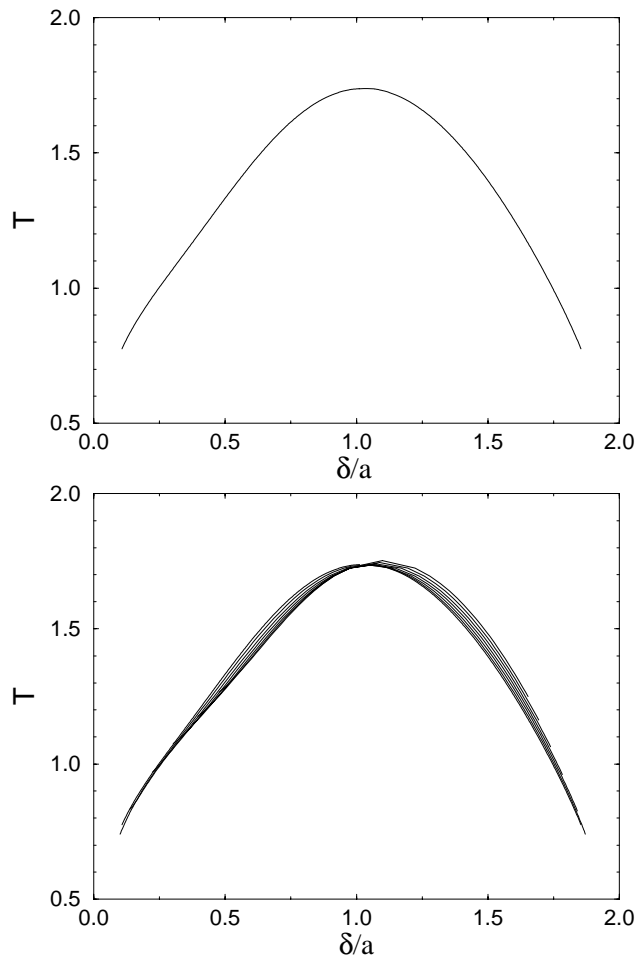


Figure 3.5. *Solid-solid coexistence curves in the $\delta/a, T$ plane (see text). The upper figure shows the binodal in the limit $\delta/\sigma=0$, while the bottom figure shows that all the scaled binodals for finite $\delta/\sigma < 0.07$ very nearly coincide with the binodal for $\delta/\sigma=0$.*

be seen from eqn. 3.7 and eqn. 3.8, the potential energy now is a function not only of α/δ and $\bar{\Delta}_i/\delta$ but also of δ/σ . If the free energy of the system is an analytic function of δ/σ , we could expand in powers of it around the limit $\delta/\sigma=0$. However, the solid-solid transition only occurs for $\delta/\sigma \leq 0.06$. Hence, δ/σ is always a small parameter. It is therefore likely that the phase diagram of the square-well model, when plotted as a function of δ/α differs only little from the behavior in the limit $\delta \rightarrow 0$. As can be seen from figure 3.5 this is indeed the case. It is interesting to point out the relation between the square-well model in the limit $\delta/\sigma=0$ and the adhesive hard-sphere model proposed by Baxter [51]. The adhesive hard-sphere model is obtained from the square-well model by considering the limit $\delta/\sigma \rightarrow 0, \epsilon \rightarrow \infty$ such that $\epsilon/kT = -\ln(\sigma/(12\delta\tau))$. This limiting procedure results in a model that has a finite second virial coefficient at finite temperature. Usually, the ratio of the second virial coefficient of the adhesive hard-sphere to that of “non-sticky” hard spheres is used to relate the parameter τ to observable quantities:

$$B_2^{\text{AHS}}/B_2^{\text{HS}} = 1 - \frac{1}{4\tau}. \quad (3.10)$$

The adhesive hard sphere system has been studied extensively, both theoretically [58–60] and numerically [61, 62]. In particular, the liquid-vapor critical point of this model has been predicted to occur at $\tau \approx 0.097$ [58]. However, if we identify the adhesive hard-sphere model with the square-well model in the limit $\delta/\sigma \rightarrow 0$, then the present simulations show that this model already has a solid-solid transition for $\tau = \mathcal{O}(\ln(\sigma/\delta))$, i.e. for $\tau \rightarrow \infty$. At all finite temperatures (finite τ) the only stable phases are the close-packed solid and the infinitely dilute gas. Hence, all other phases of the adhesive hard-sphere model are, at best, metastable. In fact, Stell [63] has already indicated that the monodisperse adhesive hard-sphere model is pathological because the 12th virial coefficient diverges. This divergence could be removed by introducing a slight size polydispersity into the model. Such polydispersity would also affect the solid-solid transition. In fact, a rough estimate of the phase-diagram suggest that in that case, the solid-fluid transition occurs at finite τ , and hence the phase diagram of the slightly polydisperse adhesive hard sphere model is non-trivial.

Cell model calculations

3.3

To gain a better intuitive understanding of the solid-solid transition in the square well model, it is instructive to compare the simulation results with a simple theoretical approach, viz. the uncorrelated cell model. The cell model is based on the idea that an atom in a solid is essentially confined to the “cell” formed by its nearest neighbors [64]. In the uncorrelated, single occupancy version of the cell model [65, 66] the configurational part of the partition function of a N-particle system is approximated by

$$Q = \int d\mathbf{r}^N e^{-\beta U(\mathbf{r}^N)} \approx N! \left(\int d\mathbf{r} e^{-\beta U(\mathbf{r}, \mathbf{r}^{\text{nn}})/2} \right)^N, \quad (3.11)$$

where $U(\mathbf{r}^N)$ is the potential energy of the system, and $U(\mathbf{r}, \mathbf{r}^{\text{nn}})$ is the potential energy of an atom and its nearest neighbors. Here it is assumed that a cell can contain at most one particle and that all correlations between cells can be ignored. If one further assumes that every particle moves independently in a regular fixed polyhedron formed by its neighbors

fixed at their lattice positions, the second integral of eqn. 3.11 can be easily evaluated. We use the square-well model to describe the short ranged attractive interaction. Because the square well potential is a step function, the cell volume can be divided into different regions characterized by the number of neighbors within the range of its attractive well. The partition function can now be expressed in terms of cell volume fractions α_k in which the particle interacts with k particles simultaneously

$$\frac{Q(x, \epsilon^*)}{N!} = \left(V_c \sum_{k=0}^m e^{k\epsilon^*/2} \alpha_k(x) \right)^N, \quad (3.12)$$

where $x = \delta/a$ is the parameter defined in eqn. 3.6, m is the maximum number of neighbors and V_c the volume of the cell. This volume depends on the dimensionality and the crystal structure. For a three dimensional *fcc* structure the cell is a dodecahedron with a volume $V_c = a^3/\sqrt{2}$, where a , the radius of the cell, is defined as before $a \equiv r_{nn} - \sigma$. In a two-dimensional triangular lattice, $V_c = 2\sqrt{3}a^2$.

The Helmholtz free energy of the solid is given by the logarithm of the partition function

$$\frac{\beta F_{SW}(x, \epsilon^*)}{N} = \frac{-\log Z(x, \epsilon^*)}{N} = -\log \Lambda^3 V_c - \log \left(\sum_{k=0}^m e^{k\epsilon^*/2} \alpha_k(x) \right). \quad (3.13)$$

The first term can be interpreted as the entropy of an ideal lattice gas, while the second term is the contribution due to the attractive interactions. Figure 3.6 shows for the triangular and *fcc* crystal structures the cell volume fraction α_k as a function of x . For sufficiently short-ranged potentials, the solid can be expanded to a density where a is much larger than the width of the attractive well δ . In that case, a given particle can only have a few neighbors within the range of its attractive well. When the density is increased the particle interacts with more neighbors. At $\delta/a=1$ the particle has exactly half the number of neighbors within the potential range. Once the density is so high that $\delta/a > 2$, then

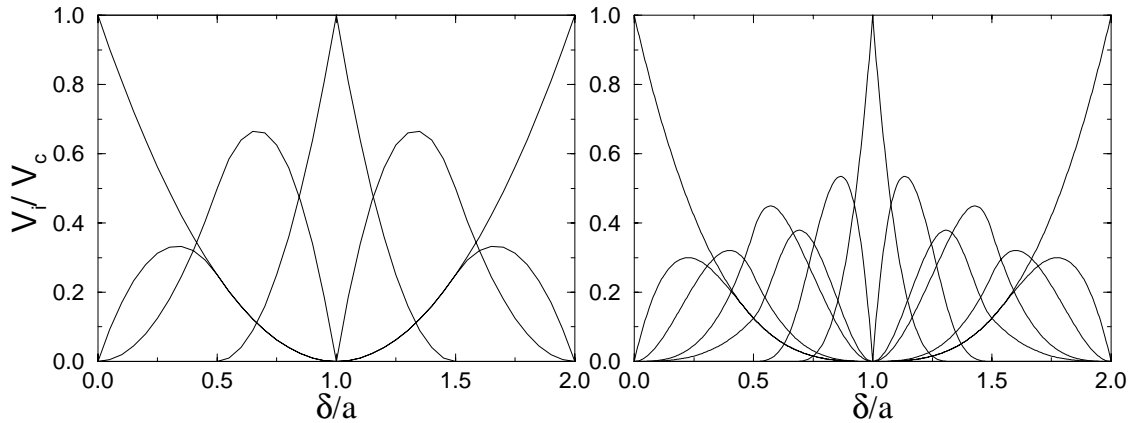


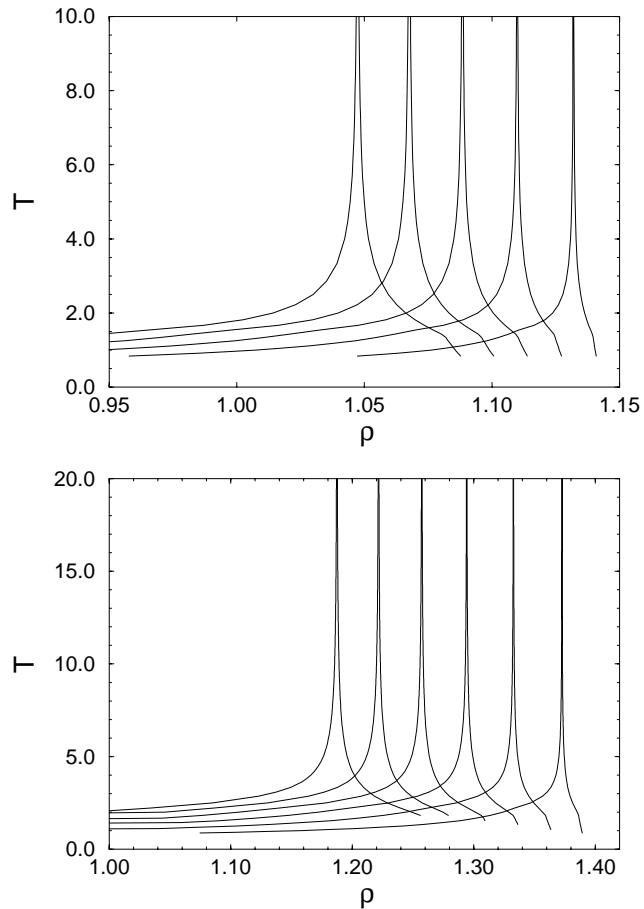
Figure 3.6. *Uncorrelated cell model calculation of the fraction of cell volume where the central particle interacts with k neighbors as a function of δ/a . Top figure: two dimensional hexagonal lattice. The curves represent from left to right, $k=0,1...6$. Bottom figure: three dimensional *fcc* structure. From left to right curves for $k=0,1...12$.*

every particle interacts with all its nearest neighbors simultaneously. This behavior leads to a fairly abrupt lowering of the potential energy of the system. At low temperatures, this decrease of the energy on compression will outweigh the loss of entropy that is caused by the decrease of the free volume V_c . The Helmholtz free energy F will then exhibit an inflection point, and a first-order transition to a “collapsed” solid will result.

By application of a double tangent construction we can compute the coexisting densities as a function of temperature. Figure 3.7 shows the coexistence curves in the temperature density plane for different values of the attractive well depth δ . Indeed the cell model predicts a phase separation at high density and small well width δ . The coexistence gap becomes larger when the temperature is lowered. A spurious feature of this simple cell model is that it does not predict a finite critical temperature. This stems from the fact that in the cell model there is always a discontinuity in the pressure and chemical potential that leads to a phase transition at all temperatures. The discontinuity originates from the sharp change in the volume fraction α at $\alpha = \delta$ (see figure 3.6) in the uncorrelated cell model approximation. As the discontinuity of the pressure always takes place at a density where $\delta = \alpha$, a very simple expression for the critical density follows

$$\rho_c = \rho_0 \left(\frac{\delta}{\sigma} + 1 \right)^{-D}, \quad (3.14)$$

Figure 3.7. Phase diagrams in the T, ρ plane for the square well potential in the uncorrelated cell model approximation. Top figure: Coexistence curves for a two dimensional hexagonal lattice. From right to left $\delta/\sigma=0.01, 0.02, 0.03, 0.04$ and 0.05 . Bottom figure: Coexistence curves for a three dimensional fcc lattice. From right to left $\delta/\sigma=0.01, 0.02, 0.03, 0.04, 0.05$ and 0.06 . In both figures no critical temperature is obtained due to discontinuities in the derivatives of the cell model free energy.



where ρ_0 denotes the density of the solid at regular close packing.

As can be seen in figure 3.8, the dependence of the critical density on δ obtained from the simulations is described remarkably well by eqn. 3.14, despite the fact that the finite critical temperature is not predicted by the cell model calculations. When all correlations are taken into account the discontinuities in the free energy derivatives should disappear and a finite critical temperature will result. Of course, more sophisticated cell model and cell cluster theories that deal with the correlations exists [57, 67], but are not necessary for our purpose. In a recent paper, Daanoun et al. [68] used a van der Waals-like approximation to compute the phase diagram of a square-well system. Although this approach also ignores all correlation effects, these theoretical calculations reproduce the essential features of our simulation data. Even better agreement has been found in recent density-functional theory calculations by Likos et al. [69].

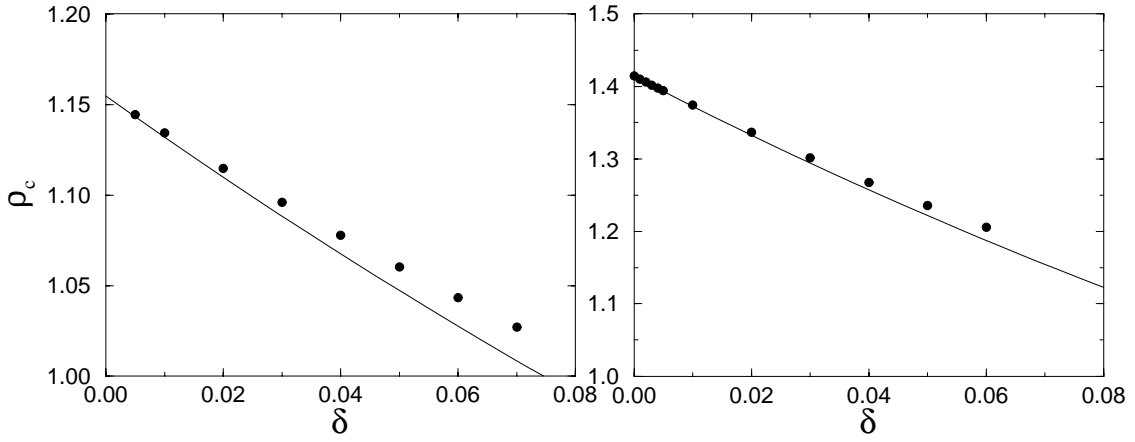


Figure 3.8. *Solid-solid critical density of square-well systems, as a function of the well width δ . The circles denote the simulation results, while the solid curve denotes the prediction of the uncorrelated cell model. The upper figure refers to two dimensions while the lower figure shows the three dimensional case.*

3.4 Yukawa potential

The square-well potential is often used as a crude approximation to the effective intermolecular potential in colloid-polymer mixtures. A better approximation for the colloid-colloid interaction in such systems is the hard-core attractive Yukawa potential, given by

$$v(r) = \begin{cases} \infty & 0 \leq r < \sigma, \\ -\epsilon \left(\frac{\sigma}{r}\right) \exp(\kappa\sigma(1 - r/\sigma)) & r > \sigma. \end{cases} \quad (3.15)$$

where ϵ is the well depth and κ^{-1} is a measure for the range of the attractive part of the potential [9, 10, 8, 7]. The phase diagram of the hard-core attractive Yukawa fluid was investigated recently by Hagen and Frenkel [70]. To see if the solid-solid transition survives in the case of a Yukawa potential, we did simulations on a 108 particle fcc crystal for $\kappa=15, 20, 25, 30, 35, 40, 45$ and 50 and in the high density limit for $\kappa \rightarrow \infty$. The

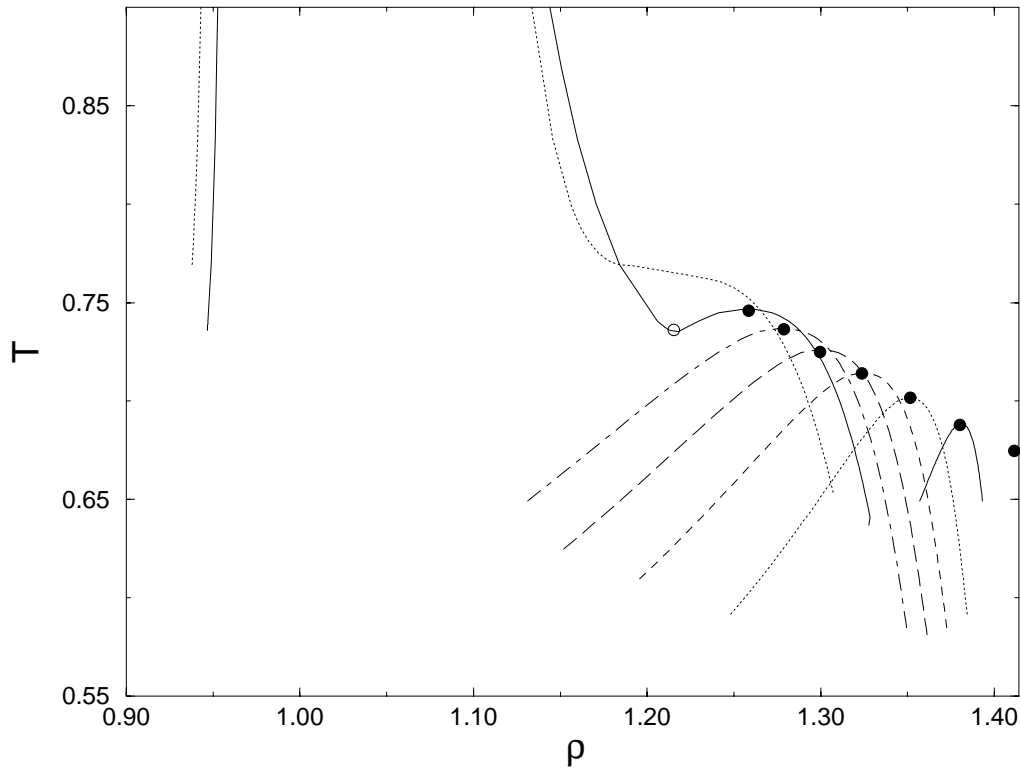


Figure 3.9. Simulated T, ρ phase diagrams for the 108 particle fcc crystal structure with Yukawa potential. Starting with the coexistence curve on the right, from right to left the curves correspond to $\kappa=200, 100, 67, 50, 40, 33$ and 25 . The critical points are indicated by filled circles, the triple points by open circles. The critical point at $\rho = \sqrt{2}$, corresponding to $\delta/\sigma=0$ was computed using the lattice model described in section 3.2.4. Only for the last two values the fluid-solid coexistence were calculated. For higher κ values, we should expect to see the range of stability of the solid-solid coexistence line increase until, in the limit $\kappa \rightarrow \infty$, it will extend down to $T=0$.

densities ranged from 1.1 to 1.38. The temperatures, in reduced units of ϵ/k_B , were varied in the same range as in the square well case, $0 \leq T^{-1} \leq 2$, in steps of 0.1. For every value of ρ, T and κ we performed some 10,000 Monte Carlo cycles to equilibrate and the same amount to collect data. The average internal energy was fitted to a polynomial in $\kappa^{-1}, 1/T$ and $\kappa^{-1}(\rho_0/\rho - 1)^{-1}$. It was not necessary to use the more complicated functional form given in eqn. 3.4 because the energies varied much more smoothly with density than in the square-well model. The Helmholtz free energy of the Yukawa solid was obtained by thermodynamic integration starting with the hard-sphere free energy (cf. eqn. 3.2) and the coexistence densities as a function of temperature were calculated by applying the double tangent construction.

As in the case of the square-well model it is essential to know the position of the fluid-solid coexistence region to determine the range of densities where a solid-solid transition can take place. We estimated the location of the melting curve by first-order perturbation theory. In ref [70] it is shown that first-order perturbation provides quite accurate estimates of the melting curve of the hard-core attractive Yukawa system.

The Helmholtz free energy of the Yukawa system can be approximated by

$$F(\rho) = F_{HS}(\rho) + \langle E_{yuk} \rangle_{HS}, \quad (3.16)$$

where $\langle E_{yuk} \rangle_{HS}$ is the average value of the attractive part of the Yukawa potential, computed in the hard-sphere reference system. From this equation it is possible to derive the fluid-solid coexistence by application of the double tangent construction. Simulations on a 108 particle hard-sphere fluid and hard-sphere *fcc* crystal were used to compute $\langle E_{yuk} \rangle_{HS}$ for $\kappa = 25$ and $\kappa=33$.

The resulting phase diagrams for $\kappa=25, 33, 40, 50, 67, 100$ and 200 are presented in figure 3.9. The solid-solid transition is found to occur for $\kappa > 25$. For values $\kappa > 33$ the fluid-solid coexistence region will shift down, which results in a larger solid-solid two phase region. The phase diagrams of the Yukawa solid exhibit the same overall features as those of the square well system. The solid-solid density gap is wide at low temperatures and shrinks when the critical point is reached. The critical density shifts to higher values when κ is increased, i.e. when the range of the attractive potential is shortened. However, in contrast to the square-well system the critical temperature is now clearly dependent on the potential range. The critical temperature has a value of 0.67 in the limit $1/\kappa\sigma = 0$. This was verified by direct simulations in this limit, using the technique described in section 3.2.4. This critical temperature is somewhat lower than for the three dimensional square-well solid. The reason is that the Yukawa potential is smoother than a square well. This results in an inflection point in the free energy curve at lower temperatures. This in turn will cause all the coexistence curves to shift to lower temperature than those found in the square-well case.

The value of $\kappa=25$ where the solid-solid transition starts to occur, corresponds to an average well width of $\kappa^{-1}=0.04$. Although one cannot directly compare the width of a square-well and a Yukawa potential, the characteristic well widths are of comparable magnitude.

3.5 Square shoulder potential

It should be noted that isostructural solid-solid transitions are known to occur in dense *Cs* and *Ce* [71]. These transitions are believed to be due to the *softness* of the intermolecular potential associated with a pressure-induced change in the electronic state of the metal ions. In fact, theoretical work of Stell and Hemmer [52], and simulations of Young and Alder [55] indicate that such softness may indeed result in solid-solid transition. In the work of Kincaid, Stell and Goldmark [72] the potential is assumed to have the form of a square shoulder, a negative square well:

$$v(r) = \begin{cases} \infty & 0 \leq r < \sigma, \\ \epsilon & \sigma \leq r < \sigma + \delta, \\ 0 & r \geq \sigma + \delta. \end{cases} \quad (3.17)$$

Using perturbation theory, Kincaid, Stell and Goldmark calculated the isostructural solid-solid phase transition in these kind of systems. Basically, the mechanism of this phase transition is the same as for the square well model as described in the introduction of this chapter. At low enough temperature, the increase in potential energy as a function of density will be very steep at the point when all shoulders begin to overlap. This will

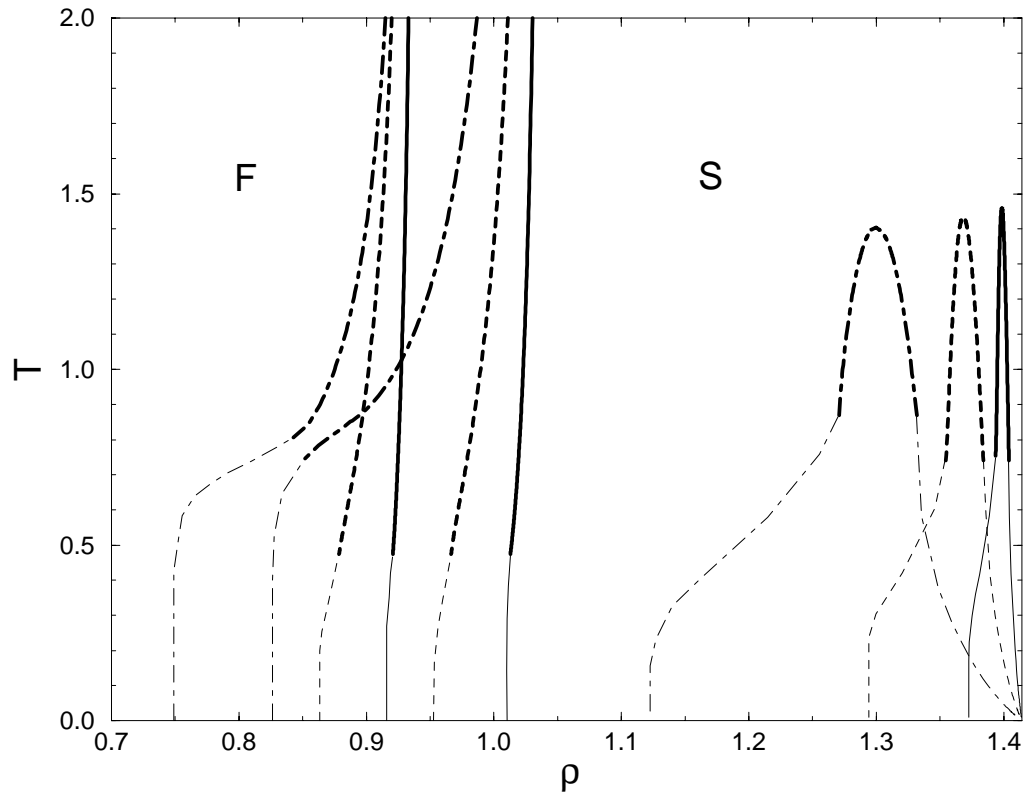


Figure 3.10. Phase diagrams in the T, ρ plane for square shoulder system. The solid curves correspond to a shoulder width $\delta=0.01$, the dashed to $\delta=0.03$ and the dot-dashed to $\delta=0.08$. The fat curves indicate simulation results. The thin curves are extrapolations to the exact results at $T=0$.

induce an inflection point in the free energy curve and cause the system to separate into two solids. There are of course differences. Because the potential energy is now positive, instead of negative as in the square well case, the inflection point of the free energy, and hence the critical density, will occur at a higher value. The other major difference will be at low temperatures, where the system experiences effectively a hard sphere potential with a diameter $\sigma + \delta$.

We performed Monte Carlo simulations for a system of 108 particles in a *fcc* crystal configuration for shoulder widths $\delta=0$ to $\delta=0.08$ and used eqn. 3.2 to obtain the free energy (where we had to take ϵ negative). The solid-fluid coexistence was calculated as well for systems with $\delta=0$ to $\delta=0.08$.

The phase diagrams for $\delta=0.01$, 0.03 and 0.08 , that were constructed as described in the previous sections, are shown in figure 3.10. Because the simulations did not extend beyond $\epsilon^*=2$, we extrapolated the binodals to zero temperature. The differences with the attractive square well are striking:

1. The critical densities are higher than those of the square well model.
2. The solid-solid binodals go all the way to $T=0$, where effectively two closed packed solids of hard spheres are in coexistence with each other: one in which the diameter of spheres corresponds to $\sigma + \delta$ and a second with a hard sphere diameter σ

3. The fluid-solid coexistence region changes gradually from the σ hard sphere case at $T = \infty$ to the $\sigma + \delta$ hard sphere case at $T=0$

Extrapolation of the critical density to larger values of δ leads to the estimate that the solid-solid transition will become metastable with respect to the fluid-solid transition at roughly $\delta \approx 0.25$. Note that this critical value of δ is much larger than for the square well case.

3.6 Polydispersity

Unlike biological colloids such as viruses, proteins and blood cells, synthetic colloids are never perfectly monodisperse. The influence of this polydispersity on the phase behavior of colloidal dispersions is not well understood. In the next chapter we discuss the effect of polydispersity on the freezing of hard spheres. In this section we combine the methods of this and the next chapter to assess the influence of polydispersity on the solid-solid transition.

As will be explained in detail in the next chapter, a simulation in the semigrand ensemble is done at constant N, V, T and $\Delta\mu(\sigma)$. Here $\Delta\mu(\sigma)$ is the chemical potential difference between a particle of diameter σ , and an arbitrarily chosen reference component σ_0 and is

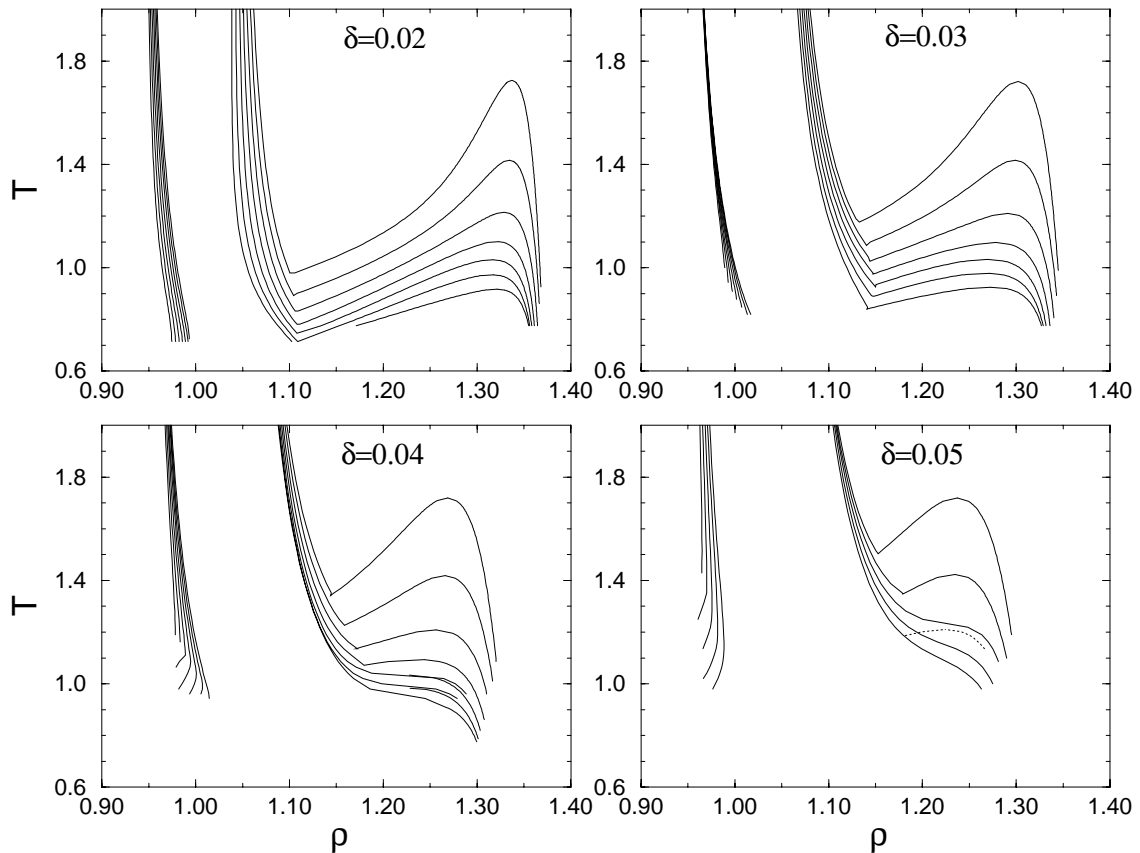


Figure 3.11. Simulated T, ρ phase diagrams for the polydisperse square-well system. Starting with the top coexistence curve, from top to bottom the curves correspond to polydispersity $v/\delta^2 = 0, 0.02, 0.04, 0.06, 0.08$ and 0.10 . The dotted curve at $\delta=0.05$ represents a solid-solid binodal that has just become metastable.

given by

$$\Delta\mu(\sigma) = \beta[\mu(\sigma) - \mu(\sigma_0)] = -(\sigma - \sigma_0)^2/2\nu. \quad (3.18)$$

Sampling the diameters of the spheres according to this chemical potential gives rise to a Gaussian activity distribution that peaks at $\sigma = \sigma_0$, with width ν . For small ν , the size composition will also be Gaussian with the peak near σ_0 and the width of this distribution is defined as the measure for size polydispersity s .

Using the same procedure as in the monodisperse case, we performed semigrand simulations for a 108 sphere system with a square well attraction in an *fcc*-configuration and measured the internal energy. The simulations were done for $\delta=0.02, 0.03, 0.04$ and 0.05 . The polydispersity ranged from $\nu/\delta^2=0$ to $\nu/\delta^2=0.1$. For every (ν, δ) a complete set of densities was simulated for a range of temperatures. The free energy was calculated using eqn. 3.2. Coexistence was obtained by applying the common tangent construction.

Figure 3.11 shows the dependence of the polydispersity s for different δ . Note that the critical temperature drops down as s increases. Table 3.3 shows the maximum value of s beyond which the solid-solid transition does not exist anymore. It appears to be essentially independent of δ .

Table 3.3. *Value of polydispersity at which solid-solid coexistence is pre-empted by melting transition.*

δ	ν/δ^2	s
0.02	± 0.25	0.010
0.03	0.14	0.011
0.04	0.08	0.010
0.05	0.04	0.010

Conclusion

3.7

Simple solids with a short ranged attractive pair potential can exhibit phase separation in a expanded solid and a more dense solid. This isostructural first-order solid-solid transition is reminiscent of the liquid-vapor transition. The transition takes place between two phases of the same structure, the coexistence curve ends in a critical point and the location of the coexistence curves depends strongly on the interaction range. The simulations on the square-well model show that the solid-solid transition takes place both in two and three dimensions for potential well-widths $\delta/\sigma < 0.07$. The analogy with liquid-vapor phase separation suggests that the solid-solid critical point should be of the 2D and 3D Ising universality class, although this still remains to be established. The critical density depends on the well-width δ and is well predicted by the uncorrelated cell-model. In contrast, the critical temperature hardly changes with δ . The critical temperature is finite for $\delta \rightarrow 0$. This has been confirmed by direct simulations in this limit. Comparison of the adhesive sphere model theories with the simulations in the limit $\delta \rightarrow 0$ shows that the solid-solid transition already occurs for $\tau \rightarrow \infty$, where τ plays the role of temperature in the adhesive sphere model. This implies that at finite τ the only stable phases are the close-packed solid and a the infinite dilute gas. All other phases are, at best, meta-stable. This pathological behavior is thought to be a consequence of the monodispersity of the system. We expect that introducing a slight size polydispersity will cause the solid-solid transition to occur at finite τ .

The results for the solid-solid transition in Yukawa systems are comparable to those for the square-well model. The solid-solid transition occurs for $\kappa\sigma > 25$, i.e. a potential well width narrower than 0.04σ . The major difference with the square-well results is that the critical temperature depends more strongly on κ .

An isostructural solid-solid transition, induced by the mechanism described above, will also occur in systems with repulsive “square shoulder” potentials. The critical temperatures are almost equal to that of the square well system, but the critical densities are significantly higher. Led by the theoretical work of Stell and Hemmer [52] and Kincaid, Stell and Goldmark [72] we have extrapolated the solid-solid binodals to $T=0$, where effectively two close packed solids are in coexistence.

An obvious question is whether the isostructural solid-solid phase transition due to short-ranged attraction, that we report here, can occur in real systems. We believe that such a transition can be observed in uncharged colloids with a short-ranged attraction. Such systems can be made, as we discussed in the previous chapters, by adding non-adsorbing polymer to a suspension of hard-sphere colloids (for a review, see e.g. ref. [8]). The polymers induce an effective attractive force between the colloidal spheres. The range of this attraction is directly related to the radius of gyration of the polymer. Hence, a colloidal crystal to which a polymer with a radius of gyration less than 7% of the radius of the colloidal spheres has been added, should exhibit the solid-solid phase behavior of the models discussed in this chapter.

However, introducing size polydispersity in the colloidal system will decrease the stability of the solid-solid transition. Our simulations show that for a colloidal dispersion with a polydispersity of more than 1% the solid-solid transition has become metastable with respect to the fluid-solid transition.

FREEZING OF POLYDISPERSE HARD SPHERES

4

In this chapter, we examine the solid-fluid coexistence region for a system of polydisperse hard spheres with near Gaussian diameter distributions, as a function of polydispersity. Our approach employs Monte Carlo simulation in the isobaric semi-grand ensemble with a Gaussian activity distribution. Gibbs-Duhem integration is used to trace the coexistence pressure as a function of the variance of the imposed activity distribution. Significantly, we observe a “terminal” polydispersity above which there can be no fluid-solid coexistence. The terminus arises quite naturally as the Gibbs-Duhem integration path leads the pressure to infinity. This pressure divergence is an artifact of the method used to evaluate the freezing transition, because the sphere diameters vanish in this limit. A simple re-scaling of the pressure with the average diameter brings the terminal pressure to a finite value. Nevertheless, the existence of this terminus only at infinite pressure precludes the construction of a continuous path from the solid to the fluid. At the terminus the polydispersity is 5.7% for the solid and 11.8% for the fluid while the volume fractions are 0.588 and 0.547 for the solid and fluid respectively. Substantial fractionation observed at high values of the polydispersity (>5%) implies that the “constrained eutectic” assumption made in previous theoretical studies is not generally valid. The results for the terminal polydispersity are consistent with experiments performed on polydisperse colloidal suspensions.

Introduction

4.1

Systems interacting via purely repulsive hard potentials are of interest because their properties have a trivial dependence on temperature, they are theoretically tractable, and they capture the qualitative effects of intermolecular repulsion on material properties. These models are particularly good at characterizing the structural features of condensed phases [2]. While they are incapable of exhibiting vapor-liquid transitions, properly formulated models have been shown to exhibit a rich array of order-disorder transitions, including freezing [56, 39], polymorphism (in hard-sphere mixtures) [73–75], and liquid crystalline phases [76, 26, 77](seen, for example, in hard spherocylinders).

As already mentioned in chapter 1, the hard sphere model gives a very good description of colloidal dispersions that consist of non-charged spherical particles interacting via a steep steric repulsion [14]. In particular, such colloidal systems, if sufficiently monodisperse in size, are known to crystallize at densities very close to that predicted by a hard-sphere model [8]. However, colloidal particles frequently exhibit considerable size polydispersity, depending on the way they are synthesized. This polydispersity will affect the thermodynamic properties, including the location and existence of any phase transitions.

The influence of polydispersity on the solid-fluid transition in colloidal suspensions was first examined by Dickinson and Parker [78–80]. Their system consisted of particles interacting via a screened Coulombic repulsion with a van der Waals attractive term. They showed via molecular simulation that the osmotic pressure of this system varies significantly with size polydispersity. They estimated the solid-fluid coexistence properties as a function of the polydispersity, but without attempting any sort of rigorous free energy calculations or considering the possibility of size fractionation (i.e., they assumed that the particle diameter distributions in the coexisting solid and fluid phases are identical). They found that the fluid-solid coexistence region narrows as the polydispersity increases, and they surmised that the transition disappears entirely at sufficiently high polydispersity. This value of the polydispersity has been called by Dickinson and Parker the “critical polydispersity”; this choice is unfortunate as the phenomenon does not likely represent a continuous transition because the solid and fluid phases have different symmetries. To avoid any confusion with critical points as they are customarily understood, we will instead refer to this polydispersity as the “terminal polydispersity”.

The terminal polydispersity has come to be the subject of considerable interest. For a triangular distribution, Dickinson and Parker extrapolated the change in volume upon melting to zero, and estimated the terminal polydispersity at 11% (we define the polydispersity as the standard deviation of the particle size distribution, divided by the mean). Later, Pusey [81] proposed a simple criterion for the terminal polydispersity based on an analogy of the Lindemann melting criterion; he also obtained a value of about 11%. Pusey [8] performed experiments in which he observed that dispersions with a polydispersity of 7.5% would (partly) freeze, while those with a polydispersity of 12% did not.

Several authors applied density functional theory (DFT) to obtain the phase diagram of polydisperse hard spheres [82, 83]. These theories are significantly more sophisticated than those employed in prior studies, and they give more attention to free energy criteria in calculating the coexistence curves. They nevertheless do not represent a completely rigorous treatment, as they too do not consider the effect of fractionation on the coexistence properties. McRae and Haymet [83] refer to this approximation as a “constrained eutectic”. The constrained eutectic is certainly valid at small polydispersity, but it likely breaks down as the distribution of diameters becomes wide. The DFT studies predict the terminal polydispersity at about 5-6%.

The purpose of the present work is to determine rigorously the phase diagram of polydisperse hard spheres by molecular simulation, establish the terminal polydispersity and test the validity of the constrained eutectic assumption made explicit in ref. [83]. To do this properly we must simulate a system having a truly continuous distribution of particle sizes, rather than a many-component but nevertheless discrete distribution. Such a simulation can be realized in the so-called semigrand ensemble, which has the added advantage that it is well suited for calculation of multicomponent phase equilibria. The semigrand ensemble is explained in section 4.2. Section 4.3 describes how the recently developed Gibbs-Duhem integration method [84] can be applied to efficiently obtain the phase diagram of polydisperse hard spheres by integration along the coexistence line. To start the integration one needs the slope of the coexistence line in the monodisperse limit; the means by which this is obtained is described in section 4.4. In section 4.5, it is shown how scaling properties of the system can be applied to greatly improve the accuracy of the simulations. The simulation results are discussed in section 4.6. The existence of a terminal polydispersity raises

questions of continuity of the fluid and solid states; we show in section 4.7 how this issue may be resolved. Concluding remarks are presented in section 4.8

Semigrand ensemble

4.2

The most straightforward approximation to a continuous mixture is based in the canonical ensemble and thus takes a finite sample from a distribution of diameters $p(\sigma)$. However, this approach is sensitive to finite size effects and, moreover, it is not practical when phase equilibria are considered as it is difficult to ensure chemical potential equilibration of each component. A better choice is a grand canonical simulation in which particles of different species are inserted and removed according to the configurational energy and the *imposed* chemical potential of that component. In this way a truly continuous distribution can be realized and phase equilibrium can be more easily treated. However, at the high densities of the liquid-solid equilibrium the insertion probability in both phases is too low to obtain reasonable statistics; further, the need to maintain the crystal structure in the solid makes insertions especially problematic.

The semigrand ensemble provides an alternative representation that combines the best features of the canonical and grand canonical ensembles for the study of continuous mixtures [85, 86]. A simulation in this ensemble has the total number of particles fixed, but the species identity of each particle is allowed to change, giving rise to a truly continuous distribution. Although the chemical potentials are imposed in a way similar to the grand-canonical ensemble, insertion of particles is avoided, so the method is suitable for high densities and crystalline phases.

We consider a system of N hard spheres with diameters σ distributed according to $p(\sigma)$. The isobaric semigrand canonical free energy Y is defined by a Legendre transform of the Gibbs free energy G . In the polydisperse limit,

$$Y = G - N \int p(\sigma)[\mu(\sigma) - \mu(\sigma_0)]d\sigma = N\mu(\sigma_0), \quad (4.1)$$

or, in differential form,

$$d(\beta Y) = Hd\beta + \beta VdP - N \int p(\sigma)\beta\delta[\mu(\sigma) - \mu(\sigma_0)]d\sigma + \beta\mu(\sigma_0)dN. \quad (4.2)$$

Here, $\mu(\sigma)$ is the chemical potential as a function of σ , and σ_0 is the diameter of an arbitrarily chosen reference component. Also, H is the enthalpy, $\beta = 1/k_B T$ is the reciprocal temperature, P is the pressure and V the volume of the system. The isobaric semigrand canonical potential Y is a function of the independent variables T, P and N and it is a functional of the chemical potential difference function $\mu(\sigma) - \mu(\sigma_0)$. In a simulation these independent variables must be fixed while the thermodynamic conjugates $H, V, \mu(\sigma_0)$ and $p(\sigma)$ are allowed to fluctuate. This implies that the composition $p(\sigma)$ can be known only after the simulation has been performed. Because the total number of particles is fixed the chemical potential of the reference $\mu(\sigma_0)$ has still to be computed. Once it is determined, the entire chemical potential distribution is known. The method is therefore well suited for phase equilibrium in continuous mixtures: for a given temperature and distribution in chemical potential differences one needs match only the values of the pressure and the reference chemical potential in both phases. This is far simpler than matching the entire

distribution $\mu(\sigma)$ in the canonical way.

We are interested in determining the influence of polydispersity on the hard sphere fluid-solid transition. Although the composition distribution and hence the polydispersity cannot be imposed directly, it can be expected that its form will be much like that of the imposed activity-ratio distribution $e^{\beta[\mu(\sigma) - \mu(\sigma_0)]}$ [86]. Therefore we choose the following quadratic form for the chemical potential difference function

$$\beta[\mu(\sigma) - \mu(\sigma_0)] = -(\sigma - \sigma_0)^2/2\nu, \quad (4.3)$$

which gives rise to a Gaussian activity distribution that peaks at $\sigma = \sigma_0$, with width ν . In the limit $\nu \rightarrow 0$, the pure monodisperse σ_0 phase is recovered. For small ν the mixture is ideal and the composition will be Gaussian with the peak near σ_0 .

The choice of eqn. 4.3 converts Y from a functional of $\mu(\sigma) - \mu(\sigma_0)$ to a function of σ_0 and ν . The fundamental thermodynamic equation now reads

$$d(\beta Y) = H d\beta + \beta V dP + \beta \mu(\sigma_0) dN - (Nm_1/\nu) d\sigma_0 - (Nm_2/2\nu^2) d\nu, \quad (4.4)$$

where m_1 and m_2 are the first and second moment of the composition about σ_0 . The n th such moment is defined as

$$m_n = \int d\sigma (\sigma - \sigma_0)^n p(\sigma). \quad (4.5)$$

In a semigrand Monte Carlo simulation, particles sample diameters in addition to the usual sampling of positions within the simulation box. Diameters are sampled by selecting a particle at random, changing its diameter by a small amount, and accepting with probability in accord with the Metropolis algorithm. Details may be found in [87].

4.3 Gibbs-Duhem integration

Evaluation of the hard sphere fluid-solid coexistence line as a function of polydispersity can be done by application of the Gibbs-Duhem integration method recently developed by Kofke [84]. In this method two phases are simulated simultaneously at the same state conditions. The technique allows a series of simulations to trace a line of coexistence in the plane of two state variables; for the purpose of describing the method let us say that these variables are the temperature and pressure, respectively. Chemical potential equality between the phases is ensured by starting the process with two known equilibrium phases, and subsequently applying thermodynamic integration to select the appropriate pressure while the temperature is varied from one simulation to the next in the series. The integration path may be derived from the Gibbs-Duhem equation

$$d(\beta\mu) = h d\beta + \beta \nu dP, \quad (4.6)$$

where $h = H/N$ and $\nu = V/N$ are the molar enthalpy and volume, respectively. For two coexisting phases to remain in equilibrium when the temperature is changed, the pressure must vary in a way that maintains chemical potential equality between them. The required change can be derived from eqn. 4.6

$$\left(\frac{dP}{d\beta} \right) = -\frac{\Delta h}{\beta \Delta \nu}, \quad (4.7)$$

where Δ indicates a difference between the two phases. Eqn 4.7 is known as the Clapeyron equation. It is a simple first order differential equation which can be integrated using a predictor-corrector scheme. The 'initial condition' is a known point at the coexistence line in the T, P plane. By simulating the two coexisting phases simultaneously at the equilibrium pressure and evaluating the right hand side of eqn. 4.7, one can predict the pressure at another temperature not far away. Simulation at this P and T yields new values of Δh and Δv , which can be used to correct the predicted pressure while the simulation continues to proceed. The process is then repeated to get the next (T, P) coexistence state point. Details of the method may be found elsewhere [84, 88].

In the case of polydisperse hard spheres we do not need the temperature as an independent variable, but instead we need a measure for the polydispersity. An obvious choice is ν , as it occurs in the fundamental equation 4.4. The Gibbs-Duhem equation for polydisperse mixtures can be derived by combining $Y = \mu(\sigma_0)N$ with eqn. 4.2

$$d(\beta\mu(\sigma_0)) = h d\beta + \beta\nu dP - \int p(\sigma)\beta\delta[\mu(\sigma) - \mu(\sigma_0)]d\sigma. \quad (4.8)$$

Using the same procedure as for the derivation of eqn. 4.4 we obtain

$$d(\beta\mu(\sigma_0)) = h d\beta + \beta\nu dP - (m_1/\nu)d\sigma_0 - (m_2/2\nu^2)d\nu. \quad (4.9)$$

To ensure phase equilibrium, $\beta\mu(\sigma_0)$ and the chemical potential difference function given in eqn. 4.3 must be the same in the two phases. The latter requirement is fulfilled simply by using the same ν (and σ_0) in both phases. The first requirement results in a Clapeyron type of equation which can be derived from eqn. 4.9 by equating the right-hand side for both phases and applying $d\sigma_0=0$ and $d\beta=0$.

$$\left(\frac{dP}{d\nu}\right) = \frac{\Delta m_2}{2\nu^2\beta\Delta\nu}, \quad (4.10)$$

We can integrate in the P, ν plane by measuring the second moment of the composition distribution m_2 and the molar volume ν in both phases and applying the predictor-corrector scheme described above.

The initial slope

4.4

The starting point we use for the Gibbs-Duhem integration is the well known freezing point of monodisperse hard spheres [56, 39]. However, the initial slope at $\nu=0$ given by eqn. 4.10 is not known here. Moreover, it cannot be calculated directly in a simulation because both m_2 and ν are equal to zero in the monodisperse limit, although the ratio m_2/ν is expected to be finite.

The second moment m_2 can be calculated if the composition $p(\sigma)$ is known. The composition in turn is related to the chemical potential by

$$\beta\mu(\sigma) = \mu^0 + \ln p(\sigma) + \beta\mu_r(\sigma), \quad (4.11)$$

where μ^0 is a collection of terms taken as independent of σ , and $\beta\mu_r(\sigma)$ is the residual chemical potential. With eqn. 4.3, the chemical potential difference function can now be

written as

$$\beta\Delta\mu(\sigma) = \ln\frac{p(\sigma)}{p(\sigma_0)} + \beta\Delta\mu_r(\sigma) = -\frac{(\sigma - \sigma_0)^2}{2\nu}, \quad (4.12)$$

or,

$$p(\sigma) \sim \exp(-(\sigma - \sigma_0)^2/(2\nu) - \beta\Delta\mu_r(\sigma)). \quad (4.13)$$

Here, $\Delta\mu_r(\sigma) = \mu_r(\sigma) - \mu_r(\sigma_0)$ is the difference in residual chemical potential between a particle with diameter σ and a particle of the reference component. This difference can be measured in a simulation of a pure σ_0 substance by performing ‘test enlargements’, in which a randomly chosen particle is enlarged from diameter σ_0 to a random diameter σ . One tabulates the frequency with which such moves result in no overlap, although the moves themselves are never accepted. This overlap probability yields the residual chemical potential according to

$$\beta\Delta\mu_r(\sigma) = -\ln\langle \exp(-\beta\Delta U(\sigma_0 \rightarrow \sigma)) \rangle, \quad (4.14)$$

where the brackets indicate the ensemble average; $\exp(-\beta\Delta U)$ is zero or unity, respectively, corresponding to the absence or presence of overlap. This ‘ghost-growing’ procedure is very similar to the Widom ‘ghost’ particle insertion technique [36]. In practice, we tabulate the distance from a randomly selected particle to its nearest neighbor; this histogram of nearest distances is then easily converted into the overlap histogram just described.

For small values of $\sigma - \sigma_0$ the measured residual chemical potential might be approximated by a quadratic function

$$-\beta\Delta\mu(\sigma) = a_1(\sigma - \sigma_0) + a_2(\sigma - \sigma_0)^2. \quad (4.15)$$

Substituting this in eqn. 4.13 results for the composition

$$p(\sigma) = C \exp(a_1(\sigma - \sigma_0) + (a_2 - \frac{1}{2\nu})(\sigma - \sigma_0)^2), \quad (4.16)$$

where C is independent of $\sigma - \sigma_0$. Because $p(\sigma)$ is a Gaussian function, the desired second moment of the composition m_2 can be analytically obtained

$$m_2 = \frac{1 + a_2/(1/\nu - 2a_2)}{(1/\nu - 2a_2)} \approx \nu + (a_1^2 + 2a_2)\nu^2. \quad (4.17)$$

The latter approximation is correct to second order in ν . The initial slope can now be written as

$$\left(\frac{dP}{d\nu}\right)_{\nu=0} = \frac{\Delta m_2}{2\nu^2\beta\Delta\nu} = \frac{\Delta(\frac{1}{2}a_1^2 + a_2)}{\beta\Delta\nu}, \quad (4.18)$$

where $\Delta((\frac{1}{2}a_1^2 + a_2))$ is the difference between the coefficient expressions evaluated in both phases. In sum, we measure the residual chemical potential in a simulation of a pure hard sphere system using eqn. 4.14, we fit it to a quadratic function for small $\sigma - \sigma_0$ and use the coefficients in eqn. 4.18 to obtain the initial slope for the Gibbs-Duhem integration.

Scaling

Application of a standard Monte Carlo algorithm yielded very poor statistics. This outcome is probably caused by the inability of the volume to adjust quickly to particle diameter changes, and vice versa. A remedy might be to introduce a combined volume- and diameter-change Monte Carlo step: while reducing the volume by a factor α , we reduce all diameters by a factor $\alpha^{1/3}$. In addition to more directly coupling the diameter and volume changes, this move is appealing because it requires no overlap test. The acceptance probability for this combined move is

$$P_{L \rightarrow L'} = \exp(-\beta P(L'^3 - L^3) + (4N + 2) \ln(L'/L) - \frac{1}{2\nu} \sum_i (\tilde{\sigma}_i L' - \sigma_0)^2 + \frac{1}{2\nu} \sum_i (\tilde{\sigma}_i L - \sigma_0)^2), \quad (4.19)$$

where L is the length of the cubic box with volume $V = L^3$ and $\tilde{\sigma}_i = \sigma_i/L$ are the scaled diameters. Although this method will produce better results, we can improve the scheme even more by scaling both the diameters and the coordinates, thereby permitting (near-) analytic evaluation of the volume integral. Consider the configurational part of the isobaric semigrand partition function

$$\Upsilon = \frac{1}{N!} \int dV \int d\mathbf{r}^N \int d\boldsymbol{\sigma}^N \exp(-\beta P V - \frac{1}{2\nu} \sum_i (\sigma_i - \sigma_0)^2 - \beta U(\mathbf{r}^N, \boldsymbol{\sigma}^N)). \quad (4.20)$$

If we now introduce scaled coordinates and diameters $s_i = r_i/L$ and $\tilde{\sigma}_i$ as above the partition function can be written as

$$\begin{aligned} \Upsilon &= \int ds^N \int d\tilde{\boldsymbol{\sigma}}^N e^{-\beta U(s^N, \tilde{\boldsymbol{\sigma}}^N)} \int dL^3 L^{4N} \exp(-\beta P L^3 - \frac{1}{2\nu} \sum_i (\tilde{\sigma}_i L - \sigma_0)^2) \\ &= \int ds^N \int d\tilde{\boldsymbol{\sigma}}^N e^{-\beta U(s^N, \tilde{\boldsymbol{\sigma}}^N)} \mathcal{W}(\tilde{\boldsymbol{\sigma}}^N). \end{aligned} \quad (4.21)$$

The outermost two integrals do not contain any volume dependence. Moreover, the 'weighting function' $\mathcal{W}(\tilde{\boldsymbol{\sigma}}^N)$ defined here can be evaluated entirely at every Monte Carlo move. In this way, there is no need for volume sampling at all. Instead, at every move we obtain the average volume by evaluating

$$\frac{\int dL L^{4N+5} \exp(-\beta P L^3 - \frac{1}{2\nu} \sum_i (\tilde{\sigma}_i L - \sigma_0)^2)}{\int dL L^{4N+2} \exp(-\beta P L^3 - \frac{1}{2\nu} \sum_i (\tilde{\sigma}_i L - \sigma_0)^2)}. \quad (4.22)$$

In this scaling method there are only two kinds of Monte Carlo moves: the regular particle displacements and the diameter changes. Both changes are made in the scaled variables. The acceptance probabilities are

$$P_{s_i \rightarrow s'_i} = e^{-\beta \Delta U(s^N, \tilde{\boldsymbol{\sigma}}^N)}, \quad (4.23)$$

$$P_{\tilde{\sigma}_i \rightarrow \tilde{\sigma}'_i} = e^{-\beta \Delta U(s^N, \tilde{\boldsymbol{\sigma}}^N)} \frac{\mathcal{W}(\tilde{\boldsymbol{\sigma}}'_i)}{\mathcal{W}(\tilde{\boldsymbol{\sigma}}_i)}, \quad (4.24)$$

where $\Delta U(s^N, \tilde{\sigma}^N)$ is the change in potential energy associated with the move. If a particle's diameter is changed the integral $W(\tilde{\sigma}^N)$ must be reevaluated. Because the exponential in the integral is a cubic polynomial this cannot be done analytically. However, if we write the integral as

$$W(\tilde{\sigma}^N) = c \int dx e^{f(x)}, \quad (4.25)$$

we can approximate it accurately by applying the method of steepest descent. Replacing the function $f(x)$ by a second-order Taylor expansion around the maximum of $f(x)$ yields

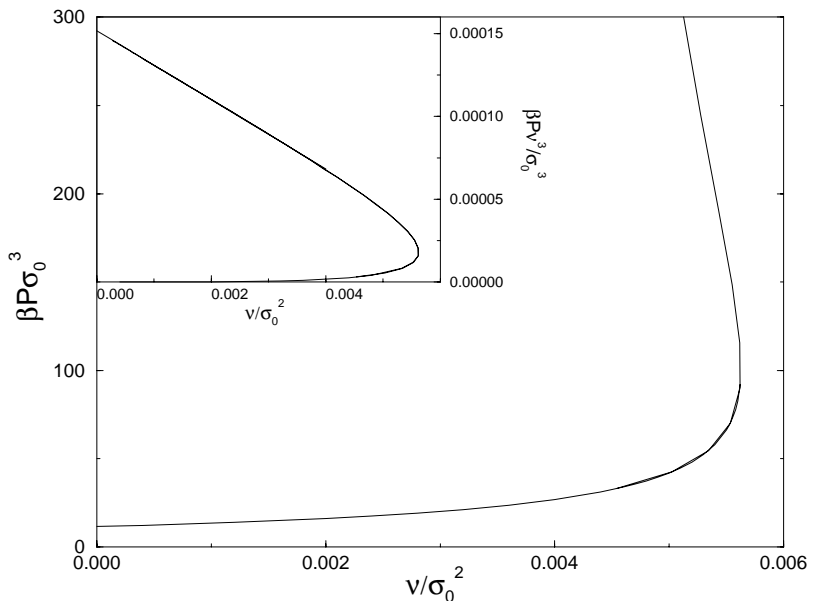
$$\begin{aligned} W(\tilde{\sigma}^N) &= c \int dx \exp \left(f(x_{\max}) + \frac{1}{2} \left(\frac{\partial^2 f}{\partial x^2} \right)_{x_{\max}} (x - x_{\max})^2 \right) \\ &= c e^{f(x_{\max})} \sqrt{-2\pi \left(\frac{\partial^2 f}{\partial x^2} \right)_{x_{\max}}^{-1}} \end{aligned} \quad (4.26)$$

This approximation is possible because the function $f(x)$ is large (being proportional to N) and it drops quickly away from the maximum.

4.6 Results

We performed a Gibbs-Duhem integration in the P, ν plane starting with an *fcc* solid and a fluid at the monodisperse hard sphere freezing point. Both systems consisted of 256 particles and were well equilibrated. Using the ghost-growing method of section 4.4 in combination with eqn. 4.18 we found an initial slope of $dP/d\nu=1400$ (± 50) (in units such that β and σ_0 are unity). This value was used in the first predictor step to go from $\nu=0$ to finite ν , where the slope could be directly measured. We evaluated the coexistence line by gradually increasing ν from one simulation to the next while integrating eqn. 4.10 to determine the pressure. In figure 4.1 the equilibrium pressure is shown as a function of the polydispersity parameter ν . The slope starts off at a value of $dP/d\nu=1400$ as we obtained from eqn. 4.18 and increases when ν is increased. At a value of $\nu/\sigma_0^2=0.0056$ the slope becomes infinite, so we had to invert the integration, taking P as the independent

Figure 4.1. *Solid-fluid coexistence pressure as a function of variance of the imposed activity distribution. In the inset the pressure is reduced to $P\nu^3/\sigma_0^3$ to show the limiting behavior.*



variable. In this case, we can calculate $\nu(P)$ for increasing values of P by applying the same integration scheme to the reciprocal of eqn. 4.10. Surprisingly, the equilibrium curve continues to bend back, approaching $\nu/\sigma_0^2=0$ at infinite pressure. In the inset of figure 4.1 we rescale the pressure to $\tilde{P} = \beta P \nu^3/\sigma_0^3$, which remains finite and follows a straight line as $P \rightarrow \infty$, $\nu/\sigma_0^2 \rightarrow 0$. The fact that \tilde{P} is finite in this limit actually allows us to perform simulations at infinite pressure as will be discussed in the next section.

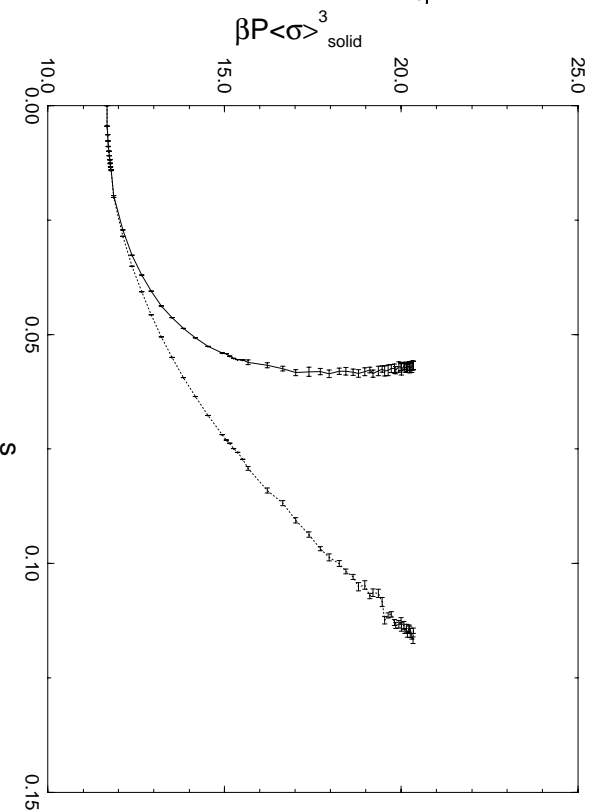
The divergence of the pressure is somewhat misleading. The pressure indeed goes to infinity on a scale characterized by σ_0 , but when reduced instead by the volume or an average diameter it remains bounded. In fact, in this limit σ_0 loses its relevance as a length scale because all particle diameters are going to values much smaller than σ_0 . Scaling by an average diameter (or the volume) makes the interpretation of the results more intuitive because in experiments the important microscopic length scale is the characteristic particle diameter. Consequently, in most of what follows we present our results in terms of $\langle\sigma\rangle$ (where the angle brackets indicate an isobaric semigrand ensemble average). We choose arbitrarily to use $\langle\sigma\rangle$ of the solid to perform the reduction; we could just as well have used the fluid value. We will continue to refer to the limit of infinite pressure because this represents a limiting behavior of our isobaric semigrand system. It should be understood that in this case the pressure is infinite on the σ_0 scale but not on, say, the $\langle\sigma\rangle$ scale.

Although the parameter ν shows a maximum as a function of P , the real polydispersity—given in terms of the width of the composition distribution $p(\sigma)$ —does not. This polydispersity s is defined as

$$s^2 = \frac{\langle\sigma^2\rangle}{\langle\sigma\rangle^2} - 1. \quad (4.27)$$

In figure 4.2 the reduced pressure $\beta P \langle\sigma\rangle_{\text{solid}}^3$ is plotted against the polydispersity s in both the fluid and the solid. The equilibrium pressure increases monotonically until at infinite pressure a limiting value of s and $\beta P \langle\sigma\rangle^3$ is reached. From this plot it becomes immediately clear that the polydispersity of the fluid and the solid at equilibrium can be very different. As reviewed in the introduction of this chapter, this fact, although anticipated, was discounted in previous studies.

Figure 4.2. Coexistence pressure of the solid (left curve) and the fluid (right curve) as a function of the width of the composition distribution, the polydispersity s .



It is convenient to choose a density variable η given in terms of the real volume fraction, because this is the quantity one measures in experiments. We define $\eta = N\pi\langle\sigma^3\rangle/(6V)$; note that $\eta=0.7405$ for monodisperse close packed spheres. The phase diagram in the η, s plane is shown in figure 4.3. Because the polydispersity variable is not linearly additive, the tie-lines are curved. A system of hard spheres prepared on one of the tie-lines will split into a solid and liquid phase with density and polydispersity given by the intersection of the tie-line with the coexistence lines. The most remarkable feature of the diagram is the fact that the fluid-solid equilibrium suddenly ends. This is generally consistent with the prediction and observation of a terminal polydispersity reported in studies on crystallization of polydisperse hard spheres [8, 83, 82] and reviewed in section 4.1. In particular, the consensus of a terminal polydispersity in the range of 5%–12% is explained by our results. According to our phase diagram, the *fcc* solid phase is thermodynamically stable for polydispersities no

Figure 4.3. Phase diagram in the plane of volume fraction and polydispersity. Coexisting phases are joined by tie lines, which are not straight because the polydispersity is not an additive variable. The circles represent the endpoints of the coexistence region at $\beta P\sigma_0^3 \rightarrow \infty$, i.e., the terminal polydispersity.

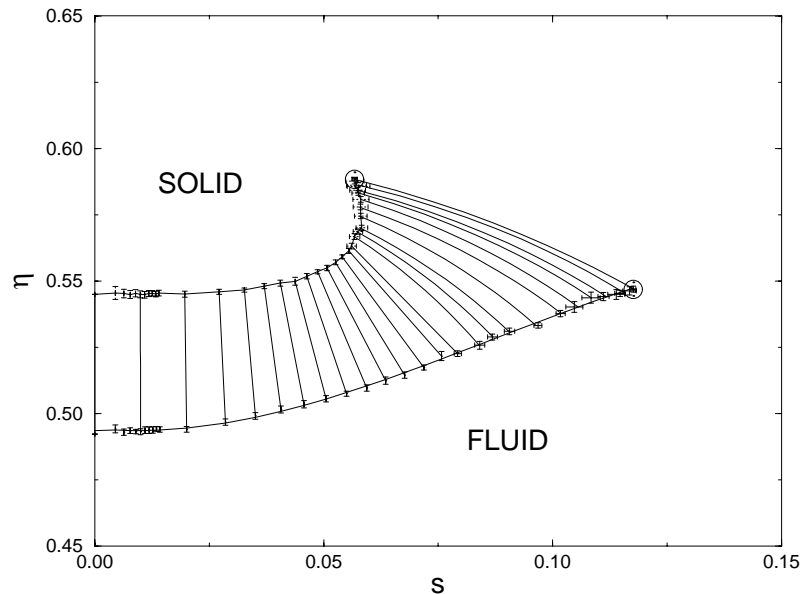
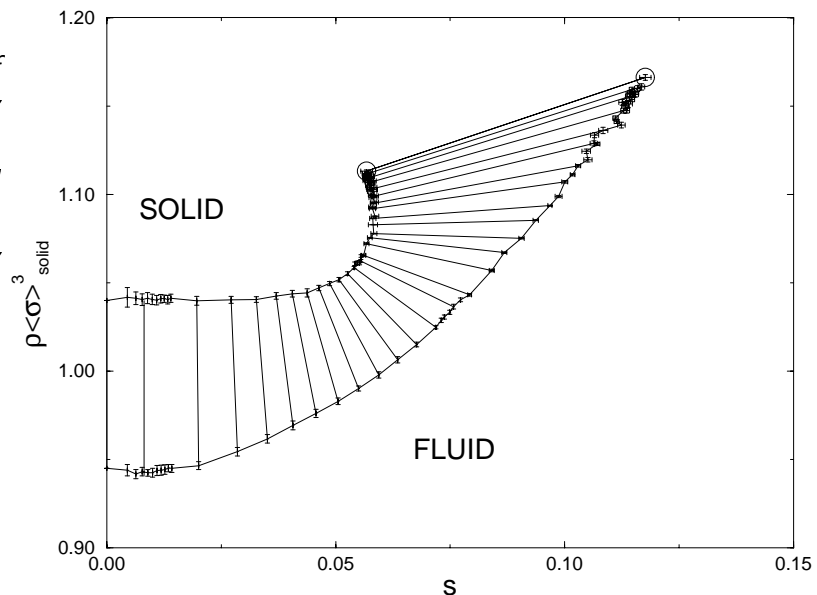


Figure 4.4. Phase diagram in the plane of reduced number density and polydispersity. Coexisting phases are joined by tie lines, which although curved in reality are rendered straight in this figure.



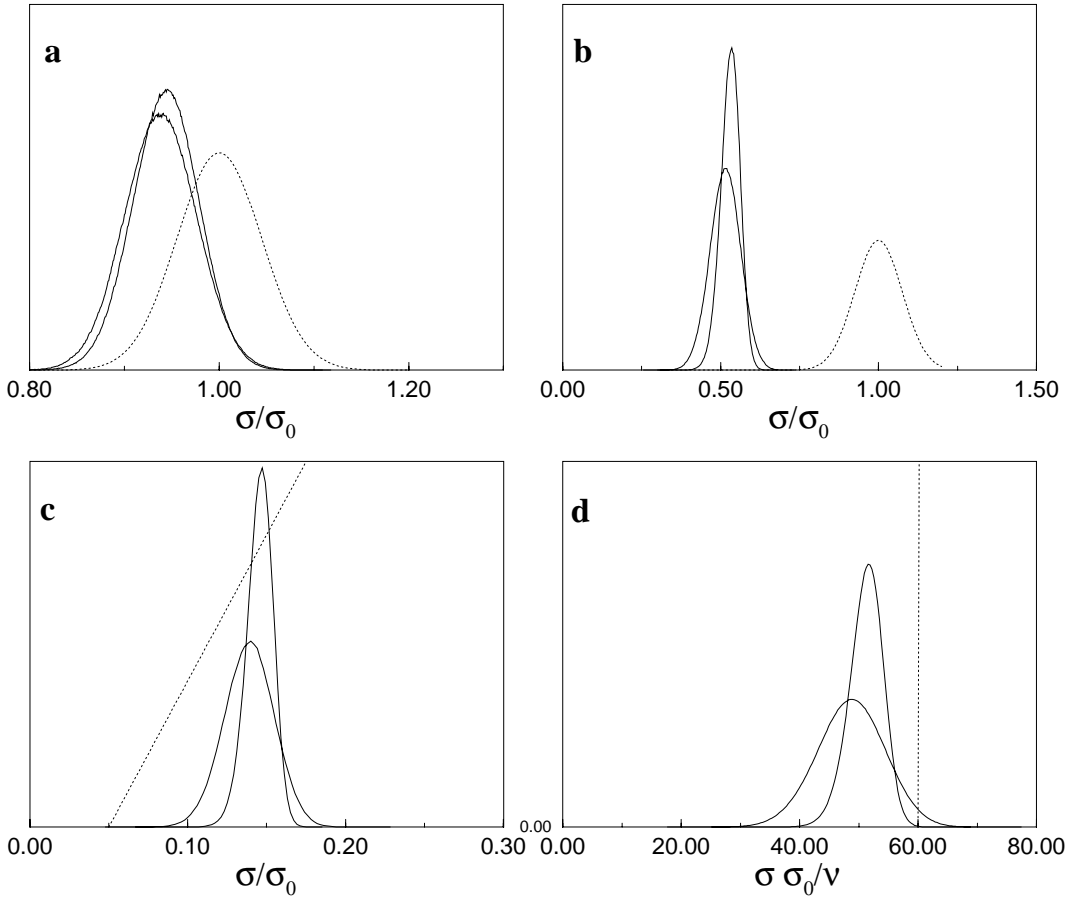


Figure 4.5. *Composition distributions $p(\sigma)$ for fluid-solid equilibrium at different pressures. In the figures, the leftmost solid curve represents the fluid composition, the rightmost one the solid phase composition. a) $p(\sigma)$ for $\beta P \sigma_0^3 = 15$. The dotted curve is the imposed (Gaussian) activity distribution. b) $p(\sigma)$ for $\beta P \sigma_0^3 = 100$. The dotted curve is the imposed (Gaussian) activity distribution. c) $p(\sigma)$ for $\beta P \sigma_0^3 = 6400$. The dotted line denotes the imposed chemical potential difference function, which is becoming straight at high βP . d) $p(\sigma \sigma_0 / \nu)$ for $\beta P \sigma_0^3 \rightarrow \infty$. In this limit the diameters are pushed to zero. By dividing them by ν / σ_0^2 they remain finite. The dotted line denotes the imposed chemical potential difference function.*

more than 5.7%, yet crystallization is possible in fluids of polydispersity up to 12% provided one allows for fractionation in the phase separation process. This is consistent with Pusey's experiments [8] in which he observed that dispersions with a polydispersity of 7.5% would freeze, while those with a polydispersity of 12% did not. The DFT studies which reported a terminal polydispersity of 5–7% are also consistent with our results given their use of the constrained eutectic, which precludes fractionation.

In figure 4.4, we plot the number density (in units of the average diameter) as a function of s . This plot illustrates the counterintuitive result that the fluid density may adopt values greater than that in the solid phase. At the point where both densities are equal the $\Delta \nu$ term in eqn. 4.10 switches sign and becomes negative, which gives rise to the maximum of $\nu(P)$ seen in figure 4.1. Of course, the fluid is able to take on larger densities than the

solid only because it is composed of particles of smaller diameter.

The composition distributions of the fluid and the solid phases are displayed in figure 4.5 for four values of the coexistence pressure. For a monodisperse equilibrium (not shown in the figures) the distributions in both phases would be equal to the imposed activity, which is a delta function at σ_0 . As the equilibrium pressure (or equivalently the value of ν) is increased, the composition distributions depart from the ideal activity. Although still almost Gaussian, they are shifted considerably to lower values of σ . The average diameter is smaller in the fluid, whereas the solid composition is located at larger diameters and is more narrowly distributed. The difference between the phases becomes more pronounced at higher pressures. At infinite pressure, all diameters go to zero on the scale of σ_0 . Interesting distributions can be recovered by proper scaling of the diameters by their average, as presented in figure 4.5d. The fluid distribution is much broader than the solid one, in accord with the larger polydispersity s we encountered above. Although the value ν/σ_0^2 has decreased to zero in this limit (and of course has the same value in the two phases), the (rescaled) composition distributions are still near-Gaussian with a finite width (on a scale of $\langle\sigma\rangle$). This curious outcome is a result of the limiting process in which $\beta P\sigma_0^3 \rightarrow \infty$ while $\nu/\sigma_0^2 \rightarrow 0$.

As the distributions are shifted to lower diameter at high pressure, the precise shape of the imposed activity distribution becomes less important and σ_0 , as discussed above, becomes irrelevant. In figure 4.5c the chemical potential difference function, the logarithm of the activity, is nearly a straight line; it becomes exactly a straight line in the infinite pressure limit. This property enables us to perform simulations in the limit of $\beta P\sigma_0^3 \rightarrow \infty$.

4.7 The infinite pressure limit

The existence of the terminal polydispersity suggests the possibility of constructing a continuous path from the solid to fluid without going through a first order phase transition. We do not expect such a process to be realizable in general, and in this section we show that it is indeed not possible in the context of our system. The explanation lies in the infinite pressure limiting behavior of the model in the isobaric semigrand ensemble.

Consider the partition function of eqn. 4.21

$$\Upsilon = \int ds^N \int d\tilde{\sigma}^N e^{-\beta U(s^N, \tilde{\sigma}^N)} \int dL^3 L^{4N} \exp(-\beta PL^3 - \frac{1}{2\nu} \sum (\tilde{\sigma}_i L - \sigma_0)^2). \quad (4.28)$$

In the limit of $\beta P\sigma_0^3 \rightarrow \infty$ the volume and hence the length L will go to zero. The quadratic term in L in the exponent vanishes in this limit, whereas the βPL^3 and the $L\sigma_0/\nu$ terms remain finite. This is equivalent to the observation that the chemical potential difference function is becoming a straight line. If we define a new, always finite, parameter $x = L\sigma_0/\nu$ and introduce \tilde{P} defined above, the limiting partition function can be written as

$$\Upsilon = C \int ds^N \int d\tilde{\sigma}^N e^{-\beta U(s^N, \tilde{\sigma}^N)} \int dx x^{4N} \exp(-\tilde{P}x^3 + (\sum \tilde{\sigma}_i)x). \quad (4.29)$$

We can conduct simulations in the infinite pressure limit by using the integral over x as the 'weighting function' $W(\tilde{\sigma}^N)$ and imposing the reduced pressure \tilde{P} . This limiting state is governed by two length scales, namely $(\beta P)^{-\frac{1}{3}}$ and ν/σ_0 . The pressure βP drives the diameters to smaller values whereas ν/σ_0 drives them to large ones (σ_0/ν is equal to the

now-constant slope of $\Delta\mu(\sigma)$ as is shown in figure 4.5d). The ratio of these two lengths, as expressed via \tilde{P} , represents the balance between the two forces.

The reduced coexistence pressure can be obtained from extrapolation of \tilde{P} to $v/\sigma_0^2=0$ as suggested by figure 4.1. The equilibrium densities and volume fractions of the solid-fluid coexistence in the limit $\beta P\sigma_0^3 \rightarrow \infty$ are displayed as open circles in figure 4.4 and 4.3 respectively and are given in table 4.1. Because these equilibrium points are at infinite pressure, these are really the end points of the phase coexistence. For the choice of chemical potential distribution given by eqn. 4.3, there is no phase transition at higher polydispersities, volume fractions or densities.

This method makes it possible to address the question of solid-fluid phase continuity posed above: given that the coexistence region terminates abruptly, why is it not possible to go from the solid to the fluid via a continuous path in the η, s plane, that is, without encountering a first order phase transition? The answer is made clear by simulations at other, off-coexistence values of the reduced pressure \tilde{P} . The results are included in figure 4.6. The curve bounding the solid region from monodisperse close packing ($s=0, \eta=1$) to the solid-fluid coexistence represents the infinite pressure line; a similar curve is shown for the fluid phase (let us call these curves the “ \tilde{P} -lines”). The \tilde{P} -lines provide an upper limit, above which the system cannot be compressed. This upper bound implies that it is not possible to go from the solid to the fluid avoiding a first order transition.

Although all semigrand \tilde{P} states are of infinite pressure, the \tilde{P} -line does not correspond to close packed states one would achieve in a canonical ensemble. The linear chemical potential that arises in the infinite pressure limit is incapable of producing the tight packing one normally associates with infinite pressure (i.e. in a fixed-composition ensemble). In order to determine the maximum volume fraction η_M of the solid phase as a function of polydispersity, we performed simulations starting with a configuration obtained by semigrand simulation at the \tilde{P} -line and compressing at fixed composition until every particle was constrained by its neighbors. The maximum volume fraction η_M so obtained was averaged over ten different starting configurations with a different diameter distribution snapshot. These averaged η_M as a function of polydispersity are included in figure 4.6.

It is immediately clear that there is a large difference between the semigrand \tilde{P} -curve and the canonical results for η_M . Simulations of larger systems indicate that this is not a finite-size effect. The explanation is that the imposed linear chemical potential difference function in the semigrand simulations is simply not the one that produces the maximum volume fraction η_M . To remove the difference between the canonical and semigrand picture one could study other forms of $\Delta\mu(\sigma)$.

In the fluid phase there is also a fixed-composition maximum volume fraction boundary: the random close packing volume fraction η_{RCP} . Schaertl et al. [89] have studied η_{RCP} as a function of polydispersity. Their results are included in figure 4.6. The difference between the semigrand \tilde{P} -curve and the η_{RCP} -curve is increasing with polydispersity. As in the solid case, this difference can be reduced by choosing other forms of the chemical potential

Table 4.1. *Polydispersities, densities and volume fractions of the solid fluid equilibrium at $\beta P\sigma_0^3 \rightarrow \infty$. The subscript numbers indicate the error in the last digit(s).*

	Solid	Fluid
s	0.0567 ₁₂	0.1176 ₁₂
$\rho < \sigma >_{\text{solid}}^3$	1.1131 ₇	1.1662 ₁₆
η	0.5884 ₇	0.5468 ₁₃

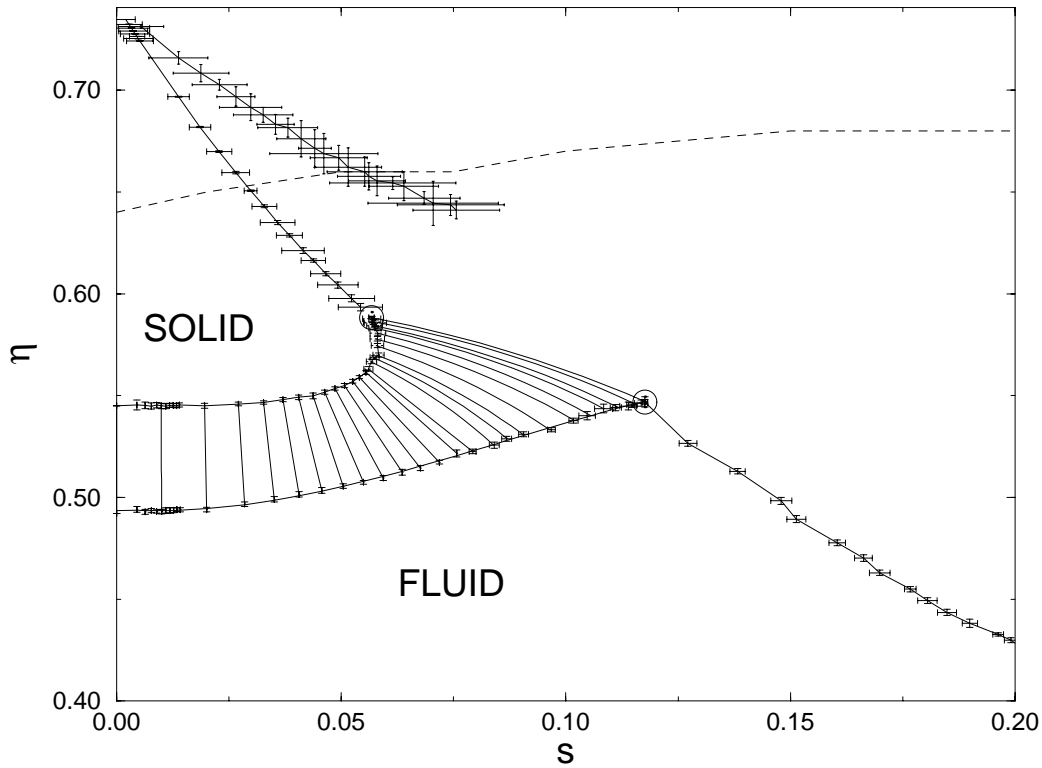


Figure 4.6. Phase diagram of polydisperse hard spheres in the η, s plane. The coexistence region is as in figure 4.3. The curve joining the terminal solid-phase coexistence point to the $s=0$ closed-packed limit is the solid-phase \tilde{P} -line (see text), while that emanating from the liquid-phase terminus is the liquid-phase \tilde{P} -line. The solid line above the solid-phase \tilde{P} -line describes the packing fractions obtained from the fixed-composition compressions described in the text. Fluid-phase random close packing obtained by Schaertl et al. [89] is described by the dashed curve.

distribution function. We demonstrate via application of the hard-sphere mixture equation of state of Mansoori et al. [90], which is applicable to the fluid phase only. In figure 4.7, we plot the packing fraction versus polydispersity according to this equation of state, for the linear chemical potential distribution used in the simulations, and for distributions that are quadratic or cubic in the sphere diameter:

$$\beta\Delta\mu(\sigma) = c_1\sigma + c_2\sigma^2 + c_3\sigma^3, \quad (4.30)$$

where we have examined cases in which only one of c_1, c_2 , and c_3 is non-zero. The figure simply shows how other chemical potential forms can give rise to larger densities than the “infinite pressure” results studied here. We note several points: (i) the case where $c_1 = c_2 = c_3 = 0$ results in a so-called infinitely polydisperse mixture [91], at which $s=0.7414$ and $\eta=0.104$; this situation arises as $\tilde{P} \rightarrow \infty$; (ii) the Mansoori equation agrees very well with the Monte Carlo data we have taken at and near the freezing transition, as well as at the infinitely polydisperse limit; however, one would not expect the equation to apply at conditions appropriate to random close packing, so we cannot describe this limit in the present analysis; (iii) the c_3 line is terminated at a point ($c_3/\beta P=0.507$) where the

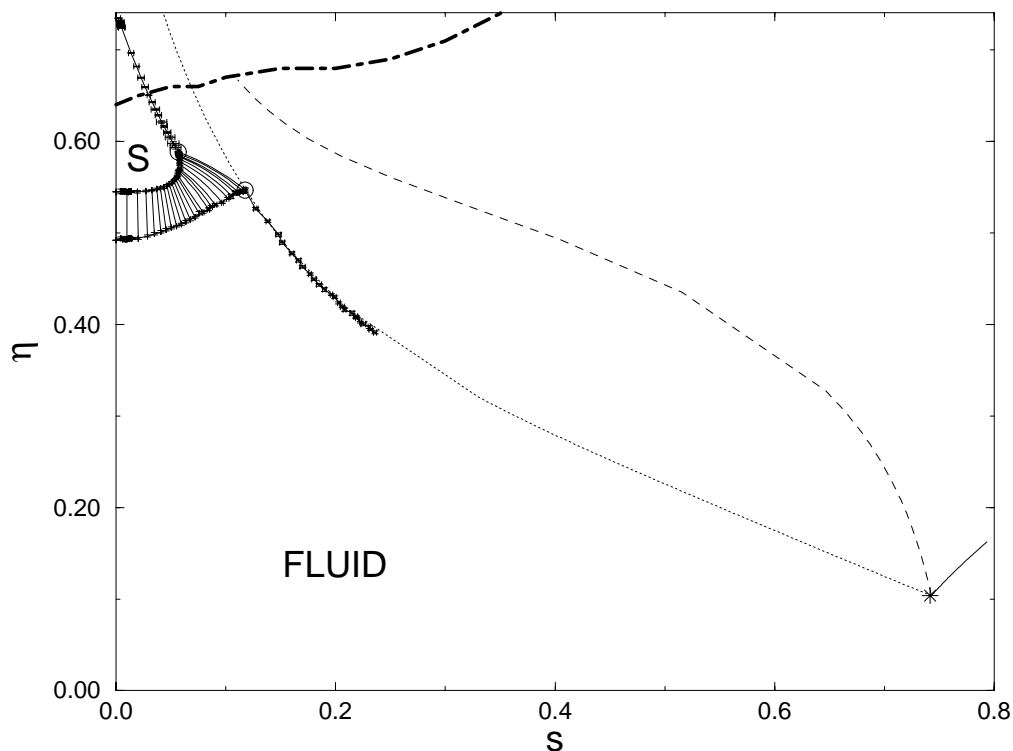


Figure 4.7. Behavior of polydisperse hard spheres in the η, s plane. Phase diagram, \tilde{P} -lines, and random-close packing curves from figure 4.6 are included. Fluid-phase curves according to the Mansoori et al. [90] equation of state are presented for chemical potential distributions linear (dotted curve), quadratic (solid curve), and cubic (dashed curve) in the sphere diameter. The three lines converge at the infinitely polydisperse limit, for which a Monte Carlo datum [91] is indicated.

computed composition—which is an exponential of a cubic polynomial in σ —diverges because the coefficient of the cubic term becomes positive (the c_1 and c_2 lines are terminated on the figure at arbitrary points).

Conclusion

4.8

We have established a solid-fluid coexistence region for a system of polydisperse hard spheres with near Gaussian diameter distributions, as a function of polydispersity. Our approach employs simulation in the isobaric semi-grand ensemble with a Gaussian activity distribution. Gibbs-Duhem integration is used to trace the coexistence pressure as a function of the variance of the imposed activity distribution. The Gibbs-Duhem integration is initiated with a monodisperse hard sphere fluid and *fcc* solid, and throughout the integration process the solid remains in an *fcc* structure. We do not explore the possibility of a polymorphic transition in the solid.

Both the fluid-solid coexistence densities and volume fractions are monotonically increasing functions of the polydispersity s , which is given in terms of the standard deviation in the particle diameter distribution function. The volume change at the freezing transition decreases as a function of s and eventually takes on negative values, which implies that the

number density of the fluid phase is greater than that of the solid. However, the packing fraction of the fluid remains always less than that of the coexisting solid phase. Connected to this is the observation of significant fractionation between the two phases, which permits the fluid phase to comprise particles of a smaller average diameter.

Significantly, we observe a terminal polydispersity, i.e., a polydispersity above which there can be no fluid-solid coexistence. This terminus arises quite naturally as the Gibbs-Duhem integration path leads the pressure to infinity. The existence of this terminus only at infinite pressure precludes the construction of a continuous path from the solid to the fluid. While it was anticipated in previous studies that such a continuous path could not be constructed, the issue was not addressed as fully as we are able to here.

At the terminus the polydispersity is 5.7% for the solid and 11.8% for the fluid while the volume fractions are 0.588 and 0.547 for the solid and fluid respectively. Large fractionation observed at moderate values of s (>0.05) implies that the constrained eutectic assumption implicit in previous studies is not valid over a very large range of polydispersity. The constrained eutectic approximation is perhaps the reason that McRae and Haymet [83] obtained the smaller value of 6% for the terminus. Our results for the terminal polydispersity are consistent with experiments performed on polydisperse colloidal suspensions.

We feel that the qualitative conclusion that a terminal polydispersity exists is generally correct and that it is of the order of 5% in the solid and 12% in the fluid. However, we have not examined the sensitivity of the terminal polydispersity to variation in the chemical potential distribution function (and thus the composition). It seems likely that the terminal polydispersity would not be very sensitive to details of composition, and as our distributions are near-Gaussian we expect our conclusions to be generally valid.

THE PHASE DIAGRAM OF HARD SPHEROCYLINDERS

5

We have mapped out the complete phase diagram of hard spherocylinders as a function of the length-to-width ratio L/D . Special computational techniques were required to locate phase transitions in the limit $L/D \rightarrow \infty$ and in the close-packing limit for $L/D \rightarrow 0$. The phase boundaries of five different phases were established: the isotropic fluid, the liquid crystalline smectic A and nematic phases, the orientationally-ordered solids — in AAA and ABC stacking — and the plastic or rotator solid. The rotator phase is unstable for $L/D \geq 0.35$ and the AAA crystal becomes unstable for lengths smaller than $L/D \approx 7$. The triple points isotropic-smectic-A-solid and isotropic-nematic-smectic-A are estimated to occur at $L/D=3.1$ and $L/D=3.5$ respectively. For the low L/D region, a modified version of the Gibbs-Duhem integration method was used to calculate the isotropic-solid coexistence curves. This method was also applied to the isotropic-nematic transition for $L/D > 10$. For large L/D the simulation results approach the predictions of the Onsager theory. In the limit $L/D \rightarrow \infty$ simulations were performed by application of a scaling technique. The nematic-smectic-A transition for $L/D \rightarrow \infty$ appears to be continuous. As the nematic-smectic-A transition is certainly of first order nature for $L/D \leq 5$, the tri-critical point is presumably located between $L/D = L/D$ region, the plastic solid to aligned solid transition is first order. Using a mapping of the dense spherocylinder system on a lattice model, the initial slope of the coexistence curve could even be computed in the close packing limit.

Introduction

5.1

Intuitively, one associates increased order with a decrease in entropy. It is therefore surprising that a large number of phase transitions exist in which both the structural order and the entropy of the system increase. In particular, all ordering transitions in systems of particles that have exclusively hard-core interactions, are of this type. Already in the forties, Onsager showed [25] that thin hard rods must form a nematic liquid crystal at sufficiently high densities. In the fifties, the computer-simulation studies of Alder and Wainwright, and Wood and Jacobson [92, 93] provided the first conclusive evidence that hard spherical particles undergo a first order freezing transition. Subsequently, computer simulations of a variety of models of non-spherical hard-core models showed that excluded volume effects could not only account for the stability of nematics [94, 95] but also for the existence of smectic [96, 97, 76, 26] and columnar [98, 99] liquid-crystalline phases (for a review, see [77]).

As already mentioned, simulations of hard particles are of considerable practical relevance for the study of colloidal materials consisting of anisometric inorganic colloids [17] or rodlike

virus particles [100]. To a first approximation, hard spherocylinders (cylinders of length L and diameter D capped with two hemispheres at both ends) provide a good model for rodlike colloidal particles with short-ranged repulsive interactions. The parameter that characterizes the phase behavior of such particles is the length-to-width ratio L/D . Of course, the behavior of real rodlike colloids may differ from that of rigid hard spherocylinders, either because the colloid-colloid interaction is not truly a hard-core repulsion or because real colloids are never completely rigid. It is clearly of interest to know where the analogy between real colloids and the corresponding hard-core model breaks down. However, in order to detect such differences in behavior, it is obviously important to have a good knowledge of the hard-spherocylinder (HSC) phase diagram over a wide range of L/D values.

A first attempt to map out the HSC phase diagram was reported by Veerman and Frenkel [26]. However, this study focused on only a small number of rather widely spaced L/D values. As a consequence, the phase boundaries for intermediate L/D values could only be sketched, while some phase boundaries were not studied at all. This situation is clearly unsatisfactory, as the HSC system is now often used as a reference system to compare both with experiment and with theory. For precisely this reason, McGrother et al. [27] recently performed more extensive simulations in the region $3 < L/D < 5$. The aim of the present study is to compute the *complete* phase diagram of the spherocylinder model (i.e. from $L/D=0$ to $L/D = \infty$, and from low-density to close packing. In order to achieve this, we employ several computational techniques that have been developed in the past few years that enable us to map the HSC phase diagram over a wide range of L/D values.

In this study we pay special attention to three aspects of the phase diagram. The first is the location of the orientational order-disorder transition in the solid (for small anisometries). This transition has, thus far, not been studied for spherocylinders. More interestingly, using the novel computational technique from section 3.2.4 and [101], we are now able to trace the coexistence curve between rotator phase and orientationally ordered crystal all the way to close packing. Second, we are interested in the behavior of spherocylinders for large L/D and in particular the Onsager limit. The third point of special interest is the location of the triple points in the phase diagram. Specifically, there is a maximum L/D value beyond which no crystalline rotator phase can exist and similarly, there are lower limits for L/D below which the smectic-A, nematic and the crystalline AAA phases become thermodynamically unstable.

Veerman and Frenkel [26] made no attempt to estimate the first triple point and could only give rather wide margins for the other three. In particular, they found that whereas rods with a length-to-width ratio $L/D=5$ can form both a stable nematic and a stable smectic phase, at $L/D=3$ the smectic phase is only meta-stable while the nematic phase is even mechanically unstable. Clearly, the only conclusion that could be drawn from the simulations in ref. [26] is that the triple points that terminate the range of nematic and smectic stability must be located somewhere between $L/D=3$ and $L/D=5$. But it remained unclear where exactly this would happen and which triple point would come first.

Moreover, one should expect the nematic-smectic transition to be first order for small L/D values and continuous for long spherocylinders. Different theories make different predictions about the location of the tricritical point: in refs. [102, 103] is estimated that the tricritical point corresponds to $L/D \approx 5$ while the theoretical analysis in ref [104] suggest that it should occur at $L/D=50$. The present simulations strongly suggest that

this tri-critical point occurs at an L/D values appreciable larger than 5 , but are not suited to determine the exact location of the tri-critical point.

The recent NPT Monte Carlo simulations of McGrother et al.[27] were performed on a system of spherocylinders with L/D range 3 to 5. They found that the isotropic-smectic-A-solid triple point occurs at $L/D \approx 3.2$ and that the isotropic-nematic-smectic triple point is located around $L/D=4$. Further they also found evidence for a first order nematic-smectic transition at $L/D=5$.

The outline of the remainder of this chapter is as follows. For readers who are less interested in the technical details of the simulations, section 5.2 summarizes the main results concerning the phase behavior of spherocylinders. Subsequently, different aspects of the simulations are discussed in some detail. Section 5.3 describes the simulation techniques and the methods we used to calculate the free energy of the different phases. In particular, section 5.3.3 describes how we have modified the Gibbs-Duhem integration technique of Kofke [84] to trace the melting curve for $0.4 \leq L/D \leq 3$. The results for $L/D < 5$ are presented in section 5.4. The location of the first order transition between solid and rotator is discussed in section 5.5. This section also describes the computational technique used to study this transition in the limit of close packing of the spherocylinders. In section 5.6 results for long rods (up to $L/D=60$) are presented. The isotropic-nematic transition is studied both by Gibbs-ensemble simulation and Gibbs-Duhem integration. For $L/D \rightarrow \infty$ this transition is expected to approach the behavior predicted by the Onsager theory. We discuss the nematic-smectic and smectic-solid transitions for long rods ($L/D=40$). We also present a rough estimate for the AAA phase boundaries in this section. Finally, in section 5.7 the simulation of spherocylinders in the limit $L/D \rightarrow \infty$ are discussed.

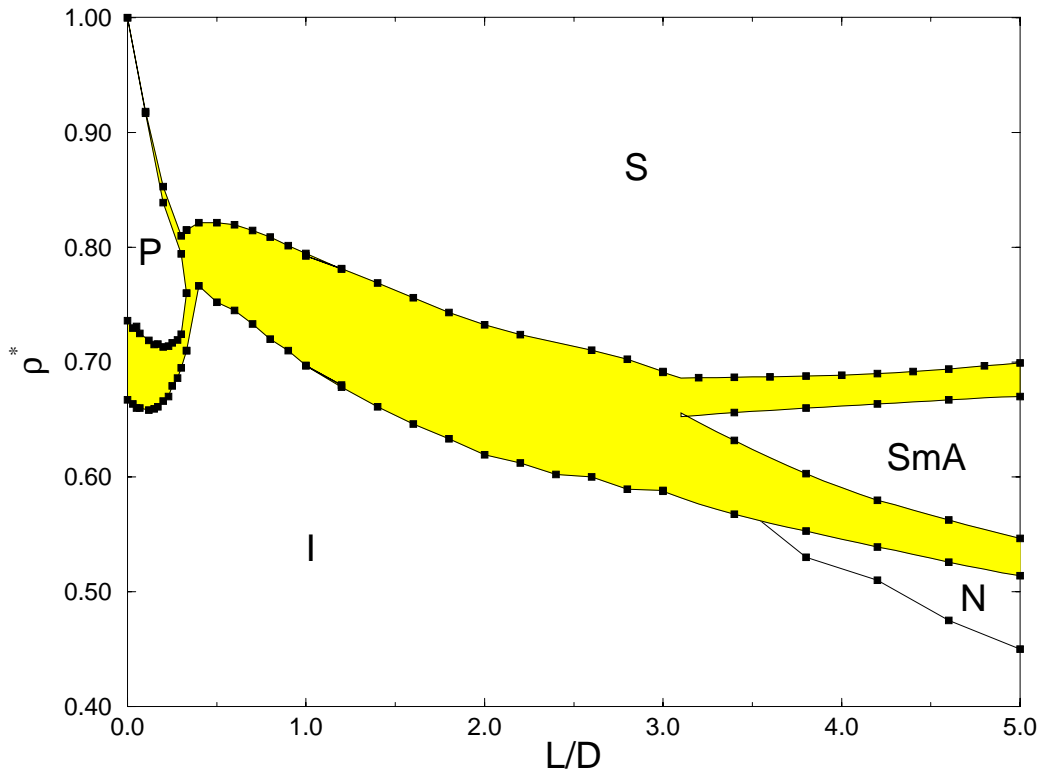


Figure 5.1. Phase diagram for hard spherocylinders of aspect ratio $L/D < 5$. All two-phase regions are shown shaded. In the figure, the following phases can be distinguished: the low-density isotropic liquid, the high-density orientationally-ordered solid, the low- L/D plastic solid and, for $L/D > 3.5$, the nematic and smectic-A phases

5.2 Brief summary of the phase diagram

5.2.1 Phase diagram for $L/D \leq 5$.

Figure 5.1 shows the computed phase diagram of hard-spherocylinders in the region between $L/D=0$ (hard spheres) and $L/D=5$. The black squares indicate the reduced transition densities for L/D values at which simulations were performed. In this and following figures, the reduced density $\rho^* = \rho/\rho_{cp}$ is the density relative to the density of regular close packing of spherocylinders:

$$\rho_{cp} = 2/(\sqrt{2} + (L/D)\sqrt{3}).$$

For particles with $L/D \leq 0.35 \pm 0.05$, the isotropic fluid freezes to form a plastic crystal (rotator phase). At higher densities, the rotator phase undergoes a first-order transition to the orientationally ordered phase. As L/D is lowered to zero, this transition moves towards the density of regular close packing $\rho^* = 1$. Between $L/D=0.35$ and $L/D=3.1$, only two phases occur: the low-density isotropic phase and the high-density, orientationally ordered, crystal phase. The smectic phase first becomes stable at the I-SmA-S triple-point which is located $L/D=3.1$. The nematic phase becomes stable at $L/D=3.5$. The nematic-smectic transition takes place around $\rho^*=0.5$ and is initially clearly first order, but the density jump

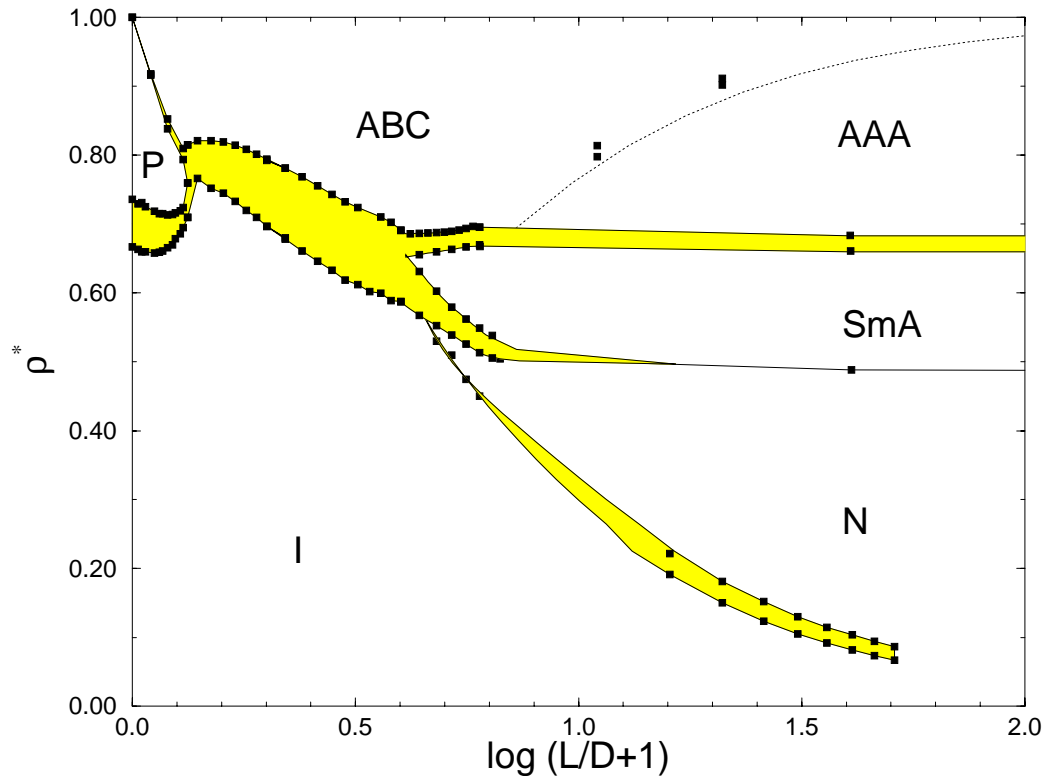


Figure 5.2. Summary of the phase diagram of hard spherocylinders with L/D between 0 and 60. In order to give equal emphasis to all parts of the phase diagram, we have plotted ρ^* as a function of $\log(L/D + 1)$. The dashed line is a crude estimate for the first order AAA-ABC transition as given in eqn. 5.51.

at the N-S transition shrinks with increasing L/D . The smectic to solid transition is located at $\rho^* = 0.66 - 0.68$ and is also first order.

Phase diagram for $L/D > 5$.

5.2.2

In figure 5.2, the phase behavior for long rods is depicted as a function of $\log(L/D + 1)$ to give equal emphasis to the different parts of the phase diagram. For larger values of L/D , the I-N transition moves to lower densities and the density jump at the I-N transition, which is too small to be measured for rods with $L/D \leq 5$, increases to almost 20%, as $L/D \rightarrow \infty$, as predicted by Onsager theory. In contrast, the density of the nematic-smectic transition is not very sensitive to the length-to-width ratio of the rods and approaches the finite limit $\rho^* = 0.47$ as $L/D \rightarrow \infty$. Similarly, the smectic-to-solid transition exhibits only a weak dependence on L/D and occurs still at $\rho^* \approx 0.66$ in the $L/D \rightarrow \infty$ limit.

At L/D values greater than approximately 7 a crystal phase with an 'AAA' stacking becomes stable between the smectic and the ABC stacked solid. This crystal phase is characterized by hexagonal planes which are stacked precisely on top of each other. At higher density the ABC stacked solid, which has the hexagonal planes shifted with respect to each other, will still be the most stable structure. The density of the AAA-ABC transition increases quickly for $L/D > 7$ to reach the close packing limit at $L/D \rightarrow \infty$.

More details on the phase behavior of long spherocylinders can be found in section 5.6.

5.3 Simulation techniques

5.3.1 Equilibration

Knowledge of the equation of state often provides a rough estimate of the limits of stability of the various phases. By starting with different configurations at different densities the range of mechanical stability of the observed phase can be estimated. If only one phase is mechanically stable at a given density, this will also be the thermodynamically stable phase. If more phases appear to be stable at the same density, a free-energy calculation is necessary to identify the one that is thermodynamically stable.

In our simulation studies of the equation of state of hard spherocylinders, we generated initial conditions both by expansion and by compression. Specifically, we prepared the configurations of a (dense) spherocylinder system in the following ways

- *Expansion of a solid phase.* A close packed *fcc* lattice of spheres with its (111) plane in the *xy* plane was stretched in the *z*-direction by a factor of $(L/D + 1)$ in order to accommodate a close packed crystal of spherocylinders. This 'ABC'-stacked lattice was subsequently expanded to the desired density and allowed to equilibrate. In the crystalline and smectic phases, the box shape should have the freedom to fluctuate in order to obtain a isotropic pressure. In those cases, we used variable-shape constant-volume Monte Carlo (VSMC). Otherwise, simple constant-volume Monte Carlo was employed.
- *Compression of an isotropic liquid phase.* At low density an ABC stacked lattice of spherocylinders was allowed to melt into an isotropic liquid using NVT Monte Carlo. This configuration was subsequently compressed to the desired density using constant-NPT Monte Carlo and allowed to equilibrate again with constant-NVT Monte Carlo.
- *Starting from a smectic configuration.* In studying the smectic to nematic transition and the smectic to solid transition it is preferable to start with a stacking of hexagonal ordered layers and let this equilibrate by VSMC. The configuration obtained was subsequently compressed by NPT MC or expanded and allowed to equilibrate again.
- *Starting from a nematic configuration.* In studying the nematic-smectic transition by compression it is preferable to start with a defect-free nematic phase. However, the nematic phase that forms upon compression of the isotropic liquid usually contains long-lived defects. To prepare a defect-free nematic phase, we first generated a hexagonal crystal lattice ("AAA"-stacking) at a density where the nematic phase is known to be the stable one. From this configuration, we first prepare an aligned columnar phase, by displacing every column in the hexagonal crystal by a random shift along the *z*-axis. Subsequently, we allowed the spherocylinders to rotate but not yet translate in order to suppress an initial fast relaxation to the smectic phase. After a few thousand cycles translation was allowed as well and the system was allowed to equilibrate. The equilibrated nematic configuration was compressed by NPT MC to the desired density and equilibrated again. In principle, we kept the box shape fixed in the nematic phase. However, close to the smectic phase boundary, where appreciable smectic fluctuations are already present in the system, we found it advantageous to use VSMC even in the nematic phase, to speed up equilibration.

After preparing well equilibrated configurations of the various phases, we used Molecular Dynamics simulations to measure the pressure of the system using the method described in ref. [105, 106]. Occasionally, we also used Molecular Dynamics to speed up the equilibration.

This proved to be particularly useful near the nematic-smectic transition where equilibration involves collective rearrangements of large numbers of particles – something that is not easily achieved using single-particle Monte Carlo moves. Whenever MD simulations are performed, we choose the mass m of the spherocylinder as our unit of mass, and hence the unit of time is $\tau \equiv D\sqrt{m/kT}$. The moment of inertia was computed, assuming a uniform mass distribution in the spherocylinder. The MD simulations that we used to measure the pressure in a well-equilibrated system were typically of 2000 collisions per particle. The number of particles we used to calculate different parts of the equation of state and the length of a typical simulation are summarized in table 5.1.

Table 5.1. *Simulation parameters for the various parts of the phase diagram of hard spherocylinders. In the column for the type of simulation C stands for compression, E for expansion and GD for a Gibbs-Duhem integration. In the “phase” column I stands for isotropic, N for nematic, Sm for smectic, R for rotator and S for solid (ABC) phase. The column MC gives the total number of Monte Carlo cycles; the column MD the number of collisions per particle during a MD simulation. Gibbs Duhem integrations have two numbers at N_{part} column, because both phases are simulated simultaneously*

L/D (increment)	type	phase	ρ^* range	N_{part}	MC ($\times 10^5$)	MD ($\times 10^3$)
0.01	C	R-S	0.982-0.994	144	1	20
	E	R-S	0.992-0.996	144	1	20
0.1	C	R-S	0.80 -0.96	144	1	4
	E	R-S	0.92- 0.98	144	1	4
0.2	C	R-S	0.76 -0.90	144	1	4
	E	R-S	0.82- 0.98	144	1	4
0.3	C	R-S	0.70 -0.84	144	1	4
	E	R-S	0.80- 0.98	144	1	4
0.0 - 0.3 (0.025)	G-D	I-R	-	200/240	-	1
0.4 - 3.0 (0.2)	G-D	I-S	-	200/240	-	1
3.0 - 5.0(0.4)	C	I	0.20 -0.54	512	8	2
	C	I-N	0.40 -0.60	512	4	2
	E	I-N	0.40 -0.60	512	4	2
	C	N-Sm	0.54 -0.60	512	3	2
	E	N-Sm	0.54 -0.66	540	10	2
	C	Sm-S	0.64 -0.72	336	4	2
	E	Sm-S	0.62 -0.72	336	4	2
	E	S	0.66 -0.90	144	2	2
15 - 50(5)	G-D	I-N	-	480/480	-	0.5
40	E	I-N	0.05 - 0.15	2950	-	0.5
	C	N-Sm	0.46 - 0.58	1980	2	1
	E	N-Sm	0.46 - 0.66	1980	4	2
	E	Sm-S	0.60 - 0.76	504	2	2

5.3.2 Free energy calculations

In order to locate first order transitions, accurate free energy values are necessary. For our computation of the coexistence curves between the different phases as a function of L/D , we calculate the free energy of the isotropic, nematic, smectic and solid phases by means of thermodynamic integration. This method links the original system for which we want to know the absolute free energy to a reference state of known free energy via a reversible path. If the path is denoted by parameter λ we can define $F(\lambda = 0)$ as the free energy of the original system and $F(\lambda = 1)$ as the known free energy of the reference system. Integration along the path yields

$$F_{\lambda=1} - F_{\lambda=0} = \int_0^1 \left(\frac{\partial F}{\partial \lambda} \right)_{NVT\lambda} d\lambda. \quad (5.1)$$

5.3.2.1 Isotropic and nematic phases

For the isotropic phase we can take the ideal gas as a reference and integrate along the equation of state using the density ρ as the integration parameter

$$F(\rho, L) - F_{id}(\rho) = \int_0^\rho \frac{P(\rho', L) - \rho'}{\rho'^2} d\rho'. \quad (5.2)$$

Because the isotropic-nematic transition shows only a very small density jump at low L/D , it is possible to extend the integration through the transition and obtain the free energy of the nematic phase as well.

5.3.2.2 Solid phase

The strong first order transition separating the solid phase from the other phases rules out the integration along the equation of state. Instead, we choose as reference system for the solid an Einstein crystal with the same structure [39]. Now the reversible path transforms the original system to an Einstein crystal with fixed center-of-mass, by gradually coupling the atoms to their equilibrium lattice position. For the hard-spherocylinder system the orientation also needs to be coupled to an aligning field. The Hamiltonian that we use to achieve the coupling is the same as given in [26]

$$H_{\mu,\lambda} = \mu \sum_i \left(\vec{r}_i - \vec{r}_i^0 \right)^2 + \lambda \sum_i \sin^2 \theta_i, \quad (5.3)$$

where μ and λ are the coupling constants which determine the strength of the harmonic forces. The free energy of the HSC system can be related to the (known) free energy of an Einstein crystal by thermodynamic integration

$$\frac{\beta F(\rho^*)}{N} = \frac{\beta F_{ein}}{N} - \int_0^{\mu_{max}} d\mu \langle \Delta r^2 \rangle_\mu - \int_0^{\lambda_{max}} d\lambda \langle \sin^2 \theta \rangle_\lambda - \frac{\ln V}{N}. \quad (5.4)$$

Here $\langle \Delta r^2 \rangle_\mu$ is the mean-square displacement and $\langle \sin^2 \theta \rangle_\lambda$ the mean square sine of the angle between a particle and the aligning field in a simulation with Hamiltonian $H_{\mu,\lambda}$. The free energy of the Einstein crystal (with fixed center-of-mass) in the limit of large coupling

constants is given by

$$\beta F_{\text{ein}} = \frac{3}{2} \ln N - \frac{3}{2} (N-1) \ln \frac{\pi}{\beta \mu} - N \ln \frac{2\pi}{\beta \lambda}. \quad (5.5)$$

By performing several simulations at different values of μ and λ one can numerically evaluate the integrals in eqn. 5.4. As the values μ and λ at which the integrand is evaluated can be chosen freely, the error in the integration can be minimized by using Gauss-Legendre quadrature. Occurrence of any first order transition was avoided by performing two Gauss-Legendre integrations in succession. The first fixes the positions while leaving $\lambda = 0$, the second aligns all spherocylinders while keeping $\mu = \mu_{\text{max}}$. It is convenient to choose the maximum values of λ and μ such that in a simulation at these maximum values, there are essentially no overlaps between the particles. Otherwise it is necessary to correct eqn. 5.5 for the occurrence of overlaps [95].

Smectic phase

5.3.2.3

The smectic phase does not have an obvious reference state for which the free energy is known. Veerman [26] used the parallel spherocylinder system as a reference. However, the free energy of a parallel smectic itself is subject to numerical error. We chose to couple the spherocylinders with an harmonic spring to the smectic layer to which they belong and subsequently align them. In this way, the smectic phase can be transformed into what is essentially a 2D hard disk fluid for which the free energy is well known [56]. In principle, one could apply the Einstein integration method used in the previous section with one difference: the position field couples only the z-coordinates of the particles to the layer positions and leaves the x,y coordinates completely free. If we consider the first part of the integration, where the particles are confined to their layers, the free energy of smectic phase can be related to this planar system by

$$\frac{\beta F_{\mu=0}}{N} = \frac{\beta F_{\mu=\mu_0}^{\text{planar}}}{N} - \int_0^{\mu_0} d\mu \langle \Delta r^2 \rangle_{\mu} - \frac{\ln V}{N}. \quad (5.6)$$

In the second integration, the difficulty arises that an infinite amount of aligning energy is needed to get all spherocylinders completely parallel.

$$\frac{\beta F_{\lambda=0, \mu=\mu_0}^{\text{planar}}}{N} = \frac{\beta F_{\lambda=\infty, \mu=\mu_0}^{\text{planar, aligned}}}{N} - \int_0^{\infty} d\lambda \langle \sin^2 \theta \rangle_{\lambda}. \quad (5.7)$$

To keep the energy values finite, we subtract on both sides of this equation the free energy of an ideal rotator in the same field.

$$\frac{\beta F_{\lambda=\lambda_0, \mu=\mu_0}^{\text{planar, id}}}{N} = \frac{\beta F_{\lambda=\infty, \mu=\mu_0}^{\text{planar, aligned, id}}}{N} - \int_{\lambda_0}^{\infty} d\lambda \langle \sin^2 \theta \rangle_{\text{id}, \lambda}, \quad (5.8)$$

which results in

$$\begin{aligned} \frac{\beta F_{\lambda=0, \mu=\mu_0}^{\text{planar}}}{N} &= \frac{\beta F_{\lambda=\lambda_0, \mu=\mu_0}^{\text{planar, id}}}{N} + \frac{\beta F_{\lambda=\infty, \mu=\mu_0}^{\text{planar, aligned, ex}}}{N} - \int_0^{\lambda_0} d\lambda \langle \sin^2 \theta \rangle_{\lambda} \\ &\quad - \int_{\lambda_0}^{\infty} d\lambda \left[\langle \sin^2 \theta \rangle_{\lambda} - \langle \sin^2 \theta \rangle_{\text{id}, \lambda} \right]. \end{aligned} \quad (5.9)$$

The excess free energy of the completely aligned planar system $\beta F_{\lambda=\infty, \mu=\mu_0}^{\text{planar, aligned, ex}}$ is equal to the excess free energy of a 2D hard disk fluid. The free energy of the ideal planar system (with fixed center-of-mass) in the limit of large coupling constants is given by

$$\beta F_{\lambda=\lambda_0, \mu=\mu_0}^{\text{planar, id}} = \frac{1}{2} \ln N - \frac{1}{2} (N-1) \ln \frac{\pi}{\beta \mu} - N \ln \frac{2\pi}{\beta \lambda}. \quad (5.10)$$

The integral over the difference of the \sin^2 terms in eqn. 5.9 is finite. We can change the integration boundaries by substituting $\lambda = 1/\xi^2$.

$$\int_{\lambda_0}^{\infty} d\lambda \left[\langle \sin^2 \theta \rangle_{\lambda} - \langle \sin^2 \theta \rangle_{\text{id}, \lambda} \right] = \int_0^{\frac{1}{\sqrt{\lambda_0}}} d\xi 2\lambda^{\frac{2}{3}} \left[\langle \sin^2 \theta \rangle_{\lambda} - \langle \sin^2 \theta \rangle_{\text{id}, \lambda} \right]. \quad (5.11)$$

In conventional MC sampling, the statistical error of both terms in the integrand is larger than the difference itself. We therefore applied the following scheme to evaluate the difference directly in the Monte Carlo program. Instead of rotating a spherocylinder i around an angle $d\theta_i$ we choose a completely new trial value of θ_i from the probability distribution

$$P(\theta) \sim \exp(-\beta \lambda \sin^2 \theta). \quad (5.12)$$

This is the equilibrium distribution for an ideal rotator with a Hamiltonian according to eqn. 5.3 and results in the correct value for $\langle \sin^2 \theta \rangle_{\text{id}, \lambda}$. If no overlap occurs the trial move will be accepted and we will have

$$\sin_{\lambda}^2 \theta_i - \sin_{\text{id}, \lambda}^2 \theta_i = 0. \quad (5.13)$$

If an overlap does occur the trial move will be rejected and the particle will retain its old value. The difference now will be

$$\sin_{\lambda}^2 \theta_i - \sin_{\text{id}, \lambda}^2 \theta_i = \sin_{\lambda}^2 \theta_i^{\text{old}} - \sin_{\lambda}^2 \theta_i^{\text{new}}. \quad (5.14)$$

The statistical error in the average of the difference is always smaller than the average itself. This will enable us to determine the integrand more accurately. By combining eqns 5.6, 5.9 and 5.11 the complete expression for free energy of the smectic phase follows

$$\begin{aligned} \frac{\beta F_{\mu=0}}{N} &= \frac{\beta F_{\text{disk}}^{\text{ex}}}{N} - \frac{\beta F_{\lambda=\lambda_0, \mu=\mu_0}^{\text{planar, id}}}{N} - \frac{\ln V}{N} - \int_0^{\mu_0} d\mu \langle \Delta r^2 \rangle_{\mu} \\ &\quad - \int_0^{\lambda_0} d\lambda \langle \sin^2 \theta \rangle_{\lambda} - \int_0^{\frac{1}{\sqrt{\lambda_0}}} d\xi 2\lambda^{\frac{2}{3}} \left[\langle \sin_{\lambda}^2 \theta - \sin_{\text{id}, \lambda}^2 \theta \rangle \right]. \end{aligned} \quad (5.15)$$

The excess hard disk free energy can be obtained by subtracting the ideal term $\beta F_{\text{disk}}^{\text{id}} = \ln \rho$ from the free energy in ref. [56]. All integrations were carried out using Gauss-Legendre quadrature. To ensure that the 2D densities in the smectic layers are equal throughout the system we used shifted periodic boundaries. In our system the periodic boundaries in the x -direction are shifted exactly one layer period along the z -axis, while leaving them the same in the y and z direction. In this way, a particle leaving the simulation box at the left side will reenter the box at the right *one layer higher*. This particle can diffuse through

the whole system, as there is effectively only one layer. This ensures that fluctuations in the number of particles per smectic layer can relax, even at high density where normal inter-layer diffusion is effectively frozen out.

Nematic-smectic free energy difference

5.3.2.4

It turned out to be rather difficult to determine the first order nematic smectic coexistence region for $L/D < 5$, because the location of the coexistence point appeared to be quite sensitive to errors in the free energy of the nematic and smectic phases. Therefore we calculated the free energy difference between a stable nematic and a stable smectic directly. In order to find a reversible path from the nematic to smectic we applied the following Hamiltonian

$$H_\lambda = \lambda \left(\sum_i \cos\left(\frac{2\pi n r_{i,z}}{L_z}\right) + 1 \right), \quad (5.16)$$

where n is the number of smectic layers, L_z the box length in the z -direction, $r_{i,z}$ the z -coordinate of particle i and λ the coupling parameter determining the strength of the smectic ordering. At low density this Hamiltonian will produce, by increasing λ , a gradual transition from a nematic to a smectic phase. We started with a smectic phase and applied a cosine field at large enough λ . Subsequently, the smectic was expanded to lower density, while measuring the pressure. Finally, the cosine field was slowly turned off. The free energy difference now simply is

$$\begin{aligned} \frac{\Delta F_{ns}}{N} &= \frac{F_{smec}}{N} - \frac{F_{nem}}{N} = \int_0^{\lambda_{max}} \left\langle \sum_i \cos\left(\frac{2\pi n r_{i,z}}{L_z}\right) + 1 \right\rangle_{smec} \\ &\quad - \int_{\rho_n}^{\rho_s} \frac{P(\rho)}{\rho^2} d\rho - \int_0^{\lambda_{max}} \left\langle \sum_i \cos\left(\frac{2\pi n r_{i,z}}{L_z}\right) + 1 \right\rangle_{nem} \end{aligned} \quad (5.17)$$

Of course, the value of λ_{max} should be chosen large enough that the first-order S-N transition is completely suppressed.

Kappa integration

5.3.2.5

It is not necessary to perform free energy calculations for all values of L/D . Once the free energy of a phase at certain density and L/D is established the free energy at other values of L/D can be obtained by a simple thermodynamic integration scheme. We can compute the reversible work involved in changing the aspect ratio of the spherocylinders from L_0/D to L/D and subsequently changing the density from ρ_0 to ρ :

$$F(\rho, L) = F_0(\rho_0, L_0) + \int_{L_0}^L \left(\frac{\partial F}{\partial L} \right)_{\rho_0} dL + \int_{\rho_0}^{\rho} \frac{P(\rho, L)}{\rho^2} d\rho. \quad (5.18)$$

Here we have set $D=1$ for convenience. $F_0(\rho_0, L_0)$ has to be determined by free energy calculations as described above. The pressure is obtained from an MD simulation in the usual way, by time averaging the virial.

$$\frac{\beta P}{\rho} - 1 = \frac{1}{3} \sum_{i \leq j} \langle \vec{f}_{ij} \cdot \vec{r}_{ij} \rangle, \quad (5.19)$$

where \vec{r}_{ij} is the vector joining the centers of mass of particles i and j , and \vec{f}_{ij} denotes the (impulsive) force on j due to i . The derivative $\kappa = (\partial F / \partial L)_\rho$ can be measured at the same time by taking the projection of the intermolecular force along the particle axis.

$$\kappa = \left(\frac{\partial F}{\partial L} \right)_\rho = \frac{1}{2} \sum_{ij} \langle \vec{f}_{ij} \cdot (\vec{u}_i + \vec{u}_j) \rangle, \quad (5.20)$$

where \vec{u} denotes the unit vector of orientation of a particle. The average κ is calculated at constant number density ρ . However, it is more convenient to measure it at constant reduced density ρ^* (i.e. at a constant fraction of the close-packing density). If we denote this derivative by κ' , we get

$$\kappa' = \left(\frac{\partial F}{\partial L} \right)_{\rho^*} = \left(\frac{\partial F}{\partial L} \right)_\rho + \left(\frac{\partial F}{\partial \rho} \right)_L \left(\frac{\partial \rho}{\partial L} \right)_{\rho^*} = \left(\frac{\partial F}{\partial L} \right)_\rho - \frac{\sqrt{3}}{2\rho^*} P(\rho^*, L), \quad (5.21)$$

and eqn. 5.18 becomes

$$F(\rho^*, L) = F_0(\rho_0, L_0) + \int_{L_0}^L dL \left(\left(\frac{\partial F}{\partial L} \right)_\rho - \frac{\sqrt{3}}{2\rho^*} P(\rho^*, L) \right) dL + \int_{\rho_0}^{\rho^*} \frac{1}{\rho_{cp}(L)} \frac{P(\rho^*, L)}{\rho^{*2}} d\rho^*. \quad (5.22)$$

5.3.3 Kofke's Gibbs-Duhem integration

The location of a fluid-solid coexistence curve can be determined by performing several free-energy calculations and measurements of the equation-of-state for a large number of L/D values. However, this approach is computationally rather expensive. To avoid this problem, we use a modification of a method that was recently developed by Kofke to trace coexistence curves [84]. The advantage of this method is that only equation-of-state information *at the coexistence curve* is required to follow the L/D -dependence of the melting curve. In its original form, the Kofke scheme is based on the Clapeyron equation which describes the temperature-dependence of the pressure at which two phases coexist (see section 4.3):

$$\frac{dP}{dT} = \frac{\Delta h}{\Delta v}, \quad (5.23)$$

where Δh is the molar enthalpy difference and Δv the molar volume difference of the two phases. This equation is not self starting, in the sense that one point on the coexistence curve must be known before the rest of the curve can be computed by integration of eqn. 5.23. Kofke refers to this method as ‘‘Gibbs-Duhem’’ integration.

In the present case, we are not interested in the temperature dependence of the coexistence curve (this dependence is trivial for hard-core systems), but in the dependence of the coexistence pressure on L/D , the length-to-width ratio of the spherocylinders. In order to obtain a Clapeyron-like equation relating the coexistence pressure to L/D , we should first write down the explicit dependence of the (Gibbs) free energy of the system on L/D :

$$dG = N\mu = VdP + \kappa dL, \quad (5.24)$$

where κ is the derivative $(\partial F/\partial L)_p$ defined in eqn. 5.20 and where we have used the fact that D is our unit of length. Along the coexistence curve, the difference in chemical potential of the two phases is always equal to zero. Hence,

$$\Delta\mu = \Delta v dP + \frac{1}{N} \Delta\kappa dL = 0, \quad (5.25)$$

where Δv is the difference in molar volume of the two phases at coexistence and $\Delta\kappa = \kappa_1 - \kappa_2$. From eqn. 5.25 we can immediately deduce the equivalent of the Clausius-Clapeyron equation

$$\frac{dP}{dL} = -\frac{1}{N} \frac{\Delta\kappa}{\Delta v}. \quad (5.26)$$

Kofke used a predictor-corrector scheme to integrate eqn. 5.23. However, we find that this integration scheme, when applied to eqn. 5.26, is not very stable. In particular, when the predicted pressure is slightly off, the predictor-corrector scheme leads to unphysical oscillations. We therefore introduce a slightly different integration procedure. Instead of calculating one new point in the phase diagram every step, we start with a set of simulations at different L values and pressure for both phases. The derivatives are calculated according to eqn. 5.26 and subsequently fitted to a polynomial in L

$$\frac{dP}{dL} = \sum_{i=0}^3 \alpha_i L^i. \quad (5.27)$$

This polynomial is integrated to give new pressures which are used in the next iteration. The old and new pressures are mixed together to improve the stability. This procedure is repeated until convergence of the pressure has occurred. The set of starting values are obtained by application of the original Gibbs-Duhem scheme.

In Kofke's application of the Gibbs-Duhem method, the MC simulations are carried out in the isothermal-isobaric (NPT) ensemble. However, in the present case (hard-core particles), it is more efficient to use Molecular Dynamics to compute the derivative κ . In practice, we use a hybrid approach where MD simulations are embedded in a constant NPT-MC scheme. True constant-pressure MD is not an attractive option for hard-core models.

Phase diagram for $L/D \leq 5$

5.4

Phase behavior for $0 \leq L/D \leq 3$

5.4.1

For hard spherocylinders with lengths shorter than $L/D = 3$ there is only a fluid phase and, at high densities, a crystalline phase. For rods with $L/D \geq 0.35$, the crystalline phase is an orientationally ordered (hexagonal) lattice. Below $L/D = 0.35$ we find that a face-centered cubic "rotator" phase becomes stable (see section 5.5).

Gibbs-Duhem simulations were performed to locate transition from isotropic fluid to the *fcc* plastic crystal in the range $L/D = 0$ to 0.3. As a reference point, we used the coexistence properties of the hard-sphere model ($L/D=0$) [56]. In the region $0.4 \leq L/D \leq 3$, we used the free energy data of ref [26] at $L/D=1$ as our fixed reference point. As a test, we checked that the computed coexistence curve did reproduce results of ref. [26] for the densities of the coexisting phases for $L/D=3$.

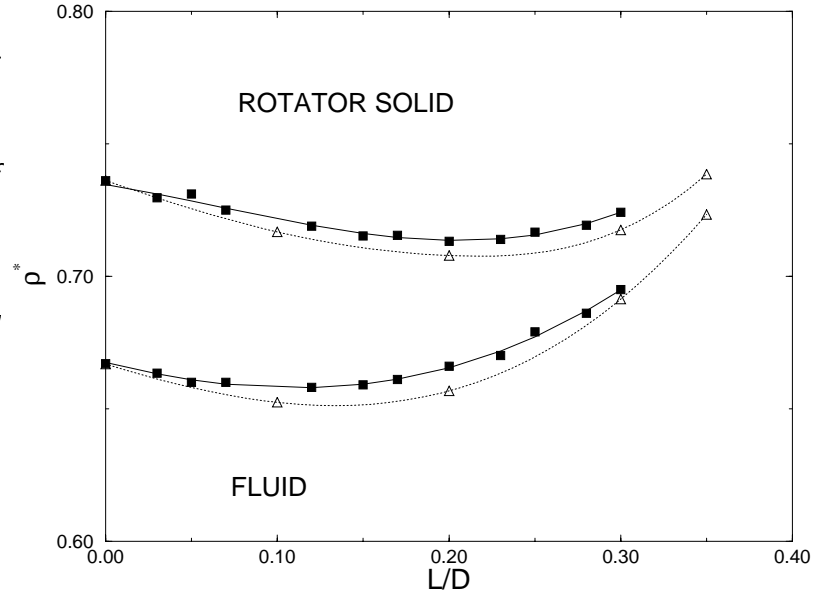
L/D	P/kT	ρ_{solid}^*	ρ_{iso}^*	L/D	P/kT	ρ_{solid}^*	ρ_{iso}^*
0.00*	11.69	0.736	0.667	0.40	21.94	0.821	0.766
0.03	11.45	0.730	0.660	0.50	20.06	0.821	0.753
0.05	11.24	0.731	0.6600	0.60	18.24	0.819	0.745
0.07	11.05	0.725	0.661	0.70	16.51	0.814	0.733
0.10	10.91	0.723	0.695	0.80	14.89	0.809	0.720
0.12	10.83	0.719	0.658	0.90	13.41	0.801	0.711
0.15	10.83	0.715	0.659	1.00*	12.09	0.794	0.698
0.17	10.93	0.715	0.661	1.20	10.12	0.781	0.680
0.20	11.14	0.713	0.666	1.00*	12.08	0.792	0.697
0.23	11.49	0.714	0.670	1.20	10.19	0.781	0.679
0.25	11.98	0.717	0.679	1.40	8.64	0.767	0.662
0.28	12.63	0.719	0.686	1.60	7.39	0.756	0.647
0.30	13.46	0.724	0.696	1.80	6.41	0.743	0.634
				2.00	5.64	0.732	0.620
				2.20	5.03	0.724	0.619
				2.40	4.56	0.706	0.602
				2.60	4.17	0.710	0.601
				2.80	3.81	0.702	0.589
				3.00	3.45	0.691	0.588

Table 5.2. *Pressure and reduced densities of coexisting isotropic and solid phases for hard spherocylinders with aspect ratios L/D between 0 and 3 as obtained by Gibbs-Duhem integration. The pressure is given in units of kT . The horizontal lines separate the results of independent integrations. The stars indicate the reference L/D values.*

The results of the Gibbs-Duhem integration are given in table 5.2 and are displayed in figure 5.1. The coexistence curves are smooth and the densities reproduce the earlier values for $L/D=3$ to within a few tenth of a percent. The solid density at $L/D=2.4$ is slightly off, presumably because the solid happened to contain a defect. In any event, as $\Delta\kappa$ (in eqn. 5.26) is evaluated as the (small) difference between two large, fluctuating numbers, it is difficult to obtain this quantity with high accuracy. An additional problem is that it takes a long time before the simulation box for the solid phase has relaxed to its equilibrium shape (i.e. the one that makes the pressure tensor isotropic).

The Gibbs Duhem integration results for the fluid-rotator transition for $0 < L/D < 0.3$ can be compared with Monte Carlo simulations of the fluid-plastic crystal coexistence in hard dumbbell systems, performed by Singer and Mumaugh [107]. Figure 5.3 shows the fluid-rotator coexistence region of the spherocylinders in combination with the results on dumbbells. As one would expect, the agreement is excellent because spherocylinder hardly differ from dumbbells in this L/D region. We found that Gibbs-Duhem integration could not be used in the region between $L/D=0.3$ and $L/D=0.4$ where three phases (liquid, plastic solid and ordered solid) compete. On basis of the available data we estimate that the liquid-solid-solid triple point is located around $L/D=0.35$ and $\rho^*=0.75$.

Figure 5.3. Comparison between the Gibbs Duhem integration results (squares) for the fluid-rotator transition of spherocylinders of length $L/D < 0.3$ and the Monte Carlo simulation results of Singer and Mumaugh (triangles) for dumbbells of small L/D



Phase behavior for $3 \leq L/D \leq 5$

5.4.2

In figure 5.4 the equations of state for spherocylinders with $L/D=3$ to 5 are displayed. The reduced pressure is defined as $P^* = Pv_0/kT$, where v_0 is the molecular volume of the particle ($v_0 = \pi(LD^2/4 + D^3/6)$).

We found for $L/D=3$ a mechanically stable isotropic, smectic and solid phase which is in agreement with the results of Veerman and Frenkel. For $L/D=5$ we find also a mechanically stable nematic phase as was reported by Frenkel, Lekkerkerker and Stroobants [76]. At values of L/D smaller than 5 the nematic phase region becomes narrower until it disappears when at $L/D \approx 3.5$ the isotropic-nematic-smectic triple point is reached.

Although the isotropic-nematic transition is a first order transition, the density jump and the hysteresis are too small to be observed in the simulations, at least for small L/D . Only for large values of L/D is the density gap sufficiently large to be observable in our simulations (see section 5.6). We therefore estimated the location of the isotropic-nematic transition for $L/D < 5$ by measuring the orientational correlation function

$$g_2(r) \equiv \langle P_2(\vec{u}(0) \cdot \vec{u}(r)) \rangle, \quad (5.28)$$

where P_2 is the second Legendre polynomial and $\vec{u}(0)$ the unit vector characterizing the orientation of a particle at the origin while $\vec{u}(r)$ denotes the orientation of a particle at a distance r from the origin. The brackets indicate ensemble averaging.

$g_2(r)$ becomes long-ranged at the isotropic-nematic transition and its limiting value at large r tends to S^2 , where S is the nematic order parameter. Of course, in a periodic system, it is not meaningful to study correlations at distances larger than half the box length, $B/2$. In figure 5.5 we have plotted the density-dependence of the nematic order parameter estimated from the value of $g_2(r = B/2)$. At the isotropic-nematic transition there is a steep increase of S . The transition densities are summarized in table 5.3.

Inspection of the equation of state suggest that the nematic to smectic phase transition is almost continuous at $L/D=5$, but becomes clearly first order for smaller values of L/D . A first order smectic-to-solid transition is found for $L/D > 3.1$ as can be seen in figure 5.4.

Table 5.3. *Pressure and reduced density of the isotropic to nematic transition for hard spherocylinders with aspect ratios L/D between 3 and 5. The pressure is expressed in dimensionless units Pv_0/kT , where v_0 is the molecular volume of the spherocylinders.*

L/D	Pv_0/kT	ρ^*
3.40	9.58	0.58
3.80	7.23	0.53
4.20	6.36	0.50
4.60	5.48	0.47
5.00	4.97	0.45

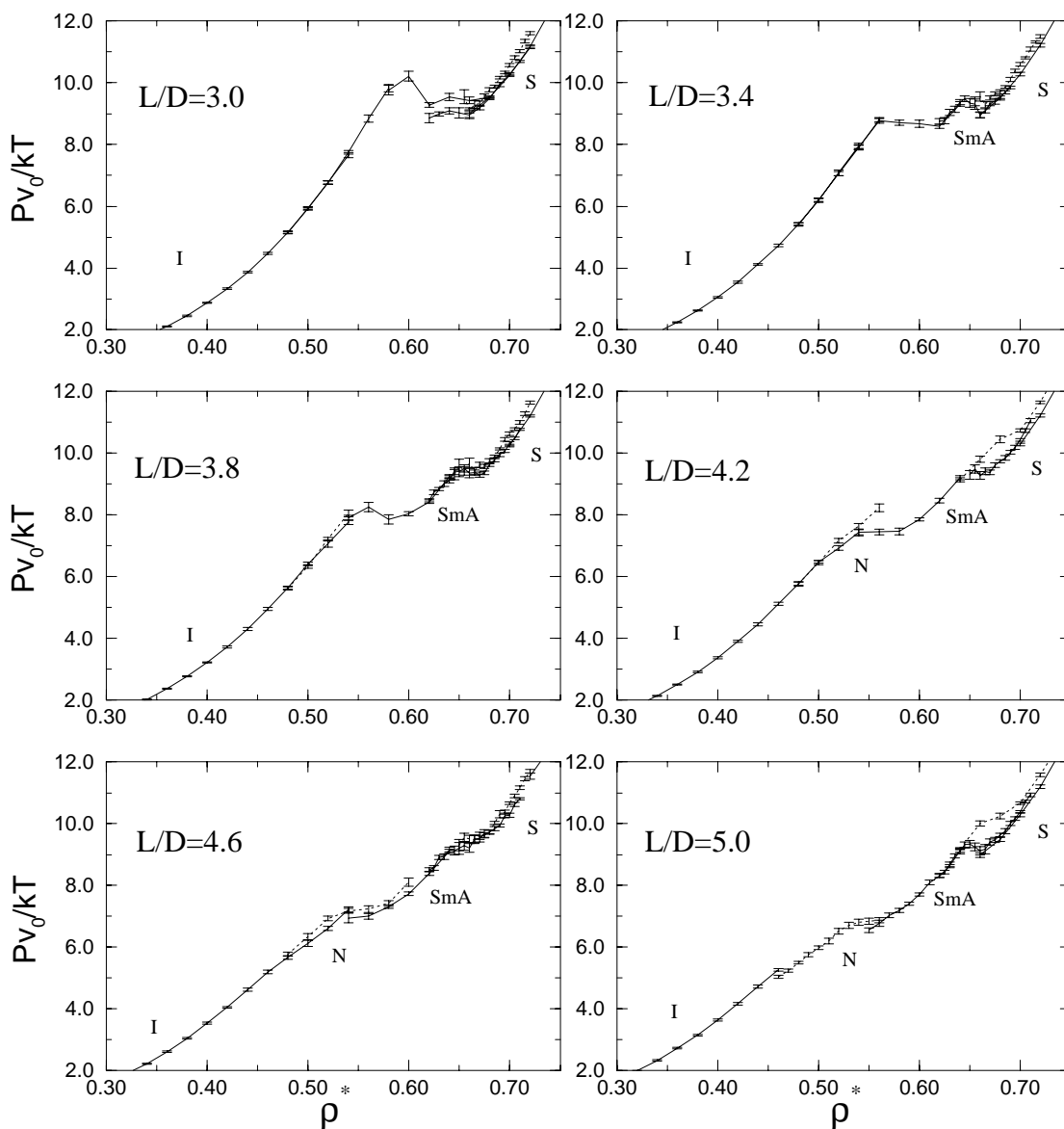


Figure 5.4. *Equations of state for spherocylinders with aspect ratio L/D between 3 and 5. The pressure is expressed in the dimensionless unit Pv_0/kT , where v_0 is the molecular volume of the spherocylinders. The dashed curves correspond to a compression whereas the solid curves denote an expansion. The different mechanically stable phases are indicated.*

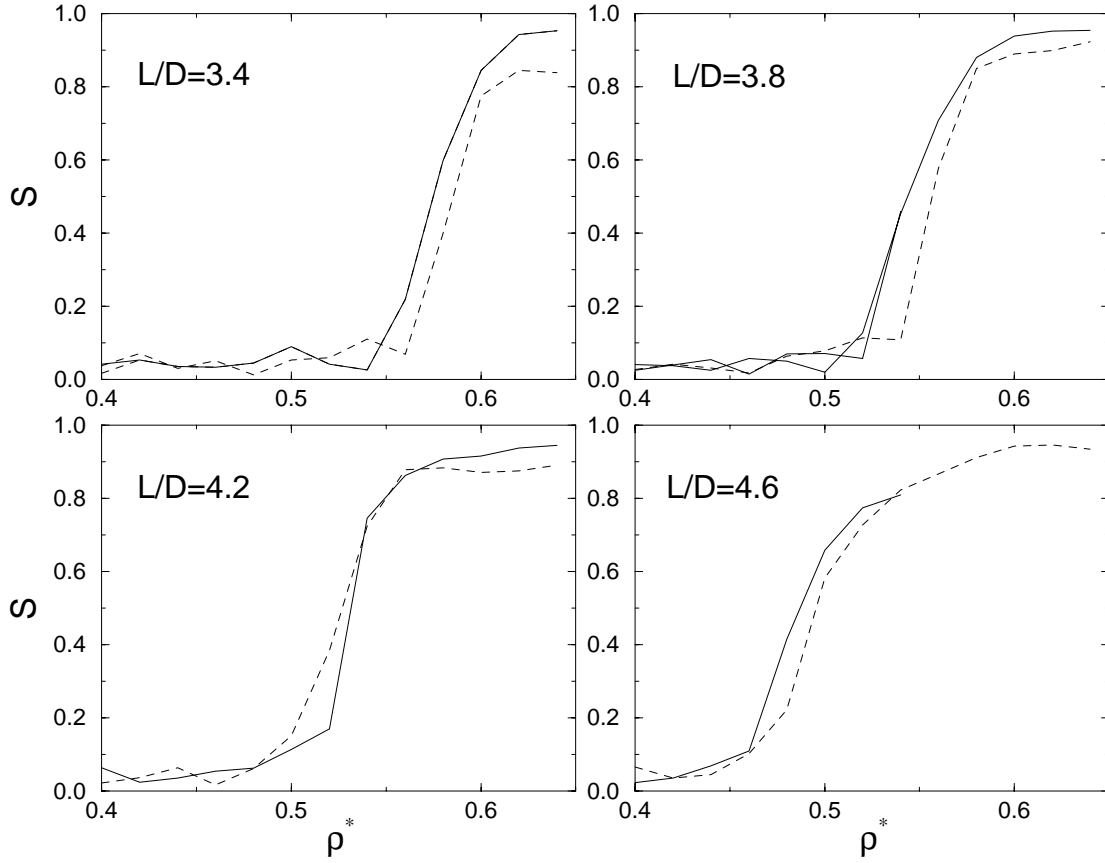


Figure 5.5. Density dependence of the nematic order parameter, as estimated from the limiting behavior of the orientational correlation function $g_2(r)$ (see text) for hard spherocylinders with L/D between 3.4 and 4.6. The solid curve corresponds to an expansion branch, the dashed curve to a compression branch

Table 5.4. Free energy and contributions to the free energy of the smectic phase. Columns 5 to 10 in the table refer to terms in the rhs of eqn. 5.15. The maximum values of μ and λ were $\mu_0=1000$ and $\lambda_0=10000$. The number of particles in the system was 540. The ideal free energy was in all cases $\beta F_{\lambda_0, \mu_0}^{p, id}/N=10.254$.

L/D	ρ^*	ρ_{disk}	$\beta F_{\text{disk}}^{\text{ex}}/N$	$\ln V/N$	$\int \langle \Delta r^2 \rangle$	$\int \langle \sin^2 \theta \rangle$	$\int \langle \Delta \sin^2 \theta \rangle$	$\beta F_{\lambda, \mu=0}/N$
3.0	0.64	0.789	1.430	0.0146	2.364	4.232	-0.005	5.079
5.0	0.66	0.810	1.624	0.0154	2.592	3.206	-0.277	6.341
5.0	0.68	0.841	1.941	0.0153	2.684	2.943	-0.312	6.864

In order to locate the coexistence curves we used thermodynamic integration as described in section 5.3.2 to compute the absolute free energy of the smectic and solid phase and the free-energy difference between a smectic and a nematic. The resulting values are displayed in respectively table 5.4, 5.5 and 5.6. Combination of these free energies with the equation of state and subsequent application of the double tangent construction leads to the coexisting densities of the nematic to smectic transition, the smectic solid transition as

Table 5.5. *Free energy and contributions to the free energy of the solid phase. Columns 6 to 9 in the table refer to terms in the rhs of eqn. 5.4. The maximum values of μ and λ are displayed as well. The number of particles in the system was 540.*

L/D	ρ^*	μ_{\max}	λ_{\max}	$\beta F_{\lambda_0, \mu_0}^{\text{ein}}/N$	$\ln V/N$	$\int \langle \Delta r^2 \rangle$	$\int \langle \sin^2 \theta \rangle$	$\beta F_{\lambda, \mu=0}/N$
3.0	0.82	22025	22025	21.438	0.014	7.529	3.812	10.082
5.0	0.76	20000	20000	21.197	0.015	8.708	3.587	8.886
5.0	0.86	50000	50000	23.485	0.015	8.138	3.194	12.140

Table 5.6. *Contributions to the free energy difference of a nematic phase at $\rho^*=0.5$ and a the smectic phase at $\rho^*=0.6$ for L/D=4.5. The different integrals in the table refer to terms in the rhs of eqn. 5.17. The maximum value of λ was chosen to be 5. The number of particles in the system was 600.*

$\int \langle \cos \rangle_{\rho^*=0.6}$	$\int_{0.5}^{0.6} P(\rho)/\rho^2 d\rho^*$	$\int \langle \cos \rangle_{\rho^*=0.5}$	$\beta \Delta F_{\text{nem-smec}}/N$
0.2849	2.034	0.893	2.64229

Table 5.7. *Pressure and densities of coexisting isotropic, nematic and solid phases for hard spherocylinders with aspect ratios L/D between 3 and 5. Units as in table 5.3.*

type of transition	L/D	Pv_0/kT	ρ_1^*	ρ_2^*
isotropic (nematic) -smectic	3.0	10.23	0.587	0.663
	3.2	9.56	0.576	0.647
	3.4	9.00	0.567	0.631
	3.6	8.54	0.559	0.616
	3.8	8.13	0.552	0.602
	4.0	7.77	0.545	0.590
	4.2	7.44	0.538	0.579
	4.4	7.10	0.532	0.571
	4.6	6.84	0.525	0.562
	4.8	6.60	0.519	0.553
5.0	6.40	0.513	0.546	
smectic	3.0	9.736	0.650	0.685
solid	3.4	9.830	0.655	0.686
	3.8	9.903	0.659	0.687
	4.2	10.009	0.663	0.689
	4.6	10.187	0.666	0.693
	5.0	10.428	0.669	0.699

well as the (meta-stable) solid to isotropic-liquid transition at L/D < 3.5. The results have been summarized in table 5.7.

The isotropic-smectic-solid triple point is located at L/D=3.1. The smectic phase is thermodynamically stable at higher L/D and is separated from the solid and the isotropic liquid by coexistence regions. The I-SmA-S triple point occurs at a smaller L/D value than the I-N-SmA triple point. This is not surprising as the smectic phase is already found to be mechanically stable at L/D=3 whereas the nematic phase is not.

In their study of the phase diagram of spherocylinders with L/D=3 to L/D=5, McGrother et al. [27] estimated the isotropic-smectic-solid triple point to occur at L/D=3.2, followed

by an isotropic-nematic-smectic point at $L/D=4$. The small disagreement between these numbers and our results may be due to the fact that their estimates are based on equations of state obtained by NPT Monte Carlo simulation of spherocylinders in a cubic box. It is known that the pressure of a smectic can become anisotropic in a cubic box, resulting in an increase of the free energy. Moreover, the free energy calculation method used here is in principle a more reliable method to obtain the phase boundary than examination of the equation of state. Yet, it should be stressed that a small error in the free energy will have a noticeable effect on the estimate of the phase boundaries.

The nematic to smectic phase transition appears to be first order even for $L/D > 5$. This is rather surprising as in previous simulations this nematic-smectic transition appeared to be continuous[26]. However, McGrother et al.[27] also found the nematic-smectic transition at $L/D=5$ to be first order, albeit with coexistence densities and pressures that are slightly different from ours. This minor difference is probably due to the fact that McGrother et al. did not use free energy calculations to locate the coexistence curves.

The reduced densities of the coexisting smectic and solid phases are $\rho^* \approx 0.66$ and $\rho^* \approx 0.68$ respectively. These densities depend only weakly on L/D and are effectively constant for L/D larger than 5. As the smectic-solid transition is closely related to the freezing of the quasi-two-dimensional liquid layers, it is interesting to compare the density where this transition takes place with the freezing density of hard disks. The quasi-2D in-layer density for the coexisting smectic and solid phases are $\rho_{2D,l}=0.789$ and $\rho_{2D,s}=0.83$, respectively. This should be compared to the most recent estimates of the solid-liquid coexistence of hard disks [108]: $\rho_{liq}=0.887$ and $\rho_{sol}=0.904$.

The rotator phase

5.5

Finite densities

5.5.1

A hexagonal crystal consisting of long rods will have a high orientational correlation as all rods are, on average, aligned. On the other hand, a solid of short spherocylinders will behave almost like a hard-sphere solid. In particular, the orientational distribution function will have cubic symmetry, approaching an isotropic distribution in the limit $L/D \rightarrow 0$. The orientationally ordered solid should (according to Landau theory [109]) be separated from the plastic solid by a first-order phase transition.

Usually, it is assumed that hard spheres form an *fcc* crystal structure. Near melting, it is known that the difference in stability of the *fcc* and *hcp* structures is very small [39]. In our simulations in the close packed limit (see next section) we found that the free energy difference between both crystal structures at close packing is less than 10^{-3} kT. In what follows, we will assume for the sake of convenience, that the stable solid structure is *fcc*, for hard spheres as well as spherocylinder systems.

We estimated the coexistence region between the aligned and rotator solids by measuring the equation of state for lengths $L/D = 0.01, 0.1, 0.2$ and 0.3 at high densities combined with free-energy calculations at these lengths. The equations of state were measured in MD simulations, as described in section 5.3.1 and are shown in figure 5.6. The free-energy of the aligned solid was calculated using thermodynamic integration as described in section 5.3.2.2. For the rotator phase, we found it more convenient to relate the free energy to that of a hard-sphere reference system. At a given density ρ , the free energy for a plastic

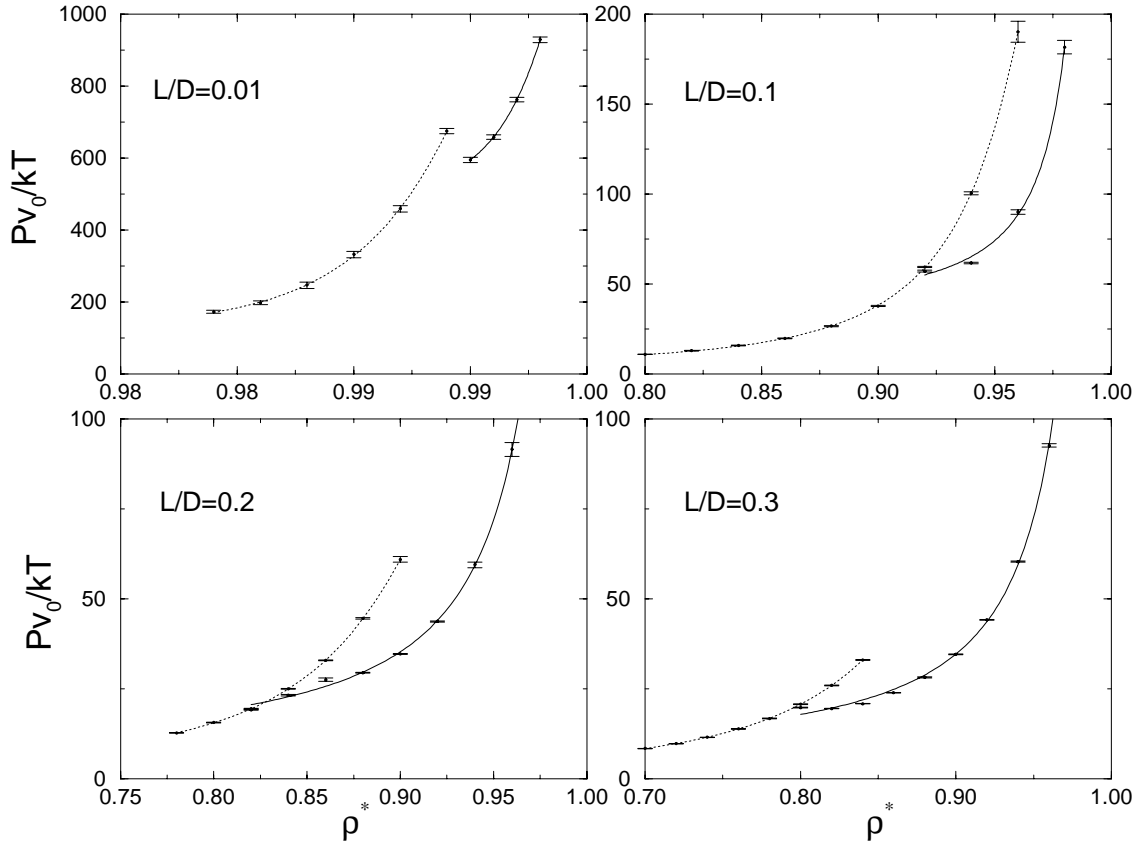


Figure 5.6. *Equations-of-state of the solid phases for $L/D = 0.01, 0.1, 0.2$ and 0.3 . The dotted curve was obtained by compression and the solid curve by expansion. The strong hysteresis is indicative of a first-order phase transition between the orientationally ordered solid and the rotator phase.*

crystal of rods with length L is given by eqn. 5.22

$$F(\rho, L) = F_{\text{HS}}(\rho, 0) + \int_0^L \kappa(\rho, L') dL'. \quad (5.29)$$

If we keep the reduced density constant, this changes into

$$F(\rho^*, L) = F_{\text{HS}}(\rho^*, 0) + \int_0^L dL' \left(\kappa(\rho^*, L') - \frac{\sqrt{3}}{2\rho^*} P(\rho^*, L') \right). \quad (5.30)$$

The free energy of the three dimensional hard-sphere solid F_{HS} is well known and can be accurately represented using the analytical form for the equation of state proposed by Hall [54] in combination with a reference free energy of a *fcc* crystal obtained by Frenkel and Ladd [39]. The equations of state are displayed in figure 5.6 and the results of the free energy calculation are given in table 5.8. Applying the double tangent construction results in table 5.9. It is clear that in the limit $L/D \rightarrow 0$ the plastic-ordered coexistence curve terminates at the density of regular close packing. As can be seen from figure 5.7, the densities of the coexisting solid phases appear to depend almost linearly on L/D . The solid curve in figure 5.7 is an estimate for the solid-solid coexistence curve obtained by

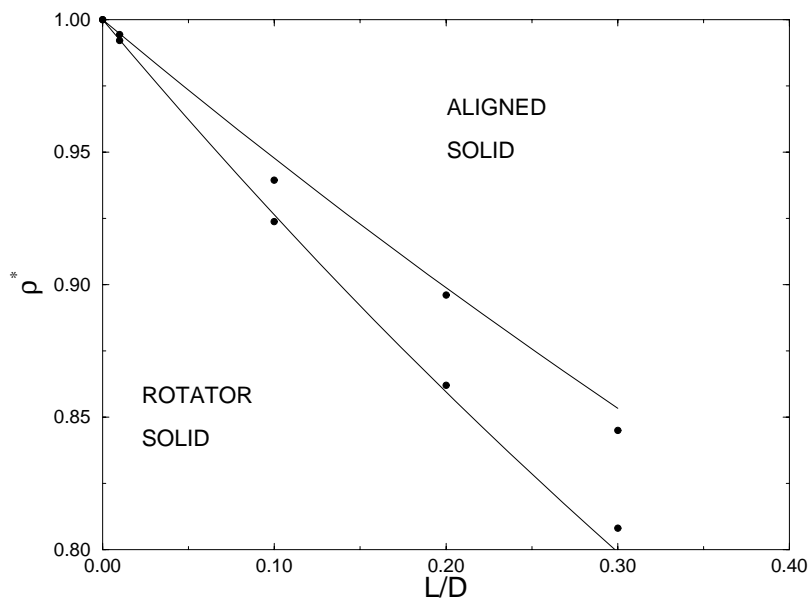
Table 5.8. Helmholtz free energy per particle for plastic and orientationally ordered phases with L/D between 0.01 and 0.3. The free energies are expressed in units of kT .

L/D	ρ_{plastic}^*	βF_{plastic}	ρ_{ordered}^*	βF_{ordered}
0.01	0.982	12.01	0.9959	20.422
0.10	0.8	3.91889	0.96	13.11
0.20	0.8	4.70662	0.9	9.52929
0.30	0.8	5.7323	0.9	10.1827

Table 5.9. Pressure and reduced densities of coexisting plastic and orientationally ordered solid phases for hard spherocylinders with aspect ratios L/D between 0 and 0.3. Units as in table 5.3.

L/D	Pv_0/kT	ρ_{plastic}^*	ρ_{ordered}^*
0	∞	1	1
0.01	1304.52	0.9921	0.99433
0.1	107.71	0.9237	0.9393
0.2	49.99	0.862	0.896
0.3	29.91	0.808	0.845

Figure 5.7. Coexistence curves for the plastic solid – orientationally ordered solid transition. The filled circles indicate the coexistence densities obtained by off-lattice simulations. The solid lines are the close-packing limit results discussed in section 5.5.2



extrapolation of the simulation data *at close packing*. The simulation technique used to study this limit will be discussed below.

Close packing limit

5.5.2

The rotator solid transition is expected to be first order even in the limit $\rho \rightarrow 1$ and $L/D \rightarrow 0$. We cannot access this region using ordinary simulation methods. However, somewhat surprisingly, it is possible to perform simulation in this limit and get useful information about the limiting behavior of the solid-solid transition.

To see how this is achieved, let us first consider the case where $\rho - \rho_{\text{cp}}$ and L/D are both small but finite. In the dense solid phase, the particles are constrained to move in the vicinity of their lattice positions and we can safely ignore diffusion. Therefore, we only have to take the deviations from the lattice positions into account. The overlap criterion of two

spherocylinders i and j is based on the shortest distance between the two cylinder axes with orientation \vec{u}_i and \vec{u}_j (see [77])

$$\vec{r}_{ij} = \vec{r}_{ij}^{cm} + \alpha \vec{u}_i - \beta \vec{u}_j, \quad (5.31)$$

where \vec{r}_{ij} is the shortest distance vector, \vec{r}_{ij}^{cm} is the center-of-mass separation of neighboring particles j and α and β are the distances along the axis of the two particles from the center of mass to the point of closest approach. In a dense solid, we can rewrite the center-of-mass separation as the vector sum of \vec{r}_{ij}^0 , the distance between the lattice positions of i and j , and $\vec{\Delta}_{ij}$, the difference of the vector displacements of particles i and j from their lattice positions. Hence,

$$\vec{r}_{ij} = \vec{r}_{ij}^0 + \vec{\Delta}_{ij} + \alpha \vec{u}_i - \beta \vec{u}_j. \quad (5.32)$$

It is important to realize that, in the limit $L/D \rightarrow 0$, all spherocylinder contacts will involve only the spherical end-caps. Moreover, near close packing, the relative particle displacements $\vec{\Delta}_{ij}$ will become negligible compared to the lattice vectors \vec{r}_{ij}^0 . In this limit, the vector distance of closest approach between two spherocylinders will therefore be parallel to the lattice vector \vec{r}_{ij}^0 . We need therefore only consider the component of \vec{r}_{ij} along the direction of \vec{r}_{ij}^0

It is most convenient to express the lattice vectors \vec{r}_{ij}^0 in terms of the unit vectors \hat{b}_{ij} that denote the directions of nearest neighbor bonds in the undistorted *fcc* lattice. In that lattice, the lattice vector \vec{r}_{ij}^0 can be written as

$$\vec{r}_{ij}^0(\text{fcc}) = D \hat{b}_{ij}.$$

In the close-packed spherocylinder crystal, the lattice is expanded along the [111]-axis by an amount $1 + (L/D)\sqrt{3/2}$. If we consider a crystal near (but not at) close packing, the crystal will expand in all three directions, but not necessarily isotropically. We assume that this expansion does not change the symmetry of the lattice – i.e. if we define the alignment direction of the spherocylinders (the [111] direction) to be the z -axis, then we assume that the expanded crystal can be generated from the close packed crystal by isotropic expansion in the xy -plane plus a (different) expansion along the z -axis. It is convenient to express the lattice vectors of the expanded lattice as follows

$$\vec{r}_{ij}^0 = \left(b_{x,ij}(D + a_x), b_{y,ij}(D + a_y), b_{z,ij}(D + a_z + L\sqrt{3/2}) \right). \quad (5.33)$$

Note that, as we consider the limit $L/D \rightarrow 0$ and $\rho^* \rightarrow 1$, L and a_x, a_y, a_z are much smaller than D . Because of the assumed symmetry in the xy -plane, $a_x = a_y \equiv a_{xy}$. We denote the average value of a_x, a_y and a_z by a . It is related to the expansion of the lattice

$$a \equiv \frac{2a_{xy} + a_z}{3D} = (\rho^*)^{-1/3} - 1. \quad (5.34)$$

If we define $\Delta \vec{u}_{ij} = \alpha \vec{u}_i - \beta \vec{u}_j$ the absolute shortest distance becomes

$$\begin{aligned} r_{ij}^s &= \vec{r}_{ij} \cdot \hat{b}_{ij} \\ &= D + a_{xy} + b_{z,ij}^2 (a_z + L\sqrt{3/2} - a_{xy}) + \hat{b}_{ij} \cdot (\vec{\Delta}_{ij} + \Delta \vec{u}_{ij}). \end{aligned} \quad (5.35)$$

As the spherocylinders can only touch with their spherical end-caps, the surface-to-surface distance is given by

$$\begin{aligned} s_{ij} &\equiv r_{ij}^s - D \\ &= a_{xy} + b_{z,ij}^2(a_z + L\sqrt{3/2} - a_{xy}) + \hat{\mathbf{b}}_{ij} \cdot \vec{\Delta}_{ij} + L/2(|\hat{\mathbf{b}}_{ij} \cdot \Delta \vec{\mathbf{u}}_i| + |\hat{\mathbf{b}}_{ij} \cdot \Delta \vec{\mathbf{u}}_j|), \end{aligned} \quad (5.36)$$

where, in the last line, we have used the values for α and β appropriate for the distance between spherical end-caps. The spherocylinder overlap criterion in the limit $\alpha \rightarrow 0$, $L/D \rightarrow 0$ is simply

$$s_{ij} < 0.$$

It turns out to be more convenient to express all distances in units of α . The density enters the problem through $x \equiv L/\alpha$. We can now perform a Monte Carlo simulation of this model by setting up an undistorted *fcc* lattice with unit nearest neighbor distances and move a randomly selected sphero-cylinder i from its initial scaled displacement $\vec{\Delta}_i$ and orientation $\vec{\mathbf{u}}_i$ to a trial displacement and orientation in such a way that microscopic reversibility is satisfied. We use the conventional Metropolis rule to accept or reject the trial move.

The system is anisotropic and we must allow box shape fluctuations to ensure equilibrium. In the simulation the box shape is determined by the ratio of a_{xy} and a_z . During trial moves that change the shape of the simulation box, the total volume should stay constant. Equation 5.34 then implies that the changes in a_{xy} and a_z are related by

$$2\Delta a_{xy} = -\Delta a_z. \quad (5.37)$$

The conventional Metropolis criterion is used to decide on the acceptance of shape-changing trial moves. To speed up equilibration, we also used Molecular Dynamics simulations of the close-packed spherocylinder model. The MD scheme that we use is essentially identical to the one used in off-lattice simulations[105, 106]. All the distances are scaled with a factor α . In the scaled space the new overlap criterion of eqn. 5.36 is used to locate colliding pairs. The virial expression for the pressure in the close-packing limit is

$$\begin{aligned} \frac{\beta P}{\rho} - 1 &= \frac{1 + \alpha}{3\alpha N} \sum_{i < j} \langle \vec{\mathbf{f}}_{ij} \cdot \hat{\mathbf{b}}_{ij} \rangle \\ &\equiv \frac{1 + \alpha}{\alpha} z(\rho), \end{aligned} \quad (5.38)$$

where $\vec{\mathbf{f}}_{ij}$ denotes the rate of momentum transfer between sphero-cylinders i and j and the last line defines the quantity $z(\rho)$ that is measured in the simulations. Simulations were performed both by compression from “low” density (i.e. low L/α) and by expansion from “high” density (high L/α). The free energy of both the rotator and the aligned phases were calculated by Einstein integration as discussed in the previous chapter. It should be noted that the free energies of both phases do in fact diverge at close packing. However the free energy *difference* is finite, and this is what we need to compute the phase coexistence.

In order to see how this can be achieved, consider the expression for the free energy of a (fixed center-of-mass) Einstein crystal in the limit of close packing. Every particle in the

hard-spherocylinder crystal is confined to move within a cell with average radius a . We wish to switch on an Einstein spring constant that is sufficiently large to suppress hard-core overlaps. This can only be achieved if the spring-constant μ_{\max} in eqn. 5.5 is of order $1/a^2$. Hence, we expect $\mu_{\max}a^2$ to be finite. It is therefore convenient to write the free energy of the Einstein crystal as follows

$$\beta F_{\text{ein}} = \frac{3}{2} \ln N - \frac{3}{2}(N-1) \ln \frac{\pi}{\beta \mu_{\text{sc}}} - N \ln \frac{2\pi}{\beta \lambda} - 3(N-1) \ln a, \quad (5.39)$$

where we have defined μ_{sc} as $a^2\mu$. Note that λ , the ‘‘orientational’’ spring constant remains finite. The expression for the free energy of the spherocylinder crystal (eqn. 5.4) now becomes

$$\begin{aligned} \frac{\beta F(L/a)}{N} + \frac{3(N-1)}{N} \ln a = & \frac{3}{2N} \ln N - \frac{3}{2}(N-1) \ln \frac{\pi}{\beta \mu_{\max, \text{sc}}} - N \ln \frac{2\pi}{\beta \lambda_{\max}} \\ & - \frac{\ln V}{N} - \int_0^{\mu_{\max, \text{sc}}} d\mu_{\text{sc}} \left\langle \frac{\Delta r^2}{a^2} \right\rangle_{\mu_{\text{sc}}} - \int_0^{\lambda_{\max}} d\lambda \left\langle \sin^2 \theta \right\rangle_{\lambda}. \end{aligned} \quad (5.40)$$

The computational scheme is essentially the same as with the conventional Einstein crystal method. The main difference is that all displacements in eqn. 5.40 are expressed in units of a . The scaled coupling constant $\lambda_{\max, \text{sc}}$ remains finite. All divergences are now contained in the $3(N-1)/N \ln a$ term. When searching for the point of phase coexistence, we need to be able to compute the variation of the free energy with density. The free energy at any value of $x = L/a$ is obtained by thermodynamic integration starting from the density ρ_0 where the direct free-energy calculation has been performed

$$\beta F(\rho) = \beta F(\rho_0) + \int_{\rho_0}^{\rho} \frac{\beta P(\rho')}{\rho'^2} d\rho'. \quad (5.41)$$

It is more convenient to change to the integration variable $x \equiv L/a$, which is related to the density through $x = L/(\rho^{*-1/3} - 1)$. In the MD simulations we do not measure the pressure $P(x)$ but rather $z(x)$ (see eqn. 5.38). The variation of the Helmholtz free energy with x can be written as

$$\beta F(x)/N = \beta F(x_0)/N + 3 \int_{x_0}^x \frac{z(x')}{x'} dx'. \quad (5.42)$$

At coexistence the pressure in both phases is equal. Using eqn. 5.38 and $x \equiv L/a$, it is straightforward to show that the condition $P_1 = P_2$ can be written as

$$\frac{1 + (x_1/L)z(x_1)(1 + L/x_1)}{(1 + L/x_1)^3} = \frac{1 + (x_2/L)z(x_2)(1 + L/x_2)}{(1 + L/x_2)^3}.$$

To leading order in $1/L$ this implies that

$$x_1 z(x_1) = x_2 z(x_2). \quad (5.43)$$

The chemical potential is given by

$$\beta \mu(x) = \beta F(x)/N + \frac{\beta P(x)}{\rho}. \quad (5.44)$$

The condition for equilibrium, $\mu_1 = \mu_2$ corresponds to

$$\beta F(x_1)/N + \beta \rho_0 P(x_1)(1 + L/x_1)^3 = \beta F(x_2)/N + \beta \rho_0 P(x_2)(1 + L/x_2)^3. \quad (5.45)$$

All terms in this equation diverge in the close-packing limit. However, all differences remain finite. This is immediately obvious for the terms involving the pressure as, at coexistence, $P(x_1) = P(x_2)$. We recall that the free energy diverges as

$$-3 \frac{N-1}{N} \ln a = -3 \frac{N-1}{N} (\ln L - \ln x).$$

We can therefore write the Helmholtz free energy of the crystal as a non-diverging part $F_r(x)$, where the subscript r stands for *regular*, and the diverging remainder

$$\beta F(x)/N \equiv \beta F_r(x)/N - 3 \frac{N-1}{N} (\ln L - \ln x).$$

The condition for the equality of the chemical potential now becomes

$$\beta F_r(x_1)/N + 3 \frac{N-1}{N} \ln x_1 + 3z(x_1) = \beta F_r(x_2)/N + 3 \frac{N-1}{N} \ln x_2 + 3z(x_2), \quad (5.46)$$

where we have dropped the terms that cancel on the left and right hand side and where we have ignored terms that vanish in the limit $a \rightarrow 0$.

Figure 5.8 shows the “equation of state” $xz(x)$ for the dense plastic crystal and ordered solid. The free energies of the reference systems are given in table 5.10. The coexistence values of x , pressure and chemical potential that follow from equations 5.43 and 5.46 are

$$\begin{aligned} x_{\text{rot}} &= 3.86317 \\ x_{\text{sol}} &= 5.52543 \\ xz(x) &= 9.77835 \\ \beta\mu_r &= 10.7092, \end{aligned} \quad (5.47)$$

Figure 5.8. Scaled equations of state for hard spherocylinder solids in the limit $a \rightarrow 0, L \rightarrow 0$ (see eqn. 5.43). The dotted curve denotes a compression and the solid curve corresponds to an expansion

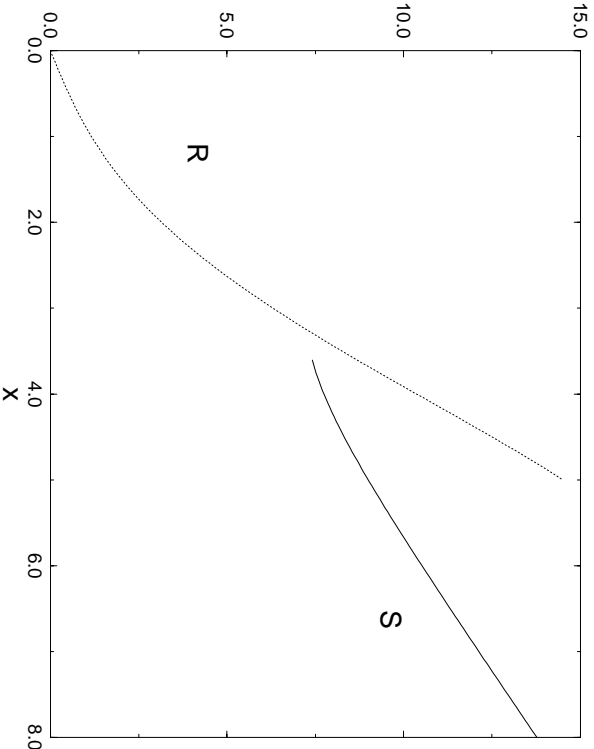


Table 5.10. *Regular part of the Helmholtz free energy per particle in the close packed limit. The values have been obtained by Einstein integration.*

x	$\beta F_r(x)$
0.5	-3.800
1.0	-1.076
5.0	0.0394
6.0	0.400
7.3	0.833
12	1.908

where μ_r , is the regular part of the chemical potential, given by eqn. 5.46. As x is defined as the ratio of L and a , eqn. 5.47 describes the initial (small L) dependence of the plastic-ordered transition on the spherocylinder length. As presented, a given value of x corresponds to a slope of the coexistence curve in the L, a plane. However, by using the definition of x ,

$$\rho^* = \frac{1}{\left(\frac{L}{x} + 1\right)^3}, \quad (5.48)$$

every value of x corresponds to a curve in the ρ^*, L plane. The resulting solid-solid coexistence curves are plotted in figure 5.7. It is interesting to note that, even at L/D as large as 0.3, the slope of rotator-solid coexistence curve is still dominated by the behavior at close packing

5.6 Phase diagram in the $L/D = 5-60$ region

5.6.1 Numerical Techniques

The numerical study of the spherocylinder phase diagram for systems of longer rods is not different in principle from the study for shorter rods. However, in practice, there are many differences. Almost all these differences imply that simulations of longer rods are more time consuming. For one thing, the simulation of long rods requires large system sizes. The simulation box should be large enough to accommodate at least two rod lengths in

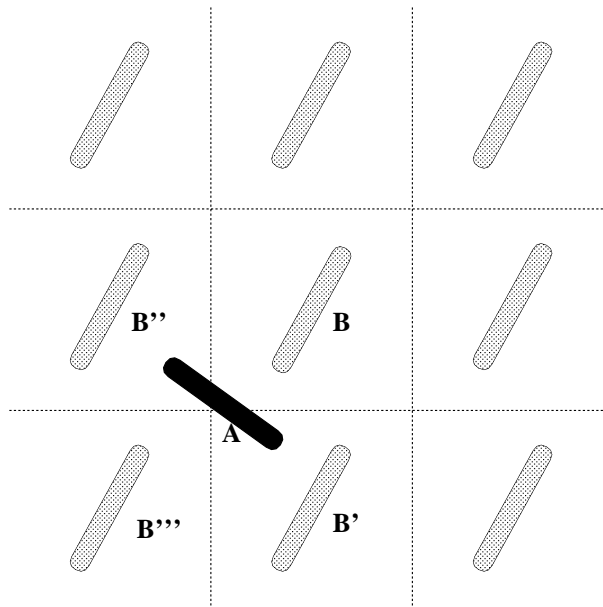


Figure 5.9. *Situation sketch in 2D for multiple overlap check. Particle A cannot overlap with a periodic image of B if the cylinder axis is outside a periodic image of the box, as indicated by the dotted lines. In principle, A could overlap with B, B' and B''. These images have to be checked, whereas all others can be ignored.*

order to avoid the situation that one particle can, at the same time, overlap with more than one periodic image of another particle. The number of particles required at a given density scales with L^3 whereas the number density at the I-N transition is expected to scale as $1/L^2$. In practice, it turns out that if we wish to impose the condition that the box diameter is larger than $2L$, then for $L/D=50$ at the isotropic-nematic transition, one needs at least 3000 particles. The disadvantage of using such a large number of particles is that the simulations become very slow and, as a consequence, the statistical accuracy tends to be poor. We therefore decided to work with somewhat smaller systems where multiple overlaps, although rare, are not completely excluded. Of course, this implies that we must now also test for overlap with more than one periodic image. The possibility of two simultaneous overlaps with the same particle is taken into account by doing three independent overlap tests. Usually, the pair overlap test routine selects a first particle, looks for the nearest periodic image of the second particle with respect to the first one and calculates shortest distance between the pair. There is an overlap if this distance is smaller than D . If the box is smaller than $2L$ more than one overlap is possible, but not more than two. Figure 5.9 illustrates this. In principle, particle A could overlap with B and its periodic images B' and B'' , but it cannot overlap with any of the other periodic images at the same time provided the box length is larger than $L+2D$. For instance, A cannot overlap with B''' if the cylinder axis of A does not enter the periodic image of the box containing B''' . We devised an overlap routine which looks for the three images B, B' and B'' and check those for overlap in the usual way. This routine is applicable to both MD and MC, including Gibbs-ensemble MC. Although this routine seems more time-consuming because it has to check for three overlaps instead of one, it is still preferable to perform an overlap test for several periodic images than to perform all simulations for a larger system. In the region $L/D=15$ to 50 the isotropic-nematic transition was studied both by Gibbs ensemble simulation [31–33] and Gibbs-Duhem integration [84].

We started with an $L/D=40$ isotropic random configuration at low density and a perfectly aligned configuration at high density. Using Gibbs ensemble MC these configurations were equilibrated to coexistence. This coexistence was used to perform a quick standard Gibbs-Duhem integration in the range $L/D=15-50$ to obtain an initial estimate for the coexistence curve. Subsequently, we used this set of configurations to start the “parallel” Gibbs-Duhem technique described in section 5.3.3. This calculation was continued until the coexistence curve had fully converged. As a check, Gibbs ensemble MC simulation were also performed for $L/D= 20, 30, 50$ and 60.

Table 5.11. *Pressure and densities of coexisting isotropic and nematic phases for hard spherocylinders with aspect ratios L/D between 15 and 50. The coexistence data in this table were obtained using the modified Gibbs-Duhem integration procedure described in the text. Units as in table 5.3.*

L/D	Pv_0/kT	ρ_I^*	ρ_N^*
15.00	0.0970	0.1978	0.2291
20.00	0.0516	0.1548	0.1902
25.00	0.0322	0.1271	0.1565
30.00	0.0220	0.1044	0.1252
35.00	0.0159	0.0919	0.1101
40.00	0.0120	0.0819	0.1043
45.00	0.0093	0.0737	0.0840
50.00	0.0072	0.0673	0.0825

Figure 5.10. *Isotropic-nematic transition in a system of hard spherocylinders with aspect ratio L/D between 15 and 60. The drawn curves have been obtained by modified Gibbs-Duhem integration. The open circles denote the results of Gibbs-ensemble simulations (see text)*

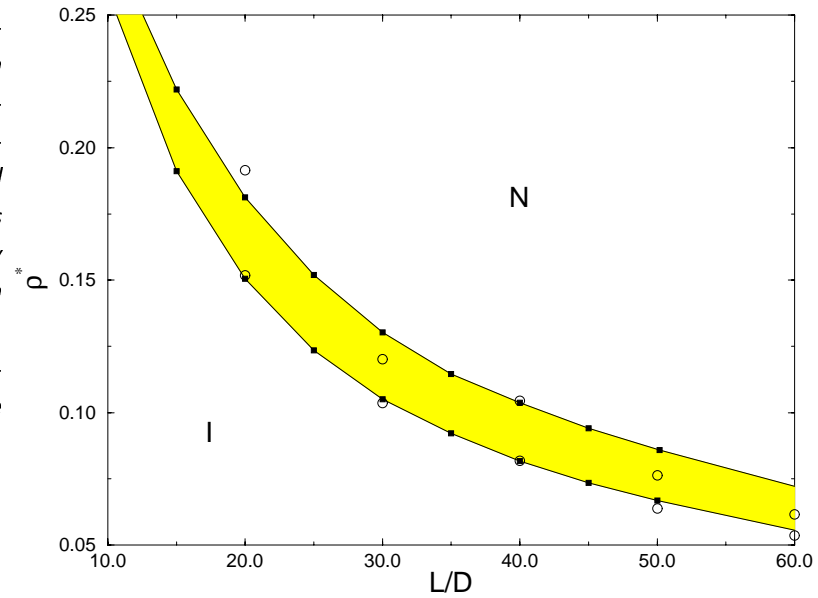


Figure 5.11. *Isotropic-nematic transition of spherocylinders in the large L/D -limit. In order to facilitate comparison with the Onsager limit, all densities are expressed in units $c = \frac{1}{4}\pi L^2 D \rho$. On the x-axis, we plot D/L rather than L/D . Hence, the Onsager limit corresponds to the value $D/L=0$. Note that our simulation results approach smoothly towards the exact solution of the Onsager model, except for a few points at low D/L .*

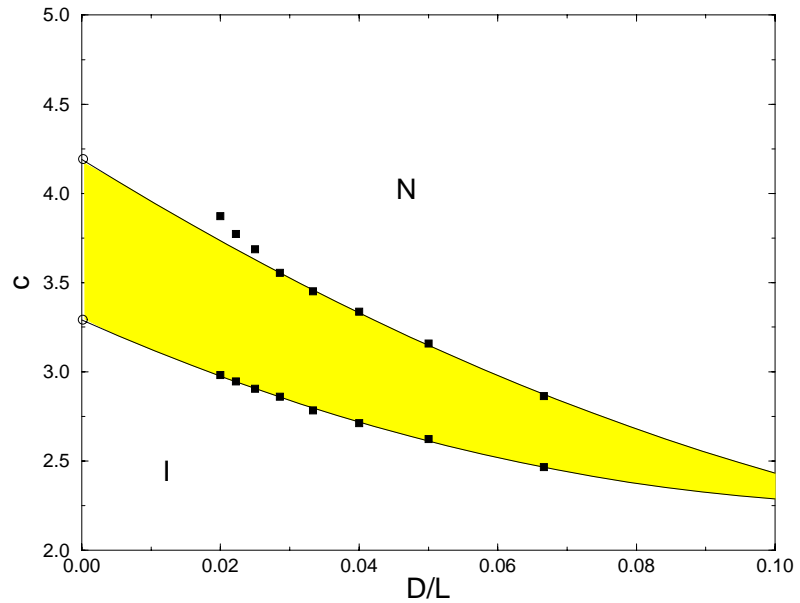
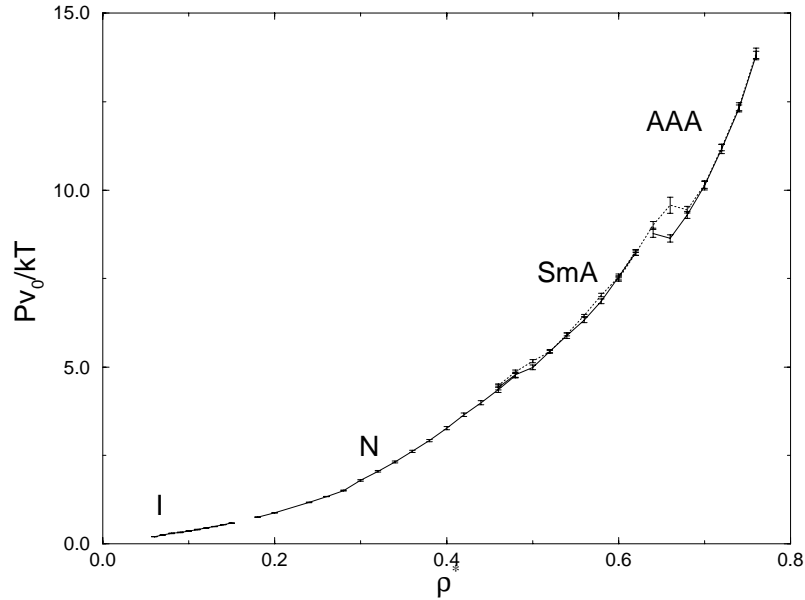


Table 5.12. *Pressure and densities of coexisting isotropic and nematic phases for hard spherocylinders with aspect ratios L/D between 15 and 50. The coexistence data in this table were obtained using Gibbs-ensemble simulations. Units as in table 5.3.*

L/D	Pv_0/kT	ρ_{iso}^*	ρ_{nem}^*
20	0.03763	0.1518	0.1915
30	0.02495	0.1036	0.1201
40	0.01263	0.0818	0.1044
50	0.00582	0.0638	0.0763
60	0.00328	0.0535	0.0615

Figure 5.12. Equation of state for spherocylinders with aspect ratio $L/D=40$. The dashed curves correspond to a compression whereas the solid curves denote an expansion. The different mechanically stable phases are indicated. All units as in figure 5.4.



Results

5.6.2

The results of the Gibbs-Duhem integration of the long rods are shown in table 5.11 and the coexistence densities are plotted in figure 5.10. The Gibbs ensemble results are displayed in table 5.12. As can be seen, the results of both methods agree quite well.

In figure 5.11 we have re-plotted the phase diagram in a way that makes comparison with the Onsager limit easier. In particular, we now use as our density variable

$$c \equiv \rho B_2 = \frac{1}{4} \pi L^2 D \rho.$$

In these units the coexistence densities remain finite in the Onsager limit $L/D \rightarrow \infty$. In order to facilitate the extrapolation to the Onsager limit, we use D/L rather than L/D as the variable characterizing the aspect ratio of the rods. Figure 5.11 shows that the I-N coexistence curves extrapolate nicely to the Onsager limit at $c_{iso}=3.29$ and $c_{nem}=4.19$ [110], except for a few points on the nematic coexistence curve at high L/D . Apparently, at these high lengths it is difficult to equilibrate the nematic phase completely. It is clear from figure 5.11 that already for rods with an aspect ratio less than $L/D=20$ (or $D/L > 0.05$), the Onsager limit dominates the phase behavior. This result is not at all obvious as, for rods with this length, the Onsager assumption that all higher virial coefficients are negligible is not yet satisfied [111]. Yet, we cannot rule out the possibility that the discrepancy at higher L/D (lower D/L) is an effect of higher virial coefficients. The agreement at lower L/D values should then be attributed to a fortuitous cancellation of errors.

Of course, the nematic to smectic and smectic to solid transition are more difficult to study, because they occur at higher density. This has two consequences: first of all, higher density means more particles in a box of a given (minimum) size, and secondly equilibration at high densities is slower. For $L/D=40$ the equation-of-state is plotted in figure 5.12. We estimate that the reduced densities of the coexisting smectic and solid phases are $\rho^*=0.66$ and $\rho^*=0.68$ respectively. The nematic-smectic transition is estimated to take place at about $\rho^*=0.5$. However, it is difficult to locate this transition accurately, as the smectic fluctuations in the nematic phase decay extremely slowly, even at lower densities.

Poniewierski [112] has studied the nematic to smectic transition in the Onsager limit using bifurcation analysis. He found that the bifurcation point of the nematic-smectic transition is located at $\rho LD^2=0.531$ which corresponds to a reduced density $\rho^*=0.46$. This agrees with the decreasing trend in the transition density if one goes from $L/D=5$ to $L/D=40$. However, it also shows that the N-SmA transition for $L/D=40$ is significantly different from the transition at $L/D \rightarrow \infty$.

In figure 5.2 we have combined our results for the phase behavior at large L/D values with the low L/D phase diagram discussed before. In order to give equal emphasis to all parts of the phase diagram, we have plotted the figure in the $\rho^*, \log(L/D + 1)$ plane.

5.6.3 The AAA crystal phase

For lengths larger than approximately 7 a hexagonal crystal phase develops between the smectic and ABC-stacked solid phase. This crystal phase is characterized by hexagonally ordered layers which are stacked in an 'AAA' fashion. That is, a particle's hemisphere is right above the end-cap of a particle in the layer below it. In contrast, an *fcc* crystal is stacked in an 'ABC' manner, with the particles end-caps in one layer shifted with respect to the next layer (see figure 5.13). The 'AAA' crystal is more stable than the ABC crystal because the particles have a larger free volume. If they move along the *z*-direction they will on average only hit the particle right above or below. In the ABC stacking the number of interactions much larger, because the layer are shifted in position with respect to each other. At higher densities, the end-caps of particles in neighboring layers start to feel each other and the AAA stacked crystal will transform again to the ABC stacking. A rough but simple estimate for the AAA-ABC transition density can be made as follows. The reduced density of a crystal can be written in terms of the expansion from a close packed crystal

$$\rho^* = \frac{1}{(1 + \alpha_z)(1 + \alpha_{xy})^2}, \quad (5.49)$$

where $\alpha_z + 1$ is the expansion of the lattice in the *z*-direction starting whereas $\alpha_{xy} + 1$ is the expansion in the *xy*-plane. Because the particles are uniaxial, the expansion in the *x* and *y* plane are equal (compare section 5.5.2). The *z*-direction expansion has in general a different value. From simulation results we can deduce that $\alpha_{xy} \approx 2\alpha_z$. Further, the expansion $1 + \alpha_z$ can be expressed as the ratio of the real box length and the close packed

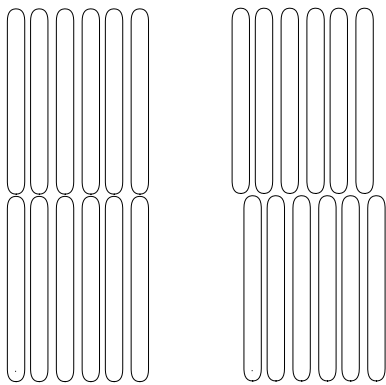


Figure 5.13. *Cartoon of the major difference between the AAA and the ABC stacking. Left: In the AAA stacking every particle is right on top of a particle in the layer below. Right: In the ABC stacking the layers are shifted.*

crystal box length in the z -direction.

$$1 + \alpha_z = \frac{\Delta/D + L/D}{L/D + \sqrt{\frac{2}{3}}} = \frac{\Delta/D - \sqrt{\frac{2}{3}}}{L/D + \sqrt{\frac{2}{3}}} + 1. \quad (5.50)$$

Here Δ is the interlayer spacing. We assume that the AAA-ABC transition takes place when the distance between layers Δ is of the order of the diameter D . At that moment the end-caps definitely start to feel each other and an ABC stacking is more favorable. This results in an estimate for the reduced transition density

$$\rho^{*-1} \approx \left(1 + 2 \frac{1 - \sqrt{\frac{2}{3}}}{L/D + \sqrt{\frac{2}{3}}}\right)^2 \left(1 + \frac{1 - \sqrt{\frac{2}{3}}}{L/D + \sqrt{\frac{2}{3}}}\right). \quad (5.51)$$

This density is plotted in figure 5.2. We could also estimate the AAA-ABC transition for $L/D=10$ and $L/D=20$ from the equations of state in the crystal state. These values are indicated as well in figure 5.2. The agreement is reasonably good and suggests that the argument of the hemispheres and the layer spacing is qualitatively correct.

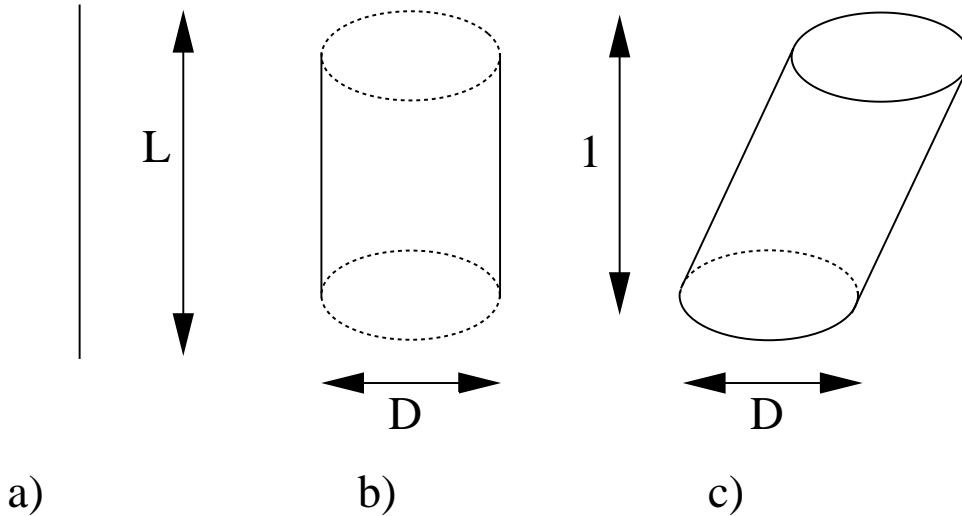


Figure 5.14. *Scaling of the spherocylinder if $L/D \rightarrow \infty$. a) shows a spherocylinder with finite L and zero D , the tilt angle goes as D/L . b) is a blown up part of length 1 of spherocylinder a on the scale of diameter D . The cylinder part still looks completely parallel to the z -axis because the tilt angle is vanishing. c) Scaled particle. The particle is scaled by a factor L along the z -axis. The hemispheres have vanished, so the upper and lower plane of the cylinder is flat and perpendicular to the z -axis. The particle is a shifted cylinder because the total displacement of the unscaled spherocylinder $L \sin \theta \sim L \sin(1/L) \approx 1$, although zero on the L scale, is not zero on the D scale.*

5.7 The Onsager limit

5.7.1 Scaling

As we saw in the previous section, spherocylinders with $L/D=40$ are too small to compare properly with the bifurcation results of Poniewierski for $L/D \rightarrow \infty$ and so it would be interesting to simulate a system of spherocylinders in this limit. At first sight this seems impossible because in general the system size scales with L^3 . However, at finite reduced density ρ^* , i.e. not in the isotropic phase or low ρ^* nematic phase, the average angle θ that a particle makes with the director scales as $1/L$, which means that the particles are (almost) completely aligned. In this regime, we can bring the volume down to finite sizes by scaling the system along the director (chosen to be along the z -axis) with a factor L . This will change the shape of the particle from a spherocylinder to a shifted cylinder of height 1 and diameter D (see figure 5.14). The height of the cylinder is always 1 because the angle $\theta \propto 1/L$ and the difference in height $1 - \cos(1/L) \approx 1/L^2$ vanishes as $L/D \rightarrow \infty$. The shift of the cylinder in the xy plane perpendicular to the director is finite because it is given by $L \sin \theta = \mathcal{O}(D)$ in the limit $L/D \rightarrow \infty$. The top and bottom end of the cylinder are flat and always perpendicular to the director. The hemispheres of the spherocylinder have completely disappeared by the scaling procedure.

Because the shape of the particle is different from a spherocylinder we need a new overlap criterion. This is given by the shortest distance between two particle axes in the xy plane. In the xy plane a cut through the cylinder results in a circle of diameter D . Therefore, if the shortest distance is smaller than the diameter D , an overlap will occur.

Scaling of the box in this particular way will not effect the reduced density because the close packing density will scale in the same way as the number density. The pressure will be multiplied by a factor L , whereas P/ρ remains unaffected by the scaling. We can therefore measure the equation of state of the Onsager limit system in the normal NPT ensemble.

Because the particles are free to shift any arbitrary amount in the xy plane it is convenient to keep the nematic director always along the z -axis. This can be achieved by starting with a complete aligned system and shift two particles with the same amount in opposite direction at every MC trial move. In order to avoid multiple overlaps, shifts larger than half the box-length are forbidden. Standard MC trial moves were not very effective in reproducing the collective motion of tilted layers. In the smectic phase, we therefore allowed for two neighboring layers to tilt collectively by equal but opposite amounts, so that the constraint of a constant director is satisfied.

5.7.2 Results

We prepared a system of 600 cylinders at $\rho^*=0.8$ in an ABC stacking and performed onsager NPT simulations, first expanding to lower densities and subsequently compressing. The equation of state of spherocylinders in the limit $L/D \rightarrow \infty$ is shown in figure 5.15. There is no isotropic phase at finite reduced densities because the I-N transition has shifted down to $\rho^*=0$. Therefore, at all reduced densities below $\rho^* \approx 0.47$ the nematic phase is stable. The nematic to smectic transition is estimated to take place at $\rho^* \approx 0.47$. This is in agreement with the predictions of Poniewierski who located the N-S transition at $\rho^*=0.46$ using bifurcation analysis [112].

At higher density the smectic phase will be thermodynamically stable, until at $\rho^* \approx 0.66$ the system crystallizes in an AAA stacking. This transition is first order as is clear from the

strong hysteresis at $\rho^* \approx 0.66$ in figure 5.15. The system prefers an AAA stacking because the particles are hindered by fewer particles in the neighboring layers than in an AB or ABC stacking and hence have more entropy. The AAA phase will undergo a transition to an ABC crystal only at close packing, because the ABC stacked lattice will be stabilized only if the distance between layers is of the order of D . At that point the particles start to feel the hemispheres of the particles in the neighboring layers. Because $D/L = 0$ this can only happen at close packing densities.

We also found evidence for a columnar structure between the smectic and the AAA phase. This columnar phase appeared meta-stable with respect to the AAA crystal.

What is the order of the nematic-smectic transition?

5.7.3

It is usually assumed that the nematic to smectic transition in the Onsager limit is continuous. However, there is no hard (theoretical) evidence to support this conjecture. On the contrary, although Poniewierski performed his theoretical analysis assuming a continuous N-S transition, he pointed out that a (weak) coupling between orientation and translational degrees of freedom would make the transition first order [112].

We tried to determine the order of the nematic to smectic transition numerically. The results appear to depend on the type of periodic boundaries used in the simulations. In the case of normal periodic boundaries, we found evidence for a first-order N-S transition, whereas by applying shifted periodic boundary conditions as described in section 5.3.2.3 the transition becomes continuous.

Normal periodic boundaries

5.7.3.1

The hysteresis at densities around $\rho^* = 0.5$ between the compression and expansion branch in figure 5.15 is an indication for a first order N-S transition. When we consider the nematic order parameter of the system, this hysteresis becomes even more clear. In the

Figure 5.15. *Equations-of-state of the spherocylinder system in the limit $L/D \rightarrow \infty$. The solid lines are expansion branches, the dotted lines are compression curves. The hysteresis around $\rho^* = 0.5$ is suggestive of a first-order nematic to smectic phase transition.*

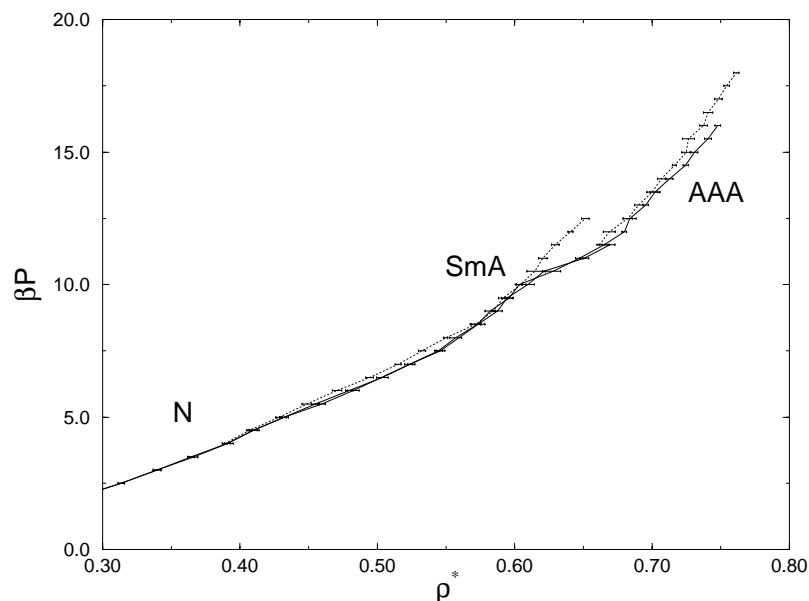
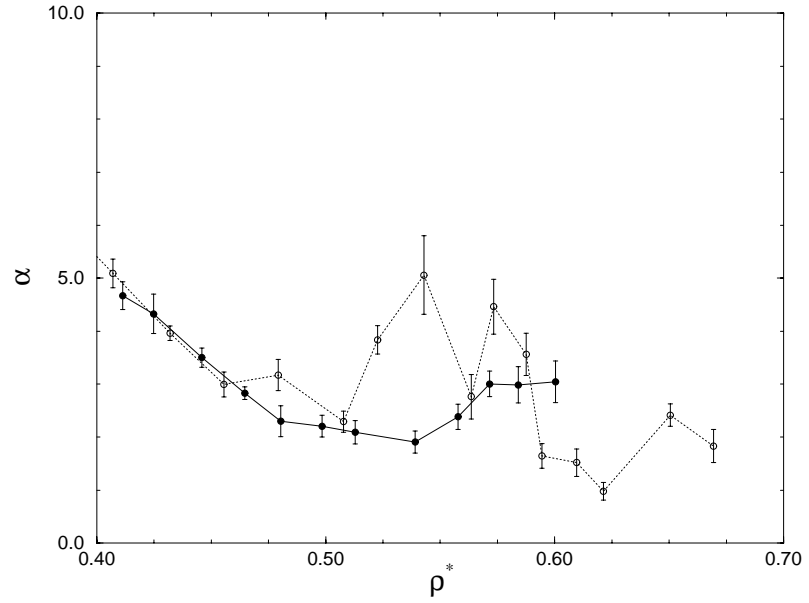


Figure 5.16. *The measure for nematic order α in an Onsager spherocylinder system as a function of reduced density ρ for a compression from the nematic (filled circles) and a expansion from the smectic phase (open circles). Note the clear hysteresis.*



limit $L/D \rightarrow \infty$ the nematic order parameter can be written to leading order in D/L as

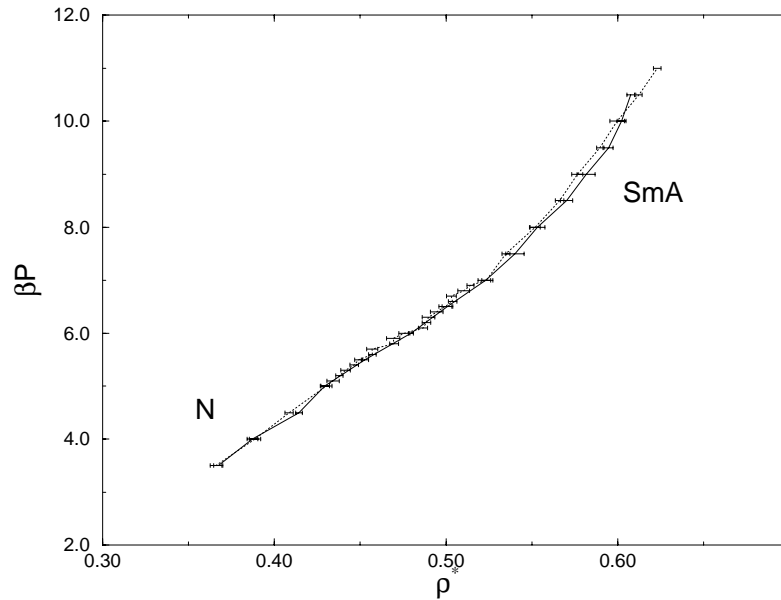
$$S = 1 - \langle \sin^2 \theta \rangle = 1 - \langle u_x^2 + u_y^2 \rangle \frac{D^2}{L^2} \equiv 1 - \alpha \frac{D^2}{L^2}, \quad (5.52)$$

where θ is the angle the particles make with the director and the latter equation defines α as the mean square shift of the cylinders. In figure 5.16 we plotted the measured value of α as a function of the reduced density for both the compression and expansion branches. The most remarkable feature is that near the transition α is larger in the smectic phase than in the nematic. This corresponds to a more orientational ordered nematic at lower densities and a less ordered smectic at higher density. There is a competition between translational and orientational entropy. In the nematic phase the translational entropy is large but the rods are restricted in their rotations. On the other hand, in the smectic phase, the layering increases the orientational entropy, which manifests itself as herringbone fluctuations of the smectic layers. Figure 5.16 also clearly shows the hysteresis between the compression and expansion branches. The compression from the nematic phase shows only increasing disorder for $\rho^* > 0.54$ whereas α in the case of the expansion from the smectic drops to low value below $\rho = 0.5$. The two examples of hysteresis given above suggests that we have a first order transition. However, as before, only free energy calculations can locate the exact transition. We performed free energy difference calculations as described in section 5.3.2.4 to estimate the free energy difference between an nematic Onsager system at $\rho^* = 0.4$ and a smectic at $\rho^* = 0.5$. Those calculations did not result in reasonable values for the nematic smectic coexistence densities.

5.7.3.2 Shifted periodic boundaries

The transition could be second order and the hysteresis might be due to a slow relaxation to the equilibrium state. The rate of relaxation is determined by the exchange of molecules between the smectic layers during compression from the nematic phase. This diffusion becomes inefficient at higher pressure. To circumvent this problem we have applied the

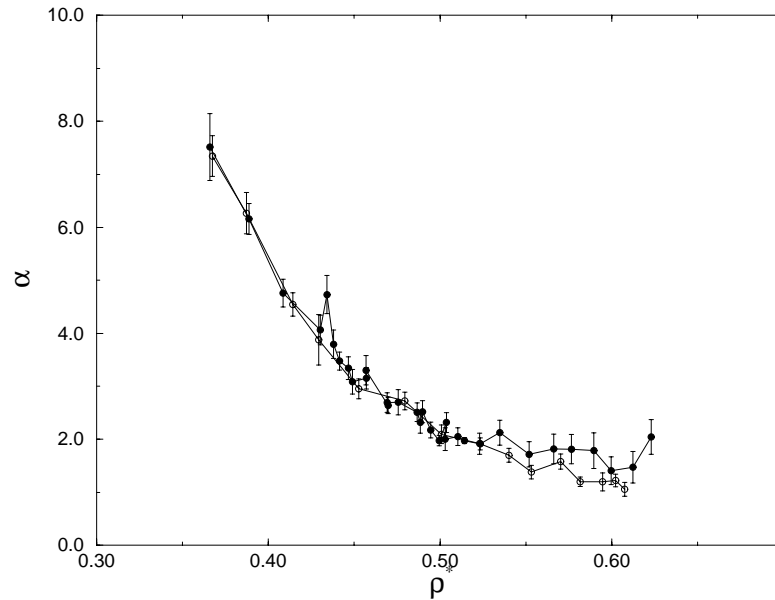
Figure 5.17. *Equations-of-state around the nematic to smectic transition of the spherocylinder system in the limit $L/D \rightarrow \infty$. The solid line is the equation-of-state for the expansion from a smectic, the dotted line is the compression curve started from the nematic. The hysteresis has disappeared due to the use of shifted periodic boundaries.*



shifted periodic boundary conditions to the Onsager system (see section 5.3.2.3) and determined the compression and expansion curves again. The results are plotted in figure 5.17. These equations of state seem to indicate that the nematic smectic transition is continuous in the Onsager limit. The continuity also follows from figure 5.18 where α , our measure for nematic order, is plotted against the reduced density.

However, the shifted periodic boundaries suppress the the herringbone structured smectic fluctuations phase and inclusion of these fluctuations could make the transition (weakly) first order again.

Figure 5.18. *The measure for nematic order α in an onsager spherocylinder system as a function of reduced density ρ for a compression from the nematic (filled circles) and a expansion from the smectic phase (open circles). The hysteresis has disappeared due to the use of shifted periodic boundaries.*



In short, we cannot establish with certainty the order of the N-S transition in the limit $L/D \rightarrow \infty$. To establish the nature of the transition, a full finite size scaling analysis is required. As the shifted periodic boundary conditions simulation offer better statistics, we tend to believe that the N-S transition is continuous. Since the transition is clearly first

order for $L/D=5$ there should be a tricritical point at intermediate L/D . This tricritical point has been the subject of theoretical studies. In refs. [102, 103] is estimated that the tricritical point corresponds to $L/D \approx 5$ while the theoretical analysis in ref [104] suggest that it should occur at $L/D=50$. The first prediction is clearly incompatible with our simulation results and those of ref [27]

5.8 Conclusion

In summary, we have mapped out the spherocylinder phase diagram over a wide range of densities and L/D values, such that it was possible to establish the link with the hard-sphere phase diagram for small L/D and with the Onsager limit for $L/D \rightarrow \infty$. We find that the liquid crystalline nematic phase is stable from about $L/D \approx 3.5$. The isotropic nematic coexistence decreases as a function of L/D and follows the Onsager theory in the $L \rightarrow \infty$ limit.

The smectic phase becomes stable at $L/D \approx 3.1$. The isotropic-smectic and later on the nematic-smectic transition starts off as a strong first-order transition for $L/D > 3.5$. The density jump becomes smaller at higher L/D . For $L/D \approx 7$ the AAA stacked crystalline phase becomes stable. The AAA-ABC transition was found to be first order. The transition density increases with L/D and reaches close packing in the Onsager limit. Between

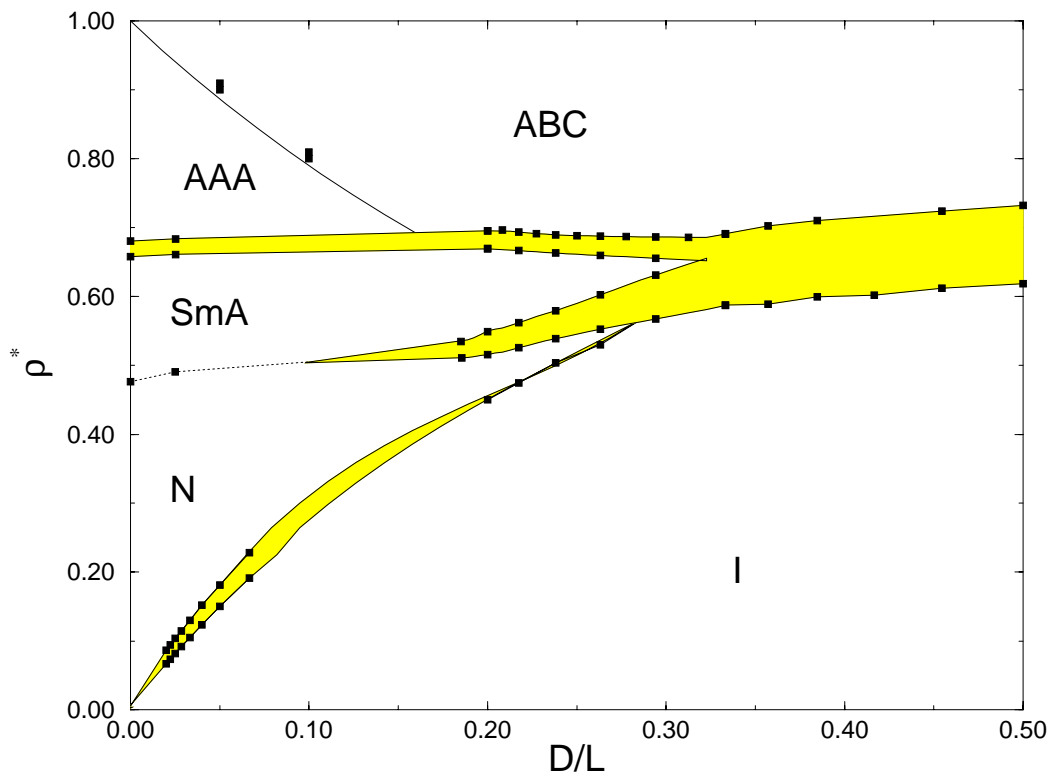


Figure 5.19. The phase diagram of hard spherocylinders plotted as a function of D/L . In this way we can establish the link between the finite length region and the Onsager limit at $D/L = 0$.

$L/D=4$ and $L/D = \infty$ the first order smectic-solid transition is located at the almost constant reduced densities $\rho_{\text{smect}}^*=0.66$ and $\rho_{\text{solid}}^*=0.68$. We determined the phase behavior of spherocylinders in the Onsager limit and estimated the location of nematic to smectic phase at $\rho^*=0.47$ which in agreement with the predicted value of $\rho^*=0.46$. In order to establish the link between the Onsager limit and the phase behavior for finite spherocylinders we plotted in figure 5.19 the phase diagram as a function of D/L .

The rotator to solid phase transition at low L/D was calculated and appeared to be strongly dominated by the behavior in the close-packed limit.

In the calculations we used three non-standard simulation techniques:

- The Gibbs-Duhem integration method of Kofke was modified to compute the L/D -dependence of phase-coexistence curves.
- The plastic-rotator transition was investigated in the close packing limit by mapping the system onto a special lattice model.
- The Onsager limit was studied by scaling the infinitely long particles to finite length.

The phase behavior we described in this chapter will considerably change for spherocylinders with an attractive potential. In the next chapter, we will study the effects of adding polymer to system of rodlike colloidal particles.

MIXTURES OF SPHEROCYLINDERS AND POLYMERS

6

We examine the influence of free non-adsorbing polymer on the phase behavior of rodlike colloids. We model the rodlike particles by spherocylinders, as we have essentially complete information on the phase diagram of such objects, for arbitrary aspect ratio (see chapter 5). In the simulations, we model the polymer-induced attraction by a suitable generalization of the square-well model for spherical particles. We find evidence for demixing transitions in the isotropic, nematic and solid phases. We compare our simulation results with predictions based on the perturbation theory of Lekkerkerker et al. [113]. A crucial input in this theory is the so-called free-volume fraction of the hard spherocylinder reference system. In the work of Lekkerkerker and Stroobants, this quantity is estimated using scaled-particle-theory. Here, we determine the free-volume-fraction using numerical simulations.

Introduction

6.1

For over half a century, experimentalists have known that the isolation and purification of rodlike viruses, such as the tobacco-mosaic virus (TMV), can be facilitated by addition of non-adsorbing polymers [114]. As purification of the virus was the central theme of these experiments, little attention was paid to the underlying physics of such mixtures of polymers and rodlike colloids. Yet, TMV dispersions provide excellent model systems to study colloidal liquid crystalline phases [100]. However, a limitation of the TMV system is that the length of the particle cannot be varied at will. Less seriously, the rod-rod interaction is predominantly electrostatic. This complicates a direct comparison to theories for hard rod suspensions. In recent years, much effort has been invested in the development of reliable techniques to synthesize sterically stabilized rodlike colloidal boehmite needles [115]. Dispersions of such particles could serve as a model system for rodlike colloids, much in the same way as dispersions of spherical latex and silica particles act as proto-typical experimental realizations of hard-sphere fluids. The boehmite rods have the added advantage that the length-to-width ratio can be varied. Thus far, these boehmite suspensions are still fairly polydisperse, but the situation is likely to improve as more sophisticated colloid synthesis techniques are developed. Buitenhuis et al. [116] conducted experiments on a mixture of polystyrene and boehmite rods with an aspect ratio $L/D=6.4$, sterically stabilized with poly-isobutene [117] and dispersed in an organic solvent. For a polymer radius of gyration which was about 80% of the rod diameter they observed phase separation into two isotropic phases at sufficiently high polymer concentration.

The phase behavior of rod-polymer mixtures has been studied theoretically in the context of the Asakura-Oosawa (AO) model. As explained in chapter 1, the AO model describes the polymer as a sphere that has a hard core interaction with the rods, but is completely

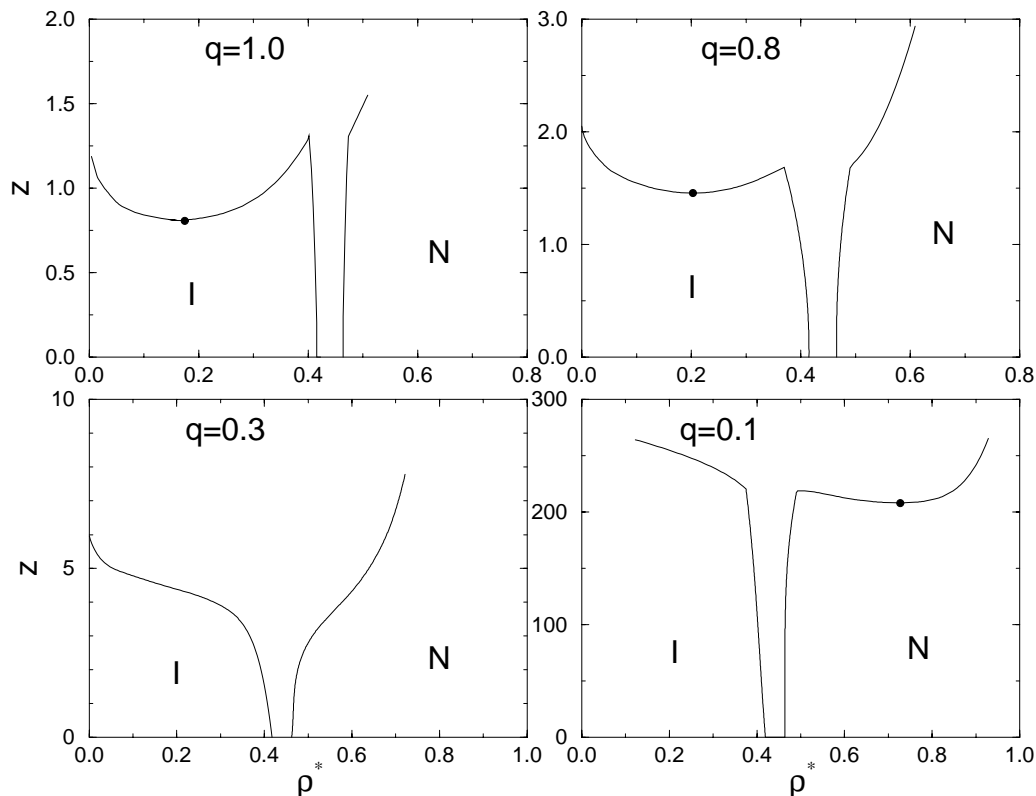


Figure 6.1. Phase diagrams of hard spherocylinders with aspect ratio $L/D=5$, plus non-adsorbing polymer, as predicted by the scaled particle theory of Lekkerkerker and Stroobants [113]. In this theory, the polymers are modeled as inter-penetrable hard sphere, in the spirit of the Asakura-Oosawa model. The ratio of the diameter of the polymer spheres to the diameter of the spherocylinders is denoted by q . The theory of ref. [113] does not consider the smectic and solid phases.

penetrable to other polymer spheres. Lekkerkerker and Stroobants [113] have used the formalism described in chapter 1 in combination with scaled particle theory to predict the phase diagram for mixtures of spherocylinders with an aspect ratio $L/D=5$ and polymers with $q=1.0, 0.8, 0.5$ and 0.1 , where q is defined as the ratio of the (hard sphere) polymer diameter and the spherocylinder hard core diameter ($q \equiv \sigma_{\text{pol}}/D$). Scaled particle theory provides the equation of state for pure hard spherocylinder systems and the free volume fraction $\alpha(\rho^*)$ required in the perturbation theory. The free energy of the nematic phase depends functionally on the orientational distribution function. The equilibrium orientational distribution minimizes the free energy. Figure 6.1 shows the results of the calculations of Lekkerkerker and Stroobants in the z, ρ^* plane. Here z , the polymer fugacity of the reservoir is related to the reservoir polymer number density ρ_p^R by $z = \rho_p^R D^3$. As can be seen from the figure, the theory predicts that for long polymers ($q \geq 0.8$), demixing will occur in the isotropic phase: this corresponds roughly to the results of the experiments on boehmite rods, mentioned above [116]. The critical point of the binodal in figure 6.1 shifts to higher density as q is lowered. For shorter polymers, this I-I transition disappears. For instance, for $q=0.5$, the I-I binodal is metastable with respect to the I-N transition. And for short polymers ($q \leq 0.1$) a demixing transition is found in the nematic phase. It

should be stressed that the theoretical prediction of the existence of a nematic-nematic phase separation should be treated with some caution: in the SPT approach of ref. [113], the smectic-A and solid phases are not considered, because the approximations that are used to compute the free-volume fraction α by scaled-particle theory, are expected to break down in translationally ordered phases. However, as Lekkerkerker and Stroobants already noted, it is unlikely that the neglect of the smectic A and the solid phase is justified. There might, for instance, be a nematic-smectic (or smectic-smectic) phase transition, preempting the nematic-nematic transition. Even a solid-solid phase transition, as was discussed in chapter 3 belongs to the possibilities. In this chapter we will therefore also consider the influence of polymer addition on the location of the N-SmA and the SmA-S transition.

In the following section we use the results of numerical simulations on hard spherocylinders with aspect ratio $L/D=5$, to compute the free-volume fraction that plays a crucial role in the thermodynamic perturbation theory as applied to the Asakura-Oosawa model. Using this perturbation theory, we arrive at a prediction of the phase diagram of the polymer-colloid mixture. It would be natural to compare the theoretical predictions with a direct simulation of the full AO model, at finite polymer fugacity z . However, such simulations would be computational quite expensive. In section 6.3, we therefore explore an alternative approach: we replace the polymer-induced depletion force by an angle dependent attractive pair potential. In section 6.4 we study the possibility of nematic-nematic phase transitions in the limit of large L/D .

Perturbation theory

6.2

The thermodynamic perturbation theory of ref. [113] requires as input the equation of state of the hard core reference system (in this case, the hard spherocylinder fluid) and the free-volume fraction α . The previous chapter (chapter 5) contains the necessary information about the equation of state of a pure hard spherocylinder fluid. In addition, we measured the free volume function $\alpha(\rho^*)$ as a function of density by use of the Widom insertion technique [36]. The advantage of the perturbation approach is that there is no need to simulate the polymers explicitly: it is sufficient to just measure the free volume available for a polymer in a pure hard spherocylinder system. We should stress that there is a slight difference in the philosophy underlying the present (numerical) implementation of perturbation theory and the scaled-particle theory approach of ref. [113]. Stroobants and Lekkerkerker minimize the free energy of the polymer-colloid mixture with respect to the orientational distribution function of the rods. Hence, in their case, the orientational distribution function of the mixture is not equal to the distribution function of the pure reference system at the same density. In our simulations, we do not attempt to vary the orientational distribution function independently of density (as this would involve performing many simulations of a hard spherocylinder fluid in a magnetic field).

In the Widom method, we attempt to insert polymers (represented by hard spheres) at random positions in the simulation box. The fraction of insertions that does not result in an overlap corresponds to the free volume fraction. In practice, we measure the distance r to the nearest surface of a spherocylinder. A polymer with a radius larger than r will overlap with the spherocylinder, while a smaller polymer will fit. We made a histogram of the insertion probability, and hence the free volume fraction α , as a function of ρ^* and q . We fitted this free volume data to a polynomial in ρ^* and q and used equations 1.19

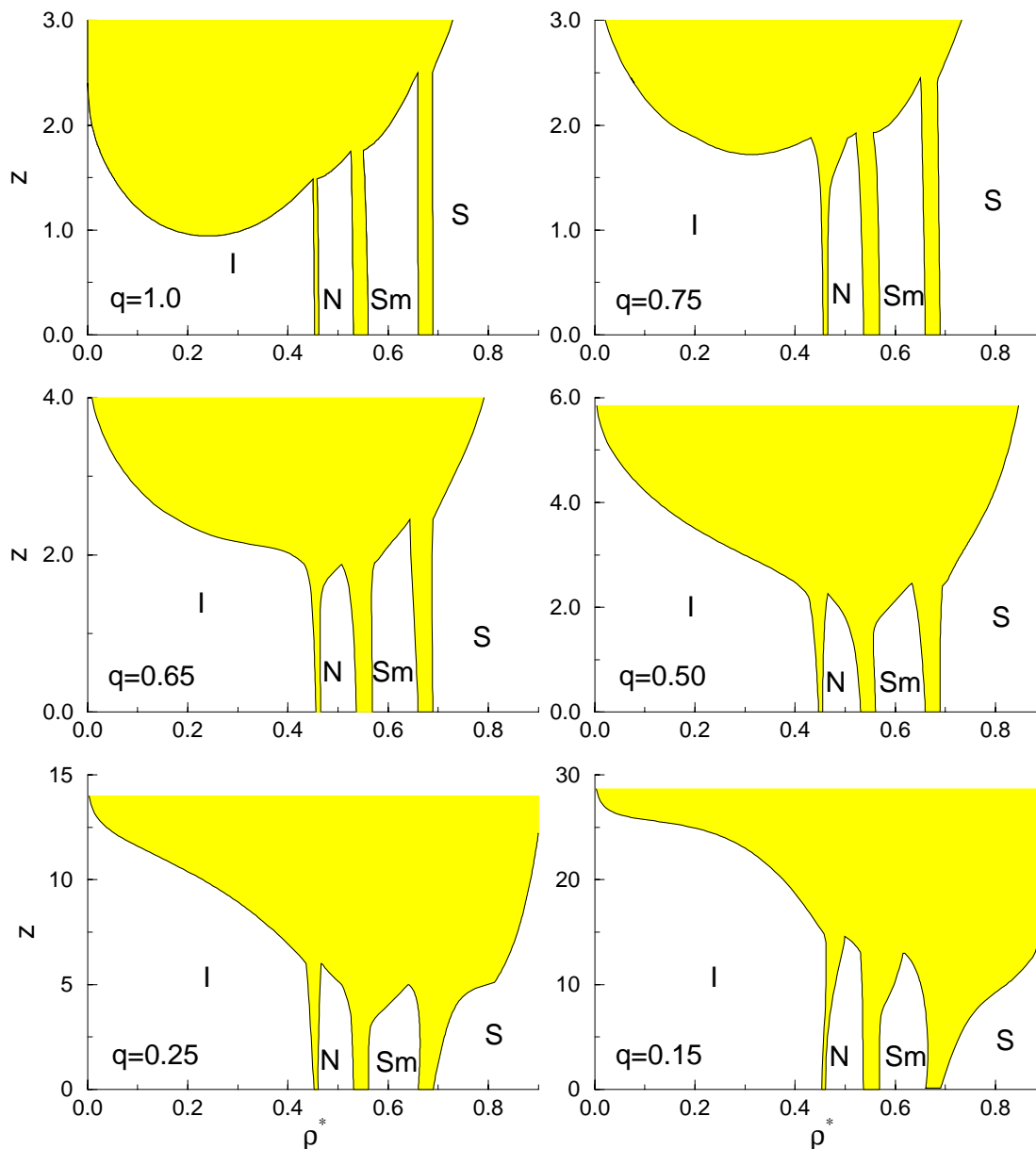


Figure 6.2. Phase diagrams for a system of spherocylinders with $L/D=5$ mixed with polymers of different diameter ratio q , as predicted by thermodynamic perturbation theory. The reference system is the hard spherocylinder model, and the perturbation was evaluated by numerical simulation of the reference system.

and 1.20 in combination with the simulation results for $L/D=5$ (chapter 5) to calculate the two-phase coexistence curves. The resulting phase diagrams in the ρ^*, z plane are presented in figure 6.2 for $q = 0.15, 0.25, 0.50, 0.65, 0.75$ and 1.0. These figures show the thermodynamically stable regions of the isotropic, nematic, smectic A and solid phase denoted respectively by I, N, SmA and S respectively. The phases are separated from each other by first-order coexistence regions indicated by a grey area. Two coexisting phases will have equal z , because z is the fugacity of the polymer reservoir that is in equilibrium with both phases. In figure 6.2 a) the phase diagram for $q=1.00$ is depicted. The isotropic fluid

phase contains the familiar binodal curve ending in a critical point. This binodal is very similar to the ones we obtained in chapter 2 and 3. At a fugacity higher than $z_{\text{crit}}=0.95$ a phase separation occurs between a vapor phase with a low density of spherocylinders, and a high density liquid phase. Upon increasing the fugacity of the polymers, the liquid becomes metastable with respect to the nematic phase and we find gas-nematic coexistence. At still higher fugacity the nematic phase also disappears and there is a two phase gas-smectic coexistence region. Eventually, at $z=2.5$ the gas-smectic is preempted by the crystallization transition. The important difference with the theoretical predictions of figure 6.2 is that the scaled-particle theory of ref. [113] does not consider the smectic and solid phases. We find that the densities of the coexisting phases at the I-N, N-SmA and the SmA-S transitions, hardly change with the polymer fugacity.

In figure 6.2 b) we consider the situation for a smaller polymer radius of $q=0.75$. As expected, the shorter interaction range results in a shift of the critical point of the I-I demixing transition to higher densities. Moreover, the transition occurs at higher polymer fugacity. We note that the I-N coexistence density gap widens (slightly) at higher polymer fugacity. The density region where the nematic phase is stable does, therefore, decrease at these high polymer fugacity. The I-I-N triple point occurs at somewhat higher fugacity. The I-N-SmA and I-SmA-S triple points are hardly affected.

When we decrease the range of interaction to $q=0.65$, the critical point of the I-I demixing curve disappears. The I-I binodal has moved to higher fugacity where the phase transition is preempted by the (successively) I-N, I-SmA and I-S transitions. The I-N-SmA and I-SmA-S triple points still occur at roughly the same polymer fugacity, although close to the triple points, all three first order phase coexistence regions widen somewhat.

For $q=0.50$ the widening of the N-SmA transition becomes very pronounced for $z > 1.5$. The I-N-SmA triple point increases in fugacity faster than the N-SmA-S triple point. This shift in the relative location of triple points continues and for $q=0.25$ the N-SmA-S occurs at lower z than the I-N-S triple point. The interaction range is now small enough to affect the SmA-S transition. The shape of the coexistence curve in the solid phase is typical of a system approaching an isostructural solid-solid transition. However, the interaction ranges is still too large to induce such a phase separation inside the solid phase. As we saw in chapter 3, in the case of spherical colloids this transition occurs only if the interaction range δ is less than 0.07. The last plot of figure 6.2 shows the phase diagram for $q=0.15$. The SmA-S transition has become even wider, and the I-N-S and the N-SmA-S triple points both move to higher z -values, but their relative position is hardly affected.

Summarizing, the global picture that follows from this perturbation theory calculation is as follows. For large polymers we have an isotropic fluid-fluid phase separation ending in a critical point which shifts to larger z and ρ^* and is preempted when the radius becomes smaller than $q=0.6$. The I-N-SmA and I-SmA-S triple points occur at $z=2.2$ and 2.5 respectively and are not very sensitive to the polymer size for $q > 0.6$. For lower q both triple points move to higher z , but the I-N-SmA overtakes the I-SmA-S triple point. For $q < 0.45$ the situation changes and we have an I-N-S and a N-SmA-S triple point. For the low q values the I-N, N-SmA and SmA-S coexistence regions fan out for high z . We find no evidence for an N-N transition, as predicted by the SPT approach of ref. [113]. In particular, for $q = 0.1$ the scaled-particle theory predicts a N-N critical point at $\rho^* = 0.6$. However, the present simulations suggest that, at that density, the nematic phase is no longer stable with respect to the smectic. The perturbation theory that we use becomes less accurate

at high z , because it neglects any structural changes induced by the polymer. Still, this limitation is unlikely to affect our conclusion that a polymer-induced N-N phase separation will not occur for rods with an aspect ratio $L/D=5$. After all, the density range over which the nematic phase is stable, is quite limited: there is hardly space for an N-N binodal. We therefore expect a nematic-nematic phase separation to take place for larger elongation of the spherocylinder, where the nematic phase extends over a much wider density range.

For the same reason, it is unlikely that there is a smectic to smectic transition for $L/D=5$. Moreover, increasing the aspect ratio of the rods will do little to facilitate the occurrence of a smectic-smectic transition, as the density range where the smectic phase is stable hardly changes with L/D . It is tempting to speculate that polydispersity of the rods may change these conclusions: polydispersity in the length of the rods enhances the nematic stability, thus making a N-N separation more likely. In contrast, polydispersity in the diameter of the spherocylinders widens the smectic range [118]: this may favor the occurrence of a demixing transition in the smectic phase.

6.3 Spherocylinders with attraction

6.3.1 The angle dependent pair potential

In the previous section we used perturbation theory to estimate the phase behavior of the Asakura-Oosawa model for rod-polymer mixtures. The crucial assumption in the perturbation theory is that we can use the properties of the hard spherocylinder reference fluid to compute the free-volume fraction α at finite fugacity. To check if this assumption is justified, we have to perform simulations of the full Asakura-Oosawa model at finite z . Although this is certainly feasible for individual state points, such calculations would become prohibitively expensive if we wish to compute phase diagrams for different values of q and different aspect ratios of the rods. The reason is that, in a full (off-lattice) simulation of the AO model, every polymer has to be simulated separately. The number of particles needed for such simulation is quite large, certainly for the small polymers at high fugacities. As an example we can estimate the number of polymers in a nematic phase of spherocylinders of $L/D=5$ at a density $\rho^*=0.5$ in equilibrium with a reservoir with polymers of diameter $\sigma_p=0.15$. As can be seen in figure 6.2, the polymer fugacity can easily be equal to $z_p=10$. The free volume fraction for this density and q -value is approximately 0.4. This corresponds to an equilibrium polymer density in the nematic phase of $\rho_p = z\phi = 4$. As the volume of the simulation box has to be larger than $(2(L + D))^3$ to avoid multiple overlaps of the spherocylinders, the minimum number of polymers needed in such a simulation is $N_p = 4 \times 12^3 \approx 7 \times 10^3$. This is a lower bound, as the polymers tend to drive the spherocylinders together and create more space for themselves. Moreover, due to the large particle concentration, the acceptance probability of moving a spherocylinder in a sea of polymers is dropping dramatically.

To avoid simulating the full polymer-colloid model, while retaining the effect of the depletion interaction on the structure of the colloidal suspension, we constructed a model of hard spherocylinders with a pairwise additive attractive “depletion” potential that approximates the real potential of mean force W as introduced in chapter 1. The most important feature of this potential is that it must be dependent on relative orientation of the rods. The depletion attraction is strong ($\sim qL$) when the spherocylinders are parallel, but much weaker ($\sim q^2$) for perpendicular rods.

The most direct way to compute the depletion pair potential is to calculate the overlap volume between the depletion zones of the two spherocylinders as a function of distance and relative orientation, and multiply this volume by the polymer osmotic pressure. This procedure yields an effective pair potential that can be used in simulations of the phase diagram. In the case of spherical colloids mixed with small polymers, this approach predicts a phase diagram that is in reasonable agreement with the “exact” phase diagram [10, 6]. Although the depletion pair-potential for spherocylinders could be computed in the same way, the resulting function would not be cheap to compute during a simulation. As the computation of the pair potential is the most time-consuming part of the program, it is useful to devise an effective pair potential that resembles the depletion interaction, but is computationally cheap. To this end, we assume that the spherocylinder can be considered as a continuous distribution of (overlapping) spheres of diameter D , with their centers distributed uniformly on a line segment of length L . The individual spheres interact through a square-well potential. The total pair potential of the two spherocylinders is then a sum (or actually, an integral) of all the individual contributions, and is expressed as:

$$V(\mathbf{r}) = -\epsilon \int_{-L/2}^{L/2} \int_{-L/2}^{L/2} d\lambda_i d\lambda_j H((\delta + D) - |\Delta\vec{r}_{ij} + \lambda_i \vec{u}_i - \lambda_j \vec{u}_j|). \quad (6.1)$$

Here $\Delta\vec{r}_{ij}$ denotes the relative position of the centers of mass of the two hard spherocylinders i and j , with orientations specified by the unit vectors \vec{u}_i and \vec{u}_j , respectively. The range of depletion interaction (δ) is a measure for the polymer diameter σ_p . The well depth ϵ can

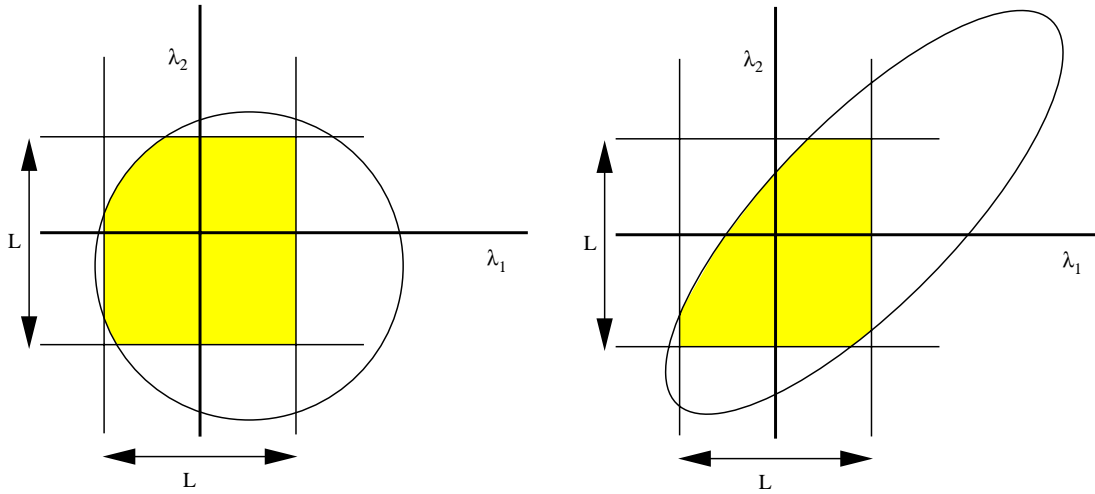


Figure 6.3. Geometrical representation of the computation of the effective depletion interaction between two spherocylinders (eqn. 6.1). On the left, the situation for two perpendicular spherocylinders is depicted. The λ_1 and λ_2 axes denote the distance from the center of mass along a cylinder axis. The circle indicates the (λ_1, λ_2) points for which the distance equals $\delta + D$. Inside this circle the distance is smaller than $\delta + D$. As the integral in eqn. 6.1 is bounded by the length of the spherocylinders, the total interaction is proportional to the cross section of the $L \times L$ square and the ellipse. On the right, the angle between the spherocylinder is less than 90 degrees. The circle therefore changes into an ellipse, with its major axes along the lines $\lambda_1 = \lambda_2$ and $\lambda_1 = -\lambda_2$. The interaction is still proportional to the area bounded by the ellipse and the condition $|\lambda_1| < L/2$ and $|\lambda_2| < L/2$.

be interpreted as a measure for the polymer concentration. The Heaviside step-function $H(x)$ is defined in the usual manner:

$$H(x) = \begin{cases} 1 & x \geq 0, \\ 0 & x < 0. \end{cases} \quad (6.2)$$

The evaluation of the integral in eqn. 6.1 can be reduced to a simple geometrical problem. First, consider the interaction between two infinitely long cylinders. If the cylinders are

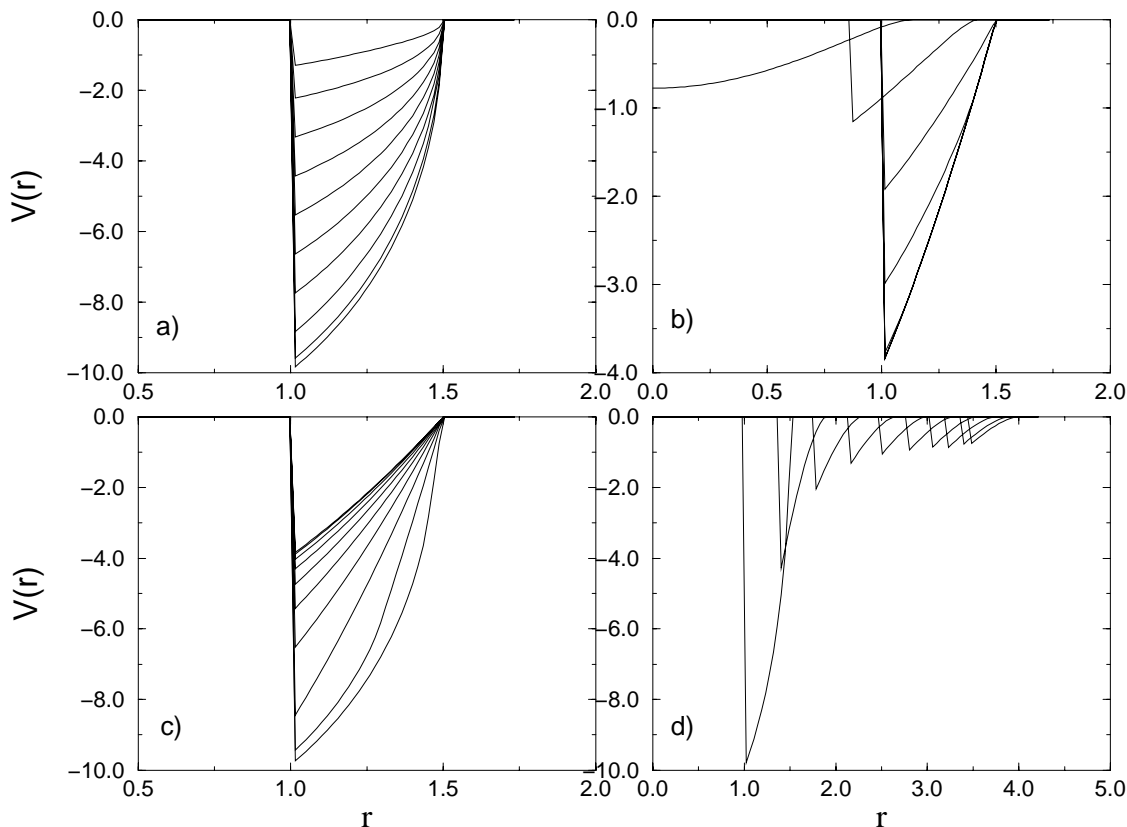


Figure 6.4. Generalized square-well interaction potentials $V(r)$, as a function of distance r for various orientations and center-of-mass distances of two spherocylinders with $L/D=5$. One spherocylinder is fixed at the origin oriented along the z -axis, while the position and orientation of the second is varied. a) Parallel spherocylinders, with the center of mass of the second spherocylinder shifted along the z -direction. From the bottom to the top the curves denote potentials for a shift of $z/D = 0, 0.5, 1.0, 1.5, 2.0, 2.5, 3.0, 3.5, 4.0, 4.5$ and 5.0 . b) Perpendicular spherocylinders, with the center of mass of the second spherocylinder shifted along the z -direction. From the bottom to the top the curves denote potentials for a shift of $z/D = 0, 0.5, 1.0, 1.5, 2.0, 2.5, 3.0, 3.5, 4.0, 4.5$ and 5.0 . c) Two spherocylinders with zero z -shift, the second one rotated around the line through the centers of mass over an angle θ . From the bottom to the top the curves denote potentials for an angle of $\theta = 0, 10, 20, 30, 40, 50, 60, 70, 80$ and 90 degrees. d) Two spherocylinders with zero z -shift, the second one rotated over an angle θ in the plane through the line connecting the centers of mass and the z -axis. From the bottom to the top the curves denote potentials for an angle of $\theta = 0, 10, 20, 30, 40, 50, 60, 70, 80$ and 90 degrees.

mutually perpendicular, the integral will reduce to the calculation of the surface of a circle with radius $\sqrt{(\delta + D)^2 - \Delta^2}$, where Δ is the minimum distance between the lines that run through the cylinder axes. As the angle between the cylinders becomes smaller, this circle changes into an ellipse by scaling one of the ellipse axes by $1/\sqrt{1 - \vec{u}_i \vec{u}_j}$. The integral diverges for parallel, infinite cylinders, because every point along the cylinder gives a finite contribution. However, the integral in eqn. 6.1 is bounded by the finite length of the spherocylinders. This is translated in the geometrical picture as cuts through the ellipse, as shown in figure 6.3. If we multiply the area enclosed by the ellipse and/or the cuts of the $L/2$ bounds by the well depth ϵ we obtain the total interaction potential.

A quantity of particular interest is the maximum interaction between two spherocylinders. The interaction between two particles is largest when they are oriented parallel with their centers of mass at the minimum distance (D).

$$\begin{aligned} V_{\max}(D) &= -\epsilon(2L\sqrt{(\delta + D)^2 - D^2} - ((\delta + D)^2 - D^2)) \\ &= -\epsilon(2L\sqrt{\delta^2 + 2\delta D} - (\delta^2 + 2\delta D)). \end{aligned} \quad (6.3)$$

In figure 6.4 we show the behavior of this pair potential for a few relative orientations and distances of the two spherocylinders.

Simulation

6.3.2

We performed NVT Monte Carlo simulation on a system of 480 spherocylinders with $L/D=5$ interacting through the generalized square-well potential described in the previous section, for $\delta = 0.1, 0.3, 0.5$ and 1.0 . The density ranged from $\rho^*=0.1$ in the isotropic phase to $\rho^*=0.66$ in the smectic phase. The reduced well depth $\epsilon^* = \epsilon/kT$ is a measure for the polymer concentration. In our simulations, it ranged from 0–2. Configurations of the system at high densities were generated by slowly expanding a perfectly aligned, close packed smectic structure. Care was taken to avoid that the system became stuck in glassy configurations, a problem that was particularly severe at low temperatures (large ϵ^*). We measured the potential energy as a function of ρ^* and ϵ^* and fitted it to a polynomial of the form

$$E(\rho^*, \epsilon^*) = \sum_{i,j}^{3,2} \rho^{*i} \epsilon^{*j}. \quad (6.4)$$

The free energy of the system could be obtained via thermodynamic integration (see chapter 3)

$$F(\rho^*, \epsilon^*) = F_{\text{HSC}}(\rho^*) + \int d\epsilon^* \left(\frac{\partial F}{\partial \epsilon^*} \right) = F_{\text{HSC}}(\rho^*) + \int d\epsilon^* \frac{\langle E \rangle_{\epsilon^*}}{\epsilon^*}. \quad (6.5)$$

where $\langle E \rangle$ is the average potential energy measured during the Monte Carlo simulations and F_{HSC} denotes the free energy of the hard spherocylinder reference system. This free energy can be obtained by integration along the equation of state in the different phases, where the reference free energies were taken from the results of section 5.4 of chapter 5. At large ϵ^* (low T), the Helmholtz free energy $F(\rho^*, \epsilon^*)$ may exhibit an inflection point, signalling the occurrence of a first-order phase transition within a single phase (e.g isotropic-isotropic). Alternatively, the increased attraction may shift the phase coexistence boundaries

of the I-N, N-SmA or SmA-S transitions. In either case, we can estimate the density of the coexisting phases by using a double tangent construction.

6.3.3 Results

The results of the thermodynamic integration are displayed in figure 6.5 for different values of $q = \delta/D$. The graphs are plotted in the ρ^*, ϵ^* plane instead of the usual ρ^*, T plane because the well depth ϵ^* is more directly related to the fugacity of the polymers in the system. In this way one can compare the phase diagrams with those of section 6.2. We note, however, that the pair potential that we use is not completely equivalent to the Asakura-Oosawa interaction. For this reason we focus on the qualitative features of the phase diagram. For $q=1$ the range of the potential is equal to the diameter of the spherocylinder and we see a phase separation between two isotropic phases ending in a critical point. The isotropic-isotropic phase separation is similar to the fluid-fluid coexistence in chapter 2. The density region where the nematic phase is stable becomes narrower as ϵ increases and it ends in an isotropic-nematic-smectic triple point at a fugacity of $\epsilon^* \approx 0.23$. This is lower than the location of the l_1 - l_2 -N triple point at $\epsilon^* \approx 0.34$. In contrast, the results of the perturbation theory in section 6.2 indicate that for $q=1$ the I-N-SmA triple point has a higher fugacity than the l_1 - l_2 -N one. Apparently, the attractive pair potential destabilizes

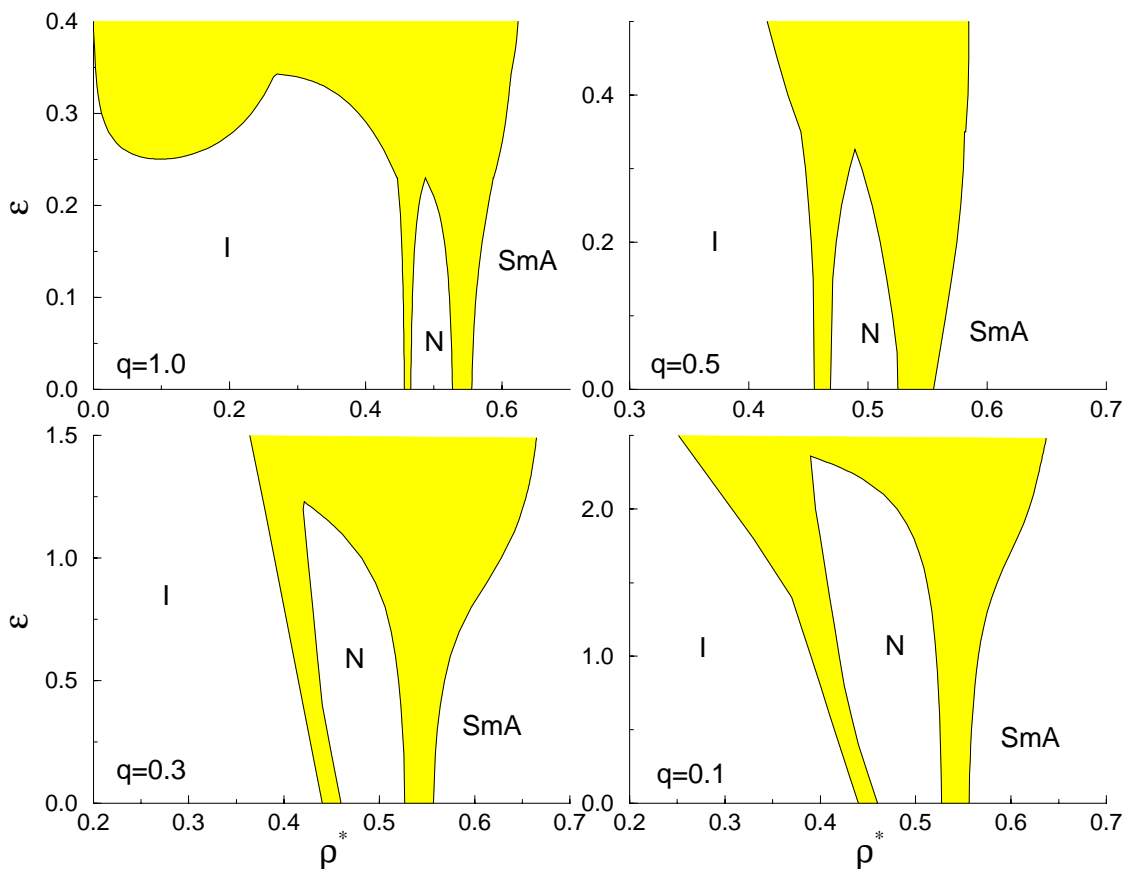


Figure 6.5. Simulated phase diagrams for $L/D=5$ spherocylinders with an attractive generalized square-well potential (eqn. 6.1). The diagrams are plotted in the ρ^*, ϵ^* plane to facilitate comparison with the Asakura-Oosawa model of rod-polymer mixtures.

the nematic phase with respect to the smectic phase.

At higher fugacity the smectic phase is expected to become metastable with respect to the solid. Although we have not included the solid in our simulation, it is likely that the general picture is similar to that found in section 6.2.

The perturbation theory of section 6.2 predicts that, for smaller values of q , the isotropic-isotropic transition will shift to higher fugacity and density and will, eventually be preempted by the isotropic-nematic transition. Indeed, for $q=0.5$ we find that the I-I transition has already disappeared. The I-N and N-SmA transitions widen at higher ϵ^* . The I-N-SmA triple point is located at $\epsilon^*=0.3$. For still smaller q , the picture remains much the same. The I-N and N-SmA transitions widen at high ϵ^* , the triple point moves to higher ϵ^* and lower ρ^* . This last feature was not predicted by the perturbation theory.

We do not observe a nematic-nematic or smectic-smectic phase separation. In section 6.2, we argued that a nematic-nematic or smectic-smectic transition will, most likely, be preempted by a transition to a phase with a different symmetry. However, for large L/D , the range of stability of the nematic phase will become very large. Under those circumstances, it is likely that a N-N phase-transition becomes possible

6.4 Nematic-Nematic coexistence in the Onsager limit

The existence of a nematic-nematic phase transition in systems of rods with an attractive potential was already predicted in the early work of Flory [119] and later by Khokhlov and Semenov [120]. They estimated that a nematic-nematic transition can occur for rods with $L/D > 15$, but will be metastable for smaller elongations.

To investigate the possibility of a polymer-induced N-N transition for suspensions of long rods, we study the phase behavior of a system of infinitely long ("Onsager") rods. The details of this type of simulation were discussed in chapter 5 in the context of hard spherocylinders. If we now wish to include the depletion interaction, we must extend the generalized square-well interaction discussed in section 6.3 to long rods in the limit $L/D \rightarrow \infty$. As in chapter 5, we assume that the system is either in the dense nematic phase, or in an even more highly ordered phase, such that the rods are almost perfectly aligned. This allows us to use an affine transformation to map the long spherocylinder system onto skewed right cylinders with aspect ratio one. Note that the same affine transformation will map an Asakura-Oosawa sphere onto a disk. All the depletion interactions are therefore limited to points on the same xy -plane. The total depletion potential can be obtained by integrating all in-plane interactions along the two rods. (i.e. by integrating z in the interval where both cylinders are intersected by the same xy -planes).

$$V(\mathbf{r}) = -\epsilon \int_{-1/2}^{1/2} dz H((\delta + D) - |\Delta\mathbf{r}(z)|). \quad (6.6)$$

where $\Delta\mathbf{r}(z)$ is the distance between the axes of the two rods in the xy -plane at height z . Of course, we should take the effect of the finite length of the rods into account. As in section 6.3.1, this integral can be given a simple geometrical interpretation.

In figure 6.6 we consider two particles i and j at a center of mass distance r_{ij} . The top surface of skewed cylinder i (j) is shifted with respect to the bottom by an amount \vec{u}_i (\vec{u}_j). We can deform the coordinate frame such that the axis of one particle (say i) is along the z -axis. Projecting cylinder i along the z -axis, we can draw a circle of radius $\delta + D$ around

the particles axis, which shows the range of the square well potential. In the same figure, we project that fraction of the axis of particle j that is located between the top and bottom planes of particle i . We denote the length of this segment by α . Next, we project this line segment on a plane perpendicular to the z -axis. The resulting line segment may intersect the circle that delimits the range of the square well potential. Let us denote by β , the fraction of the projected line segment that lies within this circle. The interaction strength of particle i and j is then given by $\epsilon\alpha\beta$. Obviously, the maximum interaction strength, $V(D) = -\epsilon$, is found for two parallel particles at contact and at equal height.

We performed simulations of the Onsager system for the nematic and smectic phases with densities between $\rho^*=0.1$ and $\rho^*=0.7$. The width of the potential well was chosen to be $\delta=1$, while the well depth ϵ^* was varied between $\epsilon^*=0$ to $\epsilon^*=2.5$. We measured the average potential energy as a function of ρ^* and ϵ^* and constructed a free-energy surface for the nematic and smectic phases by thermodynamic integration, starting from the known equation of state of the pure Onsager particles (chapter 6.4). A nematic-nematic transition shows up as non-convex behavior of the volume dependence of this free energy. The nematic-smectic transition, although presumably continuous in the pure Onsager system, becomes first order upon introducing an attraction. The calculated phase diagram is shown in figure 6.7. Clearly, the nematic-nematic separation is (just) metastable with respect to

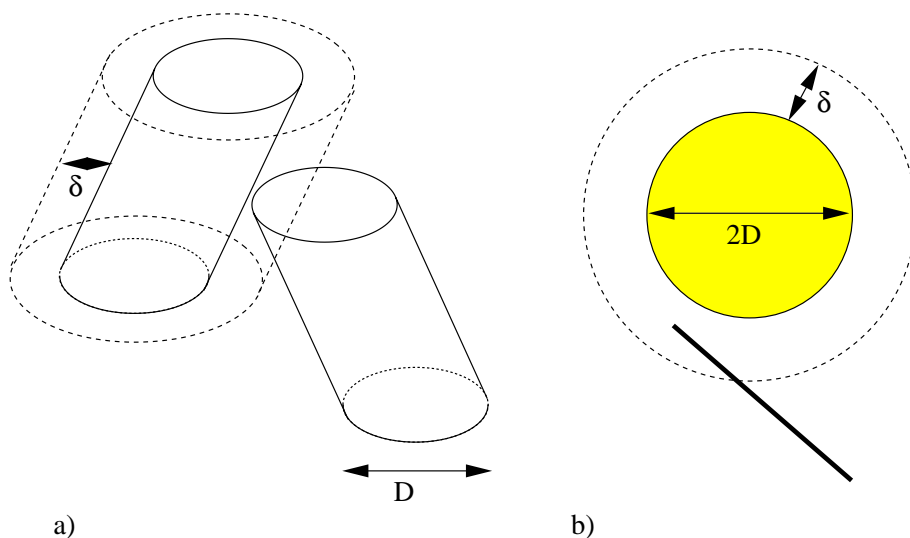
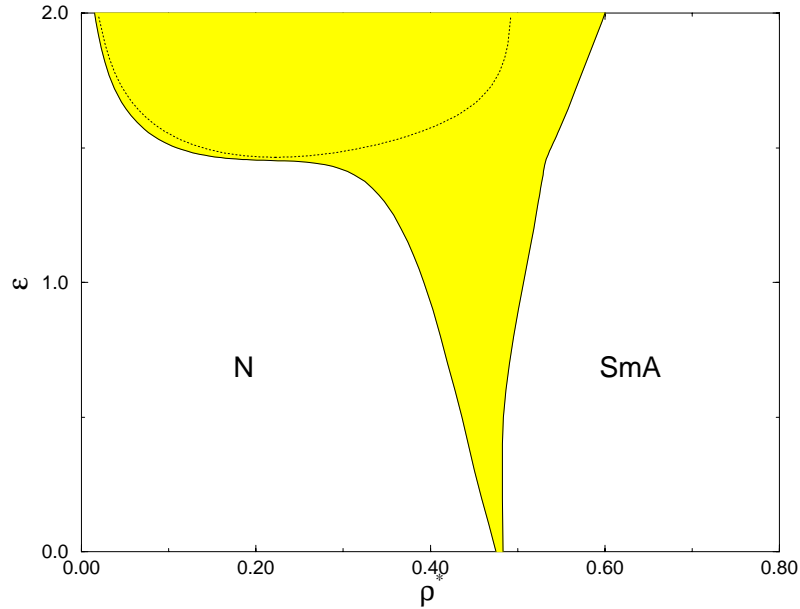


Figure 6.6. *Geometrical representation of the computation of the polymer induced depletion potential for spherocylinders in the limit $L/D \rightarrow \infty$. On the left, two interacting scaled spherocylinders are depicted. The range of the square well is indicated by the dashed spherocylinder. The fraction of the length of the right cylinder that is inside this dashed volume, is proportional for the interaction potential, according to eqn. 6.6. Figure b) is a projection along the cylinder axis of one of the scaled spherocylinders. The dashed circle gives the boundary of the square well interaction. The thick line-segment is the projection of that part of the axis of the other cylinder that is located between the top and bottom surfaces of the first cylinder. We denote the (unprojected) length of this segment by α . The fraction of the line segment inside the dashed circle is denoted by β . The value of the integral in eqn. 6.6 is given by $\alpha \times \beta$.*

Figure 6.7. *The phase diagram for a system of infinitely long hard rods, with an attractive interaction given by eqn. 6.6. The range of the attraction is $q \approx \delta=1$. The diagram is plotted in the ρ^*, ϵ^* plane to make comparison with the rod-polymer mixture possible. The dashed curve is the metastable N-N binodal.*



the nematic-smectic transition. We expect that the N-N binodal shifts to lower reduced density and ϵ^* as the range of attraction becomes larger. For sufficiently long ranged attractions, there could be a stable N-N binodal. To check this, we studied a system with infinitely long-ranged (but infinitely weak) attraction. That is, we analyse the “van der Waals” limit of the Onsager system plus attraction.

6.4.1 Infinitely long-ranged attraction for long rods

Thermodynamic perturbation theory becomes exact in the limit of infinitely weak, infinitely long attraction [5]. This is the basis of the success of the van der Waals model. We can use a similar mean-field theory to examine the phase behavior of spherocylinders with an infinitely long-ranged interaction in the limit $L/D \rightarrow \infty$. The van der Waals free energy is the sum of the free energy of the hard core reference system and the change in free energy due to the attractive interactions. In the limit of infinitely long-ranged attractions, mean field theory is exact, and the perturbation is simply proportional to the density

$$F_{\text{VdW}} = F_{\text{HSC}} - \alpha \rho^*. \quad (6.7)$$

Here, the parameter α is a measure for the strength of the attractive interactions or, equivalently, a measure for the (inverse) temperature. In the polymer-colloid case, α is a measure for the polymer fugacity. The phase diagram for the Onsager system with long-ranged attraction is displayed in figure 6.8. Clearly there now is a nematic-nematic transition, which ends in a critical point at a density of $\rho^* \approx 0.19$. We also include the I-N and the N-SmA transition in the figure, in order to show that the N-N is stable with respect to these transitions. As before, the N-SmA transition, widens at large values of α (higher fugacity). In the Onsager model, the I-N transition is located at $\rho^*=0$ and is therefore not visible in the figure. In summary, it is indeed possible to have a stable nematic-nematic phase separation in a system of infinitely long hard spherocylinders with attraction, provided that the interaction is sufficiently long ranged.

If we now consider the van-der-Waals limit for spherocylinders with a large but finite aspect ratio, the situation changes slightly. We know (see chapter 5) that the isotropic-nematic

Figure 6.8. Phase diagram for a system of infinitely long spherocylinders with an infinitely long ranged, infinitely weak, attractive potential. Note that the nematic-nematic binodal has become stable with respect to the N-SmA transition, be it over a narrow range in “temperature” (as measured by the strength of the attraction, a).

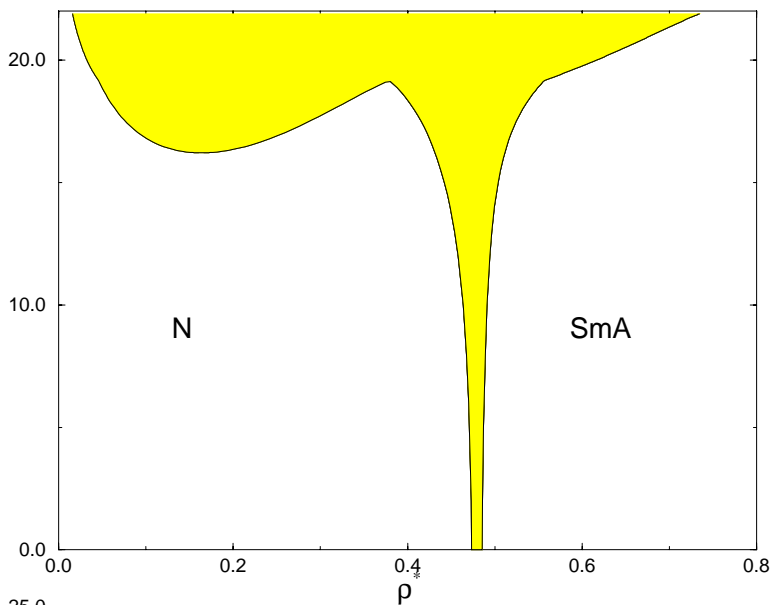
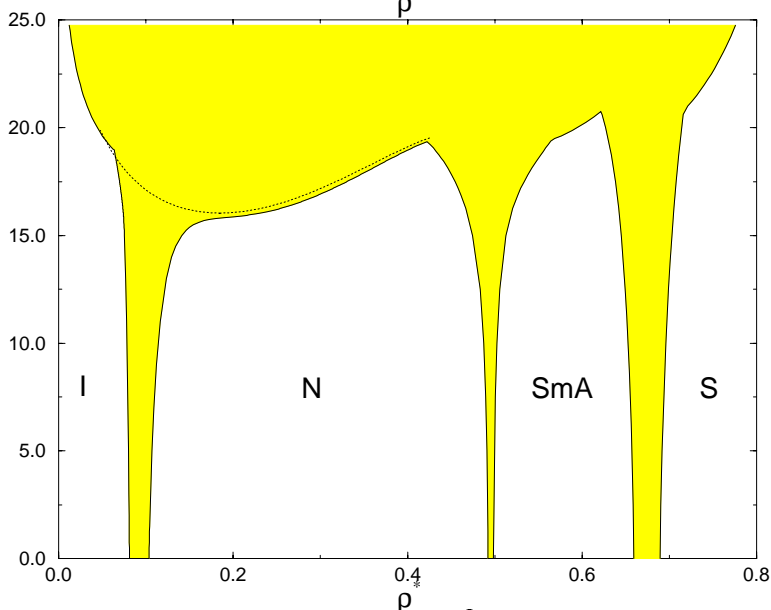


Figure 6.9. Phase diagram for a $L/D=40$ spherocylinder system with an infinitely long ranged, infinitely weak, attractive potential. The nematic-nematic binodal is preempted by the isotropic-nematic transition.



transition moves to higher densities as we move away from the Onsager limit, while the density of the N-SmA transition is hardly affected. As a consequence, it is now possible that the isotropic-nematic transition will interfere with the N-N transition. And this is precisely what happens: figure 6.9 shows that the N-N phase separation in the limit of infinitely long-ranged attractions, is preempted by the I-N transition. The figure suggests that the aspect ratio $L/D=40$ is close to the limit where N-N transitions are possible. Only slightly longer rods would be needed, to recover the N-N binodal.

The perturbation theory calculations indicate that shortening the range of attraction (i.e. decreasing the value of q) will move the critical demixing point to higher densities and will also lead to a reappearance of the N-N transition, until, in its turn, it is preempted by the N-SmA transition at small q values.

This picture corresponds qualitatively to the prediction of Khokhlov and Semenov[120] that the N-N transition is only possible for rods longer $L/D=15$. The significant difference with our lower limit $L/D=40$ cannot be explained by the isotropic attraction, because both theory and simulation use the same isotropic (exact) mean field potential. Therefore, the

discrepancy must be due to the way the orientation dependent interactions are treated. In the theory they are approximated by a simple anisotropic potential, whereas in the simulations are determined by the (many body) excluded volume of the rods.

We note that, although the depletion interaction between colloids in the limit of infinitely long polymers is well described by the van der Waals model for low polymer density, the model breaks down at higher density because of the many-body character of the depletion interaction. For instance, as we saw in chapter 1, the critical point of the fluid-fluid binodal shifts to zero colloid density in this limit, whereas the van der Waals model predicts a finite density. However, this difference will not qualitatively affect the existence of the nematic-nematic transition in a mixture of elongated spherocylinders and large polymers.

Overview of demixing transitions

6.5

On basis of the available results, we can give a rough sketch of the expected regions where demixing transitions should occur in the $q, L/D$ plane. In figure 6.10 we have combined our present knowledge about the stability regions of the phase separations in the different phases as a function of the polymer interaction range q and the colloid aspect ratio L/D . The curves give a rough indication of the regions in the $q, L/D$ plane where the depletion interaction induces a binodal in any one of the phases. The I-I critical point starts to appear for hard spheres around $q=0.3$. For rods with an aspect ratio $L/D=5$, the minimum interaction range needed to induce an I-I phase transition, has increased to $q = 0.6$ and it probably increases steeply with increasing aspect ratio. In fact, beyond a certain aspect ratio (less than $L/D=40$), stable I-I transition is not even possible in the limit $q \rightarrow \infty$. The nematic-nematic transition first appears for systems with an aspect ratio that is large enough to support a nematic phase over a reasonable density range. For finite L/D values, the region where a N-N transition is possible is bounded on both the low and high q side. The high- q boundary rises steeply with increasing L/D , and for large L/D , the region where an N-N transition can occur is only bounded for low q . In our simulations, we have not observed a SmA-SmA phase-separation, but there is no a-priori reason to exclude it either. However, as the range of stability of the smectic phase is never very large, we

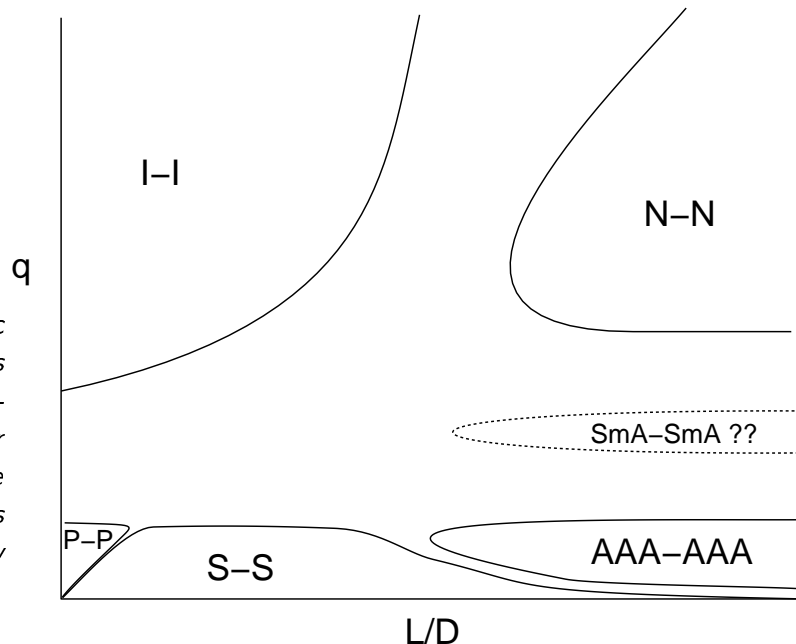


Figure 6.10. Schematic summary of the regions in the phase diagram of spherocylinder polymer mixtures, where demixing into two phases with the same symmetry can occur. See text.

expect the SmA-SmA transition, if it occurs at all, be confined to a narrow “window” in the $q, L/D$ plane. A possible location for this window has been sketched in figure 6.10. For very short-ranged attractions (low values of q), we expect to observe an isostructural solid-solid phase transition separation over the entire L/D range. This solid-solid transition was discussed in chapter 3 for the case of hard spheres. For spherocylinders, we expect to see a solid-solid transition in the plastic phase for small L/D (say, $L/D \leq 0.3$). For larger L/D values it is possible to have a solid-solid transition between two ordered solid phases (ABC-stacking). Finally, for large L/D values ($L/D \geq 10$) the solid-solid phase separation takes place between two AAA structures. For hard spheres, the S-S transition in two and three dimensions appears at approximately the same range of the attractive interaction. If we take the point of view that a solid of long spherocylinders resembles a two-dimensional crystal, then it seems reasonable to surmise that the range of q -values for which the solid-solid transition is possible, depends only little on L/D . It should, however, be stressed that the analogy between a solid of almost very long, well aligned spherocylinders in the AAA-phase, and a two-dimensional crystal of disks, is not perfect, because the orientational entropy of the rods can never be neglected. There are gaps between the three different regions of solid-solid transitions. In those gaps, the effect of the depletion interaction is to widen the density gap between two coexisting solid phases of different symmetry. Finally, it is tempting to speculate that the effect of the depletion interaction on the phase behavior of the AAA-stacked solid, may be even more complex. In a two-dimensional system, the solid-solid critical point induces a hexatic pocket in the phase diagram [50]. Possibly, the solid-solid transition in the AAA-stacked phase favors the formation of a liquid-crystalline hexatic-B phase.

6.6 Conclusion

To study the phase diagram of rodlike particles mixed with non-adsorbing polymer, we have performed simulations in a number of limiting cases, and compared the results with perturbation theory.

First of all, we simulated a system of spherocylinders with aspect ratio $L/D=5$. The effect of the added polymer was represented by an effective pair-potential. The range of this generalized square-well potential (q) is a measure for the size (radius of gyration) of the polymer. For large polymer sizes, an isotropic-isotropic phase separation takes place that ends in a critical point. This critical point shifts to higher density and higher polymer fugacity as the polymer radius is reduced. Eventually (for $q < 0.6$), the I-I transition is preempted by the I-N transition. The perturbation theory results and our simulations on spherocylinders with a generalized square-well interaction indicate that, for $L/D=5$ there is no phase separation in the nematic or smectic phase. We expect that, for very small q (≤ 0.05), there is a solid-solid transition at high densities, but we have not verified this. For large q , the I-N-SmA triple point occurs at a lower fugacity than the I-SmA-S point, but for $q < 0.45$, the I-SmA-S triple point disappears and we are left with a I-N-SmA and a N-SmA-S triple point. The latter is located at the lower fugacity.

A nematic-nematic phase separation is possible for large L/D . In the limit $L/D \rightarrow \infty$, the N-N transition is not yet possible for $q=1$. We estimate that N-N coexistence becomes possible for q -values larger than one. For finite L/D -values, the q -window of stability is

also bounded from the upper side, where the I-N transition will eventually preempt the N-N phase separation.

If a smectic-smectic separation occurs at all, it is likely to be confined to a narrow window in the $q, L/D$ plane. At high densities and small values of q , it is possible to have isostructural solid-solid transitions, involving the plastic solid, ABC-stacked solid, and AAA-stacked solid, for small, intermediate and large L/D -values, respectively.

We expect that polydispersity of the spherocylinders will have a pronounced effect on the phase behavior. Polydispersity in the length will stabilize the nematic phase and make a nematic-nematic transition possible at shorter (average) lengths. In contrast, polydispersity in the diameter of the spherocylinders will stabilize the smectic A phase, and could thereby favor the occurrence of a smectic-smectic phase transition.

Bibliography

- [1] H.B. Callen. *Thermodynamics and an introduction to thermostatistics*. Addison-Wesley Publ. Comp., Inc., 2nd edition, 1985.
- [2] J.P. Hansen and I.R. McDonald. *Theory of simple liquids*. Academic Press Limited, 2nd edition, 1990.
- [3] M.P. Allen and D.J. Tildesley. *Computer simulation of liquids*. Pergamon Press, Oxford, 1987.
- [4] J.D van der Waals. *On the continuity of the gaseous and liquid states*. PhD thesis, Hoogeschool te Leiden, The Netherlands, 1873.
- [5] P.C. Hemmer and J.L. Lebowitz. In C. Domb and M. Green, editors, *Critical Phenomena and Phase Transitions*. Academic Press, New York, 1976.
- [6] A.P. Gast, C.K. Hall and W.B. Russel. *J. Coll. Inter. Sci.*, 96:251, 1983.
- [7] S. Asakura and F. Oosawa. *J. Chem. Phys.*, 22:1255, 1954.
- [8] P.N. Pusey. In D. Levesque J.P. Hansen and J. Zinn-Justin, editors, *Liquids, Freezing and the Glass Transition*, Les Houches, session LI, 1991. North-Holland, Amsterdam.
- [9] E.J. Meijer and D. Frenkel. *Phys. Rev. Lett.*, 67:1110, 1991.
- [10] E.J. Meijer and D. Frenkel. *J. Chem Phys.*, 100:6873, 1994.
- [11] M.H.J. Hagen, E.J. Meijer, G.C.A.M. Mooij, D. Frenkel and H.N.W. Lekkerkerker. *Nature*, 365:425, 1993.
- [12] L. Mederos and G. Navascués. *Phys. Rev. B*, 50:1301, 1994.
- [13] D. Rosenbaum, P.C. Zamora and C.F. Zukoski. *Phys. Rev. Lett.*, 76:150, 1996.
- [14] W.B. Russel, D.A. Saville and W.R. Schowaltes. *Colloidal dispersions*. Cambridge University Press, Cambridge, 1989.
- [15] L. Onsager. *Chem. Rev.*, 13:73, 1933.
- [16] W.G. McMillan and J.E. Mayer. *J. Chem. Phys.*, 13:276, 1945.
- [17] H.N.W. Lekkerkerker, P. Buining, J. Buitenhuis, G.J. Vroege and A. Stroobants. In L.F. Rull M. Baus and J.P. Ryckaert, editors, *Observation, prediction and simulation of phase transitions in complex fluids*. Kluwer Academic Publishers, 1995.
- [18] E.J.W. Verweij and J.Th.G. Overbeek. *Theory of the stability of lyophobic colloids*. Elsevier, New York, 1948.
- [19] D.H. Napper. *Polymeric stabilization of colloidal dispersions*. Academic Press, London, 1983.
- [20] A. Vrij. *Pure Appl. Chem.*, 48:471, 1976.
- [21] H.N.W. Lekkerkerker, W.C-K. Poon, P.N. Pusey, A. Stroobants and P.B. Warren. *Europhys. Lett.*, 20:559, 1992.
- [22] A.K. van Helden, J.W. Jansen and A. Vrij. *J. Colloid Interface Sci.*, 81:354, 1981.
- [23] P.J. Flory. *Principles of Polymer Chemistry*. Cornell University Press, Ithaca and London, 1953.
- [24] G.J. Vroege and H.N.W. Lekkerkerker. *Rep. Progr. Phys.*, 55:1241, 1992.
- [25] L. Onsager. *Ann. N.Y. Acad. Sci.*, 51:627, 1949.
- [26] J.A.C. Veerman and D. Frenkel. *Phys. Rev. A*, 41:3237, 1990.
- [27] S.C. McGrother, D.C. Williamson and G. Jackson. *J. Chem. Phys.*, 104:6755, 1996.
- [28] M.A. Tracy, J.L. Garcia and R. Pecora. *Macromolecules*, 26:1862, 1993.
- [29] T. Biben and J.P. Hansen. *Phys. Rev. Lett.*, 66:2215, 1991.
- [30] H.N.W. Lekkerkerker and A. Stroobants. *Physica A*, 195:387, 1993.
- [31] A.Z. Panagiotopolous. *Mol. Phys.*, 61:813, 1987.
- [32] M. Stapleton A.Z. Panagiotopolous, N. Quirke. *Mol. Phys.*, 63:527, 1988.
- [33] Ph. de Smedt B. Smit and D. Frenkel. *Mol. Phys.*, 68:931, 1989.
- [34] D. Frenkel. In M.P. Allen an D.J. Tildesley, editor, *Computer simulation in chemical physics*, page 93. Kluwer Academic Publishers, Dordrecht, 1993.
- [35] T. Biben. PhD thesis, Université Claude Bernard-Lyon 1, France, 1993.
- [36] B. Widom. *J. Chem. Phys.*, 39:2808, 1963.

BIBLIOGRAPHY

- [37] N.F. Carnahan and K.E. Starling. *J. Chem. Phys.*, 51:635, 1969.
- [38] W.G.T. Kranendonk. *Computer simulation of models for colloidal systems*. PhD thesis, Rijksuniversiteit Utrecht, The Netherlands, 1990.
- [39] D. Frenkel and A.J.C. Ladd. *J.Chem.Phys.*, 81:3188, 1984.
- [40] H. Reiss, H.L. Frisch and J.L. Lebowitz. *J. Chem. Phys.*, 31:369, 1959.
- [41] P.G. Bolhuis and D. Frenkel. *Phys. Rev. Lett.*, 72:221, 1994.
- [42] Y. Mao, M.E. Cates and H.N.W. Lekkerkerker. *Phys. Rev. Lett.*, 75:4548, 1995.
- [43] J. Chang and S.I. Sandler. *Mol. Phys.*, 81:745, 1994.
- [44] D.A. Young and D.J. Alder. *J.Chem. Phys.*, 73:2430, 1980.
- [45] C.F. Tejero, A. Daanoun, H.N.W. Lekkerkerker and M. Baus. *Phys. Rev. Lett.*, 73:752, 1994.
- [46] C. Rascon, G. Navascues and L. Mederos. *Phys. Rev. B*, 51:14899, 1995.
- [47] B.I Halperin and D.R. Nelson. *Phys. Rev. Lett.*, 41:121, 1978.
- [48] D.R. Nelson and B.I Halperin. *Phys. Rev. B*, 19:2457, 1979.
- [49] A.P. Young. *Phys. Rev. B*, 19:1855, 1979.
- [50] P. Bladon and D. Frenkel. *Phys. Rev. Lett.*, 74:2519, 1995.
- [51] R.J. Baxter. *J. Chem. Phys.*, 49:2270, 1968.
- [52] G. Stell and P.C Hemmer. *J. Chem. Phys.*, 56:4274, 1972.
- [53] D. Frenkel. In G.Ciccotti and W.G. Hoover, editors, *Molecular Dynamics Simulation of Statistical Mechanical Systems*, page 151. North-Holland, Amsterdam, 1986.
- [54] R. Hall. *J. Chem. Phys.*, 57:2252, 1972.
- [55] B. Alder and D. Young. *J. Chem. Phys.*, 70:473, 1979.
- [56] W.G. Hoover and F.H. Ree. *J. Chem. Phys.*, 49:3609, 1968.
- [57] W.G Rudd, Z.W. Salzburg, A.P. Yu and F.H. Stillinger. *J. Chem. Phys.*, 49:4857, 1968.
- [58] B. Barboy. *J. Chem. Phys.*, 61:3194, 1974.
- [59] S.J. Smithline and A.D.J. Haymet. *J. Chem. Phys.*, 83:4103, 1985.
- [60] C. Cerjan and B. Bagchi. *Phys. Rev. A*, 31:1647, 1985.
- [61] N.A. Seaton and E.D. Glandt. *J. Chem. Phys.*, 87:1785, 1987.
- [62] W.G.T. Kranendonk and D. Frenkel. *Mol. Phys.*, 64:403, 1988.
- [63] G. Stell. *J. Stat. Phys.*, 63:1203, 1991.
- [64] H. Eyring. *J. Chem. Phys.*, 4:238, 1936.
- [65] J.E. Lennard-Jones and A.F Devonshire. *Proc. R. Soc. London. Ser. A*, 169:317, 1939.
- [66] J.A. Barker. *Lattice theories of the liquid state*. Pergamon Press, Oxford, 1963.
- [67] J.A. Barker. *J. Chem. Phys.*, 44:4212, 1966.
- [68] C.F. Tejero A. Daanoun and M. Baus. *Phys. Rev. E.*, 50:2913, 1994.
- [69] C.N. Likos, Zs. T. Németh and H. Löwen. *J. Phys. Condensed Matter*, 6:10965, 1994.
- [70] M.H.J. Hagen and D. Frenkel. *J. Chem. Phys.*, 101:4093, 1994.
- [71] A. Jayaraman. *Phys. Rev.*, 137:A179, 1965.
- [72] G. Stell Kincaid and E. Goldmark. *J.Chem Phys.*, 65:2172, 1976.
- [73] X. Cottin and P.A. Monson. *J. Chem. Phys.*, 99:8914, 1993.
- [74] X. Cottin and P.A. Monson. *J. Chem. Phys.*, 102:3354, 1995.
- [75] M.D. Eldridge, P.A. Madden and D. Frenkel. *Nature*, 365:35, 1993.
- [76] D. Frenkel, H.N.W. Lekkerkerker and A. Stroobants. *Nature*, 332:882, 1988.
- [77] M.P. Allen, G.T. Evans, D. Frenkel and B.M. Mulder. *Adv. Chem. Phys.*, 86:1, 1993.
- [78] E. Dickinson. *Discussions Faraday Soc.*, 65:127, 1978.
- [79] E. Dickinson, R. Parker and M. Lal. *Chem. Phys. Lett.*, 79:578, 1981.
- [80] E. Dickinson and R. Parker. *J. Physique Lett.*, 46:L-229, 1985.
- [81] P. Pusey. *J. Physique*, 48:709, 1987.
- [82] J.L. Barrat and J.P. Hansen. *J. Physique*, 46:1547, 1986.
- [83] R. McRae and D.J. Haymet. *J. Chem. Phys.*, 88:1114, 1988.
- [84] D.A. Kofke. *J. Chem. Phys.*, 98:4149, 1993.
- [85] J.G. Briano and E.D. Glandt. *J. Chem. Phys.*, 80:3336, 1984.
- [86] D.A. Kofke and E.D. Glandt. *J. Chem. Phys.*, 87:4881, 1987.
- [87] D.A. Kofke and E.D. Glandt. *Mol. Phys.*, 64:1105, 1988.
- [88] M. Metha and D.A. Kofke. *Chem. Eng. Sci.*, 49:2633, 1994.

BIBLIOGRAPHY

- [89] W. Schaertl and H. Sillescu. *J. Stat. Phys.*, 77:1007, 1994.
- [90] G.A. Mansoori, N.F. Carnahan, K.E. Starling and T.W. Leland Jr. *J. Chem. Phys.*, 54:1523, 1971.
- [91] D.A. Kofke and E.D. Glandt. *J. Chem. Phys.*, 90:439, 1988.
- [92] B.J. Alder and T.A. Wainwright. *J. Chem. Phys.*, 27:1208, 1957.
- [93] W. W. Wood and J. D. Jacobson. *J. Chem. Phys.*, 27:1207, 1957.
- [94] J. Vieillard-Baron. *Mol. Phys.*, 28:809, 1974.
- [95] D.Frenkel and B.M.Mulder. *Mol. Phys.*, 55:1171, 1985.
- [96] A. Stroobants, H.N.W. Lekkerkerker and D. Frenkel. *Phys. Rev. A*, 36:2929, 1987.
- [97] D. Frenkel. *J. Phys. Chem.*, 91:4912, 1987.
- [98] D. Frenkel. *Liquid Crystals*, 5:929, 1989.
- [99] J.A.C. Veerman and D. Frenkel. *Phys. Rev. A*, 45:5633, 1992.
- [100] S. Fraden. In L.F. Rull M. Baus and J.P. Ryckaert, editors, *Observation, prediction and simulation of phase transitions in complex fluids*. Kluwer Academic Publishers, 1995.
- [101] P.G. Bolhuis, M.H.J. Hagen and D. Frenkel. *Phys. Rev. E*, 50:4880, 1994.
- [102] A. Poniewierski and R. Holyst. *Phys. Rev. A*, 41:6871, 1990.
- [103] A. Poniewierski and T.J. Sluckin. *Phys. Rev. A*, 43:6837, 1991.
- [104] A.M. Somoza and P. Tarazona. *Phys. Rev. A*, 41:965, 1990.
- [105] D.W. Rebertus and K.M Sando. *J. Chem. Phys.*, 67:2587, 1977.
- [106] M.P. Allen, D Frenkel and J. Talbot. *Comp. Phys. Rep.*, 9:301, 1989.
- [107] S.J. Singer and R. Mumaugh. *J. Chem. Phys.*, 93:1278, 1990.
- [108] J.A.Zollweg and G.V. Chester. *Phys. Rev. B*, 46:11187, 1992.
- [109] L.D. Landau and E.M. Lifshitz. *Statistical physics*. Pergamon Press, Oxford, 3rd edition, 1980.
- [110] H.N.W. Lekkerkerker, P. Coulon, R. van der Haegen and R. Deblieck. *J. Chem. Phys.*, 80:3427, 1984.
- [111] D. Frenkel. *J. Phys. Chem.*, 91:4912, 1987.
- [112] A. Poniewierski. *Phys. Rev. A*, 45:5605, 1992.
- [113] H.N.W Lekkerkerker and A.Stroobants. *Nuovo Cimento D*, 16:949, 1994.
- [114] S.S. Cohen. *J. Biol. Chem.*, 144:353, 1942.
- [115] P.A. Buining, C. Pathmamamnoharan, J.B.H. Jansen and H.N.W. Lekkerkerker. *J. Am. Ceram. Soc.*, 74:1013, 1991.
- [116] J. Buitenhuis, L.N. Donselaar, P.A. Buining, A.Stroobants and H.N.W Lekkerkerker. *J. Coll. Interface Sci.*, 175:46, 1995.
- [117] P.A. Buining, Y.S.J. Veldhuizen, C. Pathmamamnoharan, and H.N.W. Lekkerkerker. *Colloid Surfaces*, 64:47, 1992.
- [118] R. van Roij. *Simple theories of complex fluids*. PhD thesis, Universiteit Utrecht, The Netherlands, 1996.
- [119] P.J. Flory. *Proc. R. Soc. London*, 234:73, 1956.
- [120] A.R. Khokhlov and A.N. Semenov. *J. Stat. Phys.*, 38:161, 1985.
- [121] R. van Roij and B.M. Mulder. *J. Phys. II France*, 4:1763, 1994.
- [122] L.J. Yu and A. Saupe. *Phys.Rev.Lett.*, 45:1000, 1990.
- [123] R. Bartoline, T. Chianranza and M. Meuti and R. Compagnoni. *Phys. Rev. A*, 26:1116, 1982.
- [124] Y. Galerne, A.M. Figueiredo Neto and L. Liébert. *J. Chem. Phys.*, 87:1851, 1987.
- [125] L.Q. Amaral and M.E. Marcondes Helene. *J. Phys.Chem.*, 92:6094, 1988.
- [126] P. Quist. *Liquid Crystals*, 18:623, 1995.
- [127] P. Tolédano and A.M. Figueiredo Neto. *Phys.Rev.Lett.*, 73:2216, 1994.
- [128] B. Mulder. *Phys. Rev. A*, 39:360, 1989.
- [129] M.P Allen. *Liquid Crystals*, 8:499, 1990.
- [130] A. Stroobants and H.N.W. Lekkerkerker. *J. Phys. Chem.*, 88:3669, 1984.
- [131] P.J. Camp and M.P. Allen. *Physica A*, page in press.
- [132] H.N.W. Lekkerkerker and A. Stroobants. *Physica A*, 195:387, 1993.
- [133] M. Dijkstra and D. Frenkel. *Phys. Rev. Lett.*, 72:298, 1994.

Summary

This thesis describes a series of studies investigating the influence of the inter-particle potential range on the phase behavior of colloidal dispersions. The possible existence of a liquid-vapor transition in a (colloidal) fluid depends very sensitively on this range of interaction. In the case of infinitely long ranged, infinitely weak attractive potential we recover the van der Waals model which shows a first-order liquid-vapor transition ending in a critical point. For systems with shorter interaction range the stable liquid region shrinks. When the range of attraction is about a third of the hard core diameter the liquid-vapor transition becomes metastable with respect to the fluid-solid transition. The range of interaction can be tuned by addition of non-adsorbing polymer to the colloidal dispersion. The polymers induce an effective attraction between the colloidal particles which range is directly related to the radius of gyration of the polymer. For a radius of gyration larger than approximately $1/3$ of the hard-core radius a liquid-vapor transition is observed. This behavior is well known in the case of fully flexible polymers. In chapter 2 we investigated the opposite case of a mixture of spherical colloidal particles and rigid rodlike polymers, modeled as infinitely thin needles. This mixture shows a liquid-vapor transition for polymer lengths larger than 20% of the hard core colloid diameter and sufficiently high polymer concentrations. The mechanism of this phase separation is equal to that of the colloid—flexible-polymer mixture: the gain in free volume of the polymers upon clustering of the colloidal particles outweighs the loss of entropy of these particles. When the length of the polymer increases, the critical point shifts to lower density and lower polymer concentration. When the range of interaction becomes very small a solid-solid phase separation might occur, in which a condensed solid is in equilibrium with an expanded solid of the same structure. This phase transition is reminiscent of the liquid-vapor transition. Again we might find this type of phase separation in colloidal dispersions mixed with polymer with a small radius of gyration. In chapter 3 we studied the solid-solid transition in detail for colloidal particles interacting via a simple square well attraction. In both two and three dimensions the solid-solid transition appears to be stable with respect to the melting transition for a well width smaller than 7% of the hard sphere diameter. The critical temperature only weakly depends on the square well width, whereas the critical density is sensitive to the range of interaction and is very well predicted by cell theory. The solid-solid transition is not an artifact of the square well model as we checked by simulation of the Yukawa model. The solid-solid transition is influenced by the amount of polydispersity of the colloidal dispersion and becomes metastable with respect to melting for size polydispersities larger than 1%. As every colloidal suspension exhibits a certain amount of size polydispersity it is interesting to examine how polydispersity affects the phase behavior of colloidal dispersions in general. In chapter 4 we examined the influence of polydispersity on the hard sphere freezing transitions. By combining the semigrand ensemble with the Gibbs-Duhem integration technique we were able to map out the coexistence curves of the hard sphere fluid-solid transition. As already predicted in theory and observed in experiments we found a 'terminal' polydispersity above which freezing is not possible. This terminal polydispersity is about 5% in the solid

and 15% for the fluid. This considerable fractionation upon increasing the polydispersity was not taken into account in the theoretical studies.

The second half of the thesis deals with the behavior of systems of non-spherical colloidal particles. In chapter 5 we mapped out the entire phase diagram of the spherocylinder system. This simple model system has a rich phase behavior as it exhibits at least five stable phases depending on the length to width ratio L/D and the density. At low density the isotropic phase is always stable. At high density and $L/D < 0.35$ the system crystallizes to a plastic solid with no orientational order. At higher densities there is a first order transition to an orientationally ordered *fcc*-crystal. We were able to simulate this transition all the way to close packing. For $L/D > 4$, there is a first order isotropic-nematic transition. The I-N transition density decreases with L/D and goes to zero in the Onsager limit $L/D \rightarrow \infty$. When increasing the density, a nematic-smectic transition takes place, which is first order for $L/D > 4$, but presumably becomes continuous at the tricritical point located somewhere between $L/D=6$ and $L/D = \infty$. We were able to perform simulations in the $L/D \rightarrow \infty$ limit, although we could not establish the order of the N-SmA transition. At high density the smectic phase will transform into an AAA-stacked crystal, which at very high density changes into an ABC- stacked *fcc* crystal. In the limit $L/D \rightarrow \infty$, the first order AAA-ABC transition moves to close packing. For $L/D < 7$ the AAA-stacked crystal becomes unstable. The location of the phase transitions will change upon addition of polymer. In chapter 6 we examined the phase behavior of spherocylinder-polymer mixtures. We applied perturbation theory to estimate the influence of polymers on the phase behavior of a $L/D=5$ system. For large polymer diameter there is an isotropic-isotropic phase separation which corresponds to the liquid-vapor phase separation in the spherical colloid case. The nematic phase becomes metastable with respect to the isotropic-smectic transition for high polymer fugacity and at even higher fugacity the smectic phase becomes metastable with respect to the isotropic-solid phase transition. When reducing the polymer radius, the critical point of the I-I binodal will shift to higher density and becomes eventually metastable. We do not observe a N-N or SmA-SmA phase separation for smaller polymers, although we do expect a solid-solid transition for very small polymer diameter. For $L/D > 40$ an N-N transition can occur.

To test whether or not the perturbation theory picture is valid in systems with finite fugacity we devised an anisotropic attractive potential which mimics the polymer depletion interaction. Spherocylinders of $L/D=5$ interacting through this potential showed qualitatively the same phase behavior as estimated by the perturbation theory.

The last chapter contains a numerical study of the competition between a phase separation and the formation of a biaxial phase in a mixture of rod and plate like particles. Theoretical studies showed that for sufficient particle elongation these mixtures form a biaxial phase at a composition of 50% which phase separates at higher densities in a rod-rich nematic and a plate-rich nematic. Our Gibbs-Ensemble simulations of a rod-plate ellipsoid mixture showed indeed phase separation. However, the rod-rich phase appeared to be biaxial so that there is in fact coexistence between a plate-rich nematic and a biaxial phase. This asymmetry is not present in the theoretical predicted phase diagram and is probable due to asymmetry in the higher order virial coefficients of both species.

In conclusion, by means of computer simulation we have showed that the phase behavior of a system is to a great extent determined by the range of interaction between the particles. Changing this range can lead to unexpected and new phase behavior which hopefully can be observed experimentally in polymer-colloid mixtures.

Samenvatting voor iedereen

Natuurwetenschappen worden gekenmerkt door een wisselwerking van theorie en experiment. In een experiment worden observaties gedaan die door een theorie verklaard of beschreven moeten kunnen worden. De theorie kan dan een voorspelling doen die weer getest kan worden in nieuwe experimenten.

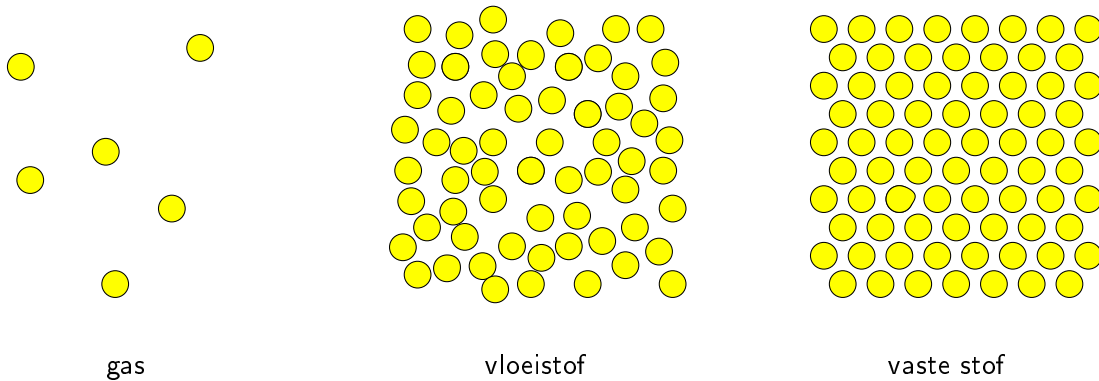
Sinds een jaar of 40 is er een onderzoeksmethode die als het ware een brug slaat tussen theorie en experiment: computer simulaties. In een computer simulatie bootsen we de echte wereld na door uit te gaan van een (simpel) model voor de allerkleinste deeltjes, de atomen waaruit iedere stof bestaat. Door duizenden atomen met elkaar te laten botsen kunnen we een uitspraak doen over de eigenschappen van het materiaal dat we bestuderen. Aan de ene kant is een simulatie als een theorie, we stoppen er een bepaald model in en wat we willen weten komt er uit. Een belangrijk verschil is dat een theorie niet alleen een model voor kleine deeltjes moet hebben maar ook veel aannamen en benaderingen moet maken om een fatsoenlijke uitspraak te kunnen doen. De simulatie kan dus gebruikt worden om de geldigheid van die aannamen en benaderingen te testen. Aan de andere kant is een simulatie als een experiment, we selecteren bepaalde omstandigheden als temperatuur en druk en berekenen in de computer hoe de stof zich gaat gedragen. Zo kunnen simulaties helpen om nieuwe laboratorium experimenten te plannen. Ook kunnen simulaties gedaan worden onder omstandigheden die nooit in een laboratorium gehaald kunnen worden. Bijvoorbeeld bij de extreme drukken in het binnenste van een ster.

In dit proefschrift worden computersimulaties beschreven die gedaan zijn met eenvoudige modellen, bijvoorbeeld met bolvormig deeltjes. Hoewel het mogelijk is om een atoom heel nauwkeurig te benaderen, kost een simulatie met zo'n nauwkeurig model een enorme hoeveelheid rekenwerk. Vaak blijkt een simpel model, zoals een bolvormig deeltje, al voldoende te zijn om alle essentiële aspecten van een natuurkundig proces op te leveren.

Alledaagse materie komt meestal voor in drie soorten toestanden of fasen: gas, vloeistof en vaste stof (ook wel kristalfase genoemd). Voor water is dit bijvoorbeeld: waterdamp, water en ijs. Welke toestand of fase optreedt, hangt af van externe factoren als de temperatuur, opgelegde druk of de dichtheid van de stof. Hoe en waarom deze factoren het fase gedrag beïnvloeden is van belang voor de fundamentele wetenschap maar ook voor industriële toepassingen en processen.

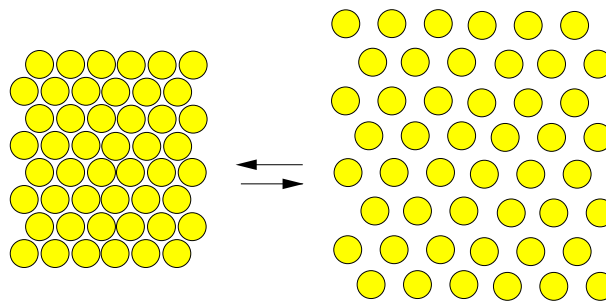
De verschillen tussen de drie fasen zijn voornamelijk bepaald door de dichtheid (aantal atomen per liter) en de ordening van de atomen op microscopische schaal. In een gas is de dichtheid laag en bewegen de atomen kris-kras door elkaar. De vloeistof is ook ongeordend van structuur maar wordt gekenmerkt door een hogere dichtheid dan de gas fase. In de vaste fase zijn de atomen netjes gerangschikt volgens een kristalrooster maar kunnen ze nog wel bewegen rond hun gemiddelde positie.

Als we een gas in een vat bij hoge temperatuur een tijdje met rust laten zal het tot evenwicht komen. In evenwicht bewegen alle atomen nog steeds razendsnel maar verandert er zichtbaar niets. Verlagen we de temperatuur dan zal het gas condenseren en zal er een



vloeistof ontstaan. Laten we het gas-vloeistof mengsel met rust bij konstante temperatuur, dan is er een opnieuw een evenwicht, waarbij twee fasen met elkaar in evenwicht zijn: een fase-evenwicht. Tussen de gas en de vloeistof fase in evenwicht worden voortdurend atomen uitgewisseld, alhoewel er zichtbaar niets verandert. Een mooi voorbeeld is het beslaan van ramen, waarbij de vloeistof druppels op het koude raam in evenwicht zijn met de waterdamp in de kamer. Koelen we het gas/vloeistof mengsel in het vat verder af dan houden we op een gegeven moment (bijna) alleen vloeistof over die bij het vriespunt kristalliseert tot vaste stof. Ook hier is dan sprake van een fase-evenwicht, waarbij bijvoorbeeld in een winters slootje water en ijs tegelijkertijd kunnen bestaan.

Atomen trekken elkaar aan op lange afstand. De grootste afstand waarop atomen elkaar nog aantrekken heet de *dracht van de attractie*. Deze dracht is meestal even groot als of groter dan de diameter van de atomen. Dit blijkt een noodzakelijke voorwaarde te zijn voor het kunnen bestaan van de vloeistof fase. Wanneer dracht van de attractie verkleind zou kunnen worden en de atomen elkaar alleen kunnen aantrekken wanneer ze elkaar bijna raken, dan verdwijnt de mogelijkheid om een vloeistof te vormen en zal een gas, bij voldoende lage temperatuur, meteen kristalliseren zonder eerst te condenseren. Wordt de afstand waarop atomen elkaar beginnen te voelen zelfs kleiner dan 7% van de diameter dan gebeurt er iets onverwachts: er kan dan een fase-evenwicht ontstaan tussen twee vaste stoffen. In zo'n vast-vast fase-evenwicht is een kristal met een hoge dichtheid in evenwicht met een kristal van lagere dichtheid. Schematisch ziet dat er als volgt uit:

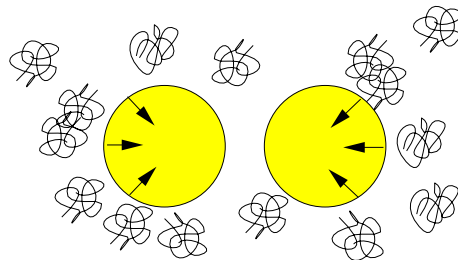


Het eerste deel van de titel van dit proefschrift —"vloeistof gedrag in vaste stoffen"— komt voort uit het vast-vast evenwicht. Dit evenwicht lijkt verrassend veel op het gas-vloeistof evenwicht, onder andere omdat er twee fasen van *gelijke structuur* in evenwicht zijn. In het gas-vloeistof geval zijn er twee ongeordende structuren en in het vast-vast geval zijn er twee geordende kristallijne structuren met elkaar in evenwicht.

In werkelijkheid kan dit fase-evenwicht voor de meeste atomen niet ontstaan omdat de afstand waarop de aantrekkende krachten werken niet gevarieerd kan worden maar al sinds de oerknal vast ligt. Maar in een computer simulatie is het natuurlijk een koud kunstje om de dracht van de attractie te veranderen. In hoofdstuk 3 beschrijf ik het effect van een korte dracht van de aantrekkende krachten op het fase gedrag van bolvormige deeltjes.

Tot nu toe heb ik het steeds over losse atomen gehad die met elkaar botsen en wisselwerken. De situatie wordt anders wanneer we het gedrag van bolvormige deeltjes bekijken die samengesteld zijn uit meer dan een miljard atomen: de zogenaamde colloïdale deeltjes. Deze colloïdale, vaste deeltjes zijn nog steeds kleiner dan een duizendste millimeter in doorsnee en kunnen gemengd worden met een oplosmiddel als water of alcohol. De brij die dan ontstaat noemen we een colloïdale suspensie of dispersie. Een paar voorbeelden uit de alledaagse praktijk zijn: melk, verf, bloed, modder en mayonaise. Met de uitzondering van biologische colloïden zoals rode bloedlichaampjes zijn colloïdale deeltjes in de natuur gewoonlijk erg onregelmatig van vorm en grootte. In het laboratorium kunnen colloïdale deeltjes gefabriceerd worden, die volkomen bolvormig zijn en (bijna) gelijk in grootte. Dispersies van dit soort deeltjes kunnen worden gebruikt om fase-evenwichten te bestuderen. Als het colloïdale deeltje wordt gezien als een gigantisch atoom (een colloïdaal deeltje is ongeveer 2000 keer zo groot in doorsnee als een atoom) dan blijkt het fase gedrag van colloïdale oplossingen heel veel te lijken op dat van atomen. De invloed van het oplosmiddel kan worden opgevat als een effectieve kracht tussen de colloïdale deeltjes. Meestal is deze kracht afstotend wanneer de deeltjes elkaar raken en aantrekkend wanneer ze verder van elkaar zijn. Op dezelfde manier als atomen vertonen colloïdale dispersies een lage dichtheids gasfase en een kristalfase waarbij alle deeltjes netjes geordenend zijn. De dracht van de attractie tussen de colloïdale deeltjes is meestal te klein om een vloeistoffase te laten ontstaan en zodoende vindt men alleen een gas-kristal evenwicht.

In tegenstelling tot de aantrekking tussen losse atomen kan de attractie tussen colloïdale deeltjes wel naar believen gevarieerd worden, onder andere door het toevoegen van polymeren aan colloïdale oplossingen. Polymeren zijn lange moleculen die enkele atomen dik zijn, maar een lengte van miljoenen atomen kunnen hebben. Toch zijn deze hele dunne draden wanneer ze volledig zijn uitgestrekt minder dan een tiende millimeter lang. In een oplosmiddel rollen ze zich op tot bolvormige kluwens die de speciale eigenschap hebben dat twee polymeer-kluwens elkaar volledig kunnen doordringen en elkaar nauwelijks beïnvloeden, maar dat een polymeer-kluwen met een colloïdaal deeltje botst als twee biljartballen. Door deze eigenschap zullen de polymeer ketens zich niet tussen twee colloïdale deeltjes in kunnen bevinden wanneer deze dicht bij elkaar zijn. Aan de andere zijden van de deeltjes kunnen zich wel polymeren bevinden die dan tegen de deeltjes botsen en ze naar elkaar toe duwen. Dit duwen kan ook gezien worden als een aantrekkende kracht, aangezien de



deeltjes efficiënt naar elkaar toe bewegen. De dracht van deze attractie is evenredig met de diameter van het polymeer-kluwen. Door het toevoegen van voldoende groot polymeer aan een colloïdale dispersie kan er een “gas-vloeistof” evenwicht ontstaan, waarbij de meeste colloïdale deeltjes in de vloeistof fase zitten en de meeste polymeren in de gas fase. Dit proces is schematisch weergegeven in figuur 1.3.

Een andere manier om tegen dit fase-evenwicht aan te kijken is in termen van entropie. Entropie kan gezien worden als het totaal aantal mogelijke verschillende toestanden dat een verzameling deeltjes kan aannemen. Dit aantal is groter wanneer er veel volume is, of liever veel vrij volume: het volume dat beschikbaar is voor een deeltje zonder dat het botst met andere deeltjes. In de gasfase is er veel vrij volume en is de entropie hoog. In een vloeistof is er weinig vrij volume omdat de deeltjes elkaar in de weg zitten, en dus is de entropie laag. Materie zal altijd proberen de entropie te maximaliseren. Een polymeer-kluwen heeft veel meer vrijheid om te bewegen in een omgeving met weinig colloïdale deeltjes. Ze zullen dus liever allemaal bij elkaar gaan zitten en een colloïdale gas fase vormen waarbij alle andere colloïdale deeltjes in de vloeistof fase gedruwd worden. Ondanks het feit dat de deeltjes in de vloeistof een lagere entropie hebben omdat ze dichter op elkaar zitten, is de totale entropie van de twee fasen bij elkaar veel hoger dan wanneer alles gemengd is. Hoofdstuk 2 laat zien dat deze beschrijving niet alleen opgaat voor polymeer-kluwens maar ook voor rechte staafvormige polymeren.

Wanneer het polymeer-kluwen een diameter heeft kleiner dan 7% van de diameter van de colloïdale deeltjes, kan het onverwachte, “onmogelijke” vast-vast fase-evenwicht plaats vinden in de kristallijne fase, waarbij een vaste fase van hoge dichtheid in evenwicht is met een vaste fase van lagere dichtheid.

Colloïdale deeltjes komen ook voor in de vorm van staafjes. Het fase gedrag van oplossingen van staafjes is heel anders dan dat van bolvormige deeltjes. Zo vertonen ze de tussen vloeistof en vaste stof gelegen vloeibaar-kristallijne fasen. In figuur 1.4 is de reeks van fasen afgebeeld die een oplossing van staafvormige deeltjes vertoont. Bij lage dichtheden is er een isotrope vloeistoffase, waarbij alle staafjes kris-kras door elkaar bewegen en willekeurig georiënteerd zijn. Bij voldoende hoge dichtheid ontstaat de nematische vloeibaar kristallijne fase. Hoewel alle deeltjes nog kris-kras door elkaar bewegen, kan de entropie verhoogd worden door alle deeltjes ongeveer in dezelfde richting te laten wijzen. Deze fase is van cruciaal belang voor de werking van LCD-schermen. Bij nog hogere dichtheden ontstaat de vloeibaar kristallijne smectische fase die gekenmerkt wordt door de vorming van laagjes. De staafjes wijzen allemaal in dezelfde richting en zijn min of meer gebonden aan een laag, alhoewel ze wel binnen een laag door elkaar kunnen bewegen. Je kunt de smectische fase zien als een vloeistof die maar in één richting gekristalliseerd. Hiernaar verwijst het tweede deel van de titel van het proefschrift: “kristallijn gedrag in vloeistoffen”. Wanneer de dichtheid nog hoger wordt, dan treedt er kristallisatie op en zijn alle deeltjes behalve georiënteerd ook aan hun plaats gebonden. Welke vloeibaar kristallijne fase onder welke omstandigheden optreedt, wordt uitvoerig uit de doeken gedaan in hoofdstuk 5.

Wanneer polymeer-kluwens aan colloïdale dispersies van staafjes worden toegevoegd zal er een attractieve kracht tussen de staven ontstaan. Deze kan ervoor zorgen dat er een gas-vloeistof fase-evenwicht optreedt in de isotrope fase, mits de dracht van de attractie groot genoeg is. Bij kleinere polymeren is de dracht kleiner en zal het gas-vloeistof evenwicht niet voorkomen. In het geval van lange staven is het wel mogelijk dat er een fase-evenwicht

tussen een nemaat van lage dichtheid en een nemaat van hoge dichtheid plaatsvind.

Samenvattend, de computer simulaties die zijn beschreven in dit proefschrift, hebben laten zien dat door de dracht van de attractie tussen deeltjes te variëren er nieuwe en onverwachte fase-evenwichten kunnen ontstaan. Nieuwe theorieën op het gebied van deze fase-evenwichten zullen in elk geval goed moeten overeenkomen met de simulatie resultaten. Theoretici kunnen de resultaten dus gebruiken om hun theorieën te testen. Het is echter aan de experimentatoren om te laten zien dat het voorspelde vast-vast fase-evenwicht ook echt voorkomt in colloïdale dispersies. Want uiteindelijk heeft de natuur het laatste woord.

Curriculum Vitae

Op 18 juni 1968 ben ik geboren te Dieren in de gemeente Rheden (Gelderland). Na het behalen van het ongedeelde VWO diploma ben ik in september 1986 begonnen met een studie Scheikunde aan de Universiteit Utrecht. Het propaedeutisch diploma kon ik ontvangst nemen in juni 1988. Na enkele bijvakken aan de vakgroepen thermodynamica en anorganische chemie te hebben afgerond, ben ik mijn onderzoeksjaar begonnen aan de vakgroep Fysische en Colloidchemie, alwaar ik onder leiding van prof. dr. H.N.W. Lekkerkerker gewerkt heb aan de lichtverstrooiing van oplossingen van polydisperse staafvormige deeltjes. In het kader van het Erasmus uitwisselingsproject heb ik in de eerste helft van 1992 samengewerkt met prof. dr. B. Jönsson aan de universiteit van Lund, Zweden. Het doctoraal examen heb ik aflegd in augustus 1992. In september 1992 ben ik als onderzoeker in opleiding aangenomen op het FOM-instituut voor Atoom- en Molecuulfysica (AMOLF). In de groep van prof. dr. D. Frenkel heb ik vier jaar lang promotie-onderzoek gedaan waarvan de resultaten vermeld staan in dit proefschrift. Tijdens deze periode heb ik enkele maanden doorgebracht aan de universiteit van New York in Buffalo, Verenigde Staten. Het onderzoek dat ik daar verricht heb in samenwerking met prof. dr. D. Kofke, staat ook beschreven in dit boekwerk.